A Six Degrees of Freedom MEMS Manipulator

Boudewijn de Jong

De promotie commissie

Voorzitter	
Prof. dr. ir. A. J. Mouthaan	Universiteit Twente
Promotor	
Prof. dr. M. C. Elwenspoek	Universiteit Twente
Promotor	
Prof. ir. H. M. J. R. Soemers	Universiteit Twente
Assistent promotor	
Dr. ir. G. J. M. Krijnen	Universiteit Twente
Leden	
Prof. dr. A. H. Dietzel	Technische Universiteit Eindhoven
Prof. dr. ir. J. van Eijk	Technische Universiteit Delft
Prof. dr. ing. J. van Müller	Technische Universität Hamburg-Harburg
Prof. dr. ir. S. Stramigioli	Universiteit Twente
Dr. ir. L. Abelmann	Universiteit Twente

The research described in this thesis is part of the Multi Axes Micro Stage (MAMS) project and has been conducted at the chair of Transducers Science and Technology of the department of Electrical Engineering at the University of Twente, Enschede. The research has been financially supported by the Innovative Oriented Research Program (IOP) Precision Technology (project IPT02308) from the Dutch Ministry of Economic Affairs.

Jong De, Boudewijn R.
A six degrees of freedom MEMS manipulator
Ph.D. Thesis, University of Twente, Enschede, The Netherlands
Cover: Artist impression of the 6 DOF manipulation concept ”under construction”
by Boudewijn de Jong

ISBN 90-365-2413-X

Printed by: Wöhrmann Print Service, Zutphen, The Netherlands

A SIX DEGREES OF FREEDOM MEMS MANIPULATOR

PROEFSCHRIFT

ter verkrijging van
de graad van doctor aan de Universiteit Twente,
op gezag van de rector magnificus,
prof. dr. W. H. M. Zijm,
volgens het besluit van het College voor Promoties
in het openbaar te verdedigen
op vrijdag 3 november 2006 om 15:00 uur

door

Boudewijn Ruben de Jong
geboren op 7 maart 1978
te Zaandam

Dit proefschrift is goedgekeurd door:

Prof. dr. M. C. Elwenspoek (promotor)
Prof. ir. H. M. J. R. Soemers (promotor)
Dr. ir. G. J. M. Krijnen (assistent promotor)

Aan mijn ouders Rein en Helen
en aan Maryana

Contents

Chapter 1

Introduction

1.1 Introduction in MEMS

MEMS is the acronym for Micro Electro Mechanical Systems. It is often revered to as Micro Systems Technology (MST) [1] as well, but conventional electric IC's are also covered by the term MST. MEMS devices refer to sensors, actuators, micro-fluidic systems and mechanical mechanisms, in the micrometer range which are typically manufactured using lithography based processing similar to semiconductor processes. These devices generally range in size from a micrometer to several millimeters. At these size scales, a human's intuitive sense of physics does not always hold. Due to MEMS large surface area to volume ratio, surface effects such as electrostatics and surface tension dominate volume effects such as inertia or thermal capacity. They are fabricated using modified silicon fabrication technology (used to make electronics), molding and plating, wet etching (KOH, TMAH) and dry etching (RIE and DRIE), electro discharge machining (EDM), and other technologies capable of manufacturing very small devices.

MEMS have the ability to integrate functions in a small package. For example a MEMS acceleration sensor is equipped with self diagnostics and a digital output. MEMS become commercially attractive if it provides cost reduction or enables new functionality. Automotive applications like pressure, acceleration and rate sensors replace or are replacing multi parts, assembled, precision engineered counterparts because of cost reduction. Cost reduction can also be established by cutting maintenance cost. New functionality is enabled by MEMS for example in the biomedical

industry, by integrating micro pumps, micro valves and micro sensors for fast analysis of liquids. The potential for future penetration in a broad range of applications is real. The Microsystems technology worldwide market has experienced a compounded annual growth rate (CAGR) in terms of shipment in dollars of 21.0% between 2000 and 2004 according to Roger Grace Associates and Nexus [2].

Although MEMS are commercially attractive especially for mass products (with integrated electronics), it can also enable new functionality in small markets. As part of the Multi Axis Micro Stage (MAMS) project a 6 Degree-of-freedom (DOF) precision Micro Electro Mechanical Systems (MEMS) based manipulator for a transmission electron microscope (TEM) is proposed. The focus is on designing and fabricating MEMS for precision manipulation in the micro domain. Not much literature is found regarding accurate positioning in MEMS. There is however no fundamental reason why positioning in MEMS cannot be accomplished on a nanometer level. In this thesis, design principles for accurate positioning in MEMS are derived.

1.2 Precision Engineering in MEMS

Precision engineering is the research and development, design, manufacture and measurement of high accuracy components and systems. It is related to mechanical, electronic, optical and production engineering, physics, chemistry, and computer and materials science [3]. From history precision engineering is associated with techniques as turning, milling, honing, lapping, polishing, grinding, electro discharge machining. Although the geometric uncertainty of these machining techniques might be at a sub-micron level, the feature size is usually not below the 0.1 millimeter range.

Precision systems potentially benefit from miniaturization. Not only does the size of devices decrease, but devices become faster, cheaper and greater functionality is offered in many cases [1]. In a keynote paper in Annals of the CIRP 2000, Corbett et al. discuss most of the following fields that will benefit increasingly from microsystems [4]. High density data storage projects like the Millipede project from IBM [5], where a thermal probe array is used for read/write data storage, require precise planar x/y-scanning and displacement in the out-of-plane direction. Furthermore, a high resonance frequency and low mass is required for fast data storage. For future ground based telescope applications, deformable micro mirrors for adaptive optics are required. Adaptive optics is used to correct for perturbations in the wavefronts of the incoming light caused by atmospheric turbulence. Conventional deformable mirrors are very expensive, whereas MEMS based deformable mirrors potentially offer a low cost alternative [6]. In the field of space applications, there is need for robust accelerometers, gyroscopes, and sensor applications to monitor and control the

harsh conditions in space. To enable further advances in nano-technology, ultra precision machines and instruments (with large trough-put and reduced cycle-time) are required. These include the various probe techniques like atomic force microscopy (AFM), scanning tunneling microscopy (STM) or magnetic, thermal and chemical reactive probes, but also energy beam tools like UV optical, ion-beam, e-beam and X-ray for structuring and Scanning Electron Microscopy (SEM) and Transmission Electron Microscopy (TEM) for characterization.

1.3 Aim of this research

Primarily, the aim of this research is to realize a multi-DOF manipulator with nanometer resolution positioning in MEMS technology. Additionally, fundamental solutions are looked for and investigated to apply design for precision systems in a MEMS system taking into account the fabrication limitations. This, among others, involves kinematic constrained design, minimizing friction and backlash, avoiding play and designing for high stiffness and low mass. Especially, fabrication process solutions to allow a large variety of mechanical functions are required in combinations with the particular process limitations and forthcoming design rules.

1.4 Transmission Electron Microscope

In order to obtain realistic specifications for the manipulation system, an example application is looked for. It is decided to adopt a manipulator for a transmission electron microscope (TEM) to obtain the required specifications. This example only concerns low frequent manipulation of masses much smaller than the manipulator. For this reason, the manipulator does not need to deliver (large) forces other than required to deflect its mechanism. This in contrast to an application for micro assembly, where relatively large forces are expected which in general are not easily predictable (one could think of adhesive bonding).

1.4.1 Introduction to electron microscopy

The TEM is a microscope which uses an imaging technique whereby a beam of electrons is used to project a magnified image of a sample on a fluorescent screen, or via imaging by a CCD camera[1]. The TEM is used in both material science/metallurgy and the biological sciences and is able to image at sub-angstrom resolution.

[1] Although electrons with enough energy can be detected with a CCD camera, usually an indirect method is applied, where the image of the fluorescent screen is projected on the CCD.

The maximum spatial resolution that one can image by optical microscopy is limited by the wavelength of the photons that are being used to probe the sample. In the early days the resolution was limited by the wavelength of 400-700 nm. Nowadays a magnification of up to 100× with a resolution of up to 0.2 micrometers is not uncommon. Using smaller wavelengths, like ultraviolet light, soon runs into problems of absorption. X-rays with wave lengths less than 10 nanometer exhibit a lack of interaction: both in focusing and actually interacting with the sample.

Electrons, have both wave and particle properties (as theorized by Louis-Victor de Broglie). The wave-like properties mean that a beam of electrons can in some circumstances be made to behave like a beam of radiation. Electrons have a wavelength in the order of a few picometers, depending on their energy (momentum). This wavelength is much smaller than that of visible light, yet electrons can still interact with the sample due to their electrical charge. It provides a resolution far better than is possible with light microscopes, and with improved depth of field. Basically two types of electron microscopes exist:

- ◇ The scanning electron microscope (SEM) looks at a surface of objects by scanning the surface with a fine electron beam and measuring reflection. It yields good depth of focus images of a surface at a resolution down to less than a nanometer.
- ◇ In transmission electron microscopy electrons pass completely through the sample, analogous to basic translucent optical microscopy. It can produce images with resolutions down to 0.08 nm at magnifications of 50 million times. The samples need to be specially prepared however to become extremely thin.

1.4.2 TEM and TEM applications

TEM A TEM consists of a long column which is vibration isolated from the floor (see figure 1.1). The column in its basic form consists of an electron gun, a number of electromagnetic lenses, the sample manipulator, a diaphragm, a fluorescent screen and a camera system. The electrons in a TEM are generated by thermionic discharge in the same manner as the cathode in a cathode ray tube, or by field emission. They are then accelerated by an electric field and focused by electromagnetic condenser lenses onto a sample. The sample is situated in the objective lens, where the electrons travel parallel to the column. The projector lenses project and magnify the image on a screen. A major advantage of these electromagnetic lenses is that the focal length can be changed without moving parts. It makes mechanical lens adjustments superfluous. However like optical lenses, these lenses also experience aberrations. To minimize aberrations the gap between the lens pole pieces focussing the electron beam on the

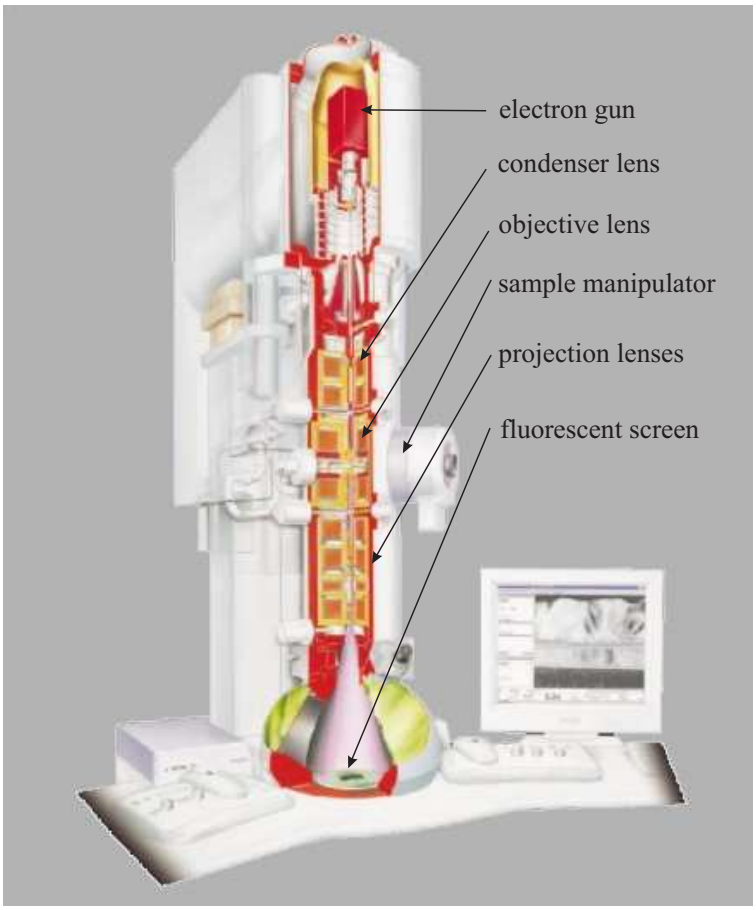

Figure 1.1: Cross-section of a TEM-column (Courtesy of FEI).

sample (see figure 1.3 on page 8) needs to be minimized. As a result little space for a sample manipulator is left.

An additional class of TEMs is the electron cryomicroscope, which includes a sample stage which is cooled by liquid nitrogen or liquid helium. The technique is used typically for biological samples, which need cooling to withstand the vacuum. The sample is first embedded in vitreous ice, or fixated using negative staining[2].

Another type of TEM is the scanning TEM (STEM), where the beam can be rastered across the sample to form the image. The rastering of the beam across the sample makes it possible to determine the elemental composition of the sample by analyzing its X-ray spectrum (EDX) or the energy-loss spectrum of the transmitted electrons (EELS).

[2]The use of an electron dense material around but not on top of the specimen to improve the contrast by scattering of the electrons coming from the surrounding.

TEM applications For biological samples, the maximum sample thickness is roughly 1 micrometer. Typical biological applications include tomographic reconstructions of small cells or thin sections of larger cells and 3D reconstructions of individual molecules via Single Particle Reconstruction. Tomography involves the generation of a three-dimensional reconstruction with help of slices or sections through a three-dimensional object obtained with the TEM.

In material science/metallurgy the samples tend to be naturally resistant to vacuum, but must be prepared as a thin foil, or etched such that some portion of the sample is thin enough for the beam to penetrate. Generally the thickness of a sample is less than 300 nm. Preparation techniques to obtain an electron transparent region include ion beam milling and wedge polishing. The focused ion beam (FIB) is a relatively new technique to prepare thin samples for TEM examination from larger samples. Because the FIB can be used to micro-machine samples very precisely, it is possible to mill very thin membranes from a specific area of a sample, such as a semiconductor or metal (figure 1.2 a and b).

The TEM has the ability to determine the positions of atoms within materials. Figure 1.2 c and d shows two high resolution images of semiconductor materials typically used in material research.

1.5 Requirements for the TEM manipulator

TEM limitations There are a number of drawbacks to the TEM technique. Many materials require extensive sample preparation to produce a sample thin enough to be electron transparent, which makes TEM analysis a relatively time consuming process with a low throughput of samples. The structure of the sample may also be changed during the preparation process. Also the field of view is relatively small, raising the possibility that the region analyzed may not be characteristic for the whole sample. There is potential that the sample may be damaged by the electron beam, particularly in the case of biological materials.

The TEM sample manipulator The maximum achievable image resolution is the most important specification of a TEM. Currently the sample manipulators instability mainly determines the maximum image resolution, making the manipulator one of the most critical mechanical parts of a TEM. A typical current sample manipulator controls 5 DOF over displacements in the mm-range. There are two rotational DOF of several tens of degrees. The drift rate is typically in the tenths of nanometers per minute directly after positioning the sample [7]. The drift decreases to less than 1 nanometer per minute if the TEM is left to homogenize for as long as half an hour. This drift rate

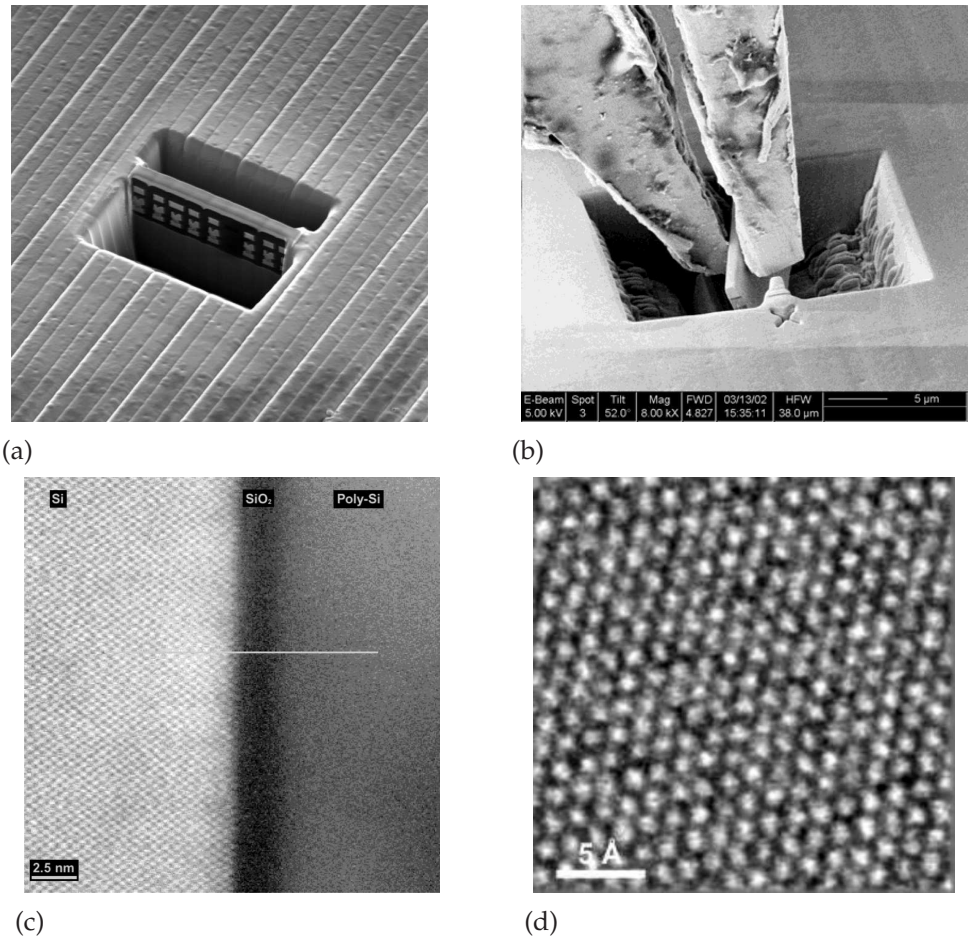

(a) (b)

(c) (d)

Figure 1.2: A semiconductor sample in a wafer, milled by a Focussed Ion Beam (FIB) (a) (Courtesy of FEI). The semiconductor sample picked by a gripper (b) (Courtesy of Philips Applied Technologies). TEM high resolution image of an interface between SCS and poly Si. The periodic atomic structure is clearly visible in the SCS, in contrast to the poly Si (c). A close up of the SCS (d) (Courtesy of FEI).

and the lost time for homogenization however remains a major drawback. It arises from the large size of the manipulator, which is about 1×10^{-3} m^3. A large manipulator intrinsically is less stable than a small manipulator in case of thermal drift. Also because of the small gap of about 5 mm (see figure 1.3 on page 8) between the TEM pole pieces, the manipulator is mounted to the exterior of the TEM column. The surroundings couple thermal and acoustic noise into the column and the manipulator. The vibration amplitude of the sample is in the order of 0.1 nm [7].

The highest resolution images are currently obtained by mounting a sample on a holder and placing the holder with sample on top of the lower pole piece with a manipulator. The manipulator is detached from the holder, and the holder rests passively on the lower pole piece. The thermal drift and vibrations of the sample with respect to the E-beam are small, as the sample is isolated from the surroundings. However

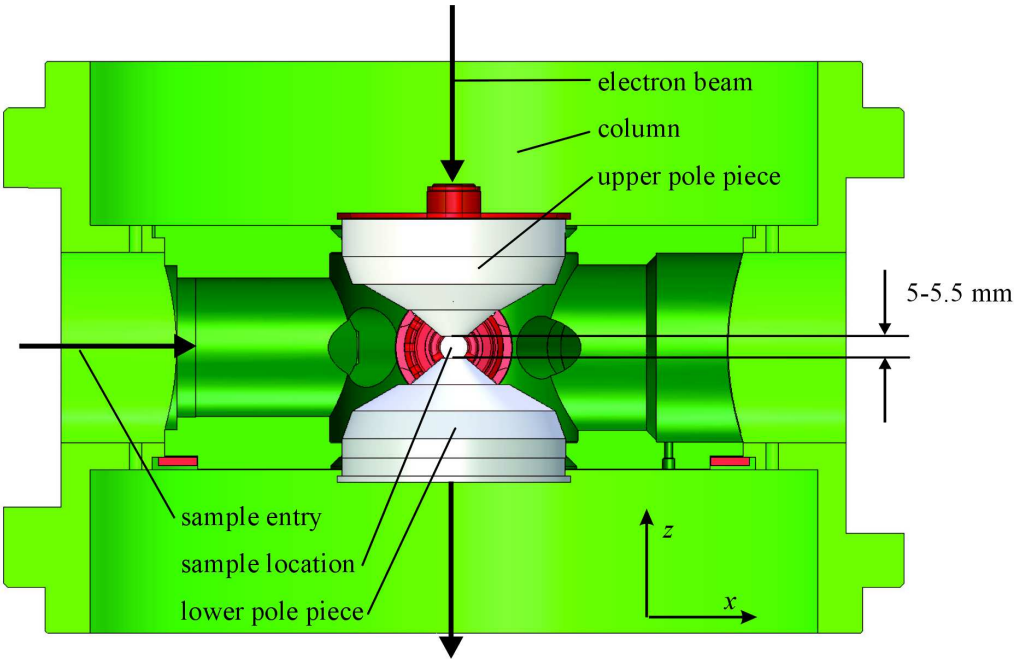

Figure 1.3: Cross-section of the pole pieces of the objective lens of a TEM.

there is no tilt freedom and z-translation possible, and the x- and y-translations have poor resolution.

The position stability of the sample with respect to the E-beam, in combination with manipulation in 5 DOF can be improved by coupling a small manipulator directly to the lower pole piece.

Specifications of a TEM sample manipulator The specifications of a next generation TEM sample manipulator as set by FEI company are given in table 1.1. The manipulator has to operate in ultra high vacuum $1 \times 10^{-8} - 1 \times 10^{-9}$ [Torr] and should not interfere with the E-beam. The requirement of stability is a combination of drift rate and vibration amplitudes.

Table 1.1: Specifications for a next generation TEM sample manipulator for FEI company.

property	value	remark
strokes x, y, z	± 10 μm	
repeatability x, y, z	10 nm	not stability
tilt R_x, R_y	$1 \times \pm 30$ & $1 \times \pm 70$ °	no R_z is required for this application
tilt repeatability R_x, R_y	0.05 °	not stability
positioning stability [7]	0.1 nm/min	within 10 sec. after positioning

Thermo-mechanical noise Thermo-mechanical noise is noise generated by thermal agitation of particles (being atoms, molecules, electrons etc.). Some examples are Brownian motion of molecules or Nyquist/Johnson noise in the voltage over conductors. Larger structures are under the influence of the agitated molecules in the surrounding gas, but also the structure itself shows noise because of fluctuations in the matter of the structure. In thermal equilibrium conditions, an energy storage mode (i.e. energy storage in a spring or a mass or a capacitance) will have an average energy equal to $\frac{1}{2} k_B T$ [J] [8], where k_B is Bolzmann's constant (1.38×10^{-23} J/K) and T is the absolute temperature [K].

Considering the vibration modes of a mechanical system as mass-spring oscillations, the vibration frequencies are determined by the mass and the stiffness for translational modes and the inertia and the rotational stiffness for rotational modes. For the fluctuations or variances in the position or angle of an object in a certain vibration mode the following equations are found [8], where $\langle x^2 \rangle$ [m^2] is the variance in position, c [N/m] is the translational stiffness, $\langle \theta^2 \rangle$ [rad^2] is the variance in the rotation angle and k [Nm] is the rotational stiffness:

$$\frac{1}{2} c \langle x^2 \rangle = \frac{1}{2} k_B T \quad \Rightarrow \quad \langle x^2 \rangle = \frac{k_B T}{c} \tag{1.1a}$$

$$\frac{1}{2} k \langle \theta^2 \rangle = \frac{1}{2} k_B T \quad \Rightarrow \quad \langle \theta^2 \rangle = \frac{k_B T}{k} \tag{1.1b}$$

With the variance known, the standard deviation of the position can be found. In worst case, it is assumed one of the in-plane translational modes has the lowest resonance frequency[3]. A resonance frequency of 1 kHz is assumed for the mode, which is common for a MEMS device. For the mass of the manipulator, a square silicon plate of 1 by 1 mm is taken, with a height of 40 μm, which together with the density of silicon of 2300 kg/m^3 amounts to 920 μg [4]. Using the relation $c = 4\,\pi^2\, {f_r}^2\, m$, the accompanying suspension stiffness is 3.6 N/m. Inserting this in equation (1.1a) results in a standard deviation of the position of 0.34 Å at 300 K.

The situation given above is a worst case situation. In case the system is bandlimited and applied well below the resonance frequency, not all the noise-energy in the mode will disturb the position-registration. In that case a high Q-factor greatly reduces the position variance. In vacuum, Q-factors of 100 for MEMS are very well possible.

In general to reduce the noise, the stiffness should be increased and/or the temperature should be lowered. Increasing the stiffness means the actuators have to deliver more force. Generating large forces in MEMS devices is by far not trivial.

[3] It is assumed the largest distortion to a image in the TEM occurs due to in-plane displacement.

[4] The dimensions given here are realistic as will follow in chapters 3 and 4

Meeting the requirements The performance of a manipulation stage potentially benefits from miniaturization. Obviously, the reduction of the device volume suits the requirement for the space between the lens poles. Miniaturization also offers stability improvement as will be explained below. However, it was shown that thermo-mechanical noise is an issue that is more relevant for small scale devices. It has to be taken into account by designing for a system with high-frequent behavior and as large as possible stiffness. As was mentioned, a limitation to the allowable stiffness is the available actuation force. Fabrication limitations will be a second factor affecting the obtainable stiffness. Especially, to achieve large enough frequency separation between the various DOFs.

1.6 TEM sample manipulator concept

Miniaturizing the manipulator potentially increases the stability in two ways. It creates the opportunity to mechanically "short-circuit" the manipulator to the column – the heart of the electron beam source – by fixing it to one of the TEM poles and isolating external thermal and vibration noise. Secondly the manipulator itself can be made more stable. Miniaturizing potentially increases the natural frequencies, decreases the thermal expansion and decreases the thermal time constant of the manipulator.

1.6.1 Two stage concept

Tilt stage Elastic mechanisms enable high positional repeatability by their deterministic behavior. Elastic mechanisms in general incorporate low hysteresis, no friction, no play and no wear [9]. All are necessary properties in precision manipulation. However large rotation angles require non-elastic mechanisms, because the elastic hinges or leaf-springs deflected over a large displacement do not constrain any degree-of-freedom, as explained by Brouwer in [10]. Therefore a separate tilt stage is to be developed which incorporates precision friction bearings for facilitating large rotations with high stiffness [11]. A MEMS manipulator is mounted in the tilt-stage and offers fine positioning in up to 6 DOF.

A rotation stage has been designed by Kruizinga [11] and is shown in figure 1.4. It comprises two tilt axes perpendicular to each other, resulting in a single rotation point. This mechanism is called a cardan joint. The R_x-axis has a stroke of $\pm 30^\circ$, the R_y-axis has a stroke of $\pm 70^\circ$ (see figure 1.5). The stage with the attached paws that rest on a ring on the lower TEM pole (see figure 1.5) has a dimension smaller than the diameter of the entry which is used to insert the stage in the TEM. The actuation used is based on Inertia Sliding Motion and shear piezo elements. Due to the small steps of the piezo, the desired resolution of 0.05° is no problem. Sapphire on Silicon

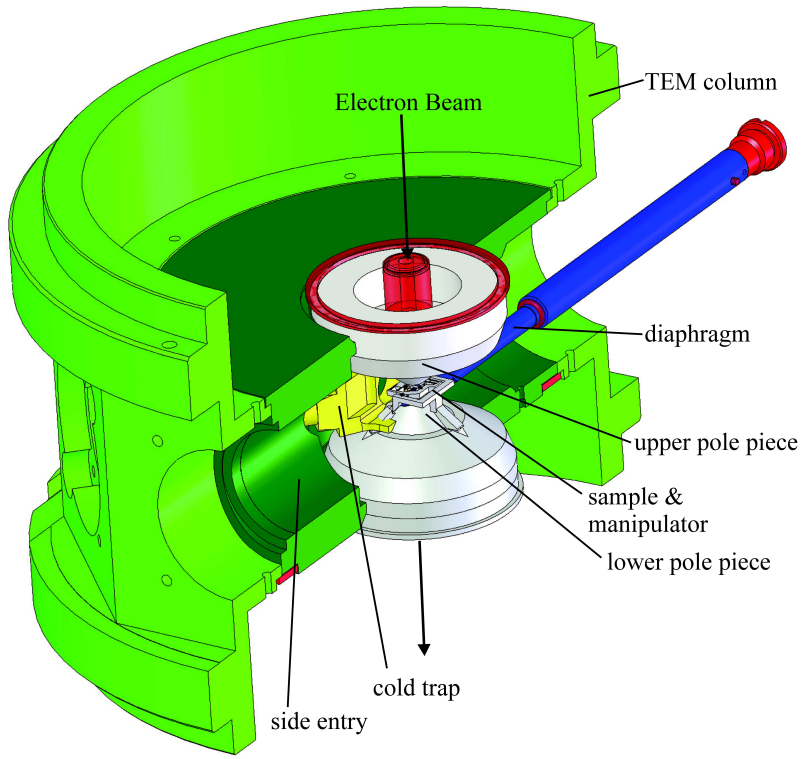

Figure 1.4: The two manipulation stages in the objective lens of the TEM column (Courtesy FEI).

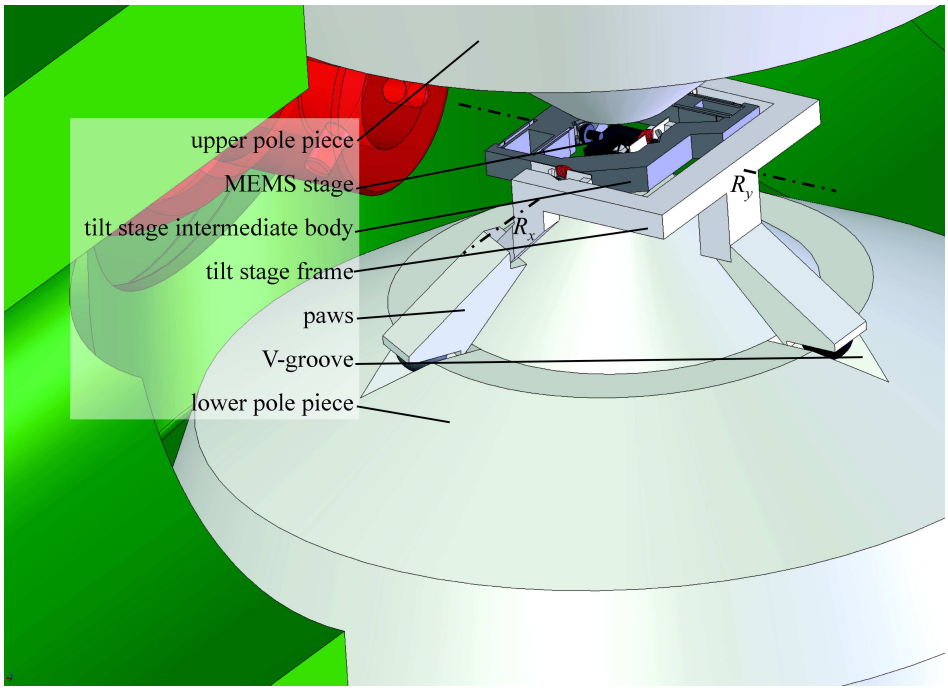

Figure 1.5: The assembly of the MEMS stage and the tilt stage on the lower pole piece (Courtesy FEI).

Nitride, proved to be a low wear yet hard contact combination in high vacuum. The total energy produced in two full stroke operations of all rotation actuators, combined with the greatest thermal length results in a maximum thermal drift of 0.044 nm. The lowest natural frequency of the rotation stage is about 3.3 kHz. Two capacitive angular positions sensors are used for feed back.

Concept of loading of the sample in a TEM A semi-conductor sample can be milled out of a wafer by a FIB in a dual beam SEM / FIB system (see figure 1.2a). By using a gas (tungsten) the FIB joins the sample to a rod by ”welding” which can be micro manipulated, or a gripper (see figure 1.2b) can be used to pick the sample. The MEMS stage is meant to be mounted in the tilt stage and the combination is loaded in the dual beam system. The sample is manipulated to the center of the MEMS stage. The FIB joins the sample to the MEMS stage by ”welding”. The FIB decouples the rod from the sample or in case of a gripper, the gripper releases the sample. The tilt and MEMS stage with the sample are loaded into the TEM via a load-lock in one of the side entries (see figure 1.3). A relatively simple manipulator with repeatability of tenth’s of a millimeter positions three spheres of the paws of the tilt stage in the three V-grooves of the lower pole piece. The repeatability of positioning spheres in a V-groove is generally in the micron domain, which means the sample is positioned at micron repeatability in the TEM. The stroke of the MEMS manipulator is large enough to compensated the assembly uncertainty.

1.6.2 Feedback

A direct way of obtaining nanometer positional resolution and sub-nanometer stability would be to use the image of the CCD camera in a feedback loop. However there are several drawbacks. The time delay due to image built up and processing can be in the order of tens of seconds for the STEM mode. Also for some experiments the camera is not available for position control. Another way of controlling the position of the sample could be to measure the position of the sample in relation to the position of the E-beam. However measuring up to five degrees-of-freedom at sub-nanometer repeatability of a micron-sized sample in the small space of the objective lens is currently impossible.

Because of the above the positional stability of the sample (mainly being drift and dynamic vibrations) has to result from the mechanical passive stability of the manipulator.

1.7 Multi-DOF positioning in MEMS

To develop an idea of the state of the art of precision positioning in MEMS, a small survey is made with respect to existing examples of multi-DOF devices in MEMS and whether the techniques used for these devices are suitable for a precision system. Because in many practical cases it seems most easy to confine a system to either planar or out-of-plane positioning, here the MEMS manipulators are distinguished with respect to systems for planar positioning, systems for out-of-plane positioning and combinations of both. Combinations often pose a much larger challenge, because the stiffness requirements for the mechanism are more complex. Other relevant characteristics of these systems are resolution, position stability, stroke, bandwidth and force.

Due to the many difficulties one confronts in MEMS design and fabrication, the challenges related to measuring and the absence of overall standardization, a complete characterization of MEMS devices with respect to the points mentioned above, is often not found in literature. Although the reasons for this absence are very real, it complicates the judgement of the potential of reported MEMS manipulators with respect to precision applications. In table 1.2 typical multi-DOF MEMS manipulators found in literature are presented and distinguished with respect to the amount of DOFs and obtainable strokes, the type of actuator used, and on what kind of mechanism the manipulator is based. The total table is split up in systems for in-plane positioning, systems for out-of-plane positioning and systems combining in-plane and out-of-plane positioning.

Hardly any data is found on position stability. Thermal drift and thermo-mechanical noise are important stability characteristics. Within the articles used for this survey only Chu et al. give an analysis of the expected thermo-mechanical position noise. The mechanism used in the manipulator is important with respect to play and back-lash. Many solutions for multi-DOF hinges offering large freedom of movement show play and friction in the linkage [12, 13, 14, 15]. This is a large drawback for precision applications. Flexible mechanisms generally do not suffer from play and back-lash and are far more suited for precision manipulation. However, the displacements are limited compared to the size of the mechanism.

Planar positioning An example of a 2 DOF planar manipulation platform is presented by Sarajlic et al. in [16]. The platform is actuated by electrostatic comb-drives and the system is fabricated by a bulk micromachining process in single crystal silicon allowing for high aspect-ratio structures and electrical insulation. In general, 2 DOF planar concepts can relatively easily be expanded to concepts for 3 DOF planar manipulation. Using comparable technology, an example of a parallel 3 DOF planar manipulator is

fabricated as part of the MAMS project [17] (see also chapter 3). The vertexes of a triangular platform are displaced in tangential direction by comb-drives. Based on the same kinematic principle a three DOF planar precision manipulator driven by piezoelectric bimorph actuators is presented in [18]. This system is made in quartz with flexible hinges made out of polyimide. The actuators are PZT elements assembled on top of the quartz. A 2 DOF position stage with thermal "bent-beam" actuation and nanometer range 2 DOF capacitive position sensing is discussed in [19]. A compliant stroke amplifier is applied to increase the capacitance change on displacement.

Table 1.2: Survey of multi-DOF positioning in MEMS.

reference	DOFs & strokes[5]	actuation	mechanism	remarks
In-plane				
[16]	2 translations ± 20 μm	comb-drives	flexible parallel	
[17]	2 translations; 1 rotation ± 10 μm; 4 $^\circ$	comb-drivse	flexible parallel	
[18]	2 translations; 1 rotation – μm; – $^\circ$	PZT bimorph	flexible parallel	assembled actuators
[19]	2 translations 19 μm	thermal bent-beam	flexible parallel	cap. position sensor sub-nm resolution
[20, 21]	1 translation/2 translations "infinite"	electrostatic parallel plate	flexible inchworm	nm resolution obtainable
Out-of-plane				
[22, 23]	2 tilt angles up to 20 $^\circ$	comb-drives vertical	flexible serial	
[24]	1 translation; 2 tilt angles ± 10 μm; 20 $^\circ$	comb-drives vertical	flexible serial/paral.	
[25]	1 translation; 2 tilt angles – μm; ± 10 $^\circ$	thermal bimorph	flexible parallel	
[6]	3 $\times$ 1 translation out-of-plane 23 μm	electrostatic parallel plate	flexible parallel	addapt. optics deform mirror
[26]	1 translation; 2 tilt angles – μm; – $^\circ$	thermal bimorph	flexible parallel	linear motor friction
[27]	1 translation; 2 tilt angles – μm; – $^\circ$	comb-drives	flexible parallel	PDMS mechanism
[28, 29]	1 translation tens of μm	thermal bimorph	flexible	enables large forces

(Continued on next page.)

Table 1.2: (Continued.)

reference	DOFs & strokes	actuation	mechanism	remarks
Combinations				
[30]	2 transl. in-pl.; 1 transl. o.o.p. 120 μm ; 250 μm	electrostatic scratch-drive	hinges parallel	play in hinges
[31]	2 transl. in-plane; 1 tilt angle 1 μm; – $^\circ$	comb-drives	flexible serial	gripper
[32]	various – μm; – $^\circ$	comb-drives	flexible	
[33]	6 DOF maximum 2 μm; – $^\circ$	PZT	flexible parallel	diced grooves PZT filled
[14, 15]	6 DOF maximum 150 μm; $\pm 5^\circ$	comb-drives	hinges parallel	play in hinges
[34]	various 13 μm; 2°	thermal bimorph	flexible	application SEM/TEM
[35]	6 DOF maximum 13 μm; 2°	thermal hot-leg/ cold-leg	flexible parallel	

Stepper or inchworms actuators are also found in the micro-domain. Examples applying electrostatic parallel plate actuators for clamping and displacement are given in [20] for single DOF displacement and in [21] for 2 DOF displacement. Theoretically, inchworms enable manipulation over an unlimited range[6] and displacements in the nanometer range are obtainable.

Out-of-plane positioning Mechanism for out-of-plane positioning are often found in scanning mirror applications. Generally these devices are capable of 2 DOF tilt motion applied to deflect a laser beam or to project an image. In [24, 22, 23, 25] 2 DOF tilt mechanisms as well as complete out-of-plane 3 DOF mechanisms based on flexures are presented for micro mirrors and other optical elements like (Fresnel) lenses and gratings. Most scanning mirrors are driven by out-of-plane comb-drives. The tilting motion is realized with a flexible torsion suspension. Many scanning mirrors are meant to be driven in resonance, which allows for much larger tilt angles than those obtained at low frequencies. In case of the 6 DOF stage in the MAMS project, manipulation is low frequent and the system is not applied in resonance. Another

[5]The reported strokes are for static displacements and rotations.

[6]Practically, the range is often restricted by suspension beams in most cases also applied to power the inchworms

application of MEMS mirrors is a 3 DOF deformable mirror for adaptive optics as presented in [6].

Out-of-plane stages for positioning of a platform are also found. In [26] a 3 DOF out-of-plane manipulation stage is presented applying three identical linear motors consisting of a slider and a pair of thermal bimorph actuators. The motors are radially positioned around a platform with 120 ° pitch and push radially inward. The propulsion is based on friction, which is a large drawback for precision positioning. Another 3 DOF out-of-plane stage applying the same kinematic principle is presented in [30]. Here electrostatic scratch-drive actuators are applied. For this stage, use is made of hinges with play instead of a flexible mechanism. A 3 DOF out-of-plane stage with flexible hinges made from polydimethylsiloxane (PDMS) is presented in [27]. Out-of-plane actuation is based on a mechanism, formed in PDMS, transforming in-plane to out-of-plane displacements. Four in-plane comb-drives are attached to four of the in-plane to out-of-plane mechanisms which in their turn are connected to a platform. The mechanisms legs and the platform are formed in PDMS and assembled on top of the comb-drive shuttles.

Deladi et al. present various combinations of thermal actuators optimized for in-plane and out-of-plane actuation with large forces in [28, 29]. These can be applied in a multi DOF stage.

Combinations A 3 DOF manipulator with two planar translational DOFs and one out-of-plane tilt DOF, combined with a gripper is presented in [31]. It employs electrostatic comb-drive actuators for all DOFs including the gripper. The system is based on an elastic mechanism. In [33] various multi-DOF flexure mechanisms obtained with silicon on insulator (SOI) wafers and surface micro-machining are reported. Out-of-plane flexures are generally based on thin film deposition on the wafer or in molds etched into the wafer. This relatively simple process offers design freedom for a large variety of flexure geometries, but the frequency separation in the out-of-plane suspension is limited. This is in general an aspect that complicates MEMS design and fabrication for out-of-plane precision manipulation.

Complete 6 DOF manipulation stages are discussed in [14] and [15]. These stages are fabricated with surface micro-machining and based on ingeniously designed multi-DOF non-flexible hinges. The manipulators allow strokes in the order of 100 μm, but are more suited for "coarse" positioning than for nanometer resolution positioning due to the play in the hinges. In [34], Zyvex presents various multi-DOF manipulators for inspection inside a TEM or SEM. These are based on flexible mechanisms and driven by thermo-mechanical bimorph actuators made in a surface micro machining process.

Culpeper has designed a symmetric flexure mechanism for 6 DOF manipulation [36] called HexFlex. In [35] a MEMS version of this mechanism is presented driven by six thermo-mechanical actuators each capable of in-plane and out-of-plane deflection. The thermal actuators are of the hot-leg/cold-leg type and are applied in a stack with a layer of oxide in between (double SOI wafer). If both actuators in the stack are powered, the deflection is in-plane, while if only the upper or lower actuator is powered a combined in-plane and out-of-plane deflection results. Driving the actuators in the correct combination and ratio allows movement in all 6 DOF. The choice for this type of thermo-mechanical actuators allows relatively simple fabrication.

In the examples for multi-DOF manipulation given above, some designs apply thermo-mechanical actuators. As was shown in section 1.5, thermo-mechanical noise plays a role in devices in the micro-domain. The noise occurs for any object with an absolute temperature higher than 0 K, but one might wonder if the application of thermo-mechanical is a practical choice from the perspective of reducing noise. Additionally, it is very important to model the thermal properties of the device with respect to the timescale in which thermal equilibrium is reached (especially in vacuum). The specifications demand thermal drift of less than 1 Å/min, while reaching this stable value within 10 seconds. Application of thermal actuators might largely complicate the design of the manipulator, since there is such little practical information on thermal noise and drift in MEMS systems.

Assembly of MEMS devices In literature, many examples of assembly of MEMS devices are found. A very nice example of assembly by wafer-bonding is a micro-turbine presented in [37], where a total of five wafers are stacked on top of each other. Another example where four wafers are stacked is given in [23] for a 2 DOF tilt mirror with buried actuators. An assembled magnetic induction machine is presented in [38] and [39]. Here, a rotor structure is assembled on top of a molded coil structure. Zyvex has developed modular construction elements made in silicon, that are assembled with help of compliant connectors and sockets [40]. This assembly requires a macroscopic external precision manipulator system. With this technique, a micro SEM is developed [41].

Application of assembly relies much on the allowable tolerances. The smallest error in the alignment in wafer-bonding, for instance, is often in the micrometer range. Of course this depends on the equipment used for the alignment. The modular assembly used by Zyvex requires the development of an external macro manipulator system. Without such a system assembly is too time consuming and expensive.

Precision driven MEMS design Non of the literature in the survey above reports characterization with respect to stability and resolution. As mentioned before this is typical for literature on MEMS systems and understandable, since obtaining the required measurement data is very challenging. However, it is also typical that hardly any of the references report anything on the desired stability and resolution and how these have an effect on the mechanism design. Designing for precision is clearly a rather new discipline within the field of MEMS. In this project, the challenge is engaged to base the design of the manipulator on the requirements for precision positioning and the knowledge available in the field of "conventional" precision engineering. MEMS specific limitations to the design will be identified and processing solutions will be looked for to stretch these limitations.

1.8 Thesis outline

The proposed concept for 6 DOF manipulation in MEMS is presented in chapter 2. First of all some generally applied mechanism elements in MEMS are discussed, followed by a section about geometry definition in MEMS-technology. Subsequently, the choice for the manipulation concept is made and the manipulation space is briefly analyzed, after which a choice is made for the actuators.

In chapter 3 the design, fabrication and characterization of the planar 3 DOF manipulation stage is discussed. Some important aspects of the design are highlighted; e.g. proper suspension of the comb-drives to prevent side pull-in instability in the operating range of the actuator. A power-port based model is presented, incorporating feed-forward control. After that the fabrication process is explained, followed by the results of the characterization.

The design of a torsion beam suspended electrostatic comb-drive actuator for vertical displacement is presented in chapter 4. The chapter starts with an analysis with respect to proper guiding of the vertical displacement and constraining of the remaining DOFs of a vertical comb-drive suspended by torsion beams. This in particular concerns pull-in instability. With help of the analysis, requirements for the torsion suspension are derived. These lead to the design of a vertical comb-drive, suspended by a torsion beam with a $\perp$-shaped cross-section.

The fabrication aspects of the vertical comb-drive elaborated in chapter 5. First a small survey is performed on which processes fulfil the challenging requirements necessary for the 3D geometry. After that the chosen fabrication process is explained, followed by characterization of the device.

In chapter 6 two alternative electrostatic actuators are presented, which do not suffer from pull-in instability in the same extent as a conventional comb-drive. First

of all the theory explaining the actuation principle is given including FEM simulation to analyze the influence of fringe fields on the stability. Subsequently, the influence of charge in the proposed actuators is analyzed. The required geometry is discussed and a fabrication process is proposed to reflect on the feasibility of the alternative actuators.

The conclusions are given in chapter 7. The research findings are discussed with respect to various topics and an outlook is given for application of this work and further research in the area of precision manipulation in MEMS.

References

[1] N. Maluf, *An Introduction to Microelectromechanical Systems Engineering*. Artech House, 2000.

[2] R. G. Associates, "Nexus." http://www.rgrace.com/papers/killerapps.html.

[3] "American society for precision engineering." http://www.aspe.net/index.html.

[4] J. Corbett, P. C. McKeown, G. N. Peggs, and R. Whatmore, "Nanotechnology: International Developments and Emerging Products," *Annals of the CIRP*, vol. 49, no. 2, pp. 523–545, 2000.

[5] P. Vettiger, G. Cross, M. Despont, U. Drechsler, U. Dürig, B. Gotsmann, W. Häberle, M. A. Lantz, H. E. Rothuizen, R. Stutz, and G. K. Binnig, "The "Millipede"–Nanotechnology Entering Data Storage," *IEEE Transactions on Nanotechnology*, vol. 1, no. 1, pp. 39–55, 2002.

[6] D. J. Dagel, W. D. Cowan, O. B. Spahn, G. D. Grossetete, A. J. Griñe, M. J. Shaw, P. J. Resnich, and B. Jokiel Jr, "Large-stroke MEMS deformable mirrors for adaptive optics," *Journal of MEMS*, vol. 15, no. 3, pp. 572–583, 2006.

[7] H. Van der Wulp, *Piezo-driven stages for nanopositioning with extreme stablity*. PhD thesis, Delft University of Technology, 1997.

[8] T. B. Gabrielson, "Mechanical-thermal noise in micromachined acoustic and vibration sensors," *IEEE Transactions on Electron Devices*, vol. 40, no. 5, pp. 903–909, 1993.

[9] M. P. Koster, *Constructie principes voor het nauwkeurig bewegen en positioneren*. Twente University Press, Enschede, The Netherlands, 2000.

[10] D. M. Brouwer, B. R. De Jong, and H. M. J. R. Soemers, "Design and modelling of a precision 6 degrees-of-freedom MEMS-based parallel kinematic TEM sample manipulator.," in *ASPE*, (Monterey, California, USA), p. Session VIII, 2006.

[11] M. Kruizinga, "Design of a sub nm Stable Rotation Stage for Application in a TEM," Master's thesis, Univesity of Twente, Enschede, The Netherlands, May 2005.

[12] K. S. J. Pister, M. W. Judy, S. R. Burgett, and R. S. Rearing, "Microfabricated hinges.," *Sensors and Actuators A*, vol. 33, pp. 249–256, 1992.

[13] R. Yeh, E. J. J. Kruglick, and K. S. J. Pister, "Surface-micromachined components for articulated microrobots," *Journal of MEMS*, vol. 5, no. 1, pp. 10–16, 1996.

[14] J. A. Walraven and B. J. Jokiel, "Failure Analysis of a Multi-Degree-of-Freedom Spatial Microstage," *Proceedings of SPIE 2003*, vol. 4980, pp. 97–105, 2003.

[15] B. J. Jokiel, G. L. Benavides, L. F. Bieg, and J. J. Allen, "Planar and Spatial Three-Degree-of-Freedom Micro-Stages in Silicon MEMS," *Proceedings of ASPE annual meeting 2001*, vol. 25, pp. 32–35, 2001.

[16] E. Sarajlic, M. J. De Boer, H. V. Jansen, N. Arnal, M. Puech, G. Krijnen, and M. Elwenspoek, "Bulk micromachining technology for fabrication of two-level MEMS in standard silicon substrate," in *Transducers'05*, vol. 2, (Seoul, Korea), pp. 1404–1405, 2005.

[17] B. R. De Jong, D. M. Brouwer, H. V. Jansen, M. J. De Boer, T. G. Lammertink, S. Stramigioli, and G. J. M. Krijnen, "A planar 3 DOF sample manipulator for nano-scale characterization," in *MEMS*, (Istanbul, Turkey), pp. 750–753, 2006.

[18] V. Henneken, "Design of a MEMS XY microstage for nanometer applications in a transmission electron microscope.," Master's thesis, Delft University of Technology, The Netherlands, 2002.

[19] L. L. Chu and Y. B. Gianchandani, "A micromachined 2D positioner with electrothermal actuation and sub-nanometer capacitive sensing," *JMM*, vol. 13, no. 2, pp. 279–285, 2003.

[20] N. Tas, *Electrostatic Micro Walkers*. PhD thesis, University of Twente, Enschede, The Netherlands, 2000.

[21] E. Sarajlic, E. Berenschot, H. Fujita, G. Krijnen, and M. Elwenspoek, "Bidirectional electrostatic linear shuffle motor with two degrees of freedom," in *IEEE MEMS'05*, (Miami Beach, Florida, USA), pp. 391–394, 2005.

[22] S. Kwon, V. Milanović, and L. P. Lee, "Vertical combdrive based 2-D gimbaled micromirrors with large static rotation by backside island isolation.," *IEEE Journal of Selected Topics in Quantum Electronics*, vol. 10, no. 3, pp. 498–504, 2004.

[23] I. W. Jung, U. Krishnamoorthy, and O. Solgaard, "High fill-factor two-axis gimbaled tip-tilt-piston micromirror array actuated by self-aligned vertical electrostatic combdrives," *Journal of MEMS*, vol. 15, no. 3, pp. 563–571, 2006.

[24] V. Milanović, "Multilevel Beam SOI-MEMS Fabrication and Applications," *J. MEMS*, vol. 13, no. 1, pp. 19–30, 2004.

[25] J. Singh, T. Gan, A. Agarwal, Mohanraj, and L. Saxon, "3D free space thermally actuated micromirror device," *Sensors and Actuators A*, vol. 123-124, pp. 468–475, 2005.

[26] W.-J. Cheng and D. L. DeVoe, "Linear micromotors and spatial micromechanisms based on UV-LIGA," in *IEEE MEMS'05*, (Miami Beach, Florida, USA), pp. 399–402, 2005.

[27] Y.-C. Tung and K. Kurabayashi, "A Single-Layer PDMS-on-Silicon Hybrid Microactuator With Multi-Axis Out-of-Plane Motion Capabilities-Part II: Fabrication and Characterization," *J. MEMS*, vol. 14, no. 3, pp. 558–566, 2005.

[28] S. Deladi, M. J. De Boer, G. Krijnen, and D. Rosén, "Innovative process development for a new micro-tribosensor using surface micromachnining," *JMM*, vol. 13, pp. S17–S22, 2003.

[29] D. Deladi, G. Krijnen, and M. C. Elwenspoek, "Parallel-beam/lever electrothermal out-of-plane actuator," in *DTIP*, (Cannes-Mandelieu, France), 2003.

[30] L. Fan, C. W. Wu, K. D. Choquette, and M. H. Crawford, "Self-assembled microactuated xyz stages for optical scanning and alignment," in *Transducers '97*, (Chicago, USA), pp. 319–322, 1997.

[31] H.-C. Chang, J. M.-L. Tsai, H.-C. Tsai, and W. Fang, "A novel 3-DOF micromanipulator," in *ASME IMECE*, (Washington D.C., U.S.A.), pp. 1–6, 2003.

[32] H.-Y. Chu, S.-W. Lee, and W. Fang, "Design and fabrication of multi-degrees-of-freedom single crystal silicon movable platforms on SOI wafer," in *IEEE MEMS*, (Seoul, Korea), pp. 737–740, 2005.

[33] D.-Y. Zhang, T. Ono, and M. Esashi, "Piezoactuator-integrated monolithic microstage with six degrees of freedom," *Sensors and Actuators A*, vol. 122, pp. 301–306, 2005.

[34] N. Sarkar, C. Baur, E. Stach, Z. Jandric, R. Stallcup, M. Ellis, G. Skidmore, J. Liu, and G. K. Fedder, "Modular MEMS experimental platform for transmission electron microscopy," in *IEEE MEMS*, (Istanbul, Turkey), pp. 146–149, 2006.

[35] S.-C. Chen and M. L. Culpepper, "Design of a six-axis micro-scale nanopositioner–μHexFlex," *Precision Engineering*, vol. 30, pp. 314–324, 2006.

[36] M. L. Culpepper and G. Anderson, "Design of a low-cost nano-manipulator which utilizes a monolithic spatial compliant mechanism," *Precision Engineering*, vol. 28, pp. 469–482, 2004.

[37] L. G. Fréchette, S. A. Jacobson, K. S. Breuer, F. F. Ehrich, R. Ghodssi, R. Khanna, C. W. Wong, X. Zhang, M. A. Schmidt, and A. H. Epstein, "High-speed microfabricated silicon turbomachinery and fluid film bearings," *Journal of MEMS*, vol. 14, no. 1, pp. 141–152, 2005.

[38] D. P. Arnold, S. Das, F. Cros, I. Zana, M. G. Allen, and J. H. Lang, "Magnetic induction machines integrated into bulk-micromachined silicon," *Journal of MEMS*, vol. 15, no. 2, pp. 406–414, 2006.

[39] F. Cros, H. Koser, M. G. Allen, and J. H. Lang, "Magnetic induction micromachine–Part II: Fabrication and testing," *Journal of MEMS*, vol. 15, no. 2, pp. 427–439, 2006.

[40] K. Tsui, A. A. Geisberger, M. Ellis, and G. D. Skidmore, "Micromachined end-effector and techniques for direct MEMS assembly," *JMM*, vol. 14, pp. 542–549, 2004.

[41] R. Saini, Z. Jandric, M. Nolan, and S. A. M. Mentink, "Microassembled MEMS minisem with carbon nanotube emitter," in *IEEE MEMS*, (Istanbul, Turkey), pp. 918–921, 2006.

Chapter 2

Six DOF manipulation concept

This chapter discusses the MEMS specific aspects of a kinematic constrained design of a 6 DOF manipulator. Typical basic elements found in MEMS mechanisms are described and the geometry definition in MEMS technology is analyzed. A decision is made with respect to serial or parallel manipulation and the chosen concept is kinematically analyzed. Furthermore, decisions are made with respect to the actuators that drive the mechanism.

2.1 Introduction

A system capable of highly stable, nanometer resolution manipulation in 6 DOFs with strokes of micrometers, requires careful design. A manipulator for positioning in six DOFs consists of a minimum of six actuators that are connected to an end-effector via a mechanism. In case a feedback control system is used, a minimum of six sensors is required to measure the position. Design for precision systems is based on a large set of engineering principles that have proven their value in macroscopic systems. MEMS precision systems can benefit from application of these principles. Two important guidelines are: Each DOF has to be constrained just once, to ensure a deterministic behavior of the mechanism, i.e. the system is *exact kinematic constrained*. Furthermore, the mechanism is preferably free of backlash and friction.

Exact kinematic constrained design is important to prevent preferential positions. Especially, in case of an assembled system, since small errors in the assembly can cause non-linear behavior in an overconstrained system. However, MEMS systems

usually are monolithic, which poses less risk of non-linear behavior in case the design is overconstrained. Furthermore, deliberated overconstrained solutions are often applied in MEMS to prevent miss-alignment due to stress-release in e.g. the suspension of a comb-drive fabricated in a layer showing residual stress. For these reasons the application of design for precision systems is not entirely comparable to design for macroscopic systems and might require a tradeoff. Constraining of DOFs in MEMS is often limited due to process limitation leading to the application of long slender beams. However, since masses are very small, resonance frequencies generally are high, offering some margin to still obtain considerable frequency separation between constrained and free DOFs.

MEMS technology poses typical limitations to the design and fabrication of a multi-DOF manipulator. Both because the structuring possibilities are limited and the geometrical accuracy is relatively poor. The limitations and some possible manipulation concepts are discussed in section 2.2. Section 2.3 introduces the chosen manipulation concept and discusses the manipulation spaces and geometrical linkage between the parts of the manipulator. Possible actuators are discussed in 2.4 and a decision is made with respect to suitable performance of the actuator combined with relatively simple fabrication demands. Conclusions follow in section 2.5.

2.2 Six DOF manipulation in MEMS

Process technology in MEMS is mostly ”2.5D” based, which means that structuring capabilities in the direction normal to the substrate are limited[1]. This is caused by the basic means of machining, namely lithography. Depending on the mask resolution, lithography allows good feature definition in the substrate plane, but for structuring in the third dimension other techniques are required. Often these techniques pose greater limits on the precision in dimensioning and shape of the structures than lithography does. This makes the design of a six DOF manipulator in MEMS quite complicated. Furthermore, the relative tolerances in MEMS processes are high compared to conventional precision machining where feature sizes are in the order of centimeters [1]. In this section an architecture is looked for that is implementable in MEMS and allows for manipulation in six DOF.

The joints in the mechanism will be based on elastic elements like (high aspect-ratio) flexure beams, because such mechanisms in principle do not suffer from friction and backlash. Furthermore, making bearings and hinges suitable for nanometer po-

[1] In the case of structuring the substrate bulk in a batch process. In surface micro-machining, layer stacks combined with sacrificial layer etching enable much more precision in height definition of structures. However it is decided to fabricate the system purely in single crystal silicon.

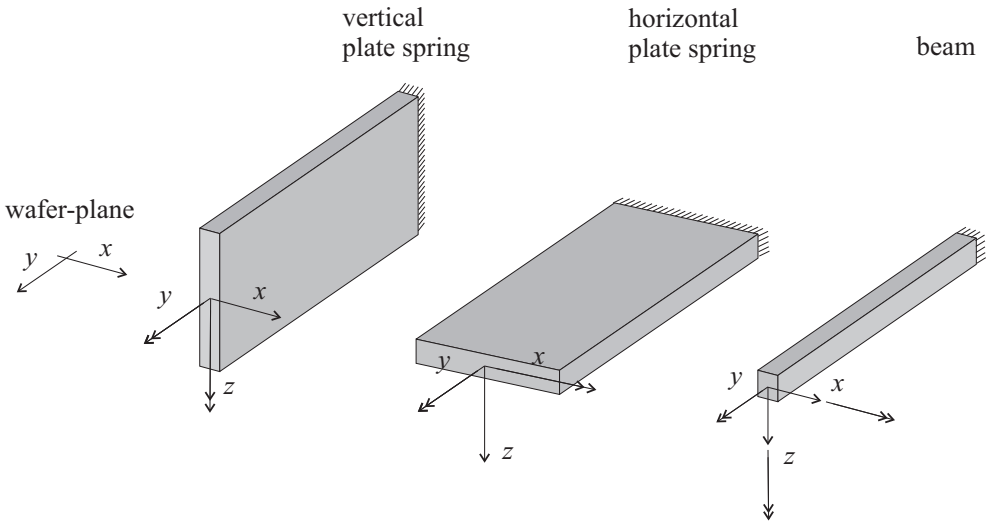

Figure 2.1: Examples of beams that can be produced with MEMS technology

sitioning in MEMS is complicated if possible at all [2, 3, 4]. As a consequence of the use of an elastic mechanism, the displacements are small compared to the size of the system. Especially since the minimum feature-size allowed by our lithography is 2 μm, beams tend to be long in order to have sufficient compliance. Another limitation to the allowable displacements follows from application of the mechanism in linear operation. For instance the stiffness, in the longitudinal direction (of a non-deflected beam), will decrease once the beam is deflected. In the deflection direction, however large deflections result in stiffening of the beam. If large deflections are allowed, these non-linear effects will be significant, complicating the predictability of the system [5].

Beams and joints compatible with MEMS technology as basic parts for the mechanism are discussed in section 2.2.1. The extend of control over the geometry of beams in MEMS technology is discussed in section 2.2.2. The influence of anisotropy in single crystalline silicon is briefly addressed in section 2.2.3. In section 2.2.4 an investigation is made with respect to the choice for serial or parallel manipulation and the advantages for MEMS systems.

2.2.1 Typical beams and joints in MEMS

A design-set is defined by regarding typical beams and joints that can be implemented in MEMS relatively easily. It is not meant to narrow down the design freedom in MEMS, but a context is required since design of mechanism in MEMS has specific limitations. Figure 2.1 shows basic types of beams that can be produced with MEMS technology. It is assumed the beams are structured in single crystalline silicon, because SCS has good mechanical properties, like low hysteresis [6] and creep

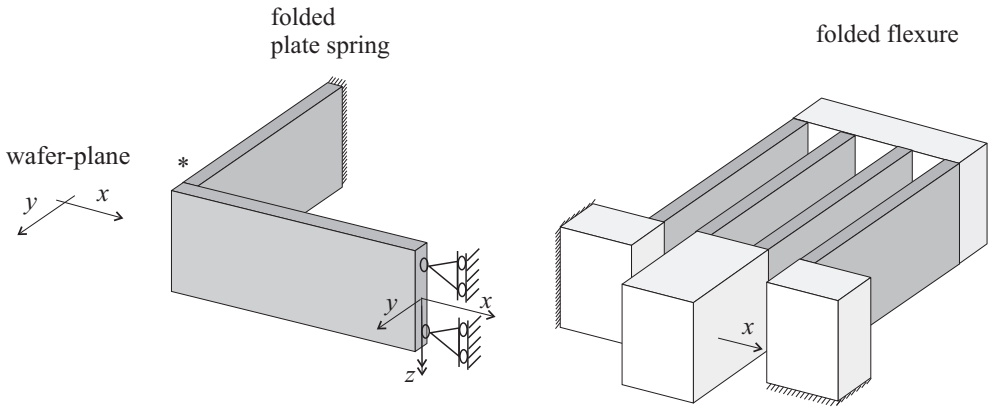

Figure 2.2: Examples of beam combinations that are often found in MEMS

[7]. Furthermore, assuming a smallest feature size of 2 μm, bulk micro-machining enables high aspect ratio structuring as opposed to surface micro-machining. High aspect ratio structuring is required for fabrication of "vertical" plate springs (oriented upright).

The first beam shown in figure 2.1, is a vertical plate-spring. It has a high aspect-ratio and is relatively easy to structure, since it only requires a mask on the topside and a highly directive etch process to remove the material around the beam. The compliant translational DOF in the x-direction is shown with arrows. Its compliance is proportional to its length to the third power and inversely proportional to its thickness in x-direction (third power)[2] [8]. Double arrows show the compliant rotation axes y and z. Both compliances are directly proportional to its length and inversely proportional to the thickness to the third power. Typically, the stiffness in z-direction (normal to the wafer plane) of MEMS systems in general is poor since the length is often required to be long to minimize the force an actuator requires to deflect the beam a certain amount. Additionally, the height (limited by the fabrication) is very small in relation to the length.

The second beam of figure 2.1 is a horizontal plate-spring. Assuming the rest of the mechanical structure is thicker than the beam, this beam is more of a challenge to structure in SCS, since it requires more complex structuring in the z-direction. It is compliant for deflection in the z-direction and for rotation about the x- and y-axis (the compliance relation to its geometry are similar to the vertical plate-spring). The last beam is a slender beam with square cross-section. This beam requires structuring in the z-direction as well. It is compliant in all DOFs but translation in the y-direction. The compliances is all directions depend on the thickness to the third power. The

[2]These notions and those below are based on Hooke's law and only apply if the geometry allows to use Hooke's law

translations are inversely proportional to the length to the third power, while the rotational compliances inversely depend on the length.

Figure 2.2 shows combinations of beams to form mechanisms often found in MEMS. The first mechanism is a folded plate-spring or "crab-leg flexure". This is a typical example of how a series combination of two vertical plate-springs, both with three constrained DOFs, results in a mechanism with just one constrained DOF. If rotation about the x- and y-axis are prevented, the z-direction is constrained at the end of the folded plate-spring. Otherwise, the z-direction is only constrained along the fold ($*$). Adding more beams in the same manner will result in a mechanism without any clearly constrained DOFs, sometimes called "serpentine spring". The second combination combines four vertical plate-springs with a rigid intermediate body. This mechanism has one compliant DOF along the x-axis (and a relatively low torsion stiffness about the y-axis). Four of these mechanism are often used as straight-guidance for a comb-drive shuttle and they are referred to as "folded flexures". This mechanism allows relatively large deflections, with largely reduced shortening effect and tensile stiffening. Due to the construction, the deflection of each plate-spring is only halve of the total displacement of the mechanism. This is caused by the fact that the intermediate body (theoretically) moves halve of the total displacement.

As a result of limitations in MEMS fabrication, compromises are often made with respect to kinematic constraints and compliances. For example, consider the case where the first beam of figure 2.1 is applied to suspend a body free to move in x-direction and free to rotate about the y- and z-axis and constrained in the other directions. To reduce the force required for deflection in such a beam, it either has to be slender or long and it should have sufficient height. Its slenderness is limited by the smallest feature size of the lithography and also the height is limited in MEMS, so the beam will be made long, reducing the stiffness in the z-direction.

2.2.2 *Controlling beam geometry in SCS MEMS*

Considering beams of SCS as joints, it is interesting to know how well the geometry can be controlled. Of course this depends on the exact process used to make the beams, but nevertheless some general remarks can be given. Figure 2.3 shows a cross-section of a beam. The symbols indicating geometrical parameters are listed in table 2.1. First of all, a beam can extend from the etch depth up to the wafer plane ($h = d$), but it can also have a tailored height ($h < d$). The first case is most simple since it is only defined by the lithography mask. For the second case additional structuring is required. In general, for each of the features d, h, w, and α, variation of the sizes of these features is determined by the uniformity of the etch process over the wafer-plane.

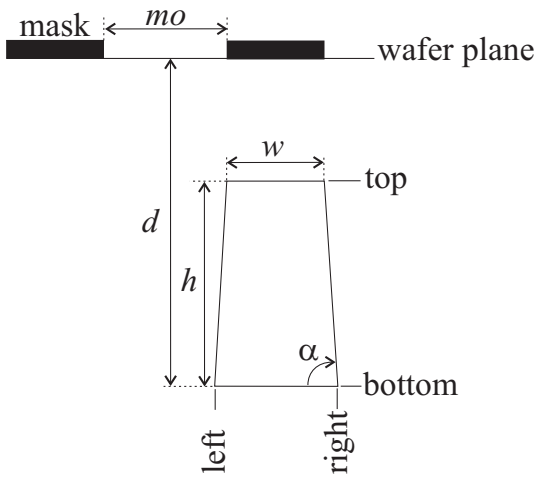

Figure 2.3: Cross-section of a beam with indication of important features

Lithographic geometry issues The width w is defined by lithography. In case of a mask of photo resist, some decrease of w caused by erosion of the edges of the mask during etching of the structure can be expected. For a hard mask like chromium or silicon-oxide the erosion is far less. However, the hard mask itself is also defined with a photo resist mask. Depending on the etch process for the hard mask, erosion of the photo resist is smaller or larger than without a hard mask. Erosion of the photo resist during the etch process is a possible cause for tapering of the etch-profile, i.e. causing α to be smaller than 90°.

w is limited by the type of lithography. Our lithography makes use of contact print with a laser-written mask-plate. The smallest feature size is limited to 2 μm and the variation is typically 0.2 μm (depending on the mask feature with respect to the scan direction of the mask-writer). If w is 2 μm the variation amounts to 10%, which is actually observed after processing (see chapter 3 on page 65). This especially has a large influence on the in-plane stiffness of beams. If an e-beam written mask is used

Table 2.1: Symbols in figure 2.3.

symbol	description
d	depth up to which the silicon is structured/etched
h	height of the beam
w	width of the beam at the topside
α	angle between bottom and sidewall, indicating the tapering
mo	size of mask opening

the resolution can be greatly improved.

The type of the resist also poses limits. For relatively long etch times, the resist has to have a certain minimal thickness to persist during the etching process. Structures in the resist obtained by lithography have a maximum aspect ratio. This means the larger the thickness of the resist, the larger the minimum feature size of the structures. Here again the pattern can be transferred from the resist to a hard mask. Depending on the process to etch the hard mask, thinner types of resist can be applied.

Deep reactive ion etching DRIE is often used to structure mechanical devices in SCS. The beam height h (and etch-depth d) depends on the etch time. This can be tuned well, however various sizes and shapes of *mo* will lead to various etch-speeds and thus various values of d. There are two effects that play an important role here. One is RIElag or aspect-ratio dependent etching (ARDE) [9, 10]. ARDE does not occur due to the difference in the size of *mo* itself, but due to the difference in aspect-ratio of the resulting etched features. The second effect is loading, which is inversely proportional to the surface of Si exposed to the plasma in the etch reactor. It occurs when the etch-reactant depletes as a consequence of excessive substrate load [9]. Here the shape of *mo* does matter. The beam height can be as large as the wafer thickness. However, to accomplish this, *mo* is required large enough since the aspect-ratio of the etched trenches at both sides of the beam is limited (typically 1 : 40 or less). This limits the amount of beams per area.

The aspect ratio of the beam itself will be limited too. In case α is smaller or larger than 90°, the cross-section of the beam might end up triangular with increasing etch depth [11]. α can be tuned near to 90°. Usually α is larger than 90° to avoid "black silicon" [9, 12] (dense packed needles of Si occurring during DRIE as a result of micro-masking). Aside from the process conditions, the angle also depends on *mo* and even with equal values for *mo* at the left and right side of the beam there can be a small variation in α. If the beam is meant to be displaced in the wafer plane and is actuated in that direction, a non-symmetrical beam cross-section induces an out-of-plane displacement component.

Finally, w reduces due to etching under the mask during DRIE (under-etch or undercut). In the Bosch process the undercut occurs, because each etch cycle is in fact almost isotropic [13].

Dimensioning of the beam height and roughness When the beam is released with a dry isotropic release etch [14], the bottom side of the beam will be eroded. The amount of erosion is considerable and not (yet) very predictable. However, the amount of erosion reproduces and it can be determined by etch tests. If h is smaller than d, h

and the flatness of the topside is depending on etch times and the process used to remove the Si up to a depth of $(d - h)$.

The erosion of the beam's bottom side also causes roughness. Roughness of the topside is very small in case d and h are equal, since the wafer comes with a polished topside. If h is smaller than d, the topside of the beam can show more roughness due to the process used to tailor its height. The side walls usually are roughened by the etching. In case DRIE is used for structuring of the beam, more roughness is caused by the "standard" Bosch process than by Cryogenic DRIE [15]. In general, to avoid large roughness, wet etching based on an alkaline etchant could be considered when possible. The etching process is depending on the crystal orientation in Si. This implies a wafer with the correct crystal orientation should be used and this process cannot be used to etch every side of the beam ($\langle 110 \rangle$ for smooth sidewalls and $\langle 100 \rangle$ or $\langle 111 \rangle$ for a smooth bottom). Roughness and the etching process applied are if significant influence on the fracture-strength of beams [16].

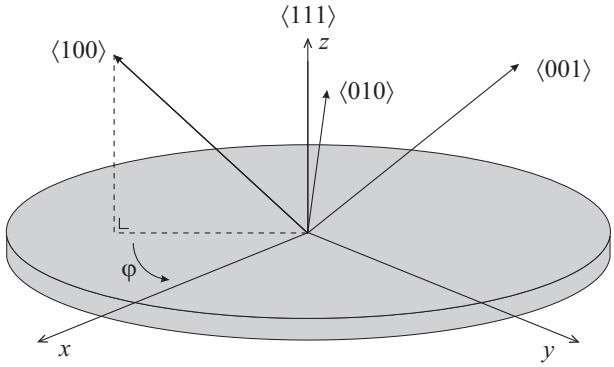

Figure 2.4: Orientation φ with respect to the $\langle 100 \rangle$-axis projection on the $\langle 111 \rangle$-wafer plane (Note that the $\langle 100 \rangle$, $\langle 110 \rangle$, and $\langle 111 \rangle$-axis are all perpendicular to each other) [17].

2.2.3 *Anisotropy in SCS*

Since silicon is an anisotropic crystalline material, its mechanical properties like Young's modulus and Poisson's ratio are direction dependent [18]. This anisotropy has consequences for the stiffness of beams in various orientations in the silicon. Once a beam is not oriented in the directions of the crystal orientations ($\langle 100 \rangle$, $\langle 110 \rangle$, $\langle 111 \rangle$), e.g. an in-plane deflection will show cross-talk in out-of-plane direction. The consequences of the anisotropy for the stiffness of beams in $\langle 100 \rangle$ and $\langle 111 \rangle$ wafers are fully described by Govindjee et al. in [17]. Resulting from this investigation, a system with triangular symmetry is best fabricated in $\langle 111 \rangle$ wafers oriented with a $\varphi = 30^\circ$ offset with respect to the $\langle 100 \rangle$-axis projection on the wafer plane (see figure 2.4).

Although notion is taken of these anisotropy effects, analytic modelling will not (fully) take into account anisotropy. To completely conceive the effects of anisotropy

Figure 2.5: Example of a parallel six DOF manipulator (Physik Instrumente [19]).

on the behavior of mechanisms, specialistic Finite Element Modelling (FEM) is required. For realization of the devices, more common and - at our lab - standard available $\langle 100 \rangle$-wafers are chosen. Although, $\langle 111 \rangle$-wafers are the better alternative, a proof of principle does not suffer from anisotropy.

2.2.4 Serial and parallel manipulation

A distinction can be made between two main basic concepts of mechanisms. One type is serial, the other is parallel. In a serial mechanism, there is one kinematic chain of links and joints between the end-effector and base. This can be accomplished by ”stacking” of the chain elements on top of each other or embedding each subsequent element into the former one. In a parallel mechanism, there exist multiple independent kinematic chains parallel to each other between the end-effector and the base. An example of a parallel mechanism is a Stewart platform often used in flight-simulators. Figure 2.5 shows a picture of a six DOF parallel manipulator also called *hexapod* (Physik Instrumente) [19]. Mechanisms can also show combinations of parallel and serial kinematics.

The two manipulator concepts have distinct properties for the implementation in MEMS. The importance of these properties for fabrication will be investigated below.

Serial manipulation requires a form of stacking. This can be either one single DOF unit on top of the other or one single DOF unit embedded in the other or a combination of both. In MEMS, stacking one unit on top of the other is not straightforward. One option is to fabricate one level in the bulk of the wafer and use surface micromachining to stack another level on top. However surface micro-machining poses

limitations to the out-of-plane stiffness of the mechanism and deposited layers often suffer from residual stress (possibly leading to non-linear behavior of the mechanism). Another means of stacking is to use wafer bonding. It is fair to say, wafer bonding requires structures to be fixed during bonding. This means post processing is required to free the mechanism from either sacrificial (fixture) material or fixture tethers [20], [21].

Embedding one unit in the other is a less complicated method of making a serial manipulator. However, the levels near to the base will turn out big since these have to embed all the subsequent levels including intermediate bodies. This will lead to lower resonance frequencies and makes the system more sensitive to vibrations coming from the environment. Furthermore, a big disadvantage of a serial mechanism is the complicated routing of the electrical connections to the actuators and sensors, since these have to be obtained through or over the beams of the mechanism (Generally no wire-bonding is possible on the fragile movable structures).

Parallel manipulation does not require stacking, although multiple actuators can be placed in series in one of the kinematic chains. In fact the complete system can be made with six of the same actuators parallel to each other between base and end-effector [22]. This has a large advantage for the electrical routing, since connections only need to go from the base directly to the actuators. Furthermore, no intermediate bodies are required. This reduces the size of the system and increases the resonance frequencies.

In principle the actuators can be defined without structuring in the height direction, except for the mechanism, since conversion of in-plane to out-of-plane motion requires a mechanism structured in height [22, 23]. The same issue might rise if three of the actuators move in out-of-plane direction. Now there is no need for a mechanism converting in-plane to out-of-plane motion, but most out-of-plane actuators require structuring in height.

2.3 Stacked parallel concept

Since 3D structuring in (bulk) MEMS is complicated, the mechanism is preferred to be simple. As indicated above out-of-plane manipulation requires at least the mechanism or the actuators to be structured in height. A mechanism converting in-plane to out-of-plane motion, generally relies on a predefined out-of-plane offset. Realizing this offset is regarded as an extra complication. Therefore the decision is made to actuate the out-of-plane DOFs with out-of-plane actuators and the in-plane DOFs with in-plane actuators. This can be realized by combining a 3 DOF in-plane manipulator

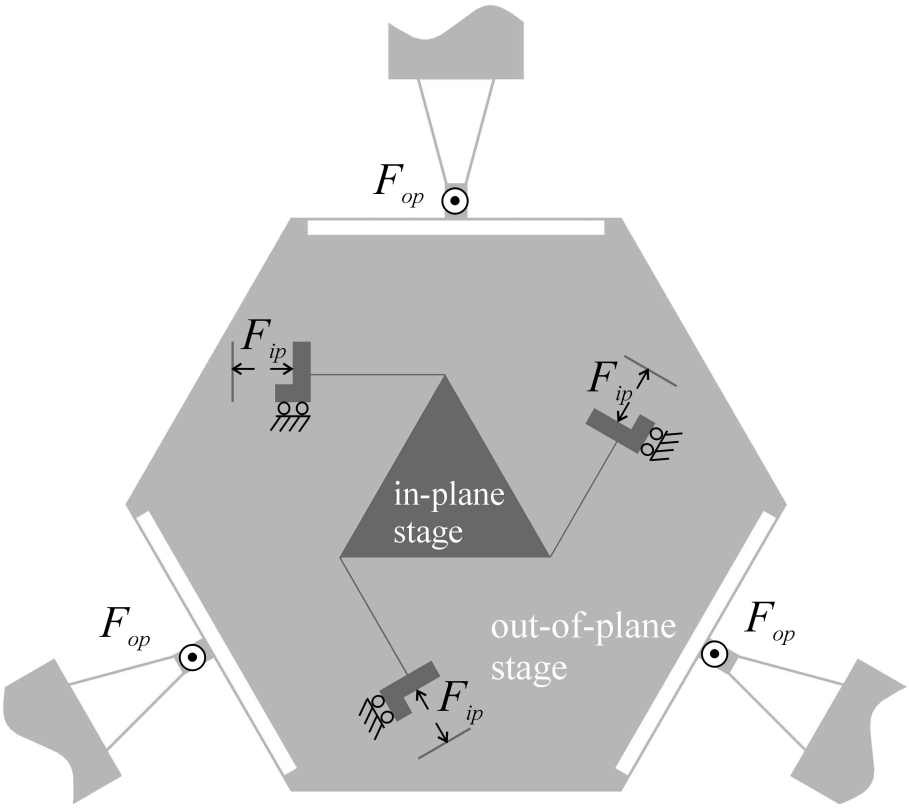

Figure 2.6: A schematic top-view of the 3 DOF planar manipulator embedded in the platform of the 3 DOF out-of-plane manipulator. Forces delivered by the actuators are indicated by F_{ip} for the in-plane stage and F_{op} for the out-of-plane stage (shown with arrowheads directed outwards of the page).

with a 3 DOF out-of-plane manipulator. The advantage of simple electrical routing and the compact nature of a parallel mechanism is preferred, so a parallel mechanism is chosen. There are various ways to connect the three planar and three out-of-plane actuators to the end-effector. It is preferred to reduce the complexity of the mechanism performing this connection. This can be achieved by separation of functionalities by stacking the stage for planar manipulation on top of the out-of-plane manipulator. For this reason it is decided to place parallel kinematic in-plane manipulation in series with parallel out-of-plane manipulation as shown in figure 2.6.

2.3.1 Manipulation concepts

The mechanism for planar manipulation (x, y-plane), as shown in figure 2.7, ideally has to be stiff in the out-of-plane directions R_x, R_y, and z. This is accomplished by supporting three vertexes of the end-effector in the out-of-plane (z) direction. The planar displacements and rotation require a rigid connection between in-plane actuators and the end-effector. The out-of-plane support and the rigid in-plane transmission

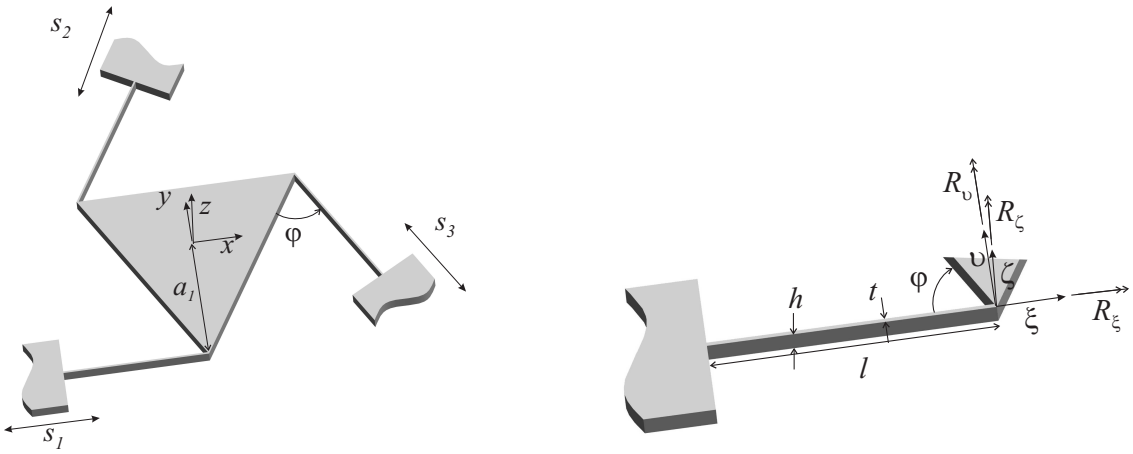

Figure 2.7: The planar manipulation concept (left) and a detail of one of its arms (right)

of the actuation force can be accomplished with three vertical plate-springs placed between the end-effector and the actuators, provided these are neither all directed at the same point nor all aligned parallel to each other[3]. Figure 2.7 (left) shows an implementation of the planar manipulator. Three vertical plate-springs connect three translational actuators to the corners of an equilateral triangular end-effector. Here φ is 60 °.

In figure 2.7 (right) one of the plate-springs is highlighted. As reasoned above the ξ and ζ direction are to be constrained at each vertex of the end-effector by the plate-springs. The other DOFs are desired to be compliant. In table 2.2 the DOFs are listed, showing wether these are constrained or compliant. Furthermore a qualitative assessment is given, defining up to which extend the geometry of the beams in the mechanism are suited to kinematically constrain the desired DOFs.

Table 2.2: Kinematic definition of the plate-spring DOF in the planar manipulator.

DOF	kinematic definition	assessment
ξ	constrained	✓
υ	compliant	✓
ζ	constrained to a lesser extent since l is large compared to h	$\pm$
R_ξ	compliant	✓
R_υ	compliant to a lesser extent; bending in height direction	$\pm$
R_ζ	compliant	✓

[3]In fact plate-springs constrain three DOFs each, meaning the mechanism technically is overconstrained. The third DOF is rotation of the free beam-end in its height direction. However, the length/height ratio is very large, meaning DOFs in height direction are only moderately constrained.

Two DOFs comply to a lesser extent to the requirements, namely constrained ζ-direction and compliant rotation in R_υ. Both due to the beam's length/height-ratio. However, a relatively large beam length is required since the force required for the beam deflections should not be too large compared to the maximum force the actuator can deliver. Additionally, assuming a 10 micron platform displacement, the stress in the beam needs to be well below the fracture stress. The minimum value of the fracture stress for SCS is 1 GPa [24]. Equation (2.1) shows the expression for the fracture stress σ_{fr} for in-plane deflection of a beam [25]. With the Young's modulus of 130 GPa, the thickness t of 2 μm and the deflection Δ of 10 μm, it turns out the beam needs to be well larger than 51 μm. This requirement is easily met since the length will be in the order of a millimeter. Another reason the beam should not be too short compared to the deflection is stiffening. For instance, a stiffening of 10 % occurs in the guiding-stiffness[4] of a beam for a deflection over length ratio of 0.3 [5].

$$\sigma_{fr} = 3\,\frac{E_Y\,t\,\Delta}{l^2} < 1\times 10^9 \quad \Rightarrow \quad l \gg 88\mu\text{m} \tag{2.1}$$

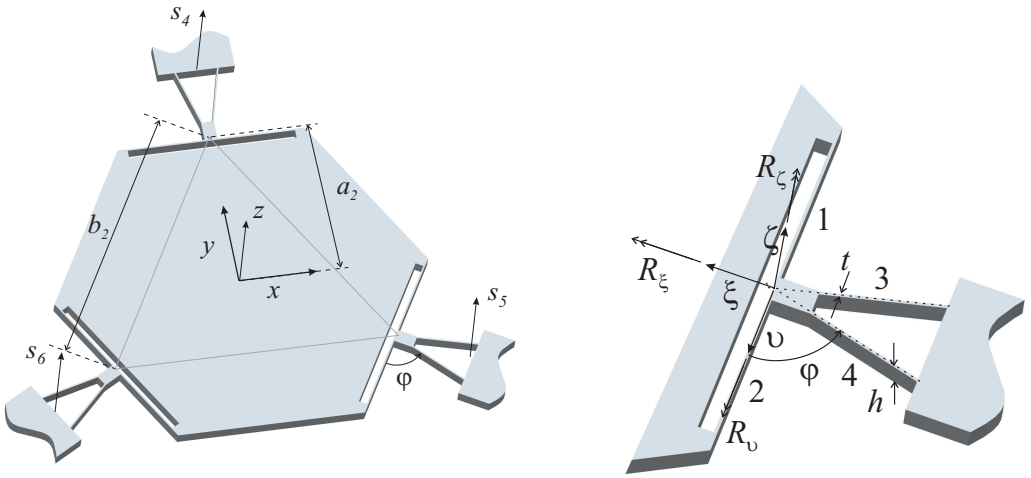

Figure 2.8: The out-of-plane manipulation concept (left) and a detail of one of its suspension mechanism (right)

The demands on the mechanism for out-of-plane manipulation are more complex for MEMS fabrication. Figure 2.8 (left) shows a hexagonal end-effector connected to three out-of-plane actuators via three identical mechanisms, each consisting of four vertical plate-springs and an intermediate body. The slanted beams (3 and 4) of the mechanism are directed towards one point, which coincides with one of the vertices of an equilateral triangle (shown in gray lines on the end-effector). To constrain the in-

[4]The free end of the beam deflects under the condition of zero angle of rotation at the free end of the beam.

Table 2.3: Kinematic definition of the three-beam mechanism DOF in the out-of-plane manipulator.

DOF	kinematic definition	assessment
ξ	compliant	✓
v	constrained	✓
ζ	constrained to a lesser extent since l is large compared to h	$\pm$
R_ξ	compliant to a lesser extent; bending in height direction	$\pm$
R_v	compliant	✓
R_ζ	compliant	✓

plane DOFs the vertices should be constrained in tangential direction. Furthermore, each four-beam mechanism should be rigid for the transfer of the out-of-plane force of the actuator to the end-effector.

Figure 2.8 (right) shows a detail of one of the four-beam mechanisms. As reasoned above, this mechanism has to constrain movement in the v- and ζ-direction and be compliant in the remaining DOFs. The v-direction is constrained since beams 1 and 2 are loaded in their stiff longitudinal direction and beams 3 and 4 are not parallel but directed to one point, which is in the plane of beams 1 and 2. In table 2.3 once again the kinematic definition of the DOFs of the four-beam mechanism are given and assessed. Here the ζ-direction is constrained to a lesser extent as well, because of the large length of the beams compared to their height. Torsion about R_ξ is compliant to a lesser extent since the beams 3 and 4 are high and not aligned with the torsion axis. Except when φ is 90 °, but then v is not constrained well. Most probably rotation about R_ξ is released by beams 1 and 2 by bending in their height direction. Instead of beams 3 and 4, the $\perp$-shaped torsion beam introduced in chapter 4 can be applied, increasing the compliance in the R_ξ direction. However, the stiffness in v direction will be decreased and structuring in out-of-plane direction is required.

For both stages, the stiffness of the platform itself is also limited by the achievable height of the applied processing. The limited height will cause the platforms to behave more like plates than like rigid bodies.

2.3.2 Inverse kinematic model and manipulation space

The relation between actuator strokes and coordinates of the end-effector are modelled with a linear inverse kinematic model. This model is derived by virtually displacing the symmetric center of the end-effector along the DOFs and analyzing the strokes required for these displacements. By this procedure a matrix is obtained linking the strokes of the actuators to the DOFs in the symmetry center. Inverting this

matrix results in the transformation matrix linking the DOFs to the actuator strokes. For the planar stage this procedure is followed in equation (2.2).

$$\begin{bmatrix} s_1 \\ s_2 \\ s_3 \end{bmatrix} = \begin{bmatrix} 1 & 0 & a_1 \\ -\frac{1}{2} & -\frac{\sqrt{3}}{2} & a_1 \\ -\frac{1}{2} & \frac{\sqrt{3}}{2} & a_1 \end{bmatrix} \begin{bmatrix} x \\ y \\ R_z \end{bmatrix} \tag{2.2a}$$

$$\begin{bmatrix} x \\ y \\ R_z \end{bmatrix} = \begin{bmatrix} \frac{2}{3} & -\frac{1}{3} & -\frac{1}{3} \\ 0 & -\frac{\sqrt{3}}{3} & \frac{\sqrt{3}}{3} \\ \frac{1}{3a_1} & \frac{1}{3a_1} & \frac{1}{3a_1} \end{bmatrix} \begin{bmatrix} s_1 \\ s_2 \\ s_3 \end{bmatrix} \tag{2.2b}$$

Following this procedure for the out-of-plane stage results in the transformation matrix linking the DOF in the symmetric center to the vertical strokes given in equation (2.3).

$$\begin{bmatrix} s_4 \\ s_5 \\ s_6 \end{bmatrix} = \begin{bmatrix} a_2 & 0 & 1 \\ -\frac{a_2}{2} & -\frac{b_2}{2} & 1 \\ -\frac{a_2}{2} & \frac{b_2}{2} & 1 \end{bmatrix} \begin{bmatrix} R_x \\ R_y \\ z \end{bmatrix} \tag{2.3a}$$

$$\begin{bmatrix} R_x \\ R_y \\ z \end{bmatrix} = \begin{bmatrix} \frac{2}{3\,a_2} & -\frac{1}{3\,a_2} & -\frac{1}{3\,a_2} \\ 0 & -\frac{1}{b_2} & \frac{1}{b_2} \\ \frac{1}{3} & \frac{1}{3} & \frac{1}{3} \end{bmatrix} \begin{bmatrix} s_4 \\ s_5 \\ s_6 \end{bmatrix} \tag{2.3b}$$

Validity of the model These models are linear. In fact the models are only valid for small displacements around the zero position. The flexure mechanisms have limited linear behavior [5]. Here it is assumed that deflections are small in comparison to the system dimensions allowing a linear model to describe the behavior of the system sufficiently accurate. A mathematically more correct approach to obtain the transformation matrixes transforming the platform position to the actuator strokes would be to express the coordinates of the platform vertices in the frame of the actuator base-points/fixations and calculate the distance between the vertices and base-points.

This is fairly simple for the planar stage, however for the out-of-plane stage commutation[5] of the two tilts and the out-of-plane translations should be taken into account. Strictly speaking rotations and translations in three dimensional space do not commutate. Therefor, first applying a tilt in R_x-direction followed by a tilt R_y-direction yields a different result than reversing the order of the tilts.

[5]The mathematically property of an operation implying the order in which the operation is applied on its arguments does not yield differences in the result of the operation.

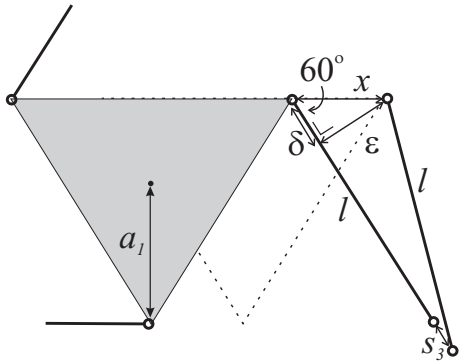

Figure 2.9: Rigid-link model used to estimate the error due to the first order approximation in the inverse kinematic model.

To obtain a model that does take into account commutation, the tilting of the platform should be expressed such that the commutation problem is avoided. Considering the resultant tilt of the combined tilts in R_x-direction R_y-direction, the orientation of the resultant tilt-axis and the amount of tilt are the two new parameters to describe the platform tilts (i.e. the orientation would be 0 rad in case of a pure tilt in R_x-direction and $\frac{\pi}{2}$ rad in case of pure tilt in R_y-direction). A model based on the orientation and amount of tilt requires an additional mathematical procedure, which is not within the scope of this thesis and is (for instance) described in [26].

The inverse kinematic model does not take into account the change in the angle at the attachment points to the platform, when the platform is displaced. Figure 2.9 shows a drawing of a rigid-link model used to calculate the error due to the first order approximation. Here the example is chosen for displacement in the x-direction (relation x and s_3). The following equations hold:

$$\begin{aligned} & l^2 = \varepsilon^2 + (l - \delta + s_3)^2 \\ & \text{with,} \\ & \delta = x \cos 60^\circ \\ & \varepsilon = x \sin 60^\circ \end{aligned} \tag{2.4a}$$

With l [m] the length of the link between the platform and the actuator, and s_3 [m] the actuator stroke required for a displacement x [m]. Using these equations, an expression for s_3 can be found. The derivative of s_3 with respect to x is:

$$\frac{\mathrm{d}s_3}{\mathrm{d}x} = \frac{1}{2} - \frac{3}{2} \frac{x}{\sqrt{4\,l^2 - 3\,x^2}} \tag{2.4b}$$

The absolute error with the relation of $\frac{1}{2}$ between s_3 and x given in the inverse kinematic model is:

$$err. = \left| \frac{\mathrm{d}s_3}{\mathrm{d}x} - \frac{1}{2} \right| \tag{2.4c}$$

For l is 1 mm and a displacement x of 10 μm the error amounts to 0.8 %. Errors due to fabrication variations (mainly affecting stiffness of the flexures) are expected to be larger than the error made by assuming a linear model. Were the model is used for feed-forward control to drive the manipulator, it will be useful for positioning of the end-effector close to the assigned position (assuming the actuator's force-displacement relation is known). For more precise positioning a look-up table, obtained by extensive characterization of the fabricated device is required.

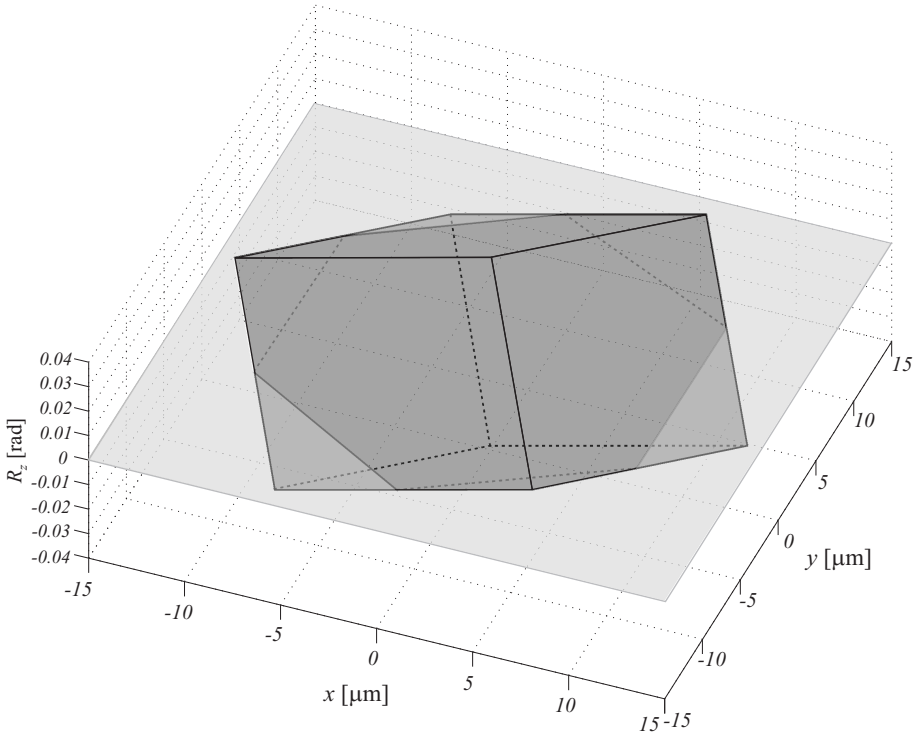

Figure 2.10: Configuration space 3 DOF in-plane

Estimation of manipulation spaces The inverse kinematic models can be used to plot an estimated manipulation space for the separate manipulator stages. Assuming a stroke from -10 to 10 μm for each actuator, the manipulation space for the planar stage will look like figure 2.10 [6]. The rotation angle R_z is plotted along the height axis and the value for $R_{z,max}$ depends on the maximum stroke and the dimension a_1 as given in equation (2.2). Clearly a larger a_1 results in a decrease of the maximum

[6]Due to shortening of the deflected flexures, which is not modelled, the outer corners and edges of the space will not be reached, so strictly these would best be shown rounded.

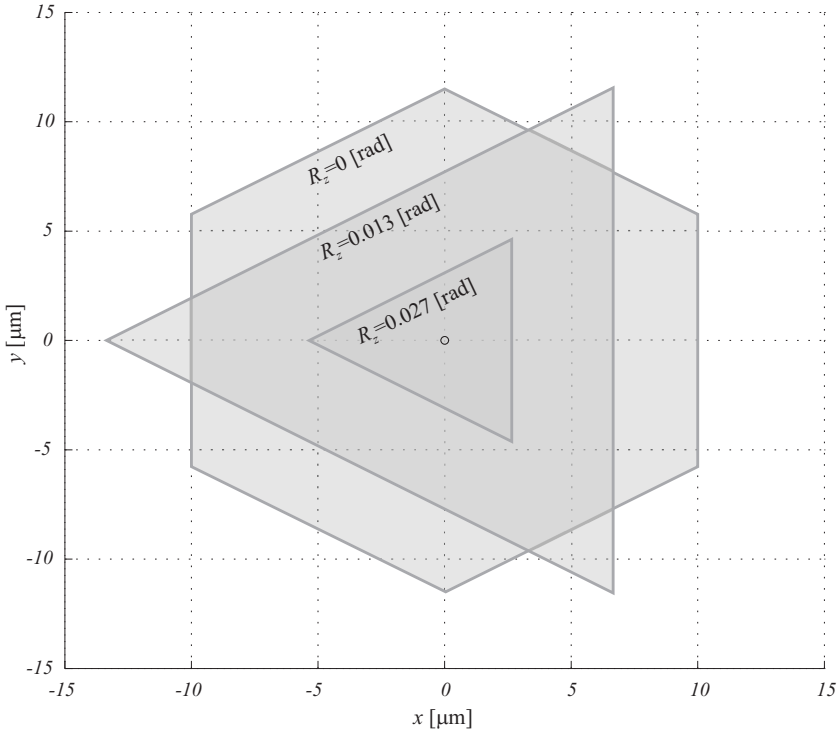

Figure 2.11: Slices of the manipulation space in figure 2.10 for R_z is zero, one-third and two-third of the maximum positive rotation angle

rotation about z. For this plot, a realistic value of 260 μm is used for a_1. At $R_z = 0$, a plane is drawn, intersecting the manipulation space. The intersection shows the plane for xy-manipulation for zero rotation. In figure 2.11, xy-manipulation planes are shown as slices of the manipulation space for respectively R_z is zero, 0.013 and 0.027 rad. For negative rotation angles the planes would be similar but rotated 180 $^\circ$ about the R_z axis. In equation (2.2), it is shown that for maximum, pure translation in the x-direction strokes s_2 and s_3 are not yet at their maximum of 10 μm while s_3 is. Increasing s_2 and s_3 will result in a larger displacement in x-direction combined with a rotation; this is reflected e.g. in the slice for $R_z = 0.013$, while beyond this value for R_z the range for x, y-manipulation only decreases. Something similar also holds for translation in the y-direction. Clearly, to allow large rotation combined with 10 μm strokes in x- and y-direction, the strokes of the actuators are required to be larger than 10 μm. Although the implementation of the planar manipulator, as will be discussed in chapter 3, is limited to strokes of 10 μm, larger strokes are feasible [27].

For the out-of-plane stage a manipulation space is drawn similarly (strokes ranging from -10 to 10 μm). In fact the shape of this space equals the one shown in figure 2.10. Figure 2.12 op page 41 shows three slices of this manipulation space for z is zero, 3.333 and 6.667 μm. The values for $R_{x,max}$ and $R_{y,max}$ depend on the values for

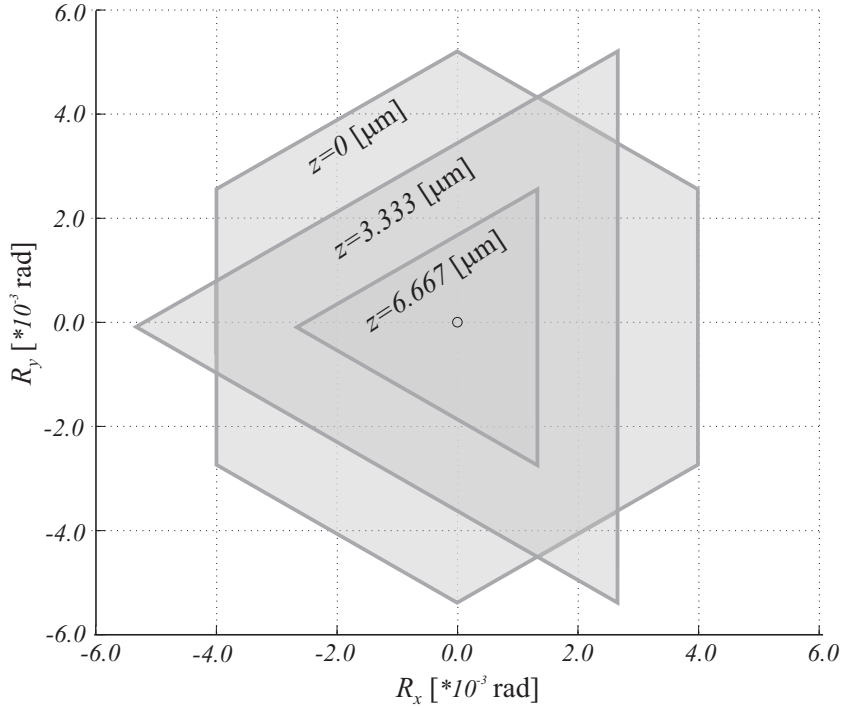

Figure 2.12: Slices of the manipulation space for the out-of-plane stage for z is zero, one-third and two-third of the maximum vertical displacement

a_2 and b_2 according to equation (2.3). Realistic values of 3.46 and 4.0 mm are chosen for a_2 and b_2 respectively, taken into account this stage will be the first manipulator, carrying the planar stage. Of course the size of the stage depends on the compactness of the design. That can be an optimization criterium for following generations. However, the main objective of this study will concentrate on the feasibility of the manipulator in MEMS technology.

As highlighted in the introductory chapter, the R_x and R_y tilt cannot meet the desired specifications as given in table 1.1. In the introduction a solution was introduced to apply a two stage approach with a 2 DOF tilt stage designed for "conventional" precision machining, carrying a 6 DOF MEMS stage for fine positioning.

2.4 Actuator selection

The manipulator concept requires in-plane or horizontal actuators and out-of-plane or vertical actuators. For horizontal actuation there are numerous possibilities in MEMS technology. A simple and easy to manufacture actuator offering sufficient force and stroke is the electrostatic comb-drive [14, 27]. This might be a good choice, however it is preferred both actuator types do not require different technologies. Furthermore,

since the vertical actuator will be most demanding with respect to fabrication, first the vertical actuator will be chosen.

Many examples of vertical actuation in MEMS can be found in literature. However, for our specific application a large number of these are not suitable. Mostly because of inadequate performance of the actuator with respect to the requirements to the system. Additionally, the type of actuation should not complicate the research unnecessarily, since its goal is largely focussed on solutions for precision mechanism in MEMS. To start with, large vertical motion based on driving the system in resonance (much seen in scanning micro-mirrors and inertia sensors [28]) is not applicable, since the stroke is not available for static positioning. Furthermore, for the system to fit in a small space, no use can be made of large sized external sources for magnetic fields, so the force generated with a micrometer-sized lorentz type actuator including magnetic source is not enough [29]. This means the actuation will not be based on magnetic transduction.

Roughly, three well known and generally good performing options remain; piezo-electric, electrothermal, and electrostatic transduction. Keeping in mind the desire to avoid assembly and the preference for a bulk micro-machined system, piezo-electric transduction is less suited. Especially in the case of thin-film actuators of PZT. Because this material is not very stable during processing since the lead concentration reduces by outgassing during the annealing step for perovskite crystal formation. This complicates the fabrication and demands for (time consuming) process optimization [30]. Thin-film alternatives like ZnO and AlN do not exhibit chemical instability during fabrication, but have a far smaller piezo-electric coefficient [31]. Furthermore, thin-film technology is often applied in uni-morph and multi-morph actuators. These thin-film beam-like structures conflict with integration in a bulk micro-machined system. For the same reason thin-film thermal-mechanic bimorph structures are not preferred. Bulk micro-machined hot-leg/cold-leg actuators for out-of-plane actuation will have a very challenging three dimensional geometry to fabricate [32], while thermal actuators in general (and especially in vacuum applications) may compromise the thermal stability requirements of sub-nanometer and fast stabilizing thermal drift.

After analyzing common actuator principles, electrostatic actuation remains. It is possible to fabricate monolithic, vertical electrostatic actuators from SCS. In case of a vertical comb-drive, a sufficiently large force can be provided over a sufficiently large stroke [33]. Gap-closing actuators are not suitable, since the force is not constant with displacement and far larger voltages are needed for a reasonable force. This is caused by the fact, that for energetic stability reasons, an initial gap of three times the stroke is required.

For sake of simplicity and compatibility with our processing experience, a choice

is made for vertical comb-drives. Since horizontal comb-drives are simple to fabricate, the fabrication demands most probably will not conflict with those for a vertical comb-drive. For this reason horizontal comb-drives are chosen for the planar manipulation. The proposed design for the manipulator is not depending on the actuators and can be used with any other actuator-type if better options appear on the scene in future.

2.5 Conclusion and discussion

In this chapter the typical aspects of design and fabrication of a precision 6 DOF manipulator in MEMS technology are discussed. The chosen mechanisms are based on flexures, because hinges and non-flexible joints in MEMS are complicated to realize especially, if these should have small enough friction and play to ensure nanometer resolution positioning. Some common flexure beams and mechanisms are discussed and an investigation is made on the definition of the desired beam geometry with MEMS technology. Because of the outstanding mechanical properties of bulk Si and the possibility of high aspect-ratio structuring, mainly bulk micro-machining of SCS is considered. Compared to other machining technologies, MEMS processing shows a large degree of indirect geometric control where many parameters and relations between parameters play an important role. Resulting from the investigation, mask precision, loading, ARDE, etch-profile/taper, and dependance on crystal orientation are regarded to be most crucial for the resulting beam geometry.

The manipulator will consist of a stack of two parallel manipulators. One for 3 DOF planar manipulation and one for 3 DOF out-of-plane manipulation. Realizing an exact kinematic constrained design for the manipulator mechanisms in MEMS, only consisting of (relatively simple) vertical beams, leaves some DOFs ill constrained. To improve the design with respect to exact kinematic constrained DOFs, 3D or height structuring is required. Furthermore, the length of the beams, required for sufficient in-plane compliance, conflicts with the preferred large out-of-plane stiffness. Here the aspect-ratio of the beams is the limiting factor, since the minimal thickness of the beams is limited by lithography to 2 μm. Thinner beams would allow for less length. However, there are limits to the reduction of the length, since a large deflection over length ratio causes significant non-linear behavior due to stiffening.

The manipulator needs to be driven both by planar and out-of-plane actuators. Various actuators are considered and the choice is made for comb-drives for both planar and out-of-plane actuation. Feasibility of the required processes played an important role. Planar comb-drives are simple structures to fabricate and do not pose complex fabrication demands. A vertical comb-drive seems to be one of the actuator options for out-of-plane actuation that is best compatible with our processing

experience. Furthermore, in case the required space is not too much of an issue, comb-drives generally are capable of sufficient force and displacement without any kind of mechanical amplification.

Although for the proposed planar manipulator, x, y-manipulation in combination with R_z rotation is limited, planar comb-drives with larger strokes are feasible. However, the available R_x and R_y tilt provided by the out-of-plane manipulator does not meet the desired specifications by far. A possible solution to realize these tilt angles, would be to apply an additional 2 DOF tilt stage designed for "conventional" precision machining.

References

[1] M. Madou, *Fundamentals of Microfabrication*. CRC Press LLC, Boca Raton, USA, 2000.

[2] B. J. Jokiel, G. L. Benavides, L. F. Bieg, and J. J. Allen, "Planar and Spatial Three-Degree-of-Freedom Micro-Stages in Silicon MEMS," *Proceedings of ASPE annual meeting 2001*, vol. 25, pp. 32–35, 2001.

[3] J. A. Walraven and B. J. Jokiel, "Failure Analysis of a Multi-Degree-of-Freedom Spatial Microstage," *Proceedings of SPIE 2003*, vol. 4980, pp. 97–105, 2003.

[4] K. S. J. Pister, M. W. Judy, S. R. Burgett, and R. S. Rearing, "Microfabricated hinges.," *Sensors and Actuators A*, vol. 33, pp. 249–256, 1992.

[5] J. Van Eijk, *On the Design of Plate-spring Mechanisms (Ph.D thesis)*. Delft University, The Netherlands, 1985.

[6] F. Niklaus, S. Haasl, and G. Stemme, "Array of Monocrystalline Silicon Micromirrors Fabricated Using CMOS Compatible Transfer Bonding," *J. MEMS*, vol. 12, no. 4, pp. 465–469, 2003.

[7] K. Bethe and J. Frank, "Creep of Sensor's Elastic Elements: Metals versus Non-metals," *Sensors and Actuators A*, vol. A21-A23, pp. 844–849, 1990.

[8] W. C. Young and R. G. Budynas, *Roark's Formulas for Stress and Stain*. McGraw-Hill, 7^{th} ed., 2002.

[9] H. Jansen, G. Gardeniers, M. De Boer, M. Elwenspoek, and J. Fluitman, "A survey on the reactive ion etching of silicon in microtechnology," *J. Micromech. Microeng.*, vol. 6, pp. 14–28, 1996.

[10] A. R. Gottscho, C. W. Jurgensen, and V. D. J., "Microscopic Uniformity in Plasma Etching," *J. Vac. Sci. Technol. B.*, vol. 10, no. 5, pp. 2133–2147, 1992.

[11] J. Li, A. Q. Liu, and Q. X. Zhang, "Tolerance Analysis for Comb-drive Actuator Using DRIE Fabrication," *J. MEMS*, vol. 125, pp. 494–503, 2006.

[12] H. V. Jansen, M. J. De Boer, R. Legtenberg, and M. C. Elwenspoek, "BSM 1: The Black Silicon Method," *J. Micromech. Microeng.*, vol. 5, pp. 115–120, 1996.

[13] R. Zhou, H. Zhang, Y. Hao, and Y. Wang, "Simulation of the Bosch process with a string-cell hybrid method," *J. Micromech. Microeng.*, vol. 14, no. 7, pp. 851–858, 2004.

[14] E. Sarajlić, M. J. De Boer, H. V. Jansen, N. Arnal, M. Puech, G. J. M. Krijnen, and M. C. Elwenspoek, "Advanced plasma processing combined with trench isolation technology for fabrication and fast prototyping of high aspect ratio MEMS in standard silicon wafers," *J. Micromech. Microeng.*, vol. 14, pp. S70–S75, 2004.

[15] B. R. De Jong, H. V. Jansen, M. J. De Boer, and G. J. M. Krijnen, "Tailored etch-profiles of high aspect ratio trenches to prevent voids after refill with lpcvd sirn.," in *MME*, (Göteborg, Sweden), pp. 60–63, 2005.

[16] Y. Taechung, L. Li, and C.-J. Kim, "Microscale material testing of single crystalline silicon: process effects on surface morphology and tensile stength," *Sensors and Actuators A*, vol. 24, no. 5, pp. 172–178, 2000.

[17] S. Govindjee and S. Klinkel, "Mechanical coupling in single crystal silicon for MEMS design," *J. MEMS.*, vol. 14, no. 4, pp. 864–871, 2005.

[18] J. J. Wortman and R. A. Evan, "Young's modulus, shear modulus and poisson's ratio in silicon and germanium," *J. Appl. Physics*, vol. 36, no. 1, pp. 153–156, 1965.

[19] Physik Instrumente; http://www.physikinstrumente.de/.

[20] L. Zhou, J. M. Kahn, and K. S. J. Pister, "Scanning Micromirrors Fabricated by an SOI/SOI Wafer-Bonding Process," *J. MEMS*, vol. 15, no. 1, pp. 24–32, 2006.

[21] Y.-C. Tung and K. Kurabayashi, "A Single-Layer PDMS-on-Silicon Hybrid Microactuator With Multi-Axis Out-of-Plane Motion Capabilities-Part II: Fabrication and Characterization," *J. MEMS*, vol. 14, no. 3, pp. 558–566, 2005.

[22] D. M. Brouwer, B. R. De Jong, and H. M. J. R. Soemers, "MEMS 6 Degree of Freedom parallel kinematic precision micro manipulator.," in *Euspen*, (Baden bei Wien, Austria), pp. 111– 114, 2006.

[23] Y.-C. Tung and K. Kurabayashi, "A Single-Layer PDMS-on-Silicon Hybrid Microactuator With Multi-Axis Out-of-Plane Motion Capabilities-Part I: Design and Analysis," *J. MEMS*, vol. 14, no. 3, pp. 548–557, 2005.

[24] C. J. Wilson, A. Ormeggi, and N. M., "Fracture testing of silicon microcantilever beams," *J. Appl. Phys.*, vol. 79, no. 5, pp. 2386–2393, 1996.

[25] J. M. Gere, *Mechanics of Materials*. Thomson Brooks/Cole, 6^{th} ed., 2004.

[26] R. M. Murry, Z. Li, and S. S. Sastry, *A Mathematical Introduction to Robotic Manipulation*, ch. 2, 3. CRC Press, 1994.

[27] G. Zhou and P. Dowd, "Tilted folded-beam suspension for extending the stable travel range of comb-drive actuators.," *J. Appl. Phys.*, vol. 13, no. 2, pp. 178–183, 2003.

[28] R. Conant, J. T. Nee, K. Y. Lau, and R. S. Muller, "A Fast Flat Scanning Micromirror," in *IEEE Solid-State Sensor and Actuator Workshop Technical Digest*, (South Carolina, USA), pp. 6–9, Hilton Head, June 2-4 2000.

[29] A. Nakai, K. Hoshino, M. K., and S. I., "Transmissive scanning micromirrors for autostereoscopic display.," in *MEMS*, (Istanbul, Turkey), pp. 40–43, 2006.

[30] P. Muralt, "Ferroelectric Thin Films for Micro-Sensors and Actuators: a Review," *J. Micromech. Microeng.*, vol. 10, pp. 136–146, 2000.

[31] S. Trolier-McKinstry and P. Muralt, "Thin Film Piezoelectrics for MEMS," *Journal of Electroceramics*, vol. 12, pp. 7–17, 2004.

[32] V. Milanović, "Multilevel Beam SOI-MEMS Fabrication and Applications," *J. MEMS*, vol. 13, no. 1, pp. 19–30, 2004.

[33] S. Kwon, V. Milanović, and L. P. Lee, "Vertical combdrive based 2-D gimbaled micromirrors with large static rotation by backside island isolation.," *IEEE Journal of Selected Topics in Quantum Electronics*, vol. 10, no. 3, pp. 498–504, 2004.

Chapter 3

3 DOF planar manipulator

The planar 3 DOF parallel manipulator introduced in chapter 2 is implemented and successfully fabricated. The design is discussed, emphasizing the side and rotational pull-in instability conditions for the comb-drives. A power-port based model of the system is presented and the device is characterized with respect to resulting geometry, measurements of the platform position, out-of-plane cross-talk and hysteresis.

3.1 Introduction

As part of the 6 DOF manipulation concept discussed in chapter 2, a planar 3 DOF parallel manipulation-stage is required. The flexure-based mechanism for planar 3 DOF manipulation is introduced in section 2.3 of chapter 2 and the choice is made to use electrostatic comb-drive for actuation. This chapter discusses the design, modelling, fabrication and characterization of the manipulator.

The design of the system, as dealt with in section 3.2, concerns the implementation of the concept, the requirements for electrical interconnect, the limitations of the fabrication process, the comb-drive requirements for stroke and force, and especially the pull-in stability analysis of the comb-drive suspension.

A simulation model is presented in section 3.3. This model deals with parallel kinematics, crystal orientation dependent flexure stiffness values and feed-forward control. In section 3.4 the fabrication process is explained and the consequences of the mask design for successful device release are highlighted.

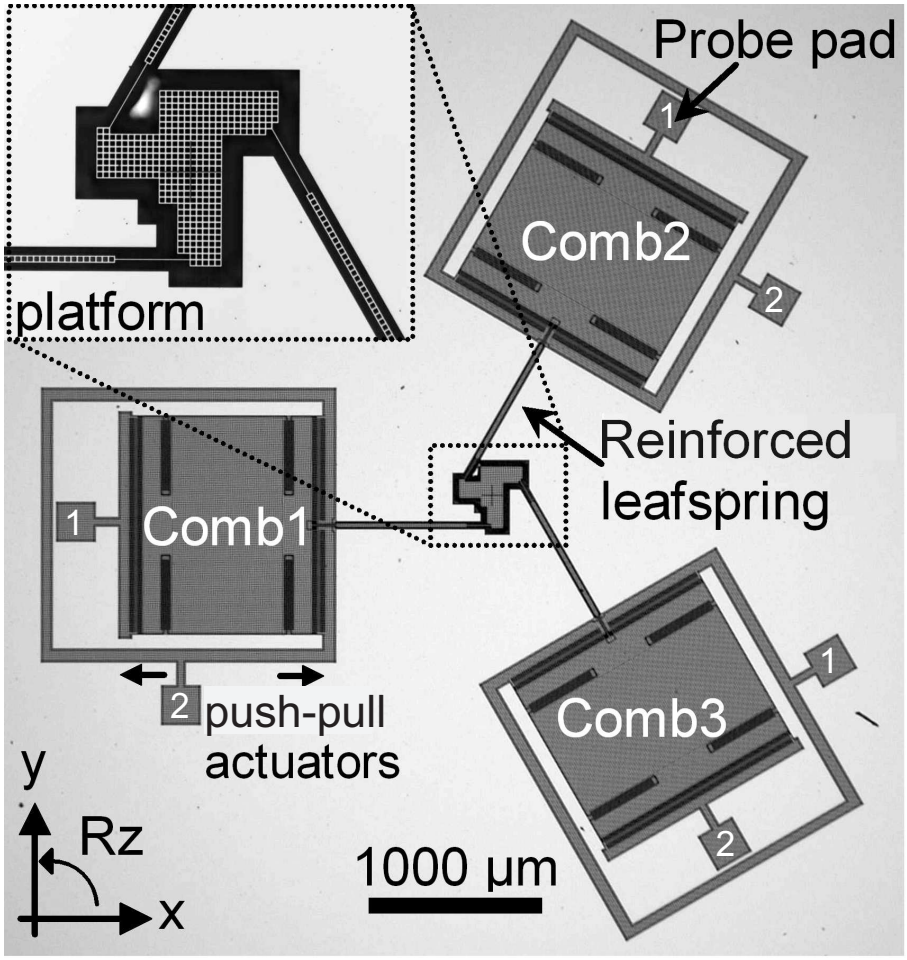

Figure 3.1: Microscope image showing the top-view of a fabricated device. Inset: an enlargement of the platform.

Section 3.5 discusses important consequences of the plate-spring geometry resulting from the fabrication for the in-plane stiffness and gives an estimation of the impact on the stiffness. Furthermore, the results of the platform position measurements for driving of the manipulator according to the inverse kinematic model are presented, as well as out-of-plane cross-talk and hysteresis measurements.

An evaluation of the realized 3 DOF manipulator with respect to the requirements and expectations follows in the conclusion in section 3.6.

3.2 Design

This section discusses the design of the 3 DOF planar manipulator. First an overview is given of the geometry of the complete device, followed by the design of the plate-springs between the actuators and the platform. Subsequently, the comb-drives are discussed including the negative electrostatic stiffness in side pull-in direction and the

pull-in conditions for instability of an individual comb-tooth. Finally, the comb-drive suspension is treated, with focus on the side-ways and rotational pull-in conditions.

3.2.1 Geometry

Figure 3.1 shows a top-view of the fabricated 3 DOF manipulator. The particular process used for fabrication of this stage, as will be discussed in section 3.4, is based on a combination of high aspect-ratio etching and dry isotropic release etching. The release step requires etch-holes in all the structures that either are free-to-move or need to be electrically insulated. This implies that the shuttles for the comb-drives, the end-effector platform and the paths of the electrical connection routing will all contain etch-holes. For proper release of the shuttles and the platform, the etch-holes should all have comparable sizes. The dark gray areas in figure 3.1 are in fact consisting of etch-holes used for device release.

The stiffest construction will be accomplished with triangular shaped etch-holes. However, there is more processing experience with square shaped etch-holes, especially where it concerns the isotropic release. To decrease the risk of complications, square shaped etch-holes are applied and application of triangular holes is regarded as a option for improvement and future optimization.

Three bidirectional, push-pull[1] comb-drives are arranged symmetrically around the end-effector platform and are connected to the platform by reinforced plate-springs. Each comb-drive is numbered and also the two probe-pads for each comb-drive have there own number. Numbers 1 connect to the pull comb-rack, while numbers 2 connect to the push comb-rack. Electrical interconnect is accomplished by under etched regions (with etch-holes) electrically insulated circumferentially by dielectric barriers. These connection-paths are found between the probe-pads and the comb-drives. The comb-shuttles are electrically connected to the grounded surrounding bulk Si via their suspension.

Although the platform itself has no triangular shape, the attachments of the plate-springs coincide with the vertices of a nearly equilateral triangle. The size of square shaped etch-holes is related to the vertical comb-drive design in the same mask. As mentioned before, for successful fabrication equal etch-holes sizes are very important. Constructing an equilateral triangle with the given etch-hole size is not entirely possible, but is closely approximated. However, one error was made during the design of the mask; the arm coming from comb-drive 1 should have been attached to the lowest point of the platform, i.e. one etch-hole lower. It turns out, as shown in figure 3.2, that

[1]Electrostatic actuators are only able to exert attractive forces, however in this comb-drive configuration the pulling force of both comb-racks are in opposite direction. As a result, the force of one of the two racks can be seen as a pushing force.

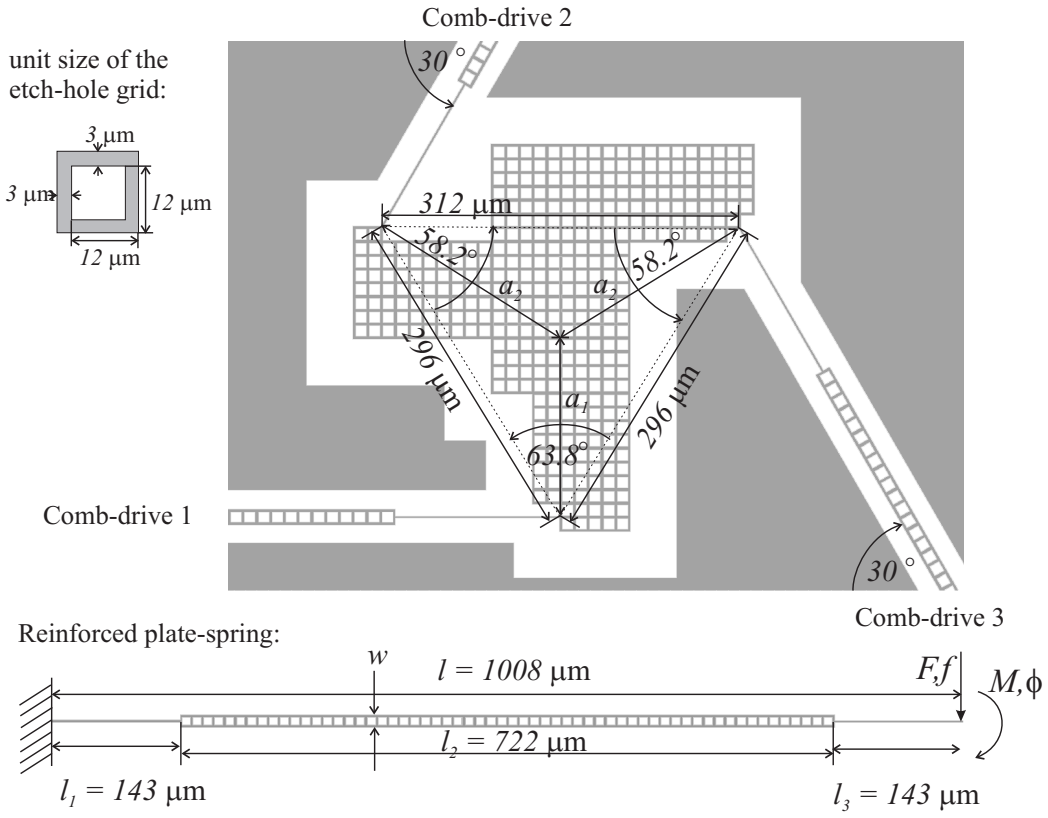

Figure 3.2: Top-view of the design of the platform and one of the reinforced plate springs.

the inner angles of the triangle where comb-drive 2 and 3 attach to the platform are 58.2° in stead of 60° and the angle whereto comb-drive 1 attaches amounts 63.8°. As a consequence the inverse kinematic model derived in section 2.3.2 of chapter 2 is not entirely correct; for equal strokes of all comb-drives, the platform will rotate about a different point than was assumed to derive the model.

The inverse kinematic model can be derived for the new situation. Although the angles of the triangular platform are not equal to 60°, the orientational angles between the three suspension beams are equal to 60° as proposed in the design in chapter 2. As a consequence, only the new values for the radii between the three vertices of the platform and the rotation center are to be used in the kinematic model (see a_1 and a_2 in figure 3.2). The new transformation matrix between the position of the platform and the required strokes will be:

$$\begin{bmatrix} s_1 \\ s_2 \\ s_3 \end{bmatrix} = \begin{bmatrix} 1 & 0 & a_1 \\ -\frac{1}{2} & -\frac{\sqrt{3}}{2} & a_2 \\ -\frac{1}{2} & \frac{\sqrt{3}}{2} & a_2 \end{bmatrix} \begin{bmatrix} x \\ y \\ R_z \end{bmatrix} \tag{3.1}$$

3.2.2 Plate-springs

The plate-springs are reinforced for robustness with respect to buckling (see figure 3.2). Application of reinforcement is chosen to stay on the safe side with the design of the relatively long plate-springs, although this particular system is not potentially sensitive to buckling. The reinforcement has consequences for the stiffness matrix of a reinforced beam with respect to a normal beam. The consequences of the geometry on the stiffness matrix will be analyzed below.

Stiffness matrix First a stiffness matrix is derived (see appendix A), relating the force F and moment M to the deflection f and angle ϕ (see figure 3.2). The out-of-plane stiffness is not considered here, since the consequences for out-of-plane stiffness do not relate to the force required to drive the manipulator. However, the reinforcement will also increase the out-of-plane stiffness, which is beneficial. Equations (3.2) gives the stiffness matrix of the reinforced plate-spring.

$$\begin{bmatrix} M \\ F \end{bmatrix} = -\frac{1}{a\,(4d - 3b^2)} \begin{bmatrix} \dfrac{4\,E_Y I\,d}{l} & \dfrac{-6\,E_Y I\,b\,c}{l^2} \\ \dfrac{-6\,E_Y I\,b\,c}{l^2} & \dfrac{12\,E_Y I\,c^2}{l^3} \end{bmatrix} \begin{bmatrix} \phi \\ f \end{bmatrix} \tag{3.2a}$$

Where E_Y [Pa] is the Young's modulus and I [m^4] is the moment of inertia of the thin plate-spring parts. The matrix is derived with small deflections theory and superposition of the equations for the deflection f and the angle ϕ for the different beam sections. The coefficients a, b, c and d are given by:

$$\begin{aligned} a &= p - 1 && \text{with } p = \frac{l_2}{l} \quad 0 \le p < 1 \\ b &= (p+1)(q-1) + 2 && \text{with } q = \frac{l_1}{l_3} \\ c &= q + 1 \\ d &= a^2 + c^2 + p\,(p+1)\,q\,(q-1) + 3p\,q - 1 \end{aligned} \tag{3.2b}$$

Where p and q respectively give the relative size and position of the reinforcement.

Buckling The critical load for buckling is directly related to the moment of inertia in the bending direction of the buckled beam and inversely related to the beam-length squared. The width w of the reinforcement greatly increases the moment of inertia for in-plane buckling, while reduction of the length of the slender parts increases the critical load to large extend as well. The critical load for out-of-plane buckling also increases slightly.

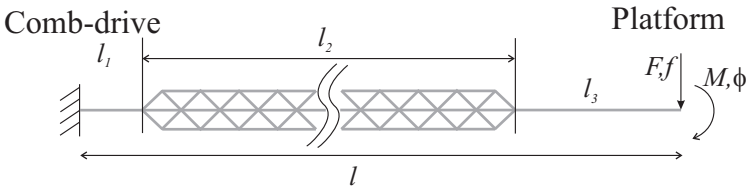

Figure 3.3: Top-view of a plate-spring were the reinforcement has triangular etch-holes, and is placed further away from the platform.

Guiding stiffness The relative position and size of the reinforcement is chosen such that its guiding stiffness (relation between F and f for small deflections) is almost equal to that of a "normal" plate-spring with a $\frac{7}{8}$-times shorter length. This is achieved for $p = \frac{5}{7}$ and $q = 1$ [1]. These values can be derived with help of the stiffness matrix.

Rotational stiffness The reinforcement largely increases the rotational stiffness for in-plane rotations. Once an optimization criterium is chosen for the guiding and rotational stiffness, a different relative position q and size of the reinforcement p can be derived. According equation (3.2) placing the reinforcement further away from the platform and/or shortening its size, as shown in figure 3.3, will reduce its stiffening effect on the rotational stiffness at the cost of increasing the guiding stiffness or reducing the robustness[2].

Discussion All the above accounts for an ideal, rigid reinforcement. However, here the reinforcement is pierced with square etch-holes. It was already mentioned, these etch-holes reduce the stiffness. Furthermore, the slender parts of the reinforced beam do not continue into the reinforced part as shown in figure 3.2. This is another cause for reduced stiffness compared to a rigid reinforcement. A better alternative is shown in figure 3.3, where both use is made of triangular etch-holes and the slender part is continued into the reinforcement. To implement this alternative however the fabrication process first requires testing with triangular etch-holes, to tune the etch-recipe and obtain design-rules for the mask dimensions.

3.2.3 Comb-drives

The comb-drives are bidirectional as shown in figure 3.4. In other words, at both sides of the intermediate bodies or shuttles, interdigitated racks of fixed and movable

[2]The rotational stiffness (the upper left element of the matrix in equation (3.2)) has a minimum for a q-value smaller than 1, while the minimum for the translational stiffness (lower right element) has a minimum at $q = 1$ independent of p.

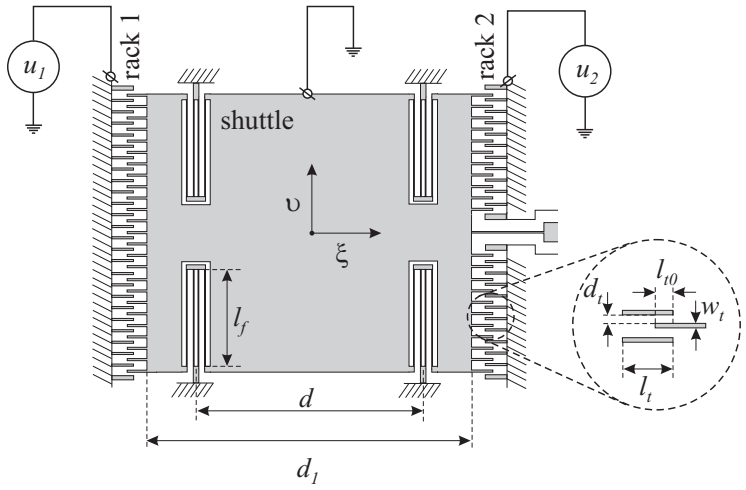

Figure 3.4: Top-view of a comb-drive with an enlargement of the comb-drive teeth.

comb-drive teeth are situated. Applying a voltage over one rack will move the shuttle in one direction and applying a voltage over the other rack will result in movement in the opposite direction.

The force each comb-rack can deliver as a function of the applied voltage, is found by considering the following Legendre transform of the energy stored in the capacitances between the teeth (i is comb-rack index 1 or 2 and q_i is the charge on a comb-tooth):

$$\begin{aligned} \mathrm{d}E_i^*(u_i,\xi,v) &= \mathrm{d}E_i(q_i,\xi,v) - \mathrm{d}(u_i\,q_i) \\ \mathrm{d}E_i^*(u_i,\xi,v) &= F_{\xi,i}\,\mathrm{d}\xi + F_{v,i}\,\mathrm{d}v - q_i\mathrm{d}u_i \\ E_i^*(u_i,\xi,v) &= E_0 - \frac{1}{2}C_i(\xi,v)\,u_i^2 \end{aligned} \tag{3.3a}$$

The forces (F_i [N]) delivered by the comb-drives are found by partial differentiation of E_i^* with respect to ξ while u_i and v are kept constant. γ_i defines the direction in which the comb-drive works and is equal to -1 for rack 1 and equal to 1 for rack 2.

$$\begin{aligned} F_{\xi,i}(u_i,v) &= \left[\frac{\partial\, E_i^*(u_i,\xi,v)}{\partial\xi}\right]_{u_i,v} = \frac{\gamma_i\, n\, \varepsilon_0\, h_t\, u_i^2}{2}\left(\frac{1}{d_t+v}+\frac{1}{d_t-v}\right) \\ \text{with}\quad C_i(\xi,v) &= n\,\varepsilon_0\,h_t\,(l_{t0}+\gamma_i\,\xi)\left(\frac{1}{d_t+v}+\frac{1}{d_t-v}\right) \end{aligned} \tag{3.3b}$$

The number of teeth-pairs in the comb-drive racks (n) is 100. The spacing between the teeth (d_t) is 4 μm, the width of a tooth (w_t) is 2 μm, the height of the teeth (h_t) is

37 μm, and the length of the teeth (l_t) is 50 μm, with an initial overlap (l_{t0}) of 20 μm. ε_0 is the dielectric permittivity of vacuum; 8.854×10^{-12} F/m.

Electrostatic stiffness The formula for the capacitance between the teeth, given in equation (3.3b), shows a dependence on the lateral position of the shuttle (v). As a consequence, there is also a force in the v-direction. This force is responsible for the infamous side pull-in instability of comb-drive actuators. The suspension of the comb-drive has to withstand this lateral force in the operation range of the comb-drives. In the next section, the suspension will be analyzed by comparing the suspension stiffness with the lateral *electrostatic stiffness* of the comb-drive. The electrostatic stiffness of each comb-drive is found by partially differentiating ${E_i}^*$ twice with respect to v under condition of constant u_i and ξ.

$$\begin{aligned} c_{el,i}(u_i, \xi, v) &= \left[\frac{\partial^2 {E_i}^*(u_i, \xi, v)}{\partial v^2} \right]_{u_i, \xi} = \\ -n\, \varepsilon_0\, h_t\, u_i^2\, (l_{t0} + \gamma_i\, \xi) &\left(\frac{1}{(d_t + v)^3} + \frac{1}{(d_t - v)^3} \right) \end{aligned} \tag{3.4}$$

Comb-tooth failure A comb-drive tooth has a limited, individual stiffness. As a result, instability can also occur due to failure of a tooth. Elata presents the following relation for the side pull-in of an individual comb tooth in [2]:

$$\tilde{u}_{pi}{}^2 = 24 \frac{\varepsilon_0\, {l_t}^4}{E'_y\, {w_t}^3\, {d_t}^3} u^2 \quad \text{with,} \quad E'_y = \frac{E_y}{1 - \nu^2} \tag{3.5}$$

Here, $\tilde{u}_{pi}$ is the normalized pull-in voltage depending on the relative overlap of the comb-teeth. The minimal value given for the normalized $\tilde{u}_{pi}$ is 3.516. Furthermore, E_Y [Pa] is the Young's modulus and ν is the Poisson's ratio. Assuming the Young's modulus of silicon is 130 GPa and the Poisson's ratio is 0.27 [3] the pull-in voltage for instability of an individual comb-tooth for the given dimensions is found to be about 0.8 kV. In the instability analysis for side pull-in and rotational pull-in given in section 3.2.4, pull-in will be predicted for lower values of the driving voltage. In other words, pull-in of a individual comb-tooth is not the limiting instability for this design.

Linear-drive The push-pull configuration allows linear-driving of the comb-drives with respect to the applied voltage, whereas the voltage-force relation for a single

[3] The assumed Young's modulus is the minimum of the crystal orientation dependent Young's modulus and the Poisson's ratio is maximum of the crystal dependent Poisson's ratio in the plane of a $\langle 100 \rangle$ wafer [3]

comb-drive is quadratic. The linear operation is accomplished by applying equal dc-voltages (U_{dc}) to both comb-drive racks and adding a voltage related to the desired displacement (u_i) to the side where the shuttle should be attracted to and subtracting the same voltage at the other side. The resulting force dependence of the voltages is shown in equation (3.6).

$$\Sigma F_\xi = F_{\xi,2} + F_{\xi,1} \propto (U_{dc} + u)^2 - (U_{dc} - u)^2 = 4\,U_{dc}\,u \tag{3.6}$$

This principle is based on totally equal comb-drives. In practice there might be a difference between the comb-drives. In that case the forces for both comb-drives will be proportional to:

$$F_{\xi,1} \propto p_1\,(U_{dc,1} + u_1)^2 = p_1\,({U_{dc,1}}^2 + 2\,U_{dc,1}\,u_1 + {u_1}^2) \tag{3.7a}$$

$$F_{\xi,2} \propto p_2\,(U_{dc,2} - u_2)^2 = p_2\,({U_{dc,2}}^2 - 2\,U_{dc,2}\,u_2 + {u_2}^2) \tag{3.7b}$$

For linear-drive, the following conditions need to hold:

$$\begin{aligned} p_1\,{U_{dc,1}}^2 &= p_2\,{U_{dc,2}}^2 \\ p_1\,{u_1}^2 &= p_2\,{u_2}^2 \end{aligned} \tag{3.7c}$$

Which is satisfied once $U_{dc,2} = \sqrt{\frac{p_1}{p_2}}\,U_{dc,1}$ and $u_2 = -\sqrt{\frac{p_1}{p_2}}\,u_1$. This could relatively easily be accomplished in electronics.

Linear-drive can mean an important improvement for nanometer resolution positioning. Without linear-drive, the voltage source should be variable and stable over a large range. Moreover, the larger the voltage applied, the more sensitive the position is for voltage variations. For example, if the shuttle suspension has a stiffness in driving direction of 2.5 N/m and a 10 μm displacement is achieved for a voltage over one of the comb-drives of 50 V, the voltage required for 1 nm displacement from zero position is 0.5 V, but the extra voltage required to go from 10 μm to 10.001 μm displacement is only 2.5 mV. In case of linear-drive, a large, stable dc voltage combined with a variable source, stable over a much smaller range is required. These requirements are far more easy to meet.

3.2.4 Shuttle suspension

The shuttle of the comb-drive is suspended by four folded flexures (see figure 3.5 on page 56). This suspension is overconstrained; just two folded flexures would be enough to constrain all DOFs except the driving direction. However, since the device is monolithic and the uniformity of the processing is high on the scale of the device

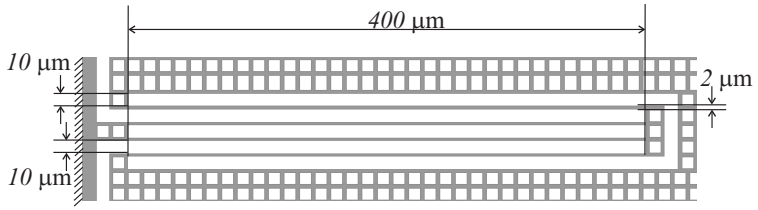

Figure 3.5: Top-view of one of the folded flexures that suspend the comb-drive shuttle.

dimensions, this practically does not lead to indeterministic behavior, as evidenced by many well performing examples, e.g. [4, 5, 6] [4].

Ideally, the suspension has zero stiffness in the actuation direction (the push-pull configuration strictly does not require restoring force from the suspension) while it has to be infinitely stiff in all other DOFs. This is a hypothetical situation. Achieving relatively small stiffness in actuation direction is limited by the minimum feature size in lithography, the desired minimum stiffness in out-of-plane direction (the length cannot be increased unlimitedly) and the linear operation regime of the stiffness in actuation direction. Below an analysis will follow of the suspension stiffness in the various DOFs and especially the side and rotational pull-in conditions will be analyzed.

Guiding stiffness The first order model for the guiding stiffness of one folded flexure is [7, 8] (where I_ζ [m^4] is the area moment of inertia about the out-of-plane ζ-axis):

$$c_{f,\xi} = 12\frac{E_Y I_\zeta}{{l_f}^3} = \frac{E_Y h_f {t_f}^3}{{l_f}^3} \tag{3.8}$$

Because of the nature of a folded flexure, initially no stiffening occurs, since the plate-springs in the folded flexure are free to shorten. Therefore, equation (3.8) provides a suitable model for displacements in the order of 10 μm for the following dimensions of the plate-springs: the length (l_f) is 400 μm, the thickness of a plate-spring (t_f) is 2 μm and the height (h_f) is 37 μm. Inserting these values in equation (3.8) and multiplying by 4 (the shuttle is suspended by four folded flexures) results in a value for the suspension stiffness in ξ-direction of 2.4 N/m . With help of equation (3.3b) the required voltage to be applied to one of the comb-racks for 10 μm displacement is calculated to be 53 V [5].

[4] Although additional characterization on the nanometer scale should verify the exact effect of the overconstrained suspension on the linearity of the force-displacement relation.

[5] The driving voltage can be reduced by reducing d_t. This occurs in case the process for the vertical comb-drive is applied (see chapter 5). However, the pull-in voltage will lower as well and needs to be calculated anew.

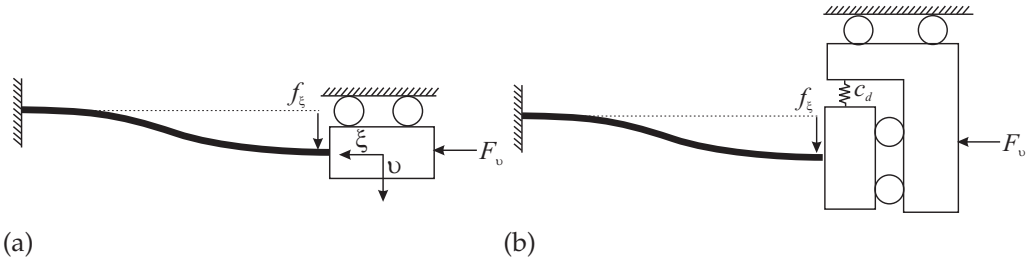

Figure 3.6: Two cases of a force F_υ loading a deflected plate-spring. Plate-spring deflected, but fixed for additional movement in ξ-direction (a), deflected plate-spring free to move in both ξ- and υ-direction(b).

Lateral stiffness The first order model for the stiffness in the initial longitudinal direction of one folded flexure is [7, 8]:

$$c_{f,\upsilon} = \frac{E_Y A}{l_f} = \frac{E_Y t_f h_f}{l_f} \tag{3.9}$$

Where A [m^2] is the cross-sectional area of the plate-spring. This stiffness is largely depending on the geometry of the plate-spring. This means that deflection of the plate-spring will alter the geometry in such amount that a significant reduction of the stiffness occurs. Equation (3.9) will not be accurate enough to predict the stiffness in case of deflection, especially for side pull-in analysis.

Van Eijk [9] and Legtenberg [8] have modelled two different situations for the deflected plate-springs. These two situations are shown in figure 3.6 (a) and (b). Van Eijk considers a deflected straight-guided beam fixed for additional deflections and loaded by a force F_υ, while in Legtenberg's model, additional deflection is allowed. In [10], Brouwer notices the first situation does not apply to straight-guided beams as applied in a folded flexure comb-drive suspension. Brouwer takes into account, that stiffness c_d is finite. He presents simulation results obtained with SPACAR [11] for the stiffness in longitudinal direction depending on the beam's deflection for various values of c_d, including infinite and zero. c_d is infinite coincides with Van Eijk's model and c_d is zero coincides with the model of Legtenberg. To illustrate the difference between both situations, the stiffness reduction factors resulting from both models are given below.

The first model (see equation (3.10)) predicts a stiffness reduction factor (δ_1) of 10% in case of a deflection over thickness ratio of 2.5 (5 μm deflection for each plate-spring in case of a 10 μm stroke).

$$\delta_1(\xi) = \frac{c_{f,\upsilon}(\xi)}{c_{f,\upsilon}(0)} = \left(1 + \frac{12}{700}\left(\frac{\xi}{2\,t_f}\right)^2\right)^{-1} \tag{3.10}$$

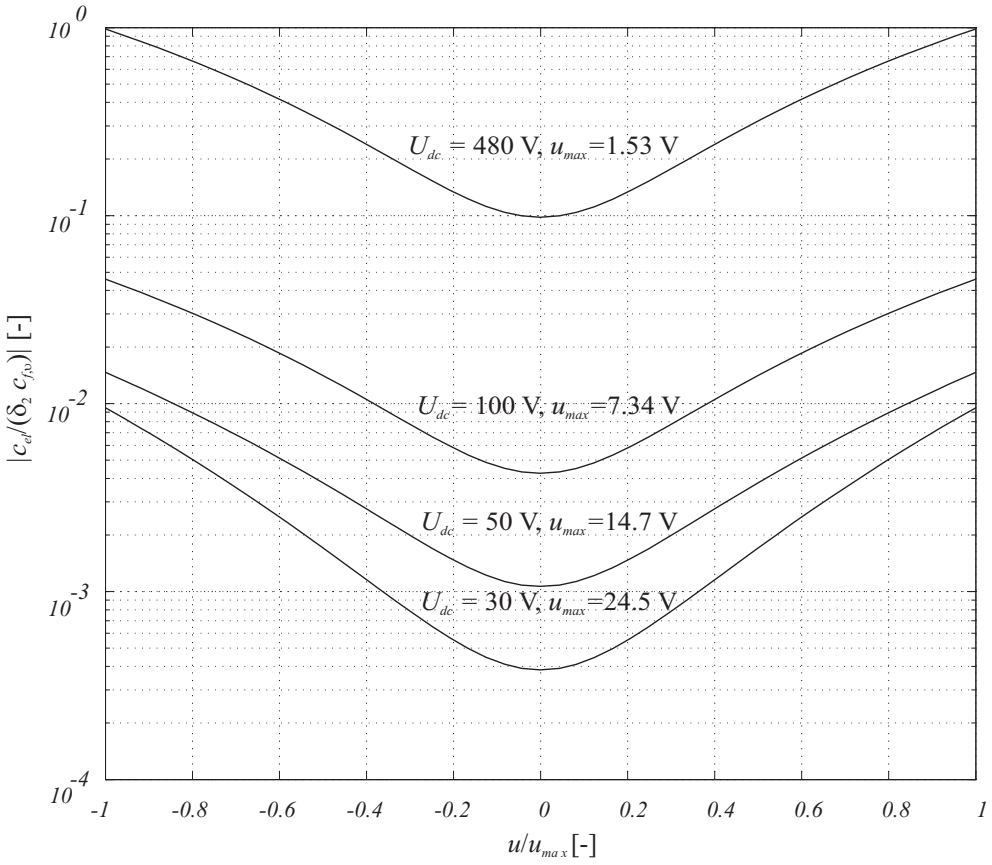

Figure 3.7: Equation (3.12) plotted against $\dfrac{u}{u_{max}}$ *for different values for* U_{dc}.

The second model predicts an enormous stiffness decrease of 90% for a total folded flexure displacement of 10 μm. The stiffness reduction factor resulting form the second model (δ_2) is:

$$\delta_2(\xi) = \frac{c_{f,v}(\xi)}{c_{f,v}(0)} = \left(1 + \frac{9}{25}\left(\frac{\xi}{2\,t_f}\right)^2\right)^{-1} \tag{3.11}$$

A side pull-in analysis is performed for the case of c_d is zero for a push-pull comb-drive operating in linear-drive (see equation (3.6)). The following expression (giving the absolute value of the electrostatic stiffness over the lateral stiffness) is plotted for different values of U_{dc} against $\dfrac{u}{u_{max}}$, where u_{max} is the value for u for a displacement of 10 μm at the given value of U_{dc}:

$$\left|\frac{c_{el}(\xi)}{4\,\delta_2(\xi)\cdot c_{f,v}}\right| \quad \text{with} \quad \xi = \frac{F_\xi(u, U_{dc})}{c_{f,\xi}} \tag{3.12}$$

Where c_{el} is the electrostatic stiffness as given in equation (3.4) on page 54.

The plot is shown in figure 3.7 for $v = 0$ μm and for the following U_{dc}-values: 30, 50, 100, and 480 V. The linearity of the linear-drive benefits from a large U_{dc}-value, however the plot shows that for a value of 480 V, the electrostatic stiffness exceeds the suspension stiffness in v-direction, causing side pull-in. U_{dc} does not need to be as high as 480 V. A U_{dc}-value up to 100 V will certainly be enough and the design leaves a large enough margin for increased displacements and/or extra force to drive an external load. However, another type of instability, rotational pull-in, is still to be analyzed to draw a final conclusion about the safe operating conditions.

Rotational stiffness The rotational electrostatic stiffness about the center point of the comb-drive shuttle is equal to $k_{el} = c_{el} \cdot (\frac{1}{2} d_1 + l_t)^2$, where d_1 is the length of the shuttle as defined in figure 3.4, acting as arm for the force F_v to exert a moment around the symmetric center of the shuttle. It is assumed the shuttle will rotate around this point, because the comb-drive forces and the suspension are both symmetric with respect to this point for zero position of the shuttle. The rotational stiffness of the suspension evaluated around the center of the shuttle is calculated as follows:

$$k_f(\xi) = 4\,\delta_2(\xi)\,c_{f,v}\left(\frac{d}{2}\right)^2 \tag{3.13}$$

To analyze the rotational pull-in, the following expression is plotted in a similar way as was done for the side pull-in:

$$\left|\frac{k_{el}(\xi)}{k_f(\xi)}\right| \quad \text{with} \quad \xi = \frac{F_\xi(u, U_{dc})}{c_{f,\xi}} \tag{3.14}$$

Figure 3.8 on page 60 shows the plot of the stiffness ratio. Clearly the device is more sensitive to rotational pull-in than to side pull-in. Rotational pull-in occurs at $U_{dc} = 320$ V. Like for the case of side pull-in, U_{dc}-values up to 100 V can be considered safe. Following from the rotational pull-in analysis as well, additional stroke and/or external loading are possible within the safety margins for this suspension design.

Out-of-plane stiffness The first order out-of-plane guiding stiffness at the free end of one of the leaf-springs in a folded flexure is given by [7]:

$$c_\zeta = 12\frac{E_Y I_\xi}{{l_f}^3} = \frac{E_Y\, t_f\, {h_f}^3}{{l_f}^3} \tag{3.15}$$

Where I_ξ is the area moment of inertia about the ξ-axis. For a length over height ratio of more than 10 and a deflection over thickness ratio of 2.5 (one plate-spring deflects halve of the total stroke of the folded flexure) the guiding stiffness in ζ-direction is

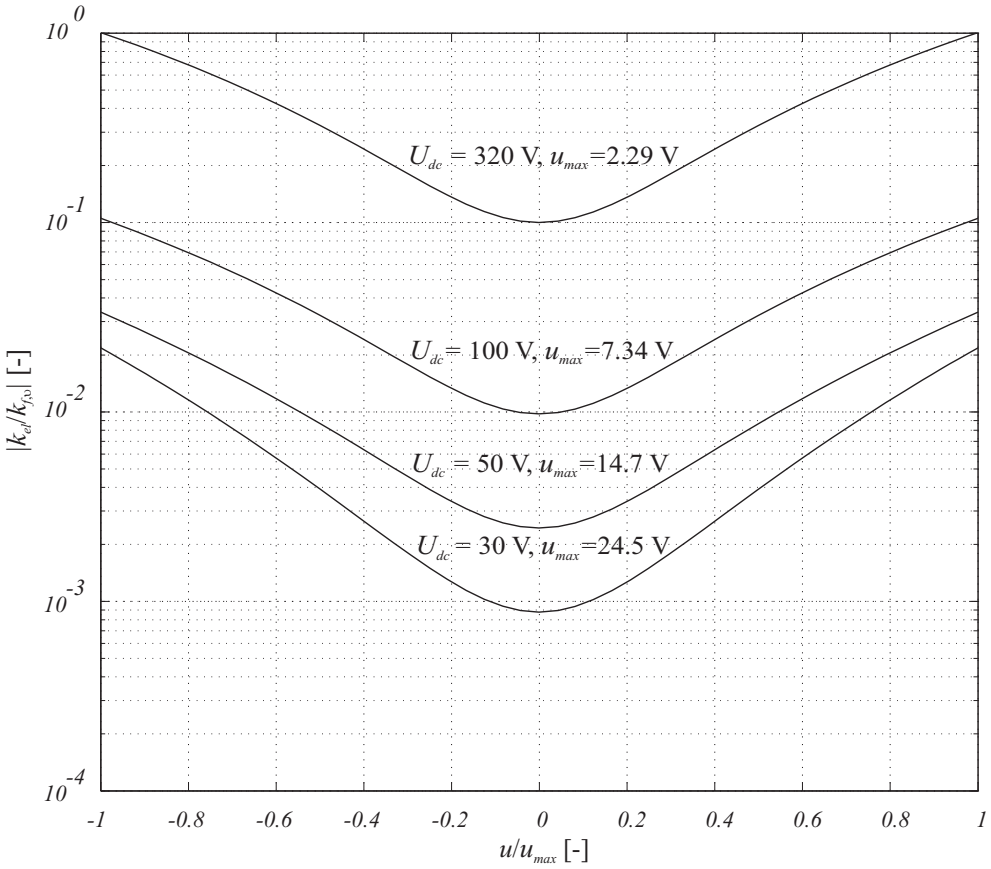

Figure 3.8: Equation (3.14) plotted against $\frac{u}{u_{max}}$ *for different values for* U_{dc}.

practically constant with deflection [9]. In each folded flexure, two series of plate-springs are placed in parallel. In other words, c_ζ for one folded flexure is equal to equation (3.15). The total out-of-plane stiffness of the shuttle suspension is four times the value of one folded flexure, resulting in 0.82×10^3 N/m. This can be considered relatively stiff, compared to the forces expected in the device.

Discussion of assumptions The pull-in analysis does not give rise to concern for typical driving conditions of the comb-drive. The design even allows larger displacements and significant external loading, without risking pull-in. This is backed by the experience in the experimental situation, where no pull-in was observed for typical operation (see section 5.4.2). However, in the stiffness analysis the intermediate bodies of the folded flexure have been assumed rigid. In reality, these are pierced by square-shaped etch-holes for the release. The compliance of the intermediate bodies will thus be significant. The exact contribution to the compliance of the total suspension is best to be analyzed by FEM simulation. Once design rules for triangular-shaped etch-holes for device release are available, the design can be largely improved by applying triangular holes.

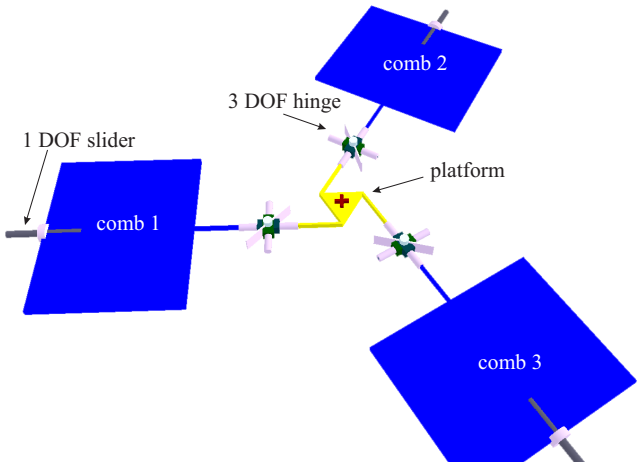

Figure 3.9: 3D model made with the rigid body editor of 20-sim.

3.3 Power-port modelling

A simulation model has been made with the help of a power-port model in 20-sim 3.6 [12, 13]. This program is able to model parallel mechanisms and is equipped with an editor to draw a 3D model of rigid bodies and define geometrical linkage between the bodies. The editor generates code defining the geometric relations which is imported into the simulation program. In the simulation program, the equations modelling the behavior of the flexures, masses and inertias are defined and the power-ports are linked to each other via bond-graphs.

Figure 3.9 shows the geometrical representation of the model as obtained with the rigid body editor. The simulation model in total incorporates the 3 DOF manipulator geometry, symmetric 3 DOF stiffness matrixes for the reinforced leaf-springs between the comb-drives and the platform, a 1 DOF force and stiffness model for each of the comb-drives, and feed-forward position control with help of a higher order inverse kinematic model enabling the platform to be positioned in a given set-point of x, y and R_z coordinates. In this model the crystal depended Young's modulus has been taken into account as well as amplification factors in the inverse kinematic model to compensate for the difference in suspension-stiffness each comb-drive is loaded with. Figure 3.10 shows the "static" response of the simulated system for a setpoint of x=8.5 μm, y=8.5 μm, R_z=0.035 rad [6]. Figure 3.10a shows the set-point coordinates and the displacements and rotation of the platform, while figure 3.10b shows the voltages applied to the actuators calculated with the feed-forward model for *non-*

[6]By "static" response is meant, the response to a driving signal well below the resonance frequency of the system.

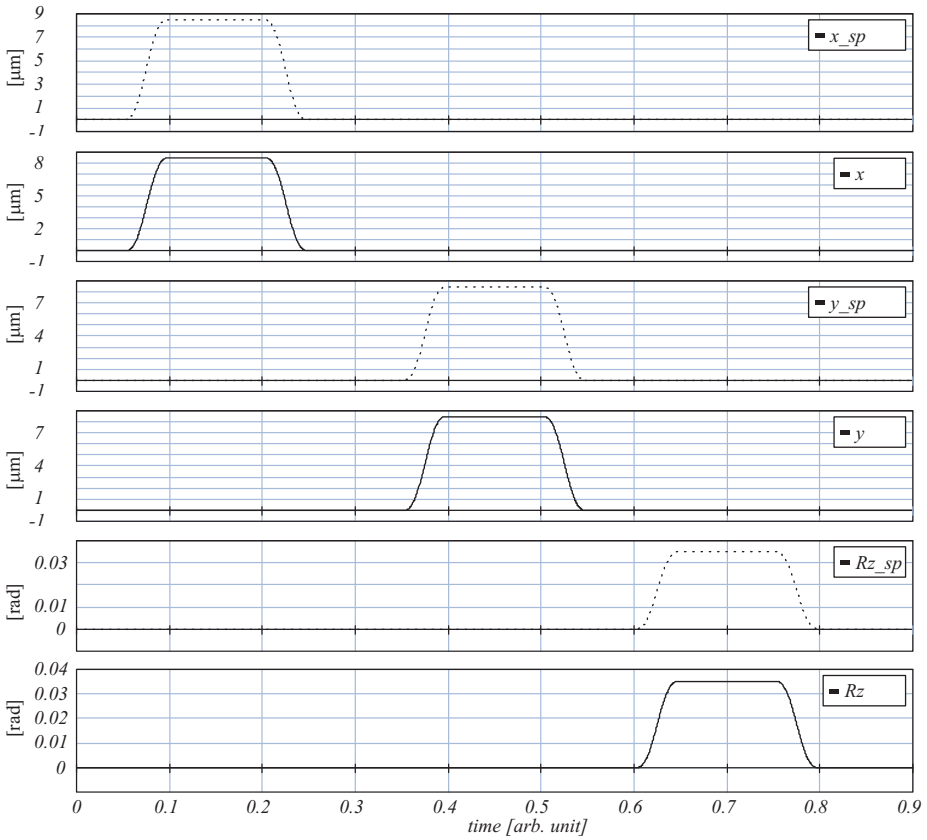

(a)

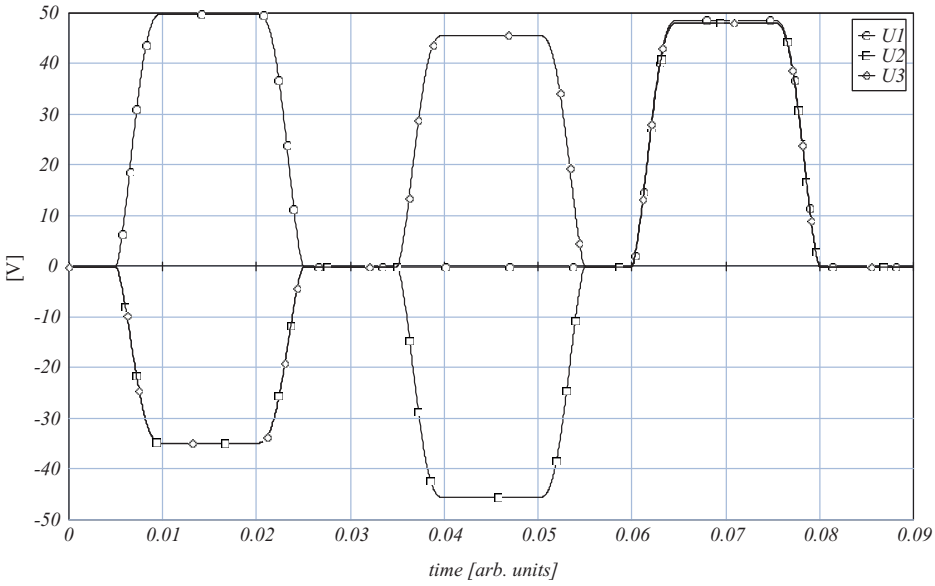

(b)

Figure 3.10: Simulation results for "static" response obtained with the 20-sim model for a set-point of x=8.5 µm, y=8.5 µm, R_z=0.035 rad. Setpoints, denoted with _sp and displacements of the platform. Voltages applied to the comb-drives (b).

linear drive. The set-point and the displacement of the platform match very well and the relation between applied voltage and platform position agrees up to large extend to the measured relation as shown in figure 3.14 in section 3.5.2 on page 69.

The model can be applied in future to actually drive the system using the feed-forward control and, once position sensing is added, feed-back control for nanometer scale resolution positioning. Furthermore, the simulation model can be expended and improved to more closely match the behavior of the actual device[7] to study the implications of fabrication artifacts by taking resulting variances in the stiffness into account in the model.

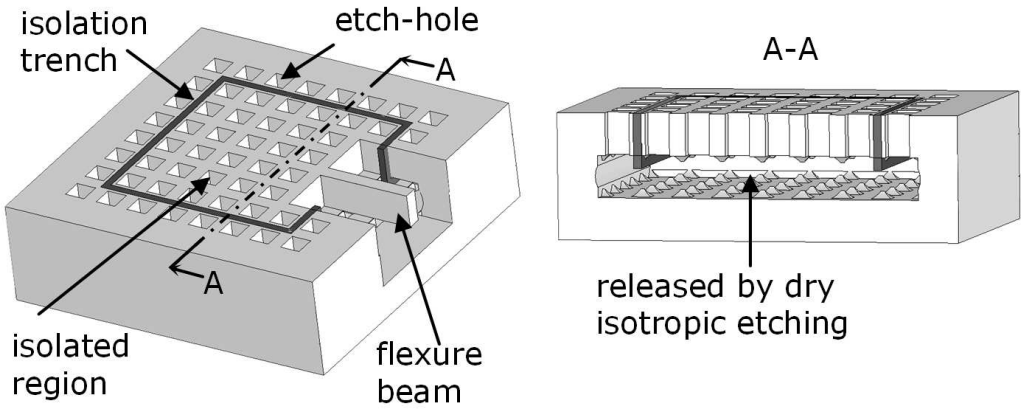

Figure 3.11: Generic functional structure.

3.4 Fabrication

The planar manipulator is fabricated with a simple two-mask process [6], that enables high aspect-ratio structures made in highly doped SCS combined with electrical insulation. With the help of trenches refilled with a dielectric material, the process allows structures in conventional $\langle 100 \rangle$ wafers to be mechanically connected, while being electrically insulated from each other. Insulation from the bulk and release of free-to-move structures is performed by dry isotropic etching. A generic functional structure is shown in figure 3.11.

Process flow Figure 3.12 on page 64 shows the process overview. The process starts with a highly doped (p^+) $\langle 100 \rangle$ wafer. Into a layer of Olin 907-17 resist, the mask for the 2 μm wide insulation trenches is transferred. The trenches are etched to a depth of 40 μm by advanced silicon (ASE) or Bosch etching with an Adixen SE100 plasma etch

[7] Once measurement data of the manipulators position in the nanometer range is available.

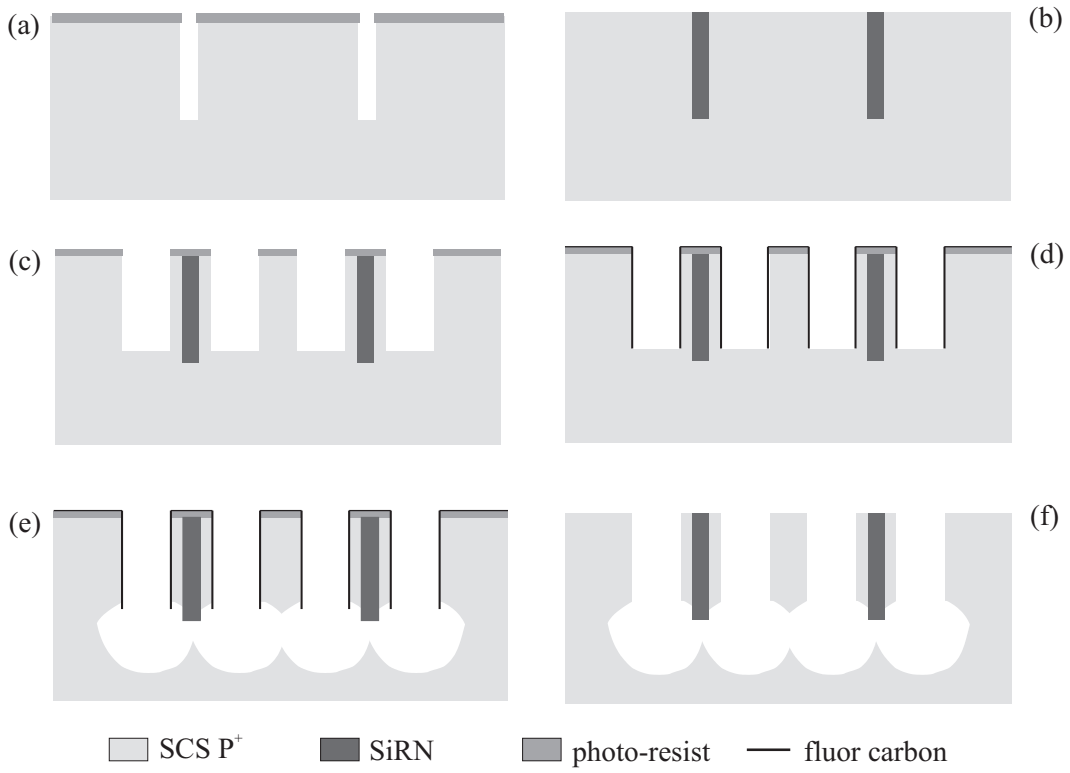

Figure 3.12: The process used for the 3 DOF manipulator [6].

system. Next, the resist is stripped in a barrel etcher (O_2 plasma) and the fluor-carbon side wall protection is ashed in an oxidation oven at 800 °C (remaining oxide etched in 50% HF), figure 3.12 (a). Subsequently, the trenches are filled with low-stress LPCVD silicon-rich-silicon-nitride (SiRN) (see [14] for the process requirements for successful filling) and the SiRN is removed from the topside by dry etching, figure 3.12 (b). The second mask, defining the device structures, is transferred into an Olin 907-17 resist layer, and the uncovered silicon is etched to a depth of 37 μm by Bosch etching with an Adixen SE100 plasma etch system, figure 3.12 (c). The wafer remains inside the reactor, and an extra layer of fluor-carbon is applied covering the complete trench. The bottom of the trench is selectively removed by a directional etch step, figure 3.12 (d). Still keeping the wafer inside the reactor, the process conditions are switched to isotropic etching with SF_6. This step releases the device and electrically insulates the device layer from the rest of the wafer, figure 3.12 (e). Finally, the resist is stripped in an oxide plasma and the fluor-carbon is ashed, figure 3.12 (f).

Process issues Some remarks ought to be made with respect to the design rules for this process. The etch-rate [μm/min] of the Bosch process is dependent, among other things, on the size and shape of the mask openings. E.g., etching a larger opening

proceeds faster than etching a smaller opening. Furthermore, the etch-rate in an outstretched opening will be larger compared to the rate in a square etch-hole of equal width. This effect is known as loading [15] and is caused by the difference in exposed Si. Also the difference in aspect-ration (ARDE) has influence on the resulting etch-depth [15, 16]. The effect, for some part, is caused by difference in diffusion of the etching agent towards the bottom of the trench and can be weakened by reducing the overall etch-rate so transport is less significant or by applying more fluor-carbon. In the latter case, use is made of the fact that more fluor-carbon is deposited in large openings, thus primarily reducing the etch-rate in these openings. However, ARDE cannot be completely canceled. Therefore, the width of the openings should not show a large spread to make sure the isotropic release starts everywhere at more or less the same depth and the release is successful.

The isotropic release produces etch profiles with a more or less heart-shape. The shape and size is again depending on the size of the trench or hole from which the release starts. In larger sized trenches or holes the profile often shows a slight dependence on the crystal orientation (As shown in figure 3.12 (e) and (f)). What matters for the success of the process, is that the beams are undercut. This means the radius of the profile requires to be large enough in the horizontal direction. However, the duration of the under-etch is limited by the erosion of the fluor-carbon. When the fluor-carbon is completely eroded the formerly protected structure damages.

Finally, to succeed in electrical insulation, the SiRN refilled trenches need to extent beyond the released Si structures. Hereto, the etch-depth of the device structures (mask 2) has to be considerably less than the depth of the insulation trenches. For this device the insulation trenches extent up to a depth of 40 μm and the rest of the device structure extents up to a depth of 37 μm.

3.5 Characterization

This section discusses the profile, due to lithography, found in the width of the plate-springs and the measurements of the platform displacement by pattern recognition.

3.5.1 Plate-spring geometry

The width of the beams of the platform suspension and the folded flexures is taken as small as possible to reduce the stiffness of the suspensions in their compliant directions and eventually the required voltage and size of the actuators. The limitations to the attainable smallest feature-sizes are the mask, the required resist thickness and the achievable aspect ratio of the beams with Bosch etching. A feature-size of 2 μm is

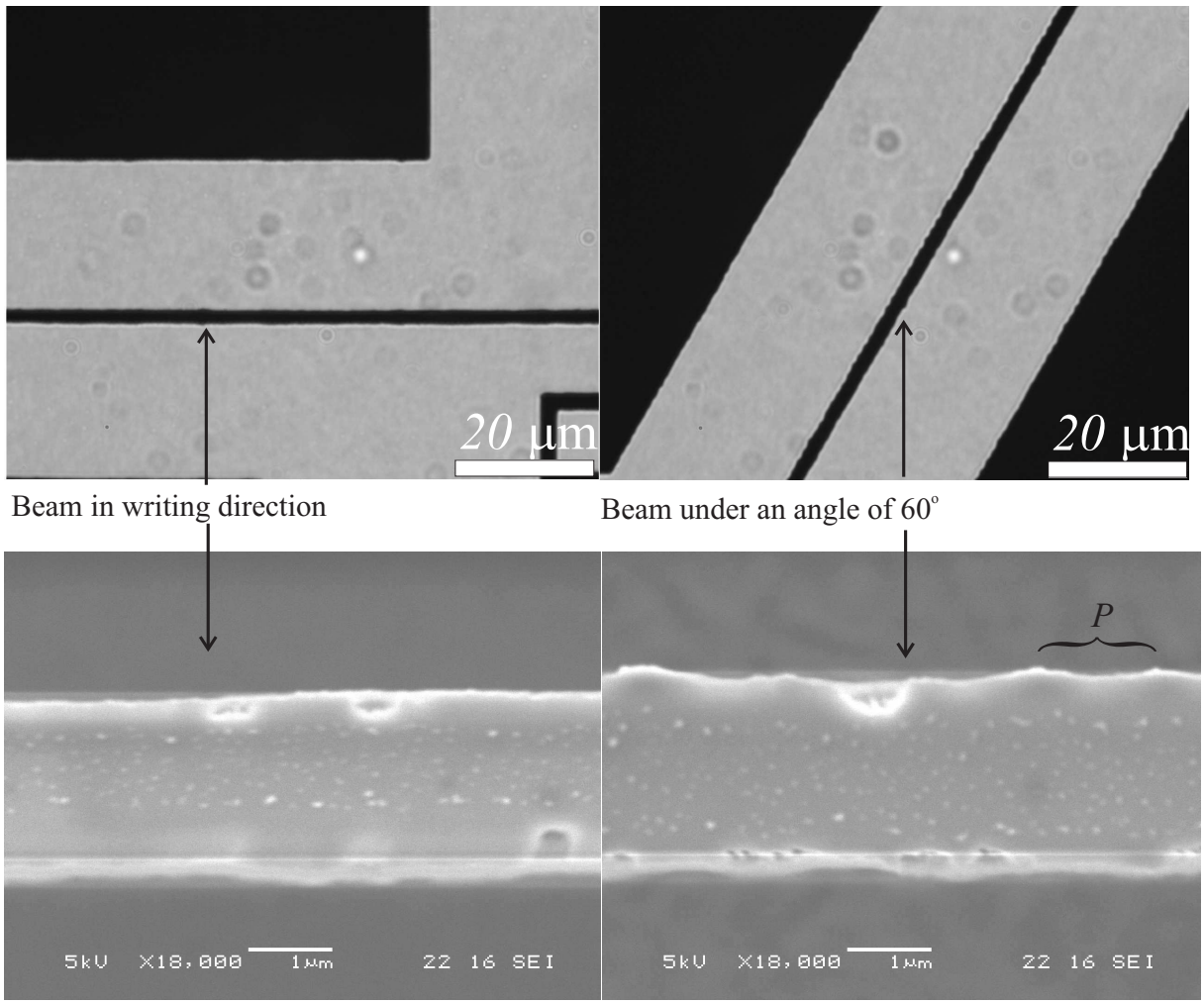

Figure 3.13: Microscope images showing the masks (top row) and SEM images (bottom row) of a beam in writing direction (left), and a beam under an angle of 60° (right).

achievable where it concerns the resist and the etching, but the mask shows a significant variation of up to 10 % on the width of the beams. This has a large effect on the in-plane stiffness of the beams. The mask consists of a glass plate with a chromium layer. The chromium is structured by a lithographic process and is protected by a photo-resist in which the mask patterns are written by a laser. This laser is scanned over the mask and it writes dots to build up the pattern. In case mask-openings for the beams are oriented under an angle with respect to the laser, the spatial frequency of the width-variation increases as shown in figure 3.13. The resolution of the mask features can be improved if electron-beam writing is applied, however this is a lot more expensive.

The profile shows some periodicity as indicated in figure 3.13 by *P*. However, it is not entirely regular and asymmetric with respect to the center-plane along the

length of the beam. Furthermore, it is not sure how far the profile extents over the height of the beams. Since the stiffness of the beam for bending in its thin direction is depending on the beam-width to the third power, the actual stiffness might show a large deviation from the design stiffness. Because the profile cannot simply be fitted in an analytic expression (mainly due to lack of symmetry), a worst case stiffness deviation will be calculated. For a beam-width of 2 μm with a variation in the width of 10 %, the worst case ratio between the moment of inertia for a 10 % increase (2.2 μm thickness) and the moment of inertia for 2 μm thickness would be 1.33. This means a deviation of the design stiffness of 33 % (for a decrease of 10 % this ratio is 0.73 resulting in a 27 % deviation). This is a large overestimation since it assumes a beam-width of 2.2 μm over the complete length of the beam. If a cosine profile is assumed, a lower limit for the stiffness variation can be found with an effective moment of inertia value:

$$I_{eff} = \frac{h}{24\,\pi} \int_0^{2\,\pi} (w - \epsilon\, w \cos l')^3 \mathrm{d}l' \tag{3.16}$$

Where w is the beam-width of 2 μm, and ϵ is the variation of 0.1, and h is the beam height of 37 μm. Dividing I_{eff} by the moment of inertia for the designed values results in a ratio of 1.02. The lower limit for the stiffness variation is 2 %.

It will be hard to model the effect of the profile exactly. If no other means of mask writing is used, these deviations should be taken into account when designing flexure mechanisms. There are no indications the general mechanical behavior of flexures is influenced undesirably. Furthermore, the extent of the profile over the beam-height requires additional characterization.

3.5.2 *Displacement measurements*

Applied method With help of the inverse kinematic model, the three push-pull comb-drives are powered in the correct proportion to each other to move the platform to a certain position and give it a certain rotation. However, the model does not provide the absolute voltage required for a given displacement, since it does not include any information about stiffness and applied forces; it is purely geometrical. To know the voltage required for a certain displacement, the displacement of a comb-drive is measured in relation to the applied voltage (no linear-driving is applied, i.e. no dc bias voltage is used). This results in an approximately linear relation between the displacement and the voltage squared.

Knowing the displacement-voltage relation, the platform is moved along the x- and y-axis and rotated about the z-axis. The positions are measured with help of *National Instruments Vision Assistant* 7.1 [17]. Pictures are taken of the platform in

each position also showing the fixed surrounding. With pattern recognition, based on correlation, the relative position between the fixed surrounding and the platform is determined. The pattern recognition is calibrated by counting the number of pixels spanning the length of a row of etch-holes found in the device. The period of the etch-holes is 12 μm, thus by counting the number of pixels spanning the length of 10 etch-holes, the number is related to microns by dividing it by 120. This results in 0.34 μm per pixel for a picture resolution of 1280×960 pixels. The pattern recognition also outputs the orientation of the recognized pattern. This orientation provides the rotation about the z-axis. The measurement error is determined by measuring the distance between two points with a fixed distance to each other for 28 times and determining the standard deviation of the results.

The relation found between the driving voltage and the displacement of a single comb-drive shuttle is: $\xi(U) = 3.4 \times 10^{-3}\, U^2$ μm. Where U is the voltage applied to one of both comb-racks, while the other remains at zero volt. The voltages applied to the comb-drives range from 0 to 50 V. Since the displacement is related to the square of the applied voltage, the square-root should be taken of the relations between the three comb-drives given in the inverse kinematic model, e.g. the voltages for moving along the positive x-axis will be U for rack 2 of comb-drive 1, and $\sqrt{\frac{1}{2}}\,U$ for rack 1 of comb-drives 2 and 3 (see figure 3.1).

Measurement results Figure 3.14 shows three graphs of the measurements of the displacement in x- and y-direction and of R_z-rotation as a function of the squared voltage. Negative values for U^2 indicate displacement in opposite direction. Furthermore, for the voltage along the horizontal axes a choice has to be made concerning which of the voltages applied to the comb-drives is given. For displacement in x-direction, the voltage applied to comb-drive 1 is given. In case of displacement in y-direction, the voltage applied to comb-drive 3 is given. For rotation about the z-axis, there is no difference between the voltages applied to the comb-drives.

The measurement points given in the graphs show error bars equal to the standard deviations evaluated as discussed above. For the x- and y-displacement the error is ± 0.07 μm, while for the R_z-ration the error is ± 0.02 $^\circ$. For the displacement graphs, measurement points of the cross-talk in the orthogonal direction are given as well. Trend-lines are given for x- and y-displacement and the R_z-ration for the positive and the negative direction separately. Furthermore, each graph shows the result of simulations in 20-sim, modelling the displacements and rotation (see section 3.3).

Predominantly, the results show a very encouraging behavior of the manipulator that closely matches the expected linear relation between the displacements and rotation with respect to the squared driving voltages. Moreover, the behavior is in good

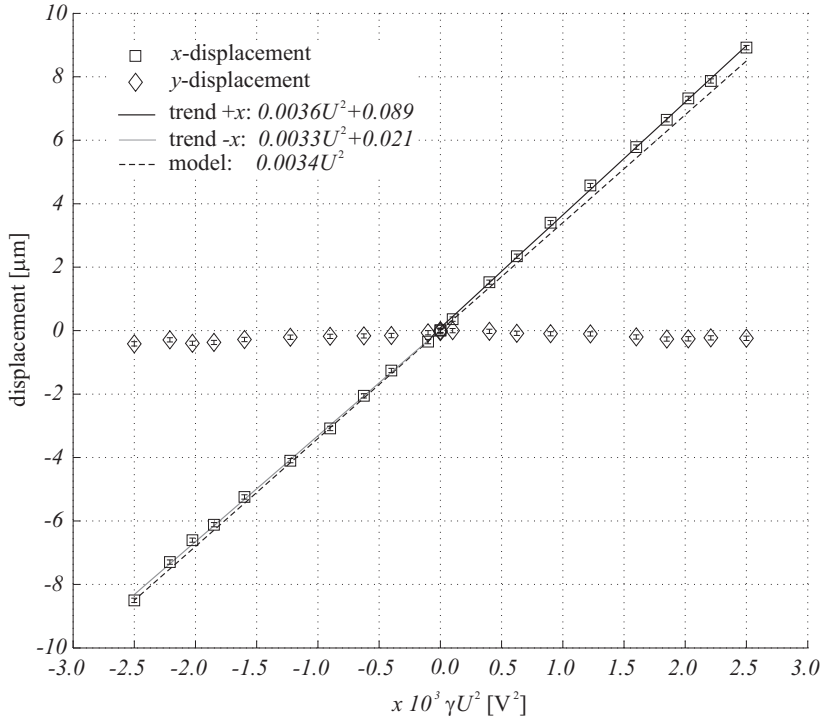

(a) x-displacement and cross-talk in y-direction.

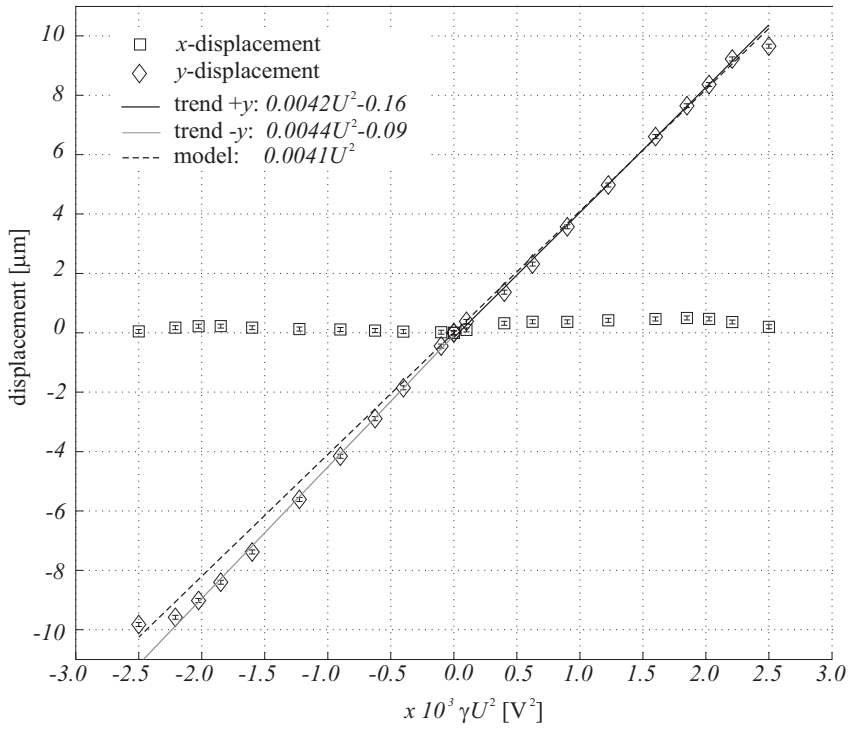

(b) y-displacement and cross-talk in x-direction.

Figure 3.14: Graphs of the measurements of the displacements in x- and y-direction and of R_z-rotation as a function of the squared voltage. Graphs (a) and (b) both show the measurement points for the displacements and cross-talk together with trend-lines for the displacements in positive and negative direction and the result of the 20-sim model.

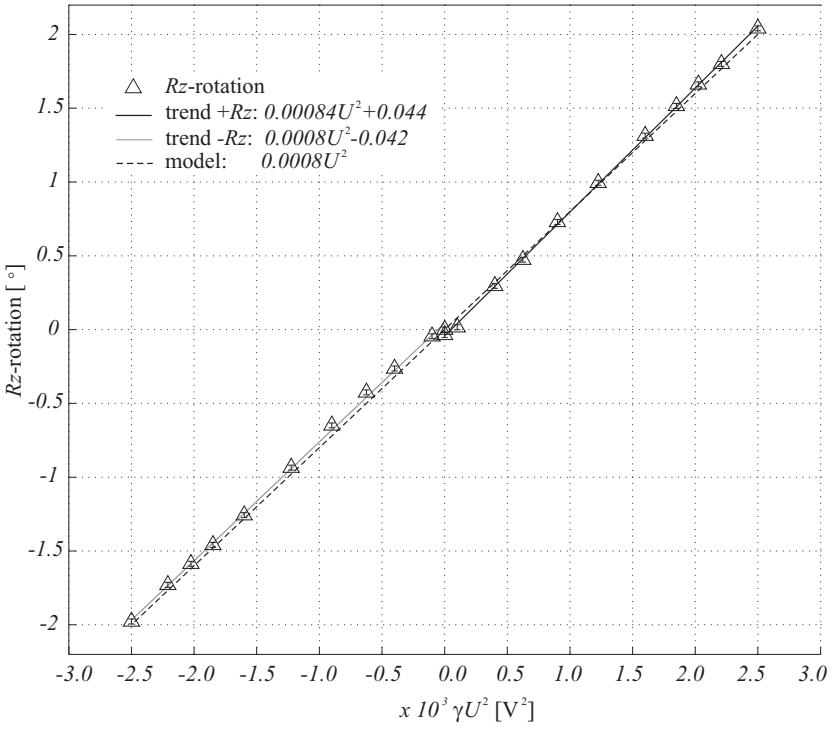

(c) R_z-rotation

Figure 3.14: Graphs of the measurements of the displacements, continued. Graph (c) shows the R_z rotation together with trend-lines for positive and negative rotation and the result of the 20-sim model.

agreement with the inverse kinematic model and the 20-sim simulation results.

The graphs show two types of deviations from the inverse kinematic model used to (coarsely) determine the required driving voltages. Firstly, the cross-talk towards translation or rotation not directed in the intended driving direction. Although not shown in the graphs because of presentation issues, cross-talk to R_z-rotation for the x- and y-displacement having an average of 0.02 ° with a maximum of 0.16 °. Furthermore, displacement cross-talk for R_z-rotation was found as well, having an average of -0.02 μm and a maximum of 0.8 μm. The second deviation is found in the trend-lines, showing a different slope for x- and y-displacements of the platform in positive and negative direction.

The main reason for cross-talk concerns the fact that the inverse kinematic model does not take into account compliance in the mechanism. More particularly, the fact that the Young's modulus depends on the orientation of the flexures in the $\langle 100 \rangle$ silicon wafer is not taken into account. Additionally, the profile due to the mask writing as discussed in section 3.5.1 is not represented in that model. Finally, geometric imperfections cause differences between the actual manipulator behavior and the inverse kinematic model. The difference in the trend-lines for the positive and the negative translation directions would intuitively be explained by a difference in

the comb-rack geometry at both sides of a comb-shuttle. However, considering the forces of the comb-drives for displacement in x- and y-direction, no difference between the total force will be found as a result of different forces in positive and negative direction of the individual comb-drives. Consider the case that the force of the comb-drives in positive ξ-direction is a times the force in negative ξ-direction. For x-displacement the total force in positive direction would be (using the inverse kinematic model): $F_{x+} = a\,F_{\xi} + 0.5\,F_{\xi} + 0.5\,F_{\xi} = F_{\xi}\,(1+a)$, while in the negative direction the total force would be: $F_{x-} = F_{\xi} + 0.5\,a\,F_{\xi} + 0.5\,a\,F_{\xi} = F_{\xi}\,(1+a)$, which is equal to the force in the positive direction. Similarly, for the positive y-direction we find: $F_{y+} = a\,F_{\xi} + F_{\xi} = F_{\xi}\,(1+a)$ and $F_{y-} = F_{\xi} + a\,F_{\xi} = F_{\xi}\,(1+a)$. Only for rotation about the z-axis, one would find differences between the positive and negative direction. In spite of that, no difference is found in the trend-lines for positive and negative direction for the rotation.

Apparently a difference in force in positive and negative directions of the comb-drives does not lead to significant results related to the measurement accuracy. The found difference in trend-lines might result from the relatively small number of measurement points.

3.5.3 *Out-of-plane cross-talk*

In plane movements may be accompanied with out-of-plane cross-talk. Possible reasons for this cross-talk are asymmetry of the suspension beam's cross-section with respect to the height-axis (see appendix B) and in-plane beam orientations not parallel to one of the main crystal directions of the silicon crystal (as discussed on page 30 in chapter 2).

To measure possible out-of-plane cross-talk for in-plane movements, *scanning laser-doppler vibrometry* through a microscope is applied. This vibrometry is part of the *MSA-400 Micro System Analyzer* of *Polytec* [18] and is able to scan over a surface to visualize vibration modes of the measured surface. Furthermore, it is equipped with a reference laser beam, allowing to select a reference point and distinguish between the vibrations of the object to be measured and the vibrations of its substrate and determine the relative phase of the vibration. Vibrometry is a very sensitive method; this particular system has a displacement resolution of at least 0.4 pm/$\sqrt{\text{Hz}}$.

Applied method The cross-talk out-of-plane vibration component for in-plane movement is measured for two devices. One device is a single push-pull comb-drive identical to the comb-drives in the 3 DOF manipulator and oriented along the $\langle 100 \rangle$ crystal direction. The second devices is a comb-drive oriented along an in-plane angle of 60° with respect to the $\langle 100 \rangle$-direction. This actuator is part of the manipulator, thus it is

loaded by the platform and the other two comb-drives.

During the measurement the frequency of the comb-drive is scanned and for each frequency value the out-of-plane velocity and the phase is measured. This results in a frequency spectrum with peaks at the frequencies of the vibration modes. The velocity-data can be used by the software to calculate the displacement enabling a plot of the displacement versus frequency. Since the comb-drives are compliant for in-plane displacement, the in-plane vibration is expected in the lower frequency range, while the higher frequency modes are either out-of-plane modes of the complete shuttle or plate vibration modes within the shuttle. The assumed in-plane resonance is compared to the calculated resonance frequency and an in-plane displacement measurement is performed with the *Planar Motion Analysis* also part of the MSA-400 Micro System Analyzer.

The software allows to define multiple points on the device to be measured. The points are connected in a mesh to form a surface that is animated to show the vibration modes. Although, a reference beam can be applied, it only compares the vibrations of two points. Since the substrate is a thin plate, non-rigidly attached to the measurement chuck, the wafer plane shows vibrations and one single point is not sufficient for reference. Therefore, apart from defining a mesh of points on the shuttle of the comb-drive, an extra mesh is defined on the "fixed" surrounding. Once a peak is found in the measured frequency spectrum, the animation is used to check if the shuttle vibrates significantly more than the surrounding area, before deciding the peak is a vibration of the shuttle.

The comb-drive actuators are driven asymmetrical (only one of both comb-racks is powered) by a periodic chirp with an amplitude of 6 V and an offset of 3 V. The offset prevents a frequency doubling of the shuttle movement with respect to the driving signal, however the movement will still show some harmonic distortion.

Measurement results Figure 3.15 shows the out-of-plane displacement measurement results obtained with the vibrometer. Figure 3.15a shows a single resonance peak at 1433 Hz, while figure 3.15b shows multiple peaks at 1074, 1163, and 1414 Hz. This last result is explained by the fact that the second actuator was loaded by the rest of the 3 DOF manipulator. A similar result with multiple peaks at comparable frequency values was found by Wei Zhou (Ph.D. student of the MAMS project at control engineering) with impedance measurements on a comb-drive loaded by the complete system. The first two peaks found in figure 3.15b are related to the complete system while the third peak is the resonance frequency of the comb-drive itself (these all are out-of-plane cross-talk components of in-plane vibration modes). The calculated resonance frequency for a single comb-drive moving in-plane is found by:

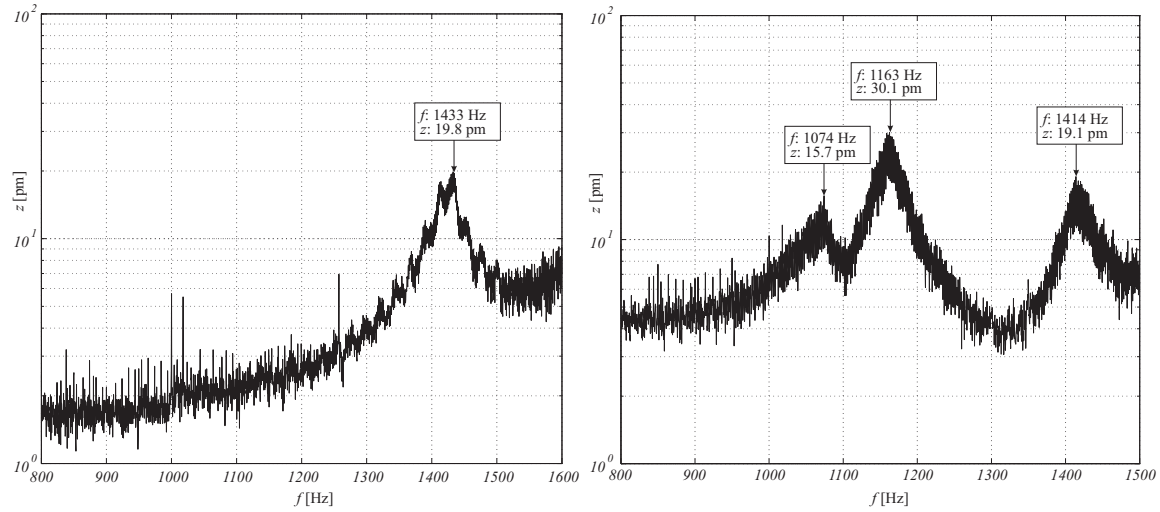

(a) (b)

Figure 3.15: Vibrometer measurement results showing the out-of-plane displacement spectra for the comb-drive oriented along the ⟨100⟩ crystal direction (a), and for the comb-drive oriented along an angle of 60° with respect to the ⟨100⟩-direction.

$$f_r = \frac{1}{2\,\pi}\sqrt{\frac{4\,c_\xi}{m_s}} \quad \text{with} \qquad m_s = \rho\, f\, A_s\, h_s \tag{3.17}$$

Where, the stiffness c_ξ is given in section 3.2.4 on page 56, ρ is the density of Si of 2330 kg/m^3, and f is the fill-factor equal to $\frac{12^2 - 9^2}{12^2}$ compensating for the etch holes. The shuttle surface A_s is 1.035×10^6 μm^2 and the shuttle height h_s is 37 μm. These values result in a resonance frequency of 1249 Hz. This value is smaller than, but near to the values found with the laser vibrometer and the impedance measurements of Wei Zhou. The deviation is expected since the shuttle height, the folded flexure beam thickness and the fill-factor cannot be determined very accurately due to process variations.

For the single comb-drive, the in-plane displacement is measured at its resonance frequency of 1433 Hz and for a driving voltage with an amplitude of 6 V and an offset of 3 V as used with the vibrometer. The in-plane displacement amounts to ± 1 μm.

The out-of-plane displacements at resonance of the first and second comb-drive respectively are 19.8 and 19.1 pm. This is very small. Also the displacements found at the two other peaks in figure 3.15b are not significant. The manipulation can clearly be regarded planar within less than 1 nm movement in out-of-plane direction.

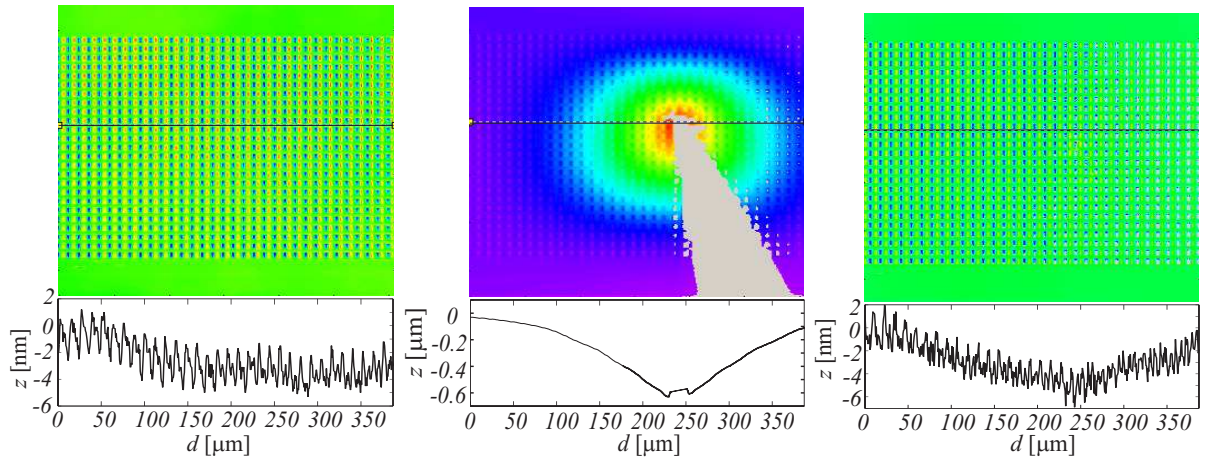

Figure 3.16: Image showing the topography (top) and profile along the line in the topography (bottom), for the grid before (a), during (b) and after (c) indentation with a probe-needle.

3.5.4 *Hysteresis indication*

Material hysteresis is a possible cause of virtual play in a flexible mechanism and compromises high resolution positioning. Single crystalline silicon is known for having very low hysteresis as can be expected from a single crystalline material, since it has no domain-walls that can shift due to loading. Furthermore, the silicon wafers are very pure (except doping) and have very little crystal defects. However, highly doped wafers (as used here) by definition do have impurities due to boron doping. To qualitatively characterize silicon structures with respect to hysteresis, an under-etched test structure consisting of a 37 μm thick plate with a mesh of etch holes is loaded by a probe needle. With the *white-light interferometric topographic profiler* of the MSA-400 Micro System Analyzer, the topography of the test-surface is measured before, during and after the loading.

Figure 3.16 shows the topographies obtained by white light interferometry. The profile of the loaded mesh in figure 3.16b shows that the loading by the probe-needle causes an indentation of 0.6 μm (note the differences in z-scale). The loading has been applied for at least 10 minutes. As shown in figure 3.16c, after the loading was removed, the profile shows a small indentation. However, this is hardly significant and could be resulting from damage due to the probe-needle. This experiment shows, that material hysteresis in highly doped P^{++} SCS wafers is of no significance for nanometer resolution positioning.

3.6 Conclusion

The parallel 3 DOF planar manipulation concept is successfully implemented and fabricated in MEMS technology. Measurements have shown that applying a simple first order inverse kinematic model leads to relatively accurate positioning of the platform. Furthermore, the expected linear relation between squared driving voltage and the platform displacements and rotation is verified to large extend by the measurements. Although, the measurement method does not allow accurate measurement of displacements on the nanometer scale, the linear behavior of the system is very promising for nanometer resolution positioning. From the mechanical point of view, the flexure-based, friction-free mechanism together with a low hysteresis material like SCS enables nanometer resolution. The hysteresis was qualitatively characterized by indentation and white-light interferometry not resulting in any significant memory effect. The bottleneck for nanometer resolution positioning will be the stability of the voltage source used to drive the actuators. Applying linear-drive can largely reduce the demands on the voltage sources used for driving.

The suspension of the comb-drives is analyzed with respect to side and rotational pull-in. It was found, rotational pull-in occurs at the lowest driving voltage. In case of linear-drive, the rotational pull-in occurs at a dc-voltage of 320 V at 10 μm displacement. The stiffness model takes into account the large decrease of the suspension with deflection. This form of non-linear modelling is shown to be very important for a good indication of the stiffness under deflection. During operation of the comb-drive no pull-in has occurred, however no voltages in the expected pull-in range have been applied. The application of analytic modelling has it limitations, especially since it is too complex to take into account the compliance contribution of the square-shaped etch-holes.

With the help of laser doppler vibrometry, out-of-plane cross-talk has been measured for in plane displacement of the comb-drives in resonance. The measured out-of-plane cross-talk for an in-plane displacement with an amplitude of 1 μm was in the order of 20 pm. The manipulation can clearly be regarded planar within 1 nm in out-of-plane direction.

The 20-sim simulation model approaches the behavior of the manipulator quite well and can be applied as a basis for a control system to drive the parallel manipulator. In case non-linear descriptions for the flexures are required, the equations can be implemented in the model. Once the system is expanded with e.g. capacitive position sensing, feed-back control can be implemented in the model. The model can serve very nicely as a tool to study control-requirements for the MEMS system.

The chosen technology poses limitations on the proposed geometry. First of all

it was decided to use equally sized square etch-holes, since we do not have experience with the release etch in combination with triangular etch-holes. Apart from an increase in stiffness of the device, triangular etch-holes are easier to construct the equilateral triangular platform. Since the size of the square etch-holes was determined by other devices on the mask and the process is sensitive to this size, points connecting the leaf-spring of the mechanism to the platform do not exactly coincide with the vertices of an equilateral triangle. Secondly the accuracy of defining the plate-spring width was limited by the variations in the mask feature-size. For the 2 μm wide plate-springs the variation amounts up to 10 % of the width. This has a large influence on the in plane stiffness of the plate-springs.

References

[1] M. P. Koster, *Constructie principes voor het nauwkeurig bewegen en positioneren*. Twente University Press, Enschede, The Netherlands, 2000.

[2] D. Elata and V. Leus, "How slender can comb-drive fingers be?," *J. Micromech. Microeng.*, vol. 15, no. 5, pp. 1055–1059, 2005.

[3] J. J. Wortman and R. A. Evan, "Young's modulus, shear modulus and poisson's ratio in silicon and germanium," *J. Appl. Physics*, vol. 36, no. 1, pp. 153–156, 1965.

[4] A. A. Kuijpers, *Micromachined Capacitive Long-Range Displacement Sensor for Nano-Positioning of Microactuator Systems*. PhD thesis, University of Twente, Enschede, The Netherlands, 2004.

[5] B. R. De Jong, D. M. Brouwer, H. V. Jansen, M. J. De Boer, T. G. Lammertink, S. Stramigioli, and G. J. M. Krijnen, "A planar 3 DOF sample manipulator for nano-scale characterization," in *MEMS*, (Istanbul, Turkey), pp. 750–753, 2006.

[6] E. Sarajlić, M. J. De Boer, H. V. Jansen, N. Arnal, M. Puech, G. J. M. Krijnen, and M. C. Elwenspoek, "Advanced plasma processing combined with trench isolation technology for fabrication and fast prototyping of high aspect ratio MEMS in standard silicon wafers," *J. Micromech. Microeng.*, vol. 14, pp. S70–S75, 2004.

[7] W. C. Young and R. G. Budynas, *Roark's Formulas for Stress and Stain*. McGraw-Hill, 7^{th} ed., 2002.

[8] R. Legtenberg, *Electrostatic actuators fabricated by surface micromachining techniques*, ch. 2, pp. 43–46. University of Twente, The Netherlands, 1996.

[9] J. Van Eijk, *On the Design of Plate-spring Mechanisms (Ph.D thesis)*. Delft University, The Netherlands, 1985.

[10] D. M. Brouwer, B. R. De Jong, and H. M. J. R. Soemers, "MEMS 6 Degree of Freedom parallel kinematic precision micro manipulator.," in *Euspen*, (Baden bei Wien, Austria), pp. 111– 114, 2006.

[11] http://www.wa.ctw.utwente.nl/Software/SPACAR/2006/.

[12] T. Lammertink, "Power-port modelling of an in-plane 3 DOF parallel micro-manipulator with feed-forward position control.," Master's thesis, University of Twente, Enschede, The Netherlands, 2005.

[13] http://www.20sim.com/.

[14] B. R. De Jong, H. V. Jansen, M. J. De Boer, and G. J. M. Krijnen, "Tailored etch-profiles of high aspect ratio trenches to prevent voids after refill with lpcvd sirn.," in *MME*, (Göteborg, Sweden), pp. 60–63, 2005.

[15] H. Jansen, G. Gardeniers, M. De Boer, M. Elwenspoek, and J. Fluitman, "A survey on the reactive ion etching of silicon in microtechnology," *J. Micromech. Microeng.*, vol. 6, pp. 14–28, 1996.

[16] A. R. Gottscho, C. W. Jurgensen, and V. D. J., "Microscopic Uniformity in Plasma Etching," *J. Vac. Sci. Technol. B.*, vol. 10, no. 5, pp. 2133–2147, 1992.

[17] http://www.ni.com/vision/software.htm/.

[18] http://www.polytec.com/eur/.

Chapter 4

Vertical comb-drive and torsion suspension: Theory and design.

A design for a vertical comb-drive with improved torsion suspension is presented. The conditions for side pull-in instability are analyzed and the 6 DOF stiffness of the improved suspension is modelled. Finally, the improvements in kinematic constraint of the comb-drive shuttle with respect to a conventional, rectangular torsion beam are visualized for variations in the geometry

4.1 Introduction

The concept for 6 DOF manipulation discussed in chapter 2 requires an out-of-plane actuator. An analysis of common actuation principles has been performed in section 2.4 on page 41. An electrostatic vertical comb-drive actuator was chosen for its suitable performance, compatibility with monolithic SCS processing and feasibility with respect to fabrication requirements.

Before discussing the design of the vertical comb-drive, some specification are required. The requirement for vertical actuation followed from the chosen manipulator concept in section 2.3 on page 32. The out-of-plane displacement requires to be 20 μm to allow for a stroke of 10 μm in up and down direction. The actuation voltage is best to be relatively low, typically 30 V. For nanometer resolution the voltage source should deliver a very stable voltage, obtaining this stability is a lot more complex for higher voltages. Furthermore, applications where strong electrical fields cause

interference, like manipulation in a transmission electron microscope (TEM), require an as low as possible driving voltage. The load mainly consists of stiffness, since there will be aimed at an application, where the timescale for manipulation is in the range of seconds and the mass of the system is typically tens of micrograms. The force generated at that available driving voltage should be enough to both deform the comb-drive suspension and drive the additional load due to stiffness of the flexible mechanism.

Section 4.2 introduces the general vertical comb-drive concept and the vertical suspension by torsion beams. Furthermore, an analysis of the side pull-in instability is given followed by an analysis of the 6 DOF torsion suspension. In section 4.3 the $\perp$-shaped torsion beam is introduced followed by the design of the comb-drive and an analysis of the torsion beam dimensions on the suspension's performance [1]. The conclusion and discussion follow in section 5.5.

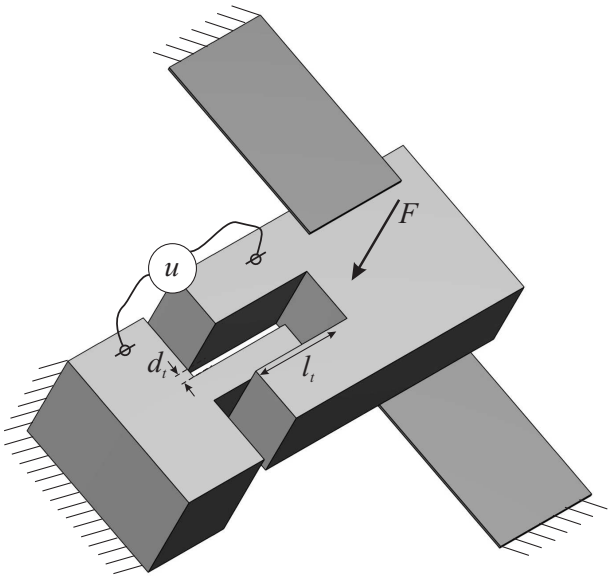

Figure 4.1: Plate-spring suspended vertical comb-drive.

4.2 Vertical comb-drive and suspension

For stable, high resolution positioning in the nanometer range, the actuator should be well constrained in all other DOF and the suspension is required to behave deterministic. First a decision is made for a suitable suspension, followed by a side pull-in stability analysis and an analysis of the 6 DOF stiffness of the suspension.

[1] The $\perp$-torsion suspension will be referred to as method 1, appendix B discusses a different shaped torsion beam, which is more challenging to analyze. This suspension is referred to as method 2.

Table 4.1: Values for vertical comb-drive force in equation (4.1).

parameter	value	unit
n	100	-
l_t	200	μm
d_t	2	μm
u	30	V

4.2.1 Vertical suspension

The requirement with respect to the maximum displacements has a technological as well as a design aspect. The first aspect is dealt with in chapter 5 and concerns the three dimensional structuring to allow the clearance for the comb-drive to move 20 μm. The second aspect involves the suspension of the translating part of the comb-drive. Because of the complications of making bearings and hinges without clearance in MEMS the suspension is based on flexures [1]. The flexure mechanism must meet the requirements with respect to exact kinematic constrained design (1 DOF free) and allow 20 μm of deflection at a reasonably low driving voltage.

Before deciding on the suspension, the force of the comb-drive is considered. A simple energy model results in the following formula (equation (4.1)) for the force F [N] inserting the comb-drive teeth into each other (figure 4.1):

$$F(u) = \frac{n\,\varepsilon_0\,l_t\,u^2}{d_t} \tag{4.1}$$

Where u is the applied voltage [V], l_t is the length of the comb-teeth overlap [m], ε_0 is the dielectric constant of vacuum, d_t is the gap between the comb-teeth [m], and n is the number of comb-teeth pairs.

Apart from increasing the voltage, the force can be increased by applying a large number of teeth pairs, choosing a relatively large length for the teeth, and, most important, a small as possible gap d_t. The gap is restricted by the smallest feature size of the applied photo-lithography, being 2 μm. l_t and n are geometrically related since many short teeth require the same area as fewer long teeth. Furthermore, longer teeth need to be thicker to be robust against side pull-in, so the number per area lowers. With realistic values as shown in table 4.1, a force of about 80 μN results. This is certainly enough to deflect a suspension together with an extra load due to a flexible mechanism. As is shown in section 4.3.2 a voltage of about 20 V is enough for a displacement of 20 μm, while the driving voltage can rise to at least three times the voltage for full range displacement before side pull-in is expected. Keeping in mind the quadratic relation between driving voltage and actuator force *and* assuming

an additional stiffness of the mechanism of twice the comb-drive suspension stiffness, the force requirements can be met.

The desired suspension constrains the movement to the vertical direction. A well known and proven solution is to suspend the translating part by two plate-springs, parallel placed at a distance from each other and perpendicular to the vertical direction as shown in figure 4.1 op page 80.

However some remarks ought to be made with respect to this suspension. The thickness over length ratio of the plate-springs should be extremely small, not to require too much force for the deflection of the suspension. This rather means very small thickness than a large length since otherwise the suspension turns out to be too compliant in the other DOFs. Such dimensions require to start of with a thin film for the flexure. This conflicts with the desire for structures entirely made of SCS. Furthermore, thin films suffer from residual stress which, once released, can be a source of initial position errors. Technologically, it will be more difficult to remove all silicon around the suspension plates. Release of the flexures will be easier if these are made of SiO_2 or SiRN, since those materials will not etch when the silicon is etched. However, these materials are non-conductive, requiring extra metal deposition and structuring.

If the constraint on moving solely in the out-of-plane direction is eased, a commonly used suspension turns up, namely a torsion suspension. If only out-of-plane torsion is compliant combined with a long arm, than the free end of that arm will move along a circle section. For small torsion angles, this circle section is approximately straight. However, there is a small second order in-plane displacement.

Simple MEMS torsion suspensions consist of a beam with rectangular cross-section [2, 3, 4, 5]. Such a beam is not only compliant for torsion around its length axis but also for deflection in the lateral direction, rotation about the height axis of the free end, and for deflection in the height direction in case the beam is much longer than its height. Especially, compliance in the rotational direction (α in figure 4.2 left op page 83) can cause side pull-in in the comb-drive to occur at low driving voltages. Furthermore, the beams are often long to reduce the torsion stiffness so less torque delivered by the comb-drive is needed. Increasing the length of the beam makes it even less stiff in the lateral direction, decreasing the side pull-in voltage. A shorter, and thus stiffer torsion beam can be used if the comb-drive is placed at the distant end of a long arm. The moment working on the torsion beam is than increased by the arm length. Unfortunately, by doing so, also the pull-in moment (in-plane rotation) working on the torsion beam is increased as will be discussed in the next section.

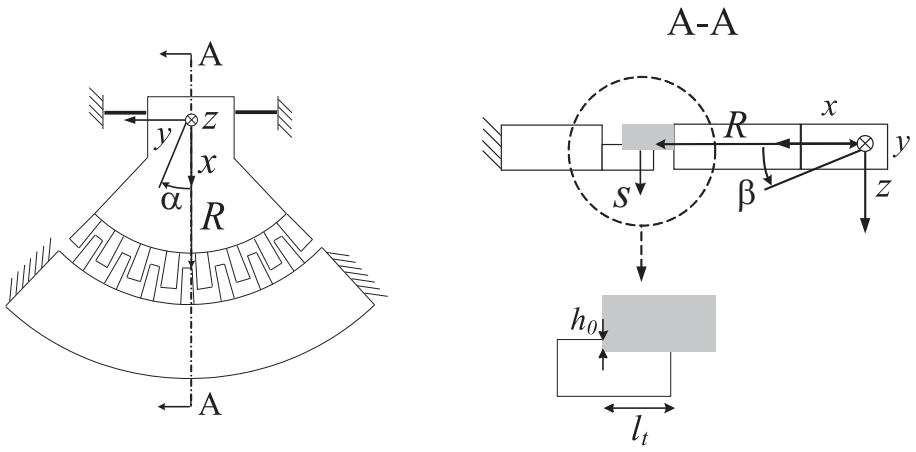

Figure 4.2: Model of the vertical comb-drive with two free DOF α and β. Topview (left) and cross-section through AA with enlargement of tooth overlap (right)

4.2.2 Stability analysis for side pull-in

Side pull-in is the instability, where the lateral stiffness of the comb-drive is fully canceled by the electrostatic stiffness of the comb-drive, which is opposite in sign to the suspension stiffness. The equation for the electrostatic stiffness is derived with help of a model of the vertical comb-drive, where it is assumed to have two compliant rotational DOFs, α and β [rad]. α represents the rotation about the z-axis, which is the potential side pull-in direction and β represents the rotation about the y-axis, which is the desired DOF causing the vertical displacement s [m] at the comb-teeth. A sketch of the model is shown in figure 4.2. Here R [m] is the arm between the suspension and the comb-teeth, and h_0 [m] is the initial overlapping height of the teeth.

The relation $s(u)$ is found from the torque T_β [Nm], which is derived from the energy equation for the system. Since the geometry is more complex compared to a regular comb-drive, the energy equation is less common and will be derived from integration of the energy density over the volume between the teeth. The energy density is expressed in the electric field, which on its turn depends on the applied voltage and the distance between the comb-teeth. The field is assumed to be uniform (parallel plate approximation).

Because the system is driven in voltage-control, a Legendre transform of the energy(-density) is used. The variation of e^* is given in equation (4.2a). Here e is the energy-density [J/m^3], $\mathbf{E}$ is the electric field [V/m], $\mathbf{D}$ is the electric flux density [C/m^2], and E is the magnitude of the electric field. By integration, the transformed energy density e^* is obtained from the variation. $\mathbf{E}$ is considered uniform, i.e. no fringe-field is assumed. From [6] we infer the influence of the fringe fields on the capacitance is

not significant for the dimensions of the design as given in table 4.2 on page 92.

$$\mathrm{d}e^* = \mathrm{d}e - \mathbf{E}\mathrm{d}\mathbf{D} - \mathbf{D}\mathrm{d}\mathbf{E} = -\mathbf{D}\mathrm{d}\mathbf{E} \tag{4.2a}$$

$$e^* = -\int_0^E \mathbf{D}\mathrm{d}\mathbf{E} = -\frac{\varepsilon_0 E^2}{2} \tag{4.2b}$$

Integrating e^* over the volume between the teeth leads to the Legendre transformed energy E^*. The integral is multiplied by n for the amount of tooth-pairs. For the electric field, the applied voltage u divided by the distance between the teeth $d(x,\alpha)$ is inserted. The integration is evaluated on the volume $z = [0, \bar{h}(\beta)]$, $y = [0, d(x,\alpha)]$, and $x = [0, l_t]$. Where $\bar{h}(\beta)$ [m] is the mean value of the height of the teeth overlap. Since the dependence of $d(x,\alpha)$ [m] on x differs for the gap at one or the other side of a tooth, the volume is split into two parts where $d_1(x,\alpha)$ and $d_2(x,\alpha)$ are respectively inserted for $d(x,\alpha)$.

$$\begin{aligned} E^* &= -n\int_V \frac{\varepsilon_0}{2} E^2 \mathrm{d}V = -\frac{n\,\varepsilon_0}{2}\int_V \left(\frac{u}{d(x,\alpha)}\right)^2 \mathrm{d}V \\ E^*(u,\alpha,\beta) &= -\frac{n\,\varepsilon_0\,\bar{h}(\beta)\,u^2}{2}\left\{\int_0^{l_t}\frac{1}{d_1(x,\alpha)}\,\mathrm{d}x + \int_0^{l_t}\frac{1}{d_2(x,\alpha)}\,\mathrm{d}x\right\} \end{aligned} \tag{4.3a}$$

Where $\bar{h}(\beta)$, $d_1(x,\alpha)$ and $d_2(x,\alpha)$ are given below, assuming small α and β.

$$\begin{aligned} \bar{h}(\beta) &= h_0 + \beta\left(R + \frac{l_t}{2}\right) \\ d_1(x,\alpha) &= d_t - \alpha(R+x) \\ d_2(x,\alpha) &= d_t + \alpha(R+x) \end{aligned} \tag{4.3b}$$

The resulting equation for the E^* looks quite complicated because of the logarithm (See equation (4.4a). However it can be proved that the limit for $\alpha \to 0$ exist and E^* reduces to the equation usually found for a comb-drive, equation (4.4b).

$$E^*(u,\alpha,\beta) = \frac{n\,\varepsilon_0\,\bar{h}(\beta)\,u^2}{2\,\alpha}\ln\left\{\frac{(d_t - \alpha\,R)(d_t + \alpha\,(R+l_t))}{(d_t + \alpha\,R)(d_t - \alpha\,(R+l_t))}\right\} \tag{4.4a}$$

$$\lim_{\alpha\to 0}(E^*) = \frac{n\,\varepsilon_0\,\bar{h}(\beta)\,u^2}{d_t} \tag{4.4b}$$

To determine if the comb-drive operates within stability limits, the *electrostatic stiffness* is derived and compared to the rotational stiffness in the direction of α. The lateral electrostatic torsional stiffness is calculated by partially differentiating the torque with respect to α for a given voltage u. This leads to equation (4.5a). The result of this

equation is not given in total since it looks quite complicated. However it is dependent of $\frac{1}{\alpha^3}$, as could be expected. The conventional analysis of a comb-drives lateral electrostatic stiffness will show a third-power dependence on the lateral displacement of the teeth.

$$k_\alpha(u,\alpha,\beta) = \left[\frac{\partial^2 E^*}{\partial \alpha^2}\right]_{u,\beta} \tag{4.5a}$$

$$\lim_{\alpha=0}(k_\alpha) = -\frac{n\,\varepsilon_0\,\bar{h}(\beta)\,u^2}{3\,{d_t}^3}((R+l_t)^3 - R^3) \tag{4.5b}$$

To find the value of k_α for $\alpha = 0$, its limit is given in equation (4.5b). Clearly, there is a large dependance on the torsion arm R and teeth-length l_t. This agrees to what was expected prior to the analysis. Obviously it is beneficial to keep the required driving voltage low. As a result, increasing the distance between the teeth d_t is not the best solution to lower k_α. The torsion stiffness of the suspension should be minimum for a low driving voltage, but the stiffness in the other DOF need to be sufficiently large; especially the stiffness in lateral direction to the teeth. Furthermore, the position restoring torque of the comb-drive is exerted by its torsion suspension. A too low torsion stiffness would result in a low-frequent system. An analysis of the 6 DOF suspension stiffness is given in the next section.

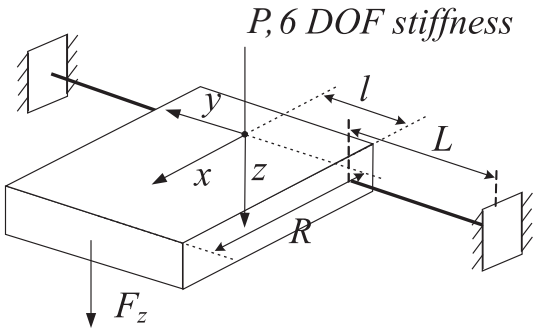

Figure 4.3: Model of body suspended by torsion beams.

4.2.3 6 DOF suspension stiffness analysis

To calculate the stiffness of the suspension for all 6 DOF, a model is proposed of a rigid body suspended by torsion-beams, see figure 4.3. In this model, linear beam theory for small deflections is applied. The suspension is meant to restrain movements in all DOF except torsion. With a maximum displacement of 20 μm, a typical arm length of 1 mm and a torsion beam length of about 200 μm, the torsion angle per micron torsion beam length is $\theta = \frac{1}{200}\arctan\left(\frac{20\times10^{-6}}{1\times10^{-3}}\right) \approx 1.01\times10^{-4}$ rad/μm. [7] gives the following expression for the maximum sheer stress due to torsion:

$$\tau_{max} = \frac{\theta\, E_Y\, r}{2(1+\nu)} \tag{4.6}$$

Here the E_Y is Young's modulus for silicon of 130 GPa, ν is the Poisson's ratio of silicon of 0.27, and r is the radius from the torsion axis to the beam's outer surface. r relates to the geometry of the torsion beam. For an estimation of τ_{max}, we take $r = 20$ μm, resulting in $\tau_{max} = 0.1$ GPa. This is well below the fracture stress of 3 GPa reported in [8].

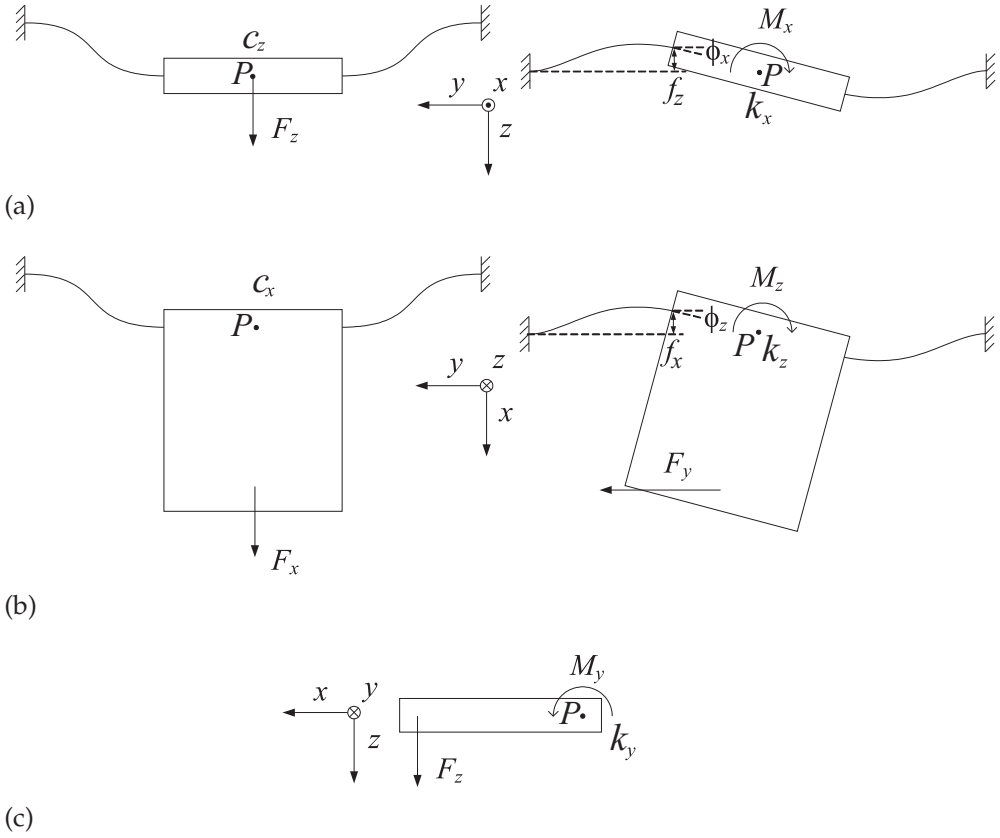

Figure 4.4: Various views of the model in figure 4.3; frontal (a), top (b), and side (c).

Figure 4.4 shows various views of the model. The translational (c_x, c_z in [N/m]) and rotational (k_x, k_y, k_z in [Nm/rad]) stiffness values in the various directions are evaluated in point P. The forces that eventually work on the suspension beams are, for this analysis, assumed to load the beam in its *shear center* (see appendix B on page 176). Both translational stiffness values are known form [9] and given in equations 4.7a and 4.7b.

$$c_x = 2\,\frac{12\, E_Y\, I_z}{L^3} = \frac{24\, E_Y\, I_z}{L^3} \tag{4.7a}$$

$$c_z = 2\,\frac{12\, E_Y\, I_x}{L^3} = \frac{24\, E_Y\, I_x}{L^3} \tag{4.7b}$$

Where E_Y [Pa] is the Young's modulus, I_x and I_z [m^4] are the moments of inertia respectively about the x and z axis, and L [m] is the length of one torsion beam.

The stiffness not shown, is the tensile-stiffness c_y. This stiffness is given by:

$$c_y = 2\,\frac{E_Y\,A}{L} \tag{4.8}$$

Where A [m^2] is the area of the beam's cross-section.
The torsion stiffness of the torsion beam k_y is given by:

$$\begin{aligned} k_y &= 2\,\frac{\kappa\,G}{L} \\ \text{with } G &= \frac{E_Y}{2\,(1+\nu)} \end{aligned} \tag{4.9}$$

Where G [Pa] is the modulus of rigidity, ν is the Poisson's ratio, and κ [m^4] is a factor depending on the shape and sizes of the cross-section (*only* in case of a circular cross-section, κ is equal to the polar moment of inertia). An approximation for k_y for the rectangular and the $\perp$-shaped torsion beam will follow on page 91.

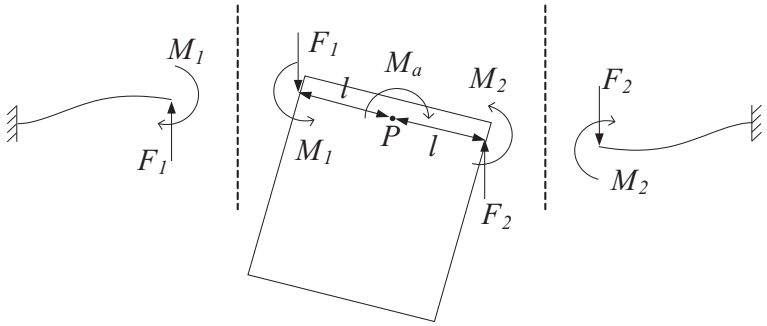

Figure 4.5: Equilibrium conditions.

To derive the expressions for k_x and k_z, standard beam theory is used for the deflection f and the bending angle ϕ at the end of one beam (see figure 4.4a and b). First the equilibrium equations are defined with help of figure 4.5. Beam 1 and 2 are assumed identical. M_a is the applied moment. This is either M_x for rotation about the x-axis (see figure 4.4a) or M_z for rotation about the z-axis (see figure 4.4b).

$$\begin{aligned} &\Sigma F = F_1 - F_2 = 0 \Rightarrow F_1 = F_2 (= F_b) \\ &M_1 = M_2 (= M_b) \\ &\Sigma M = M_a - 2M_b - 2F_b l = 0 \end{aligned} \tag{4.10}$$

Now the standard equations for $f(M_b, F_b)$ and $\phi(M_b, F_b)$ (equations 4.11a and 4.11b) can be used together with the boundary condition $\phi = -\frac{f}{l}$ for small f, to find the stiffness from $k = \frac{M_a}{\phi}$.

$$f(M_b, F_b) = \frac{M_b L^2}{2E_Y I} - \frac{F_b L^3}{3E_Y I} \tag{4.11a}$$

$$\phi(M_b, F_b) = \frac{M_b L}{E_Y I} - \frac{F_b L^2}{2E_Y I} \tag{4.11b}$$

F_b is eliminated with $\phi = -\frac{f}{l}$ after which M_b is expressed in M_a. This results in the following expressions for k_x and k_z:

$$k_x = \frac{M_x}{\phi_x} = \frac{8\, I_x\, E_Y \left(3\, l^2 + 3\, l\, L + L^2\right)}{L^3} \tag{4.12a}$$

$$k_z = \frac{M_z}{\phi_z} = \frac{8\, I_z\, E_Y \left(3\, l^2 + 3\, l\, L + L^2\right)}{L^3} \tag{4.12b}$$

To obtain equation (4.12a), ϕ_x, f_z, M_x and I_x are respectively inserted for ϕ, f, M and I in equation (4.11). Similarly, to obtain equation (4.12b), ϕ_z, f_x, M_z and I_z are respectively inserted for ϕ, f, M and I in equation (4.11).

Now the stiffness expressions are derived, a comparison can be made between a torsion beam with a rectangular cross-section and the beam with a $\perp$-shaped cross-section. Expressions depending on the dimensions (namely the moments of inertia I_x and I_z and the shape-factor κ) need to be derived for the different cross-sections. However, here it can already be observed that k_x and k_z increase for larger distance l between point P and the torsion beam. This makes sense, since increasing l compensates for the long arm R.

4.3 Design of the comb-drive and its suspension

The analysis in the previous section shows, susceptibility to side pull-in is increased by the choice for torsion over a long arm. k_z is the stiffness of the suspension in de direction of pull-in. It needs be well larger than the electrostatic stiffness k_α. k_α was shown to depend much on the arm length R; The longer the arm, the larger k_α. k_z on its turn depends much on the shuttle width ($2\,l$). So a large shuttle width is desirable. However, more effort is required to improve the stiffness k_z compared to the case of a ”normal” torsion beam with rectangular cross-section, since the length of the beam is very determining. This section will discuss a solution to increase k_z with a factor 136 while increasing the torsion stiffness with less than a factor 2.5.

4.3.1 $\perp$-shaped torsion beam: method 1

Here a torsion beam with a $\perp$-shaped cross-section is proposed (see figure 4.6 right). This shape is chosen such that it can be constructed of two types of beam elements,

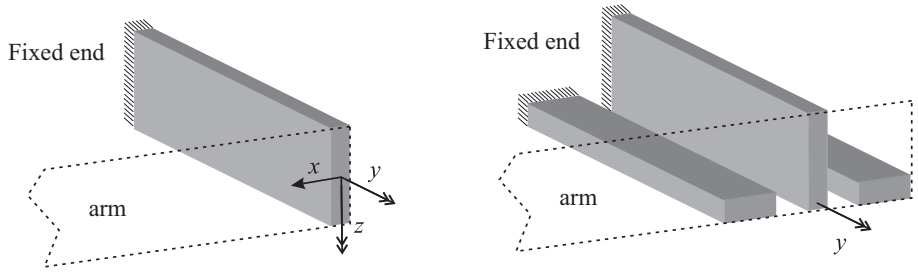

Figure 4.6: Two different kinds of beams showing the free DOF; Rectangular torsion beam (left).Torsion beam with ⊥-shaped cross-section (right). The gap between the up-right and horizontal part is required for release during fabrication.

which are feasible in MEMS technology. Preferably the beam elements are attached to each other, however to enable release from the substrate during fabrication there is a gap between the beams. Another method (method 2) is described in appendix B. There, an L-shaped cross-section is proposed. The analysis for an L-torsion beam is more complicated.

In order to find values for the various stiffness terms for the ⊥-torsion beam, the moments of inertia are required and the shape-factor for the torsion stiffness should be derived.

Moment of inertia For the moment of inertia, the neutral-planes need to be found. Since at the neutral-planes of the beam no lateral force works on the cross-section during bending, it can be found by integrating the bending stress $\sigma_y(z)$ [Pa] on the cross-section of the beam (depending on the height z) over the cross-sectional area and equating the integral to zero [7]. The boundaries for the integration can be found from the definition of the neutral-plane distances as defined in the cross-sections shown in figure 4.7 on page 90. Equation 4.13 shows the procedure to derive the neutral-plane distance Nz for a rectangular beam bending over the x-axis.

$$\int_A \sigma_y(z)\,\mathrm{d}A = -\frac{E_Y}{\rho}\int_A z\,\mathrm{d}A = 0 \quad \text{,where } \rho \text{ is the bending-radius} \tag{4.13a}$$

$$\int_A z\,\mathrm{d}A = 0 \quad \Rightarrow \quad \int_{-Nz}^{b-Nz} a\,z\,\mathrm{d}z' = 0 \quad \Rightarrow Nz = \frac{b}{2} \tag{4.13b}$$

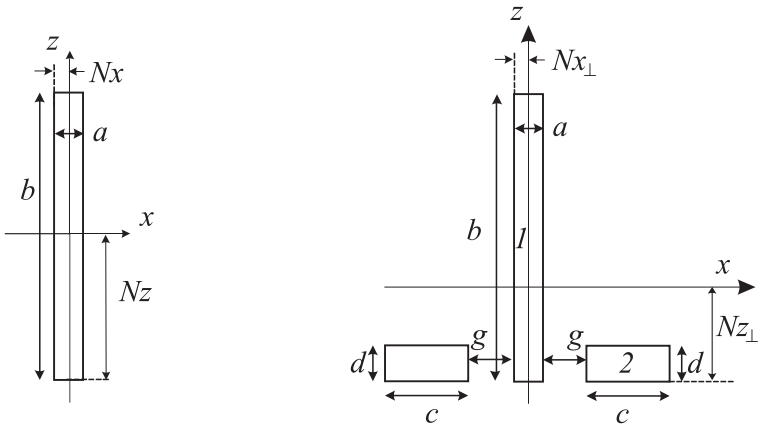

Figure 4.7: Cross-sections of rectangular torsion beam (left), and ⊥-shaped torsion beam (right), used to find the neutral-planes

Applying the same procedure, the neutral-plane distance $Nz_\perp$ for the complex of the ⊥-shaped beam bending over the x axis can be found.

$$\int_A z\,\mathrm{d}A = 0 \quad \Rightarrow \quad \int_{-Nz_\perp}^{b-Nz_\perp} a\,z\,\mathrm{d}z' + 2\int_{-Nz_\perp}^{Nz_\perp-d} c\,z\,\mathrm{d}z' = 0$$
$$\Rightarrow \quad Nz_\perp = \frac{a\,b^2 + 2\,c\,d^2}{2\,a\,b + 4\,c\,d} \tag{4.14}$$

The neutral-plane distance Nx and $Nx_\perp$ for the rectangular beam and ⊥-shaped beam for bending over the z axis respectively are derived similarly.

$$Nx = \frac{a}{2} \tag{4.15a}$$

$$Nx_\perp = \frac{a}{2} \tag{4.15b}$$

With the neutral-planes known, the moment of inertia is calculated as explained in [7]. Here the same boundaries for the integrals are used as for deriving the neutral-planes. I_x and I_z for a rectangular beam are given in equation (4.16a) and (4.16b).

$$I_x = \int_A z^2\mathrm{d}A = \frac{a\,b^3}{12} \tag{4.16a}$$

$$I_z = \int_A x^2\mathrm{d}A = \frac{a^3\,b}{12} \tag{4.16b}$$

The same procedure is used to find the expressions for $I_{x\perp}$ and $I_{z\perp}$ for the ⊥-shaped beam in equation (4.17a) and (4.17b)

$$I_{x\perp} = \frac{a^2b^4 + 4\,c^2d^4 + 4\,a\,b\,c\,d\,\big(2(b-d)^2 - b\,d\big)}{12(ab+cd)} \tag{4.17a}$$

$$I_{z\perp} = \frac{a\,b^3}{12} + 2\,\frac{c^3\,d}{12} + 2\,c\,d\left(\frac{a}{2} + \frac{c}{2} + g\right)^2 \tag{4.17b}$$

With the ratios $\frac{I_{z\perp}}{I_z}$ and $\frac{I_{x\perp}}{I_x}$ the increase in stiffness of the $\perp$-shaped torsion beam for stiffness c_x, c_z, k_x, and k_z are found.

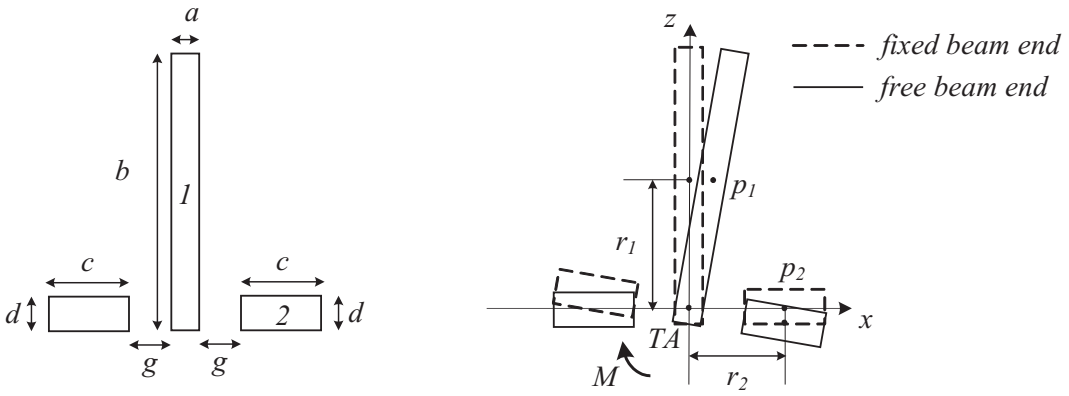

Figure 4.8: $\perp$-torsion beam cross-section used to determine the location of the torsion axis TA.

Shape-factor Shape-factors are hard to calculate for non-circular beams that are not thin-walled [9]. That is because the contour of the shear-stress flow over the transversal cross-section is hard to find. The shape-factor for torsion for a beam with rectangular cross-section is approximated by [9]:

$$\kappa \approx \frac{a^3\,b}{3} \quad \text{assuming } b \gg a \tag{4.18}$$

Since the $\perp$-shaped beam does not consist of one piece, but has a gap between the up-right (1) and the horizontal parts (2), no expression for this beam can be found in a handbook. Observing the cross-section in figure 4.8, it can be reasoned that during torsion the individual beams 1 and 2 will undergo torsion around their length axis combined with translation[1] of the points p_1 and p_2. The moment M working on the beam causes forces in points p_1 and p_2, so by transforming the translation stiffness in these points to the torsion stiffness sensed at the torsion axis of the complex beam, a contribution of the translation stiffness can be added to the torsion stiffness. This is shown in equation (4.19), where $k_\perp$ is the torsion stiffness of the $\perp$-torsion beam; k_1 and k_2 are the torsion stiffness-values of beams 1 and 2 respectively; $k_{c_{p1}}$ and $k_{c_{p2}}$ are the torsion stiffness contributions due to translation of points p_1 and p_2; and c_1 and c_2 the translational stiffness at points p_1 and p_2.

[1] Actually rotation over a circular-segment, but the angle is small so it can be approximated by translation.

$$\begin{aligned} k_\perp &\approx 2\,(k_1 + k_2 + k_{c_1} + 2\,k_{c_2}) \\ k_\perp &\approx 2\,(k_1 + k_2 + {r_1}^2\,c_1 + 2\,{r_2}^2\,c_2) \end{aligned} \tag{4.19}$$

To know the translation stiffness at points p_1 and p_2 and to know the transformation factors (r_1 and r_2), the position of the torsion axis is required. This position can be dirived by realizing bending will happen in the thin direction of beam 1 and 2. This means the points p_1 and p_2 translate in x and z direction respectively. In that case points p_1 and p_2 rotate over radii r_1 and r_2 that intersect in the torsion axis as is shown in figure 4.8. This results in the following equations[2].

$$k_\perp \approx 2\left(k_1 + k_2 + \left(\frac{b}{2} - \frac{d}{2}\right)^2 c_1 + 2\left(\frac{a}{2} + \frac{c}{2} + g\right)^2 c_2\right) \tag{4.20a}$$

$$k_\perp \approx \frac{24\,E_Y}{L^3}\left(I_1\left(\frac{b}{2} - \frac{d}{2}\right)^2 + 2\,I_2\left(\frac{a}{2} + \frac{c}{2} + g\right)^2\right) + \frac{2\,G}{L}(\kappa_1 + 2\,\kappa_2) \tag{4.20b}$$

$$\text{with} \quad \kappa_1 \approx \frac{a^3\,b}{3} \quad \kappa_2 \approx \frac{c\,d^3}{3} \quad I_1 = \frac{a^3\,b}{12} \quad I_2 = \frac{c\,d^3}{12} \tag{4.20c}$$

Table 4.2: Design parameters and constants.

symbol	description	value	unit
a	up-right beam (1) width (fig 4.7)	4	μm
b	up-right beam (1) height (fig 4.7)	40	μm
c	horizontal beam (2) width (fig 4.7)	13	μm
d	horizontal beam (2) height (fig 4.7)	5	μm
g	gap between beams (fig 4.7)	6	μm
L	torsion beam length (fig 4.9)	200	μm
E_Y	Young's modulus Si	130	GPa
ν	Poisson's ratio Si	0.3	-
l	halve of shuttle width (fig 4.9)	940	μm
R	torsion arm (fig 4.9)	840	μm
n	number of comb-drive teeth pairs	64	-
l_t	comb-drive teeth length (fig 4.9)	200	μm
d_t	distance between comb-drive teeth	2	μm

[2]Together with the derived equation for the torsion stiffness an upper limit could be given as well. The shape-factors for the cases where the $\perp$-torsion beam and the L-torsion beam consist of one part are given in [9]. For the dimensions given in table 4.2 on page 92, the increases with respect to the values found for the torsion stiffness by using equations (4.20) and (B.10), are a factor 1.3 and 1.2, respectively for the $\perp$-torsion beam and the L-torsion beam.

4.3.2 Design dimensions of the system

Now that the formulae for the stiffness of the suspension with a ⊥-shaped torsion beam are derived, the design dimensions can be determined. Because of the experimental character of this first design of the ⊥-torsion beam suspended vertical comb-drive, it is *not* meant to be an optimization of the design parameters. For this reason most dimensions are defined suitably, keeping the feasibility of the fabrication in mind. However, the effects of some dimensions are analyzed. A top-view of the vertical comb-drive design is given in figure 4.9a, with enlargements of the torsion beam and comb-teeth in given in figure 4.9b and figure 4.9c (note that for the torsion-beam, the L-shaped variant is depicted). In table 4.2 the design parameters and constants are listed.

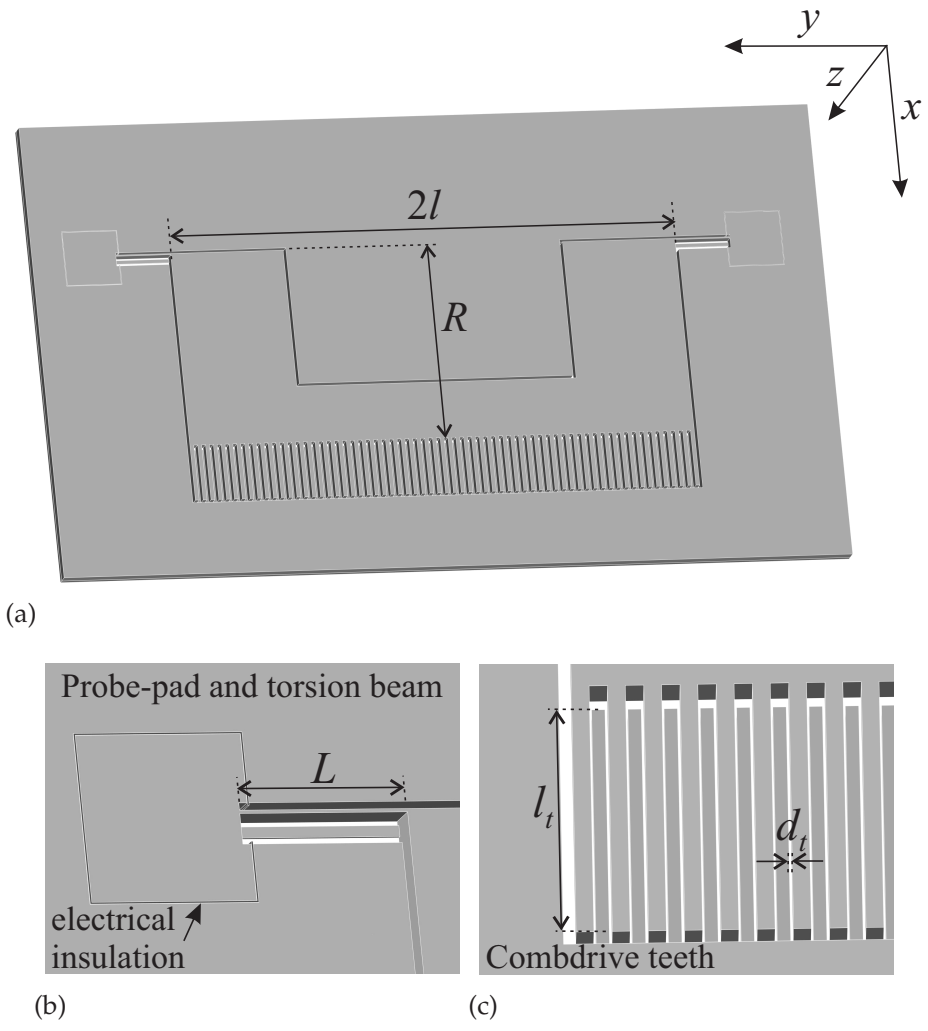

Figure 4.9: Vertical comb-drive design with L-torsion beam.

For the given dimensions, $k_\perp$ in equation (4.20b) can be approximated by $2\,\frac{G}{L}(\kappa_1 + \kappa_2)$ for $L > 100$ μm. Thus $k_\perp \propto \frac{1}{L}$, while c_x, c_z, k_x, and $k_z \propto \frac{1}{L^3}$, implying L should rather be small, provided $k_\perp$ does not exceed k too much.

The effect of the $\perp$-shape on the stiffness of the torsion beam for the given dimensions is shown in table 4.3. The $\perp$-torsion beam clearly has a large effect on stiffness in x direction and the rotation stiffness about the z axis, while the torsion stiffness only increases a factor 2.4. With an increase of 140 % in torsion stiffness, the driving voltage just needs to increase 55 %[3] to achieve the same stroke[4]. This means there really is improvement with respect to side pull-in (also see figure 4.12).

Table 4.3: Stiffness ratios for the $\perp$-torsion and the L-torsion beam.

ratio	$\frac{c_{x\perp}}{c_x}$	$\frac{c_{z\perp}}{c_z}$	$\frac{k_{x\perp}}{k_x}$	$\frac{k_{z\perp}}{k_z}$	$\frac{k_\perp}{k}$
$\perp$-torsion	136	2.04	2.04	136	2.38
ratio	$\frac{c_{xL}{}'}{c_x}$	$\frac{c_{zL}{}'}{c_z}$	$\frac{k_{xL}{}'}{k_x}$	$\frac{k_{zL}{}'}{k_z}$	$\frac{k_L}{k}$
L-torsion	35	1.1	1.1	35	1.71

Table 4.3 also shows the stiffness increase for the L-torsion beam. Accents are used to denote a "pseudo-stiffness" (see appendix B on page 176).

There are two parameters of which the influence will be further investigated, namely c and d. The first one, because it has most effect on the stiffness ratios $\frac{c_{x\perp}}{c_x}$ and $\frac{k_{z\perp}}{k_z}$. The second one, because it will be technologically more difficult to define d exactly. Furthermore, the influence of these parameters on the torsion stiffness ratio $\frac{k_\perp}{k}$ is interesting. Figure 4.10 shows graphs for the ratios $\frac{c_{x\perp}}{c_x}$, $\frac{k_{z\perp}}{k_z}$ and $\frac{k_\perp}{k}$ for respectively variation in c and d (width and thickness of the "horizontal parts"). While one parameter is varied, the other is kept at its value given in table 4.2. Also the results obtained in appendix B for the L-torsion beam are given in the graph.

Clearly, increasing c improves the stiffness even more, while the torsion stiffness does not increase dramatically. The size of c is limited by the chosen technology (see section 5.3). If d turns out larger due to technological uncertainties, the stiffness of the suspension does not benefit as much as for increase in c, however the torsion stiffness increases a lot. That has a negative effect on the driving voltage, which increases at given stroke. For this reason the second method for the suspension with an L-torsion

[3]For the L-torsion beam, the required increase of the driving voltage is just 30 %, since the increase in torsion stiffness is 70 % as is shown in table 4.3.

[4]The increase of the torsion stiffness reduces by reducing the thickness d of the horizontal beam parts. In the next chapter will be decided to make d equal to the initial comb-teeth overlap. A small overlap compromises a linear relation between the comb-drive force and the squared driving voltage.

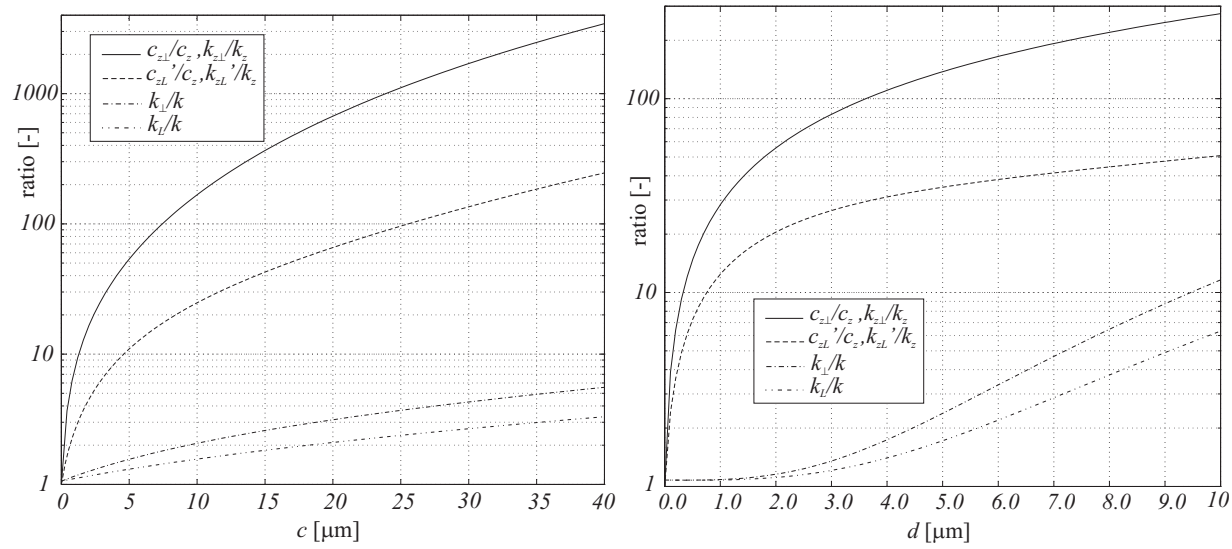

Figure 4.10: Stiffness ratios as a function of parameter c (a), and parameter d (b).

beam is investigated. By applying just one horizontal part, the torsion stiffness of the L-torsion beam is far less sensitive to the process variations in d.

The effect of an increase in d is visualized for both suspension methods in a plot of the displacement $s(u)$ against the driving voltage. Figure 4.11 shows this plot for d is 5 and 10 μm respectively and for the case of a rectangular torsion beam.

The required voltage for 20 μm displacement for the three kinds of torsion beams are found from the energy equation (4.4a). Assuming small β, the displacement is equal to the arm times β. The arm is taken equal to R added to halve of the tooth length l_t. This means the displacement is defined halfway the tooth. β is obtained by the quotient of the torque T_β and the torsion stiffness k for the given torsion beam. Differentiating E^* with respect to β, for constant α and u, results in the torque.

$$s(u,\alpha) = \left(R+\frac{l_t}{2}\right)\beta(u,\alpha) = \left(R+\frac{l_t}{2}\right)\frac{T_\beta(u,\alpha)}{k} = \frac{1}{k}\left(R+\frac{l_t}{2}\right)\left[\frac{\partial E^*}{\partial \beta}\right]_{u,\alpha} \tag{4.21a}$$

$$s(u,\alpha) = \frac{1}{k}\left(R+\frac{l_t}{2}\right)^2 \frac{n\,\varepsilon_0\,u^2}{2\,\alpha}\ln\left\{\frac{(d_t-\alpha\,R)(d_t+\alpha\,(R+l_t))}{(d_t+\alpha\,R)(d_t-\alpha\,(R+l_t))}\right\} \tag{4.21b}$$

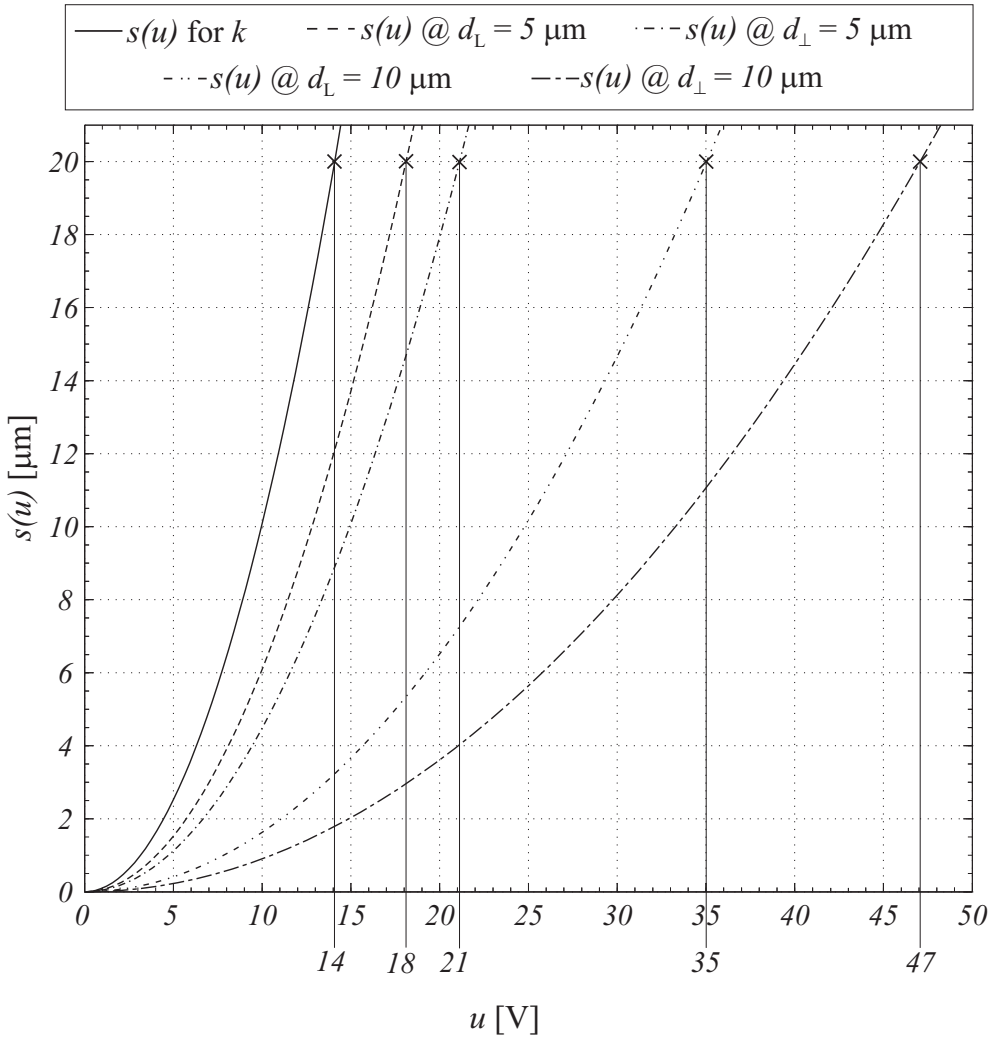

Figure 4.11: Displacement $s(u)$ as a function of the driving voltage for the rectangular torsion beam, and the $\perp$-torsion beam with d is 5 and 10 μm and for the L-torsion beam with d is 5 and 10 μm.

Figure 4.12 shows the absolute value of the stiffness-ratio of the electrostatic stiffness (k_α given in equation (4.5a)) and the rotational stiffness about z for the rectangular beam (k_z), the $\perp$-torsion beam ($k_{z\perp}$) and the L-torsion beam (k_{zL}), plotted against the driving voltage (u_n) *normalized* to the voltage required for 20 μm displacement for each particular suspension. k_z, $k_{z\perp}$ and k_{zL} are assumed to be constant. An error angle of 0.0002 rad is assumed (equal to an offset of 10% of the teeth spacing d_t). Curves for $k_{z\perp}$ and k_{zL} are shown for d is 5 and 10 μm.

In the shaded area the stiffness ratio is larger than one, which means the electrostatic stiffness is larger than the stiffness of the suspension so side pull-in occurs. As shown in the graph, no instability occurs for any of the torsion beams before a 20 μm displacement is reached. However, for the beam with rectangular cross-section, the

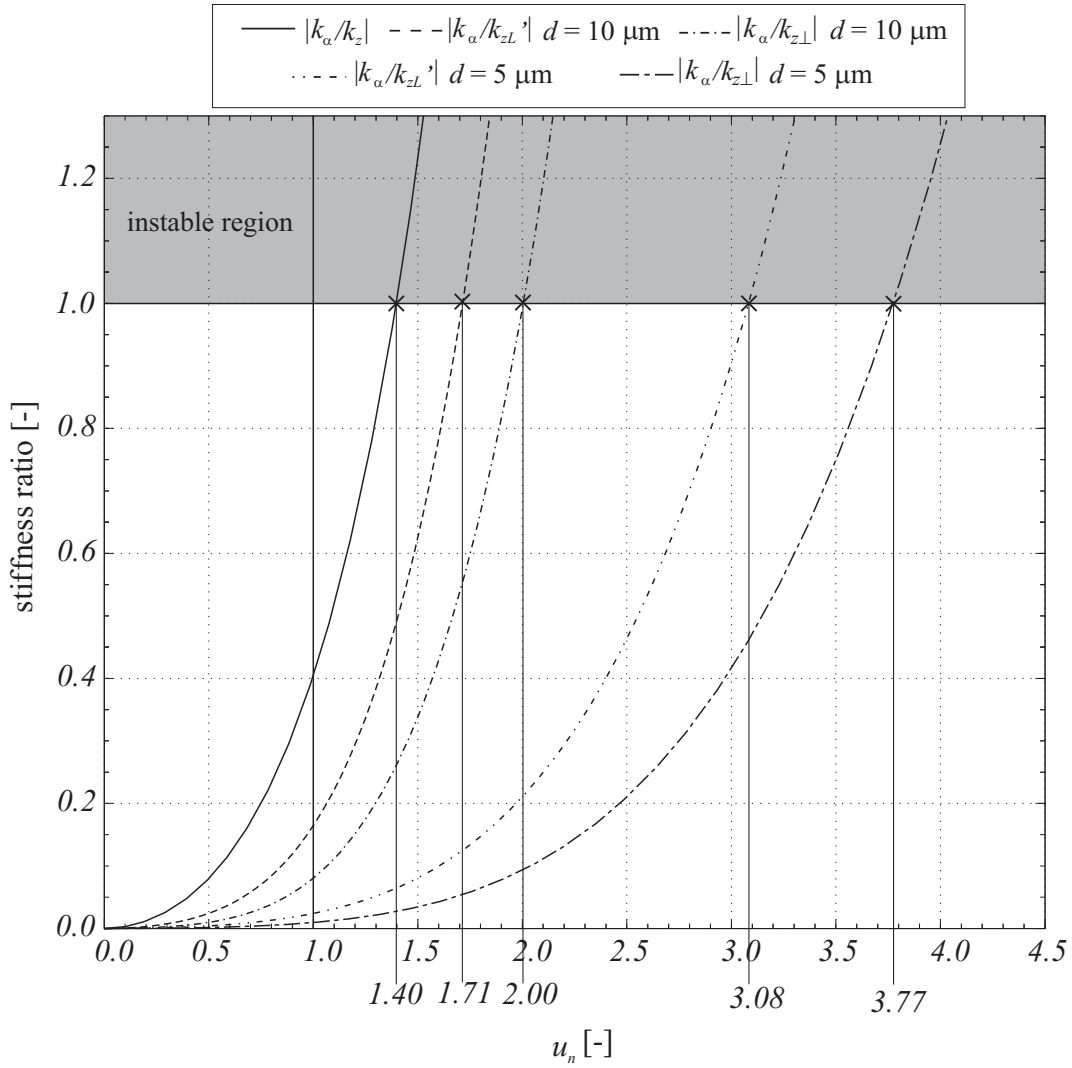

Figure 4.12: Ratio of electrostatic stiffness and rotational stiffness about z for d is 5 and 10 µm for α =0.0002 rad. Also the stiffness ratio for a torsion-beam with rectangular cross-section with L = 200 µm and L = 120 µm is shown.

margin before instability occurs is small. This implies, suspended by these rectangular beams, the comb-drive cannot drive much extra load without suffering from instability. The ⊥-torsion beam and the L-torsion beam have a margin of respectively 3.1 and 3.8 times the necessary driving voltage for a displacement of 20 μm. For a thicker d these margins decrease much since the required driving voltage has to increase.

4.4 Conclusion and discussion

A design is presented for a vertical comb-drive system with torsion suspension for kinematic constrained torsion motion, realizable in SCS for preferred mechanical

properties like low hysteresis and creep. Possible difficulties with assembly or residual stress as a result of material combinations are avoided. The design allows for 20 μm displacement at a relatively low driving voltage of typically 20 V, due to a very small gap between the comb-teeth and a sufficiently low torsion stiffness of the suspension. Following from the instability and stiffness analysis, a driving voltage up to at least 60 V (equivalent to a force of 0.2 mN at the comb-teeth) can be applied before side pull-in is expected. Therefore, it is likely the actuator is able to supply enough force to drive a flexure mechanism like for the out-of-plane stage as introduced in chapter 3.

The side pull-in stability is improved considerably by the special profile of the torsion beams. Two types of torsion beams are analyzed; one having a $\perp$-shaped cross-section and one having an L-shaped cross-section. The latter is far less sensitive to fabrication uncertainties in the thickness of the horizontal part of the torsion beam complex, since only one horizontal beam is applied, opposed to the two horizontal beams in the $\perp$-torsion beam. It was shown that the beam thickness is very determining for both the required driving voltage and the margin before side pull-in is expected.

Although the $\perp$-torsion beam is more sensitive for a larger d, it still performs better than the L-torsion beam with respect to the side pull-in margin. The performance of both beams can be largely improved by increasing c, while the torsion stiffness is not increased much. This, however, is conflicting with the fabrication process which limits the beam width c for successful release.

As discussed in appendix B about method 2 for the torsion suspension, a torsion beam with an asymmetric cross-section shows parasitic displacements if the forces and moments are not applied parallel to its primary axes of inertia. Furthermore, finding an analytical estimation for the stiffness values for the suspension with an L-torsion beam was challenging and probably introduces significant errors. Additionally *warping* effects often occurring in torsion beams are also not taken into account. For better predictions of the behavior of the torsion suspension in general, but especially for the L-torsion beam, non-linear FEM modelling is required.

References

[1] K. S. J. Pister, M. W. Judy, S. R. Burgett, and R. S. Rearing, "Microfabricated hinges.," *Sensors and Actuators A*, vol. 33, pp. 249–256, 1992.

[2] V. Milanović, "Multilevel Beam SOI-MEMS Fabrication and Applications," *J. MEMS*, vol. 13, no. 1, pp. 19–30, 2004.

[3] J.-H. Lee, Y.-C. Ko, B.-S. Choi, K.-M. Kim, and D. Y. Jeon, "Bonding of silicon scanning mirror having vertical comb fingers," *J. Micromech. Microeng.*, vol. 12, pp. 644–649, 2002.

[4] K.-H. Jeong and P. L. Luke, "A novel Microfabrication of a self-alinged vertical comb drive on a single SOI wafer for optical MEMS applications," *J. Micromech. Microeng.*, vol. 15, pp. 277–281, 2005.

[5] K. Jongbaeg, D. Christensen, and L. Lin, "Monolithic 2-D Scanning Mirror Using Self-Aligned Angular Verical Comb Drives," *IEEE Photonics Technology Letters*, vol. 17, no. 11, pp. 2307–2309, 2005.

[6] D. Hah, P. R. Patterson, H. D. Nguyen, H. Toshiyoshi, and M. C. Wu, "Theory and Experiments of Angular Vertical Comb-drive Actuators for Scanning Micromirrors," *IEEE Journal of Selected Topics in Quantum Electronics*, vol. 10, no. 10, pp. 505–512, 2004.

[7] J. M. Gere, *Mechanics of Materials*. Thomson Brooks/Cole, 6^{th} ed., 2004.

[8] K. E. Peterson, "Silicon Torsional Scanning Mirror," *IBM Journal of Research and Development*, vol. 24, no. 5, pp. 631–637, 1980.

[9] W. C. Young and R. G. Budynas, *Roark's Formulas for Stress and Stain*. McGraw-Hill, 7^{th} ed., 2002.

Chapter 5

Vertical comb-drive and torsion suspension: Fabrication and results.

Examples of 3D structuring found in literature are evaluated with respect to the requirements to fabricate the vertical comb-drive. As a result, it is decided to adapt to the process used for the planar 3 DOF manipulator to enable the required out-of-plane structuring. The geometry resulting from the fabrication is assessed and improvements to the design and process are proposed. Finally, a characterization of the devices is performed.

5.1 Introduction

In the previous chapter a vertical comb-drive system with ⊥- and L-torsion beam was introduced and analyzed. The system requires 3D structuring to realize the geometry of the vertical comb-teeth and the torsion suspension. Originally, the solution to improve the torsion suspension with respect to the stiffness for in-plane rotation and transversal displacement, consisted of one extra horizontal beam part added to a vertical torsion beam. In other words, the L-torsion beam. For this reason this chapter only deals with the L-torsion beam. However, the proposed process for 3D structuring and the assessment of the fabrication process would directly apply to a suspension with a ⊥-torsion beam as well.

Section 5.2 discusses the specifications for the fabrication process and gives an overview of common 3D process and their compatibility with the specifications. Sub-

sequently, the fabrication process used to realize the vertical comb-drive system is explained in section 5.3. The fabrication results and the device characterization follow in section 5.4. The conclusion and discussion close this chapter in section 5.5

5.2 Vertical structuring in MEMS

Vertical structuring in MEMS is not trivial; especially in case of structuring of the Si wafer itself. Two complex, well defined structures need to be fabricated. Firstly, the vertical comb-drive teeth, having a minimal overlap for linear-driving and allowing a 20 μm travel range. Secondly, the L-shaped torsion suspension, that has to consist of a vertical and horizontal beam.

Figure 5.1 shows a cross-section of the required vertical structures. Very important is the small value for d_t, in order to have a large force at relatively low voltage. Also the overlap height and the travel range are shown. Furthermore, the dimensions of the L-torsion beam are marked. Depending on the flexibility of the fabrication process, dimensions of the comb-drive teeth will coincide with dimensions of the torsion beam. For reduced complexity (at the cost of flexibility), the upper teeth height will be equal to b and the overlap will be the same as d.

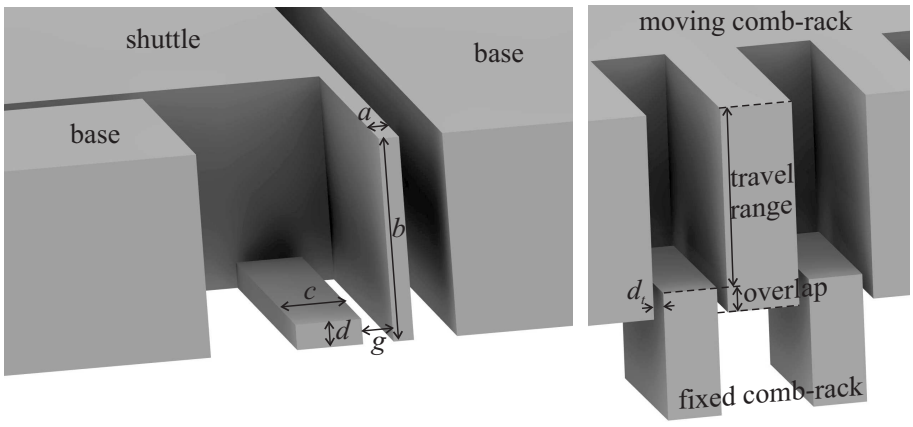

Figure 5.1: Cross-section through the required vertical structures.

A process is required that enables at least two different beam heights and an offset between beams for the comb-drive teeth. In literature various ways to define the offset are reported. Generally these can be categorized in post-processing and in 3D structuring based technologies. Post-processing involves various techniques like wafer-bonding, assembly, bending induced by thermal mismatch and plastic deformation. 3D structuring can be used directly to fabricate the system of single crystalline Si, without any additional modification, post-processing or use of other materials for

out-of-plane fixations. Below potential processes of both categories will be assessed with respect to the requirements for the vertical comb-drive.

5.2.1 Post-processing

Wafer-bonding is used in [1] to assemble a movable rack of comb-teeth on top of a fixed rack, to form a vertical comb-drive used for a scanning mirror. Wafer-bonding usually has a position resolution in the order of microns. This will require a larger space between the comb-teeth resulting in a larger driving voltage than is desired for our application. Furthermore, (rotational) offsets between the teeth potentially lower the side pull-in voltage.

Offset-fixation by assembly is used in [2]. Mechanical latches structured in poly-silicon and movable with hinges are used to fix the movable teeth rack in a offset angel with respect to the fixed rack. Although a very nice scanning mirror is reported, the process is complicated and most probably requires a lot of experiments and tuning before the desired functionality is obtained. It can be questioned if the stiffness of the latching is large enough to regard it as a fully rigid fixation. Furthermore, the assembly is not a batch process and thus very laborious.

Thermal mismatch as used in [3], adopts difference in thermal expansion between two different materials to obtain layer-stacks with built in stress. Once the stress is released, the structure (i.e. a suspension of a vertical comb-drive shuttle) will deflect in out-of-plane direction and an vertical offset is realized. This is a potentially interesting process, however it is expected that extensive modelling and experimentation is required to exactly predict the resulting vertical offset. Additionally the use of a stack of different materials in the suspension mechanism might compromise linear mechanic behavior of the device.

Plastic deformation of SCS is adopted in [4] to fix a rotational offset of a moving teeth-rack with respect to a fixed rack. This is very elegant technology, where the whole device is structured in 2D and the comb-shuttles are suspended by torsion beams. A second wafer is structured to form pillars and is used to push the comb-shuttles down and deflect their suspension beams. This occurs when the device wafer and the additional wafer are mated. The wafer stack is annealed at 900 °C to plastically deform the torsion beams and fix the offset. Afterwards the wafer with pillars is removed.

The process shows a relative simple method to obtain the offset. However it is not entirely clear if the mating of the wafers can cause any damage like mismatches

between the comb-teeth. For this reason the gap between the comb-teeth might be required to be larger than desired for our system. Furthermore, the L-shape is not obtainable without extra 3D structuring.

Non of the above discussed processes is entirely suited to fulfill the requirements for our system. Especially, non of the post processing options allows for various beam heights, while 3D structuring does allow for the required shape of the torsion beam.

5.2.2 3D structuring

Two different types of 3D structuring can be distinguished. One type is characterized by molding of poly-silicon in cavities made in SCS. The other type is characterized by directly structuring of the SCS wafer.

Molding is the key-technology in processes like HEXagonalSILicon [5], High Aspect-Ratio Combined Poly and Single Crystal Silicon (HARPSS) [6], and Molded Surface-Micromachining and Bulk Etching Release (MOSBE) [7]. In processes with poly-silicon molding there is usually a sacrificial silicon-oxide layer between the bulk Si and the poly-silicon. Once at the end of the fabrication this layer is etched, the poly-silicon is connected to the bulk via thin plates that lack stiffness. The MOSBE process is quite complicated and uses a relatively large gap between (some of) the comb-drive teeth for the exposure of the bulk $\langle 111 \rangle$ Si to perform a sacrificial bulk release (like in the SBM process discussed below). Furthermore, it should be taken into account, that the combination of materials can induce residual stress; a potential cause for non-linear mechanical behavior.

Sacrificial Bulk Micro-machining (SBM) as presented in [8], employs high aspect-ratio DRIE and the anisotropic etch-rate of Si in an alkaline etchant. Using an $\langle 111 \rangle$ wafer, structures with protected side-walls can be undercut and released while etched in KOH. Although a process offering potential mechanical design-freedom, the method to obtain the required sidewall protection structure for the comb-teeth does not allow for a small enough gap between the teeth.

Single-Crystal Silicon Etching and Metallization (SCREAM) i.e. used in [9] makes use of high aspect-ratio DRIE, side-wall protection with silicon-oxide and RIE isotropic under etching. The structures are metallized afterwards for electric powering of the devices. The SCREAM process does not allow for various beam heights, without modifications to the process.

A SCREAM-like process discussed in [10] also adopts isotropic under-etch and enables the structuring of vertical comb-teeth with a teeth spacing of 2 μm. However this process cannot directly be applied to structure the L-shaped torsion suspension.

Multilevel Beam SOI-MEMS process allows for high aspect-ratio etching from both the top- and the bottom-side of the wafer, by embedding a mask in the insulation layer of a custom-made SOI wafer [11]. The Multilevel Beam process is best suited for all the necessary beam structures. However, the required front to back alignment does not allow for a very small gap between the comb-teeth (6 μm was reported). Unfortunately the custom-made SOI wafer is not trivially made. We carried out some experiments generally following the same procedure as in [11]. A thermally oxidized Si wafer with structured oxide was bonded to a Si wafer after thorough piranha cleaning. Annealing was performed in a nitrogen environment at a temperature of 1100 °. After that, the top wafer had to be ground to the device height. The grinding of the set of bonded wafers appeared to be problematic. The adhesion to the structured oxide layer was insufficient to endure the grinding. It was concluded that this custom-made SOI wafer fabrication needs careful process development. For this reason another solution, where use is made of process-steps more common to our experience was looked for.

5.3 Fabrication Process

A very successful process for bulk micro-machining of planar mechanisms is used in [12] (also see chapter 3 on page 63). It is comparable to the SCREAM process. Instead of silicon-oxide or -nitride pasivation, in this process use is made of fluor-carbon to protect the side walls of high-aspect ratio structures. Alike in the SCREAM process the protected structures are undercut and released by dry isotropic etching with SF_6. However, this release can be performed directly after the Bosch high-aspect ratio DRIE etch step in the same reactor. For electric insulation the process makes use of trenches refilled with insulating material like low stress silicon rich silicon nitride (SiRN).

The insulation trenches are etched first and subsequently filled with SiRN by low pressure chemical vapor deposition (LPCVD). SiRN is removed from the top- and bottom-side of the substrate and the mask for the device structures is applied. This mask incorporates etch-holes used for the dry release step. In figure 3.11 on page 63 a region of Si with etch-holes, which is electrically isolated from the bulk, is shown. It can serve as a probe pad for electrical connections. Similarly, electrical leads can be structured in the SCS. From the pad a flexure beam starts that can serve as suspension and electrical connection for e.g. a free to move comb-drive shuttle. The insulation

trenches can also be applied in this shuttle to define regions having different electrical potentials.

This process is simple and convenient for the design of mechanical systems in SCS. Unfortunately it lacks structuring in height. To enable multiple beam heights the process needs modification. The difficulty of processing 3D structures lies in the fact that the mask for making various beam heights need to be latently present when the beams are tailored in their height direction. Since after etching of high aspect-ratio structures, lithography is generally not possible.

5.3.1 Vertical structuring

This problem is solved by deep oxidation of all the silicon that has to be removed to obtain a beam of a specific height. The silicon-oxide can be etched away at the end of the process. Deep oxidation is possible when high aspect-ratio trenches are etched in the silicon and the walls between the trenches are completely oxidized [13]. The oxidation is performed where beams have to be reduced in height, thus in figure 5.1 this is the lower comb-drive tooth and the horizontal part of the L-torsion beam.

The lower comb-drive teeth are required to be exactly between the two spacings d_t of 2 μm wide. To accomplish this, the mask for the comb-drive spacings and that for the oxidized trenches should be self-aligning. Here self-alignment is obtained by the use of one mask for the trenches for the deep oxidation combined with the *inverted* mask for the spacings. This mask is transferred into a layer of SiRN, and the openings for the deep oxidation trenches are selectively exposed to be able to etch the trenches. After that the oxidation is performed and oxide is growing everywhere, except where there is SiRN (local oxidation of silicon or LOCOS, also see page 111). After stripping the SiRN the deep oxidized structures are combined with an oxide mask defining the comb-drive spacings. In figure 5.2 the procedure for self-alignment is depicted. The total process will be discussed later in this section.

5.3.2 Oxidation design rules

The design rules for the deep oxidation structures are as follows. First of all, thermal oxidation of Si consumes material to form SiO_2. If 1 μm of oxide is formed (t_{Ox}), 0.44 μm of Si is consumed (t_{Si}). Figure 5.3 *on page 108* shows a top-view of a deep oxidation structure. To the left three trenches in Si are shown. Next to that dashed lines show the contours within which the oxide is formed. Finally the resulting oxide structure is shown. In equation (5.1) the relation between the dimensions from figure 5.3 are given for the case where the Si walls will be completely oxidized. There are limitations to the thickness of the grown oxide; in this case 5 μm. The minimal feature size of the mask-

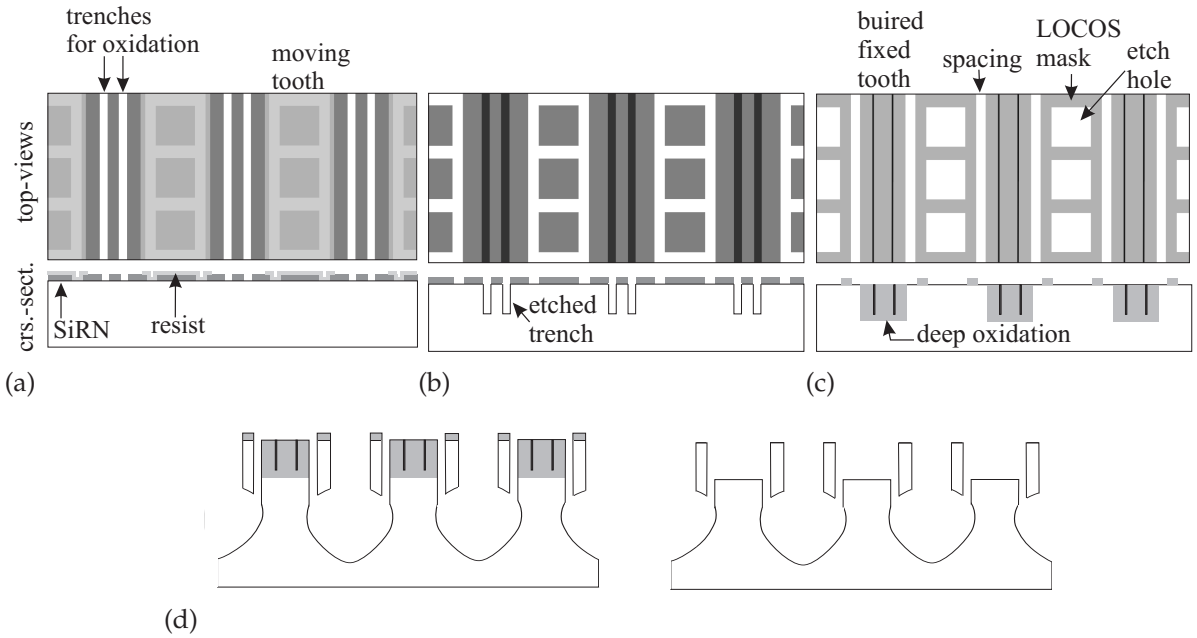

Figure 5.2: Self-alignment of comb-drive teeth spacing and oxidized trenches. Top-views in the top row, cross-sections in the bottom row (a, b and c). (a): SiRN mask with trench-openings for oxidation and inverted mask for teeth of the translating part. Resist protects these teeth. (b): Trenches are etched by Bosch etching and resist is removed. (c): Trench-walls are oxidized together with the uncovered Si. Herewith the mask for the translating teeth is formed by LOCOS and the deep oxidation structures covering the stator teeth are created. The teeth spacing is defined between the edge of the translating teeth and the deep oxidation. (d): Via the etch-holes, dry etching releases the structure after which all the oxide structures are etched.

plate (here 2 μm) defines the minimal trench width. It is profitable to minimize the Si wall thickness ($2\,t_{Si}$) to reduce the oxidation time for complete oxidation. The values of w_t and t_w are the dimensions on the mask ($w_{t,m}$ and $t_{w,m}$) including errors like under-etch (w_{err}). Furthermore, a gap with width w_g might remain after oxidation, which can be filled with LPCVD TEOS depending on the fabrication requirements. The depth of the resulting oxidized structure will be deeper than the original trench; t_{Si} is added to the initial trench depth.

$$\left.\begin{aligned} w_t + t_w &= w_g + 2\,t_{Ox} \\ t_{Si} &= \frac{t_w}{2} = 0.44\,t_{Ox} \end{aligned}\right\} \quad t_{Ox} = \frac{w_t - w_g}{1.12} \tag{5.1a}$$

$$\Rightarrow \quad t_w \approx 0.786\,(w_t - w_g) \tag{5.1b}$$

$$\begin{aligned} w_{t,m} &= w_t - w_{err} \\ t_{w,m} &= t_w + w_{err} \end{aligned} \tag{5.1c}$$

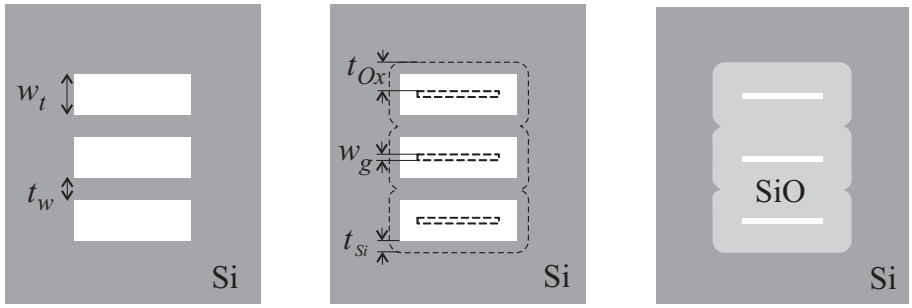

Figure 5.3: Design rules for deep oxidation. Top-view of deep oxidation trenches etched in Si (left), contours within which the oxide will be formed (center), the resulting deep oxidized structure (right).

5.3.3 Process overview

Figure 5.4 shows an overview of cross-sections of the fabrication process. Like in the process of [12] , first the 40 μm deep insulation trenches are etched in highly doped $\langle 100 \rangle$ Si (figure 5.4 a)) and filled with SiRN. The SiRN is stripped from the top and bottom and a new SiRN layer of 500 nm thick is deposited by LPCVD. After that a 500 nm thick TEOS layer is deposited by LPCVD which protects the SiRN during etching of the trenches for deep oxidation (figure 5.4 b)). Both TEOS and SiRN are structured to form the inverted mask for the device structuring (figure 5.4 c)). Then a photo-resist mask is applied that only uncovers the mask-features for the deep oxidation trenches and these trenches are etched by Bosch etching to a depth of 29 μm (figure 5.4 d)). Subsequently, the resist is removed, the TEOS is stripped in HF, the SiRN is removed from the backside (figure 5.4 e)) and the LOCOS and deep oxidation takes place in a wet oxidation quarts tube oven at 1150 °C (figure 5.4 f)). During this step the positive device mask is formed in a 2 μm thick SiO_2 layer. Failing to remove the SiRN from the back-side will cause the wafer to curve due to the compressive stress of the thermal oxide. The SiRN is etched by RIE, while also the SiO_2 layer is thinned (etch selectivity of about 0.7). Now the wafer is covered by an oxide mask (figure 5.4 g). At this point the combination of directive Bosch etching (37 μm deep) and isotropic release is performed as in [12] (figure 5.4 h)). Since the side-walls of the fixed comb-teeth are not protected, erosion will occur as a consequence of the isotropic release. A process modification to prevent this erosion will be presented in section 5.4.1 on page 122. Finally, the fluor-carbon remaining after the directional and release etch is stripped in a oxygen-plasma and all the remaining oxide is stripped in HF followed by freeze-drying to avoid sticking of the free-hanging structures [14](figure 5.4 i)).

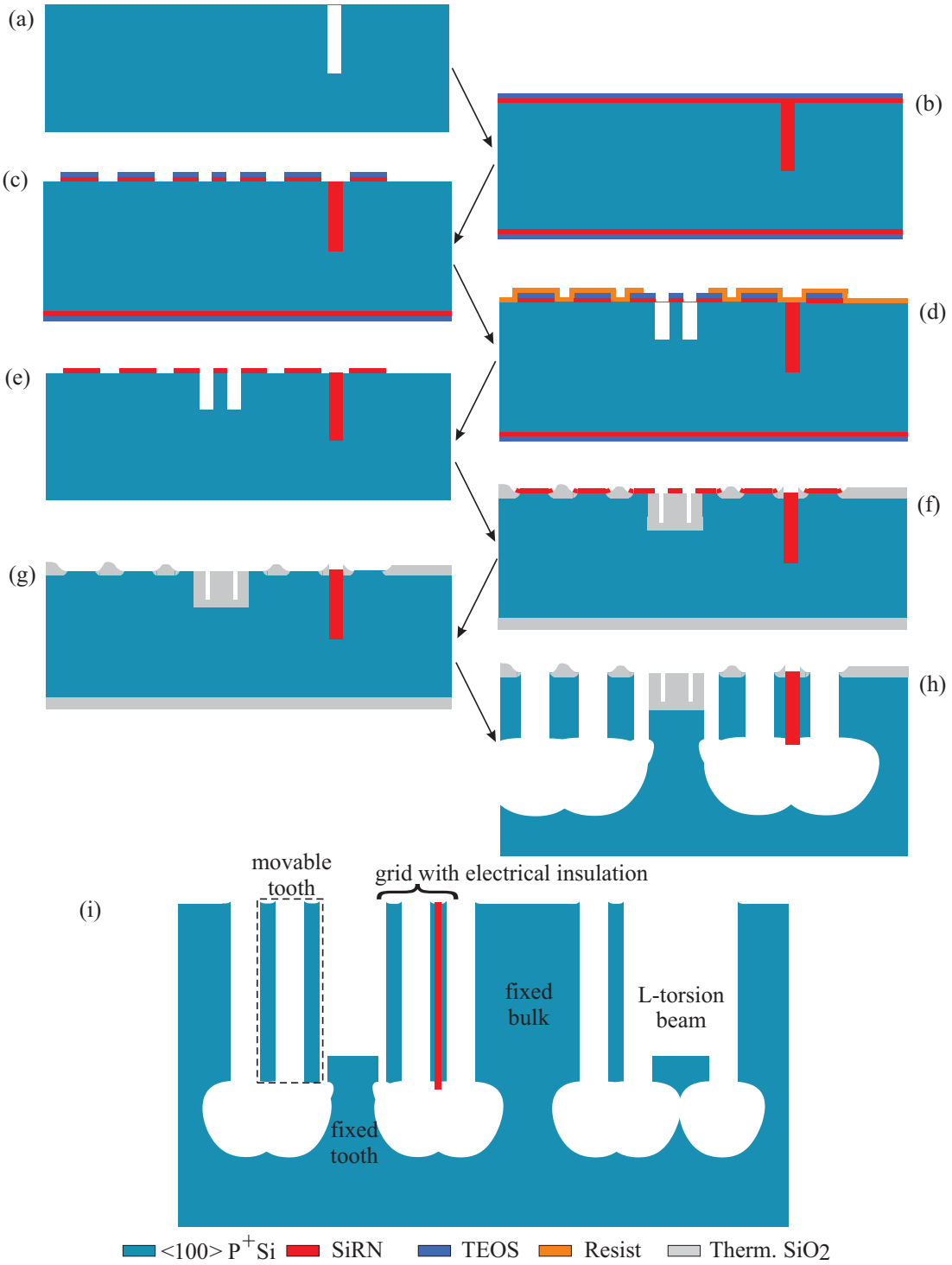

Figure 5.4: Process overview.

5.4 Fabrication results and characterization

The results of the fabrication will be discussed with respect to the geometry resulting after various fabrication steps and with respect to the characterization of the device itself. The fabrication results are discussed in section 5.4.1 and the characterization is discussed in section 5.4.2.

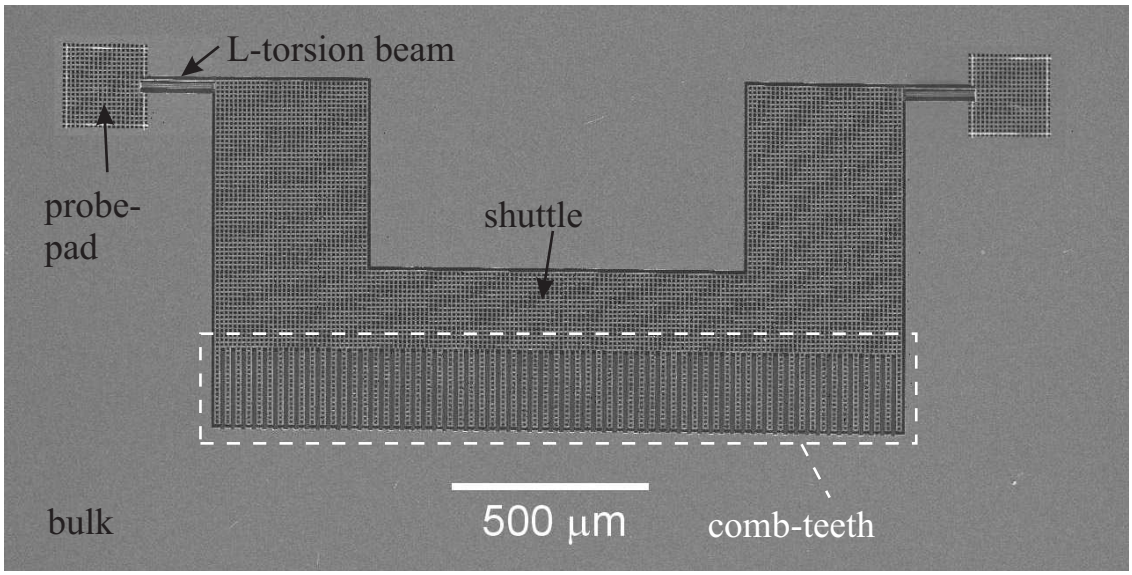

(a)

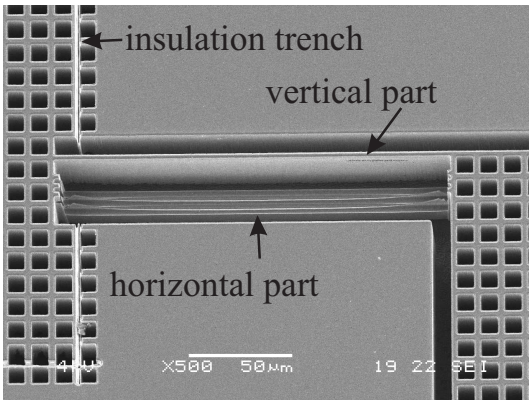

L-torsion beam

(b)

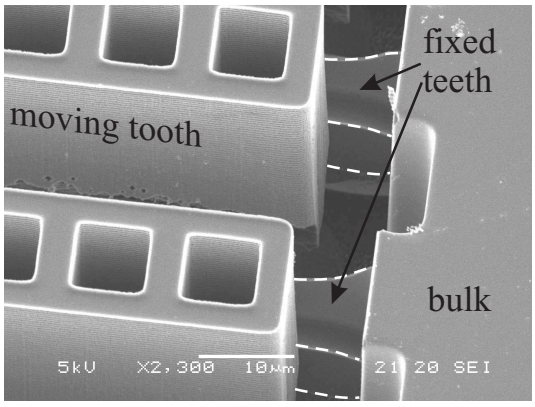

comb-teeth

(c)

Figure 5.5: SEM pictures of the vertical comb-drive. (a): picture of the top-view of a vertical comb-drive, (b): picture showing a tilted view of the L-shaped torsion beam, (c): picture showing a tilted detail of two moving comb-teeth and two buried fixed comb-teeth.

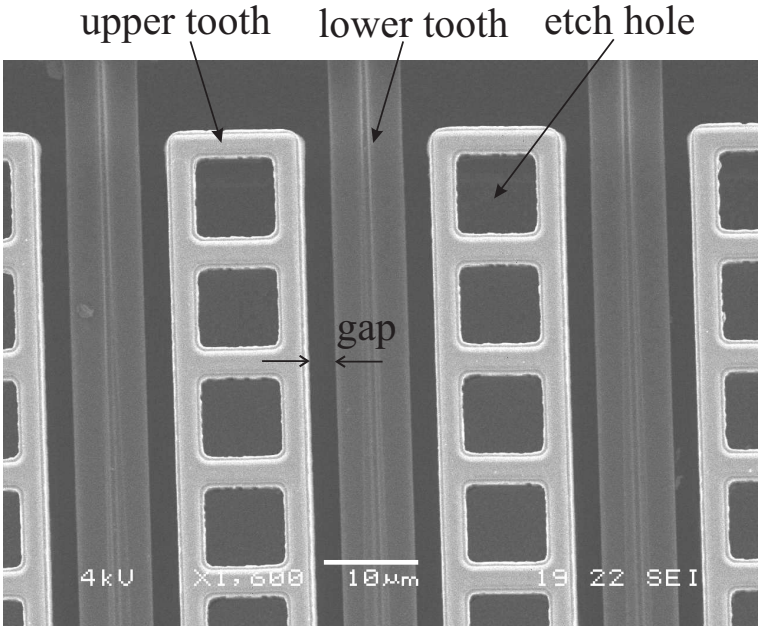

Figure 5.6: Top-view of the vertical comb-drive teeth.

5.4.1 Resulting geometry

Figure 5.5 shows SEM pictures of the fabricated device. Most of the required geometry is realized with the described process. Moreover, the compatibility with the process used in [12] is a fact, since the 3 DOF manipulator discussed in chapter 3 was successfully fabricated in this extended process as well. However, there is room for improvement. Especially concerning the geometry of the lower comb-drive teeth, the horizontal section of the L-torsion beam and the functioning of the electrical insulation trenches. The consequences of the fabrication steps on these geometrical structures will be discussed below.

LOCOS self-aligned mask The LOCOS self-aligned mask as shown in figure 5.2 on page 107 is applied to obtain a gap between the comb-teeth of about 2 μm, even though the lithography does not allow for mask alignment on this small scale. The requirement for such a small gap followed from a preferred low driving voltage of about 30 V. Figure 5.6 shows an SEM picture of the top-view of the vertical comb-drive teeth. The gap is highlighted and comparing it to the scale-bar, a size of 2.8 μm can be deduced. The gap-size is larger than 2 μm. The final gap-size is defined by the LOCOS oxidation and the erosion of the mask during stripping of the SiRN after LOCOS oxidation and etching of the silicon structure in the final stage.

Figure 5.7 (left) shows an SEM picture of a cross-section of trenches etched by

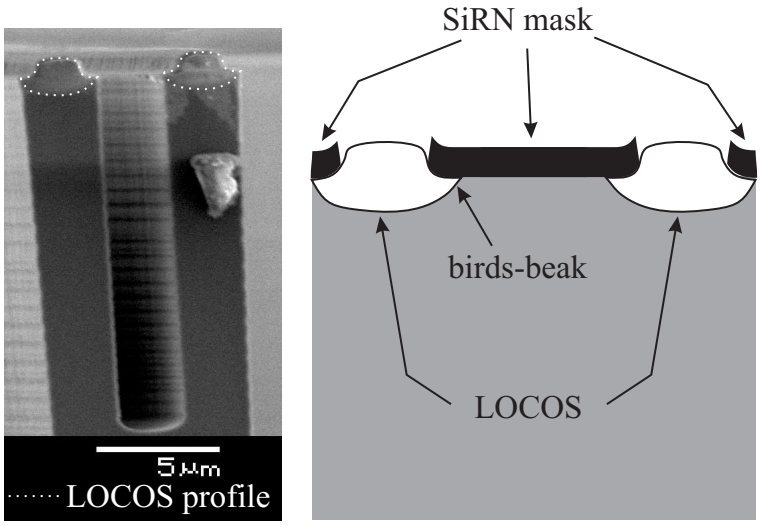

Figure 5.7: SEM picture of a cross-section of Bosch etched trenches through a LOCOS mask (left), schematic cross-section showing the SiRN mask and the LOCOS mask with bird's beak (right).

Bosch etching through a LOCOS mask. The profile of the LOCOS mask features is highlighted with a dashed line. Figure 5.7 (right) shows a schematic cross-section of LOCOS oxidized Si and the SiRN mask. SiRN masks the Si from being oxidized, but at the etches of the SiRN mask, the oxidation protrudes under the SiRN. This protrusion is known as a "bird's beak" [15]. After the SiRN is stripped, the size of bird's beak determines the openings in the LOCOS mask. However, since the tip of the bird's beak is thin, the original length of the bird's beak reduces because of erosion during stripping of the SiRN by RIE. Furthermore, the bird's beak will erode during the Bosch etching of the silicon structure. As a result, both the extension of the bird's beak under the SiRN during the LOCOS oxidation and the erosion during etching should be investigated more thoroughly to predict the resulting size of the mask opening.

Stripping of the SiRN mask was eventually intended to be done by etching in H_3PO_4 at 180 °C. This alternative would not have attacked the LOCOS oxide as much as RIE. However, the combination of LOCOS oxidation with the already present SiRN filled trenches for electrical insulation, lead to complications.

Figure 5.8 shows a micrograph of the top-view of a detail of the LOCOS mask. A detail of the vertical comb-drive shuttle is shown where it is attached to the L-torsion beam. The anomalous areas do not entirely strip in H_3PO_4. Apparently, these areas do not only consist of SiRN. The anomalous areas are explained by growth of SiO_2 under the SiRN. Although, normally this does not occur in that amount, the SiRN apparently was lifted during the oxidation process. After inspecting many areas on the wafer it was observed that anomalies occur only where platelets of SiRN are

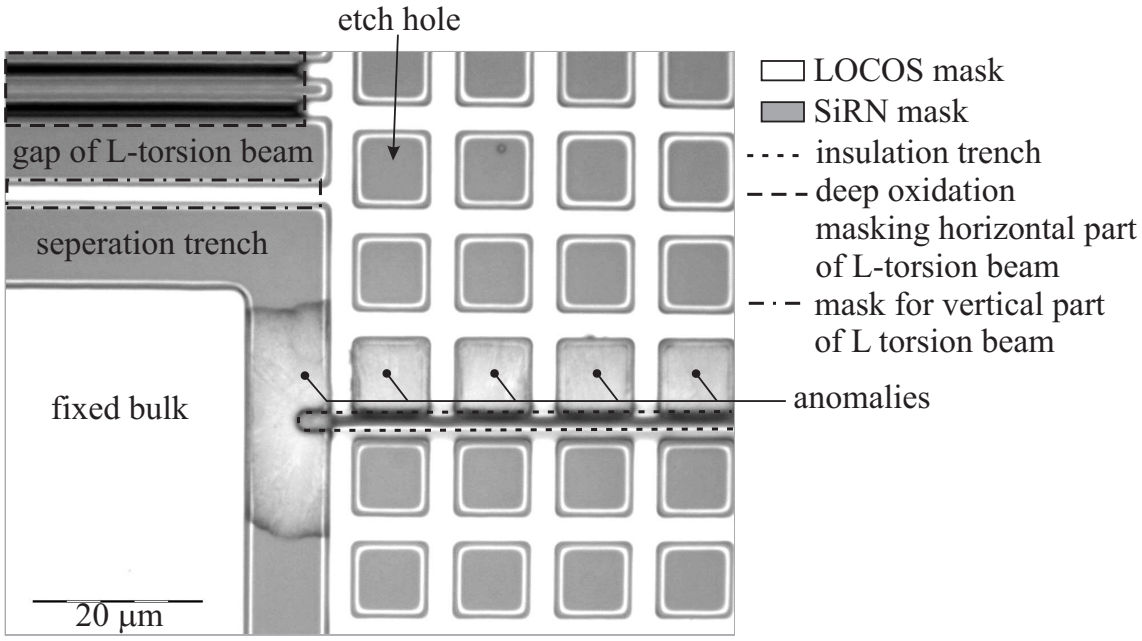

Figure 5.8: Micrograph showing the top-view of a detail of the LOCOS mask and anomalies.

located on top of insulation trenches. During wet oxidation at 1150 °C the SiRN filled insulation trenches lift up and with those the SiRN mask platelets are lifted, allowing oxide to grow under the SiRN plates. The cause for lifting might be the formation of oxinitride on top of the SiRN during the wet oxidation. Oxinitride shows compressive stress and expands.

By using RIE etching to etch the SiRN, the SiO_2 in the anomalous areas is removed as well. Although, the oxide of the LOCOS mask is thinned during this step, the thickness is sufficient to serve as a mask for the Bosch etching and release of the mechanical structure.

LOCOS mask and Bosch etching There are two ways the LOCOS mask has influence on the result of Bosch etching. Firstly, compared to a photo-resist mask, the profile can show a more negative taper for equal settings of the etching system. Photo-resist introduces a larger carbon concentration in the reactor increasing the deposition of fluor-carbon during the ”passivation” cycle. Since this larger carbon concentration is absent in case an oxide mask is used, less fluor-carbon is deposited. A second influence of the LOCOS mask is caused by the erosion of the bird’s beak. As the etching goes on, the mask opening increases by the erosion, resulting in a more positively taper of the etched trench. Both effects require to be investigated to larger extent.

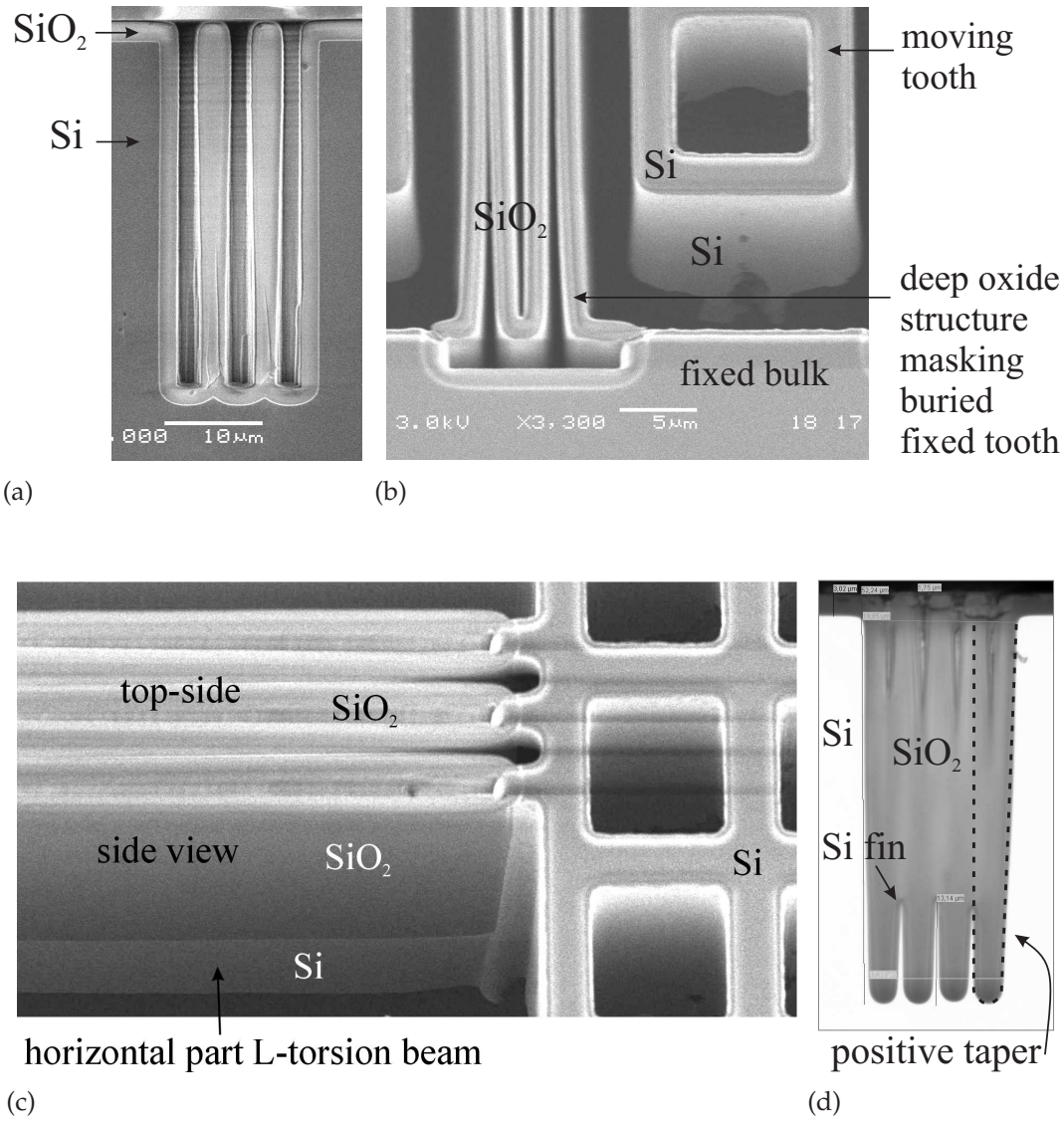

Figure 5.9: Pictures of deep oxidized structures. SEM picture of a cross-section through oxidized trenches (a), SEM picture of the deep oxidation structure masking the buried fixed comb-teeth (b), SEM picture showing a tilted view of the deep oxidation structure masking the horizontal part of the L-torsion beam (c), and a micrograph showing the cross-section of deep oxidized positively tapered trenches (d).

Deep oxide structures Figure 5.9 shows three SEM pictures and one microscope image of deep oxide structures. The first picture (figure 5.9a) shows a cross-section through three completely oxidized trenches. Picture two (figure 5.9b) shows a tilted view of a deep oxidation structure masking the buried comb-tooth. The third picture (figure 5.9c) shows a tilted view of the oxide block masking the horizontal part of the L-torsion beam. In these last two mentioned pictures, the oxidation was not entirely complete. The remaining silicon between the oxidized trenches was etched together

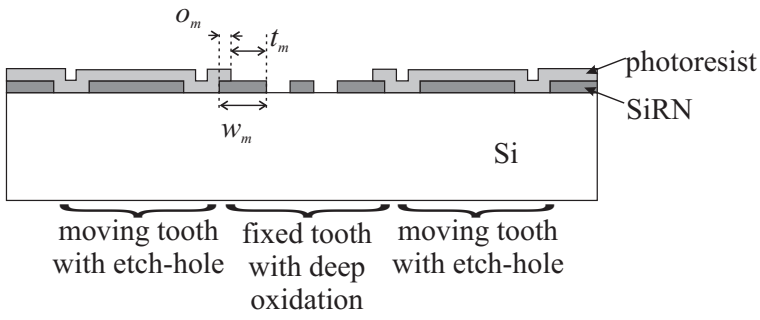

Figure 5.10: Schematic cross-section showing the alignment of the third mask with respect to the trench openings for the deep oxidation trenches. Below the drawing, the structures that eventually will be formed are indicated

with the mechanical structure of the device. The oxidation should have taken longer to completely oxidize the trench walls. The thickness of the trench walls was calculated with equation (5.1) on page 107 for an under-etch of 1 μm as was found from earlier etching experiments. In this specific situation the under-etch apparently is less and should be determined anew.

Aside from the oxidation time and the correct dimensions, one other aspect determines wether the trench-walls are completely oxidized, namely the tapering of the trenches. The trenches in figure 5.9a have an almost straight profile. Trenches with a negative profile are also suited for complete oxidation. However, if the profile is positive, the lower part of the trench walls will hardly oxidize completely. Figure 5.9d shows trenches with positive taper that are almost entirely oxidized. Since the former trenches are already blocked by oxide, no diffusion of O_2 occurs anymore and the remaining silicon fins of the trench walls will not be oxidized.

Another issue concerning the fabrication of the deep oxide structures is related to the lithography for the oxidation trenches. The exposure of the mask for these trenches, as illustrated in figure 5.2 (left) on page 107, turned out to be a critical alignment step. Figure 5.10 shows a schematic cross-section of the mask-stack, where the third mask is aligned to the trench openings for the deep oxidation trenches in the second mask (the first mask defined the electrical insulation trenches and is not shown). Important dimensions for the alignment are indicated; the mask-width defining the outer trench walls in the second mask w_m, the overlap of the third mask and the second mask o_m, and the tolerance between the openings in the second and the third mask t_m. Overlap and tolerance are always required since the alignment procedure has limited accuracy. In our case an EVG 620 mask align-system is used where alignment errors below 2 μm over the entire wafer is quite a challenge (including errors resulting from rotational mismatch).

The relation between the dimensions is as follows:

$$w_m = o_m + t_m \tag{5.2}$$

The masks are designed such that w_m is 4 μm, o_m is 1 μm and t_m is 3 μm. So by choosing a large enough tolerance, the error is made to neglect the requirement for enough overlap. This resulted in damage to the vertical comb-teeth due to alignment errors for devices at the edge of the wafer. A better choice would be to have equal sizes for tolerance and overlap, which would result in 2 μm. Increasing w_m is not desired since this dimension also defines the width of the gap between the comb-teeth (taking into account bird's beaks of 1 μm at both sides, a 2 μm gap remains). Summarizing, it is fair to say this alignment step is at the edge of what is possible with our lithography. Smaller sizes for the gap between the comb-teeth than achieved here are very, very challenging with our lithographic equipment.

One last remark should be made with respect to the used of deep oxidized structures in a mechanical device. Occasions of buckling in the vertical part of the torsion beam have been observed after the device was etched free, but before the etching of the oxide. Thermal oxide shows compressive stress. After the device is etched, the relatively compliant grid structure provides the oxide a possibility for stress release. As a result the beams in the grid deform and might exert a compressive force on the vertical part of the L-torsion beam, causing it to buckle. After the oxide is etched, the stress is released and the buckling is not observed anymore. No observable evidence of plastic deformation is found, nevertheless effects on the silicon structure or on the silicon crystal as a result of the stress in the oxidized structures cannot be ruled out [16]. This and the possible consequences have to be studied in more detail.

ARDE and loading As discussed in chapter 2 on page 29 and chapter 3 on page 65 the etch-rate of DRIE processes depend of the size and shape of the mask openings. Generally the etched feature resulting from a larger opening will etch faster than the one resulting from a smaller opening. On the one hand this is caused by the difference of aspect-ratio (ARDE) on the other hand by the difference in exposed Si. Despite the efforts to design the mask with openings of comparable sizes, ARDE and loading will be of influence.

An example of dealing with ARDE and loading in the design is shown in figure 5.11. The width of the long-stretched gap between the comb-teeth and the square etch-holes in the moveable teeth differ a factor 3 to 4 in size. However, since the gap is long-stretched and the holes are square shaped, the difference in etch-rate is not that large. As a result after etching with the standard Bosch process to a depth of 40 μm, the holes are only 10 % deeper than the trench forming the gap.

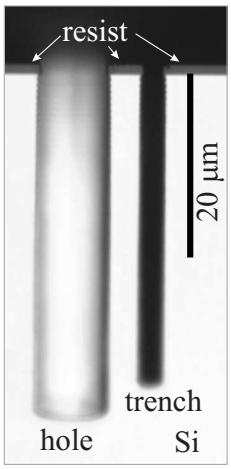

Figure 5.11: Micrograph of a cross-section through an 8 µm wide square hole and a 3 µm wide trench showing the loading effect.

Isotropic release etch After the mechanical structure is etched deep into the silicon by Bosch etching, the isotropic release is started. As discussed in chapter 3 on page 63 the side walls of the structures are protected by an extra layer of fluor-carbon before the release starts. The thickness of the deposited fluor-carbon is, among other things, a function of the aspect-ratio of the structures. Since diffusion is dominant, for high aspect-ratios the deposition is less. The thickness of the fluor-carbon posses a limit to the time the release etch can last without damage to the side-walls. However if the time is too short, the release is not completed.

Another issues concerning the release etch are ARDE and loading. A reduced depth due to ARDE or loading causes the isotropic etch to start at a smaller depth than required. This is a potential cause for damage as well. Also depending on aspect-ration are the profile and size of the isotropic under etch. Although the release is referred to as isotropic, the etch-rate is not purely equal in all directions. A large aspect-ratio will cause a more stretched shape, while a smaller aspect-ratio results in a bigger, more spherical profile.

Figure 5.12 on page 118 shows a cross-section of four trenches with decreasing aspect ratio. The development of the profile from stretched to more spherical is clearly visible, together with an increased dependence of the crystal orientation for wider trenches. The right most two trenches show an artifact at the bottom caused by reduced etch-rate due to fluor-carbon residue. The residue results in case the directional etch-step to strip the extra deposited fluor-carbon from the bottom of the trench was not sufficient.

For a successful isotropic release, both robust mask design and process-control are important. However the exact limits of the process capabilities, especially with respect to 3D structuring, are not yet known and require further research.

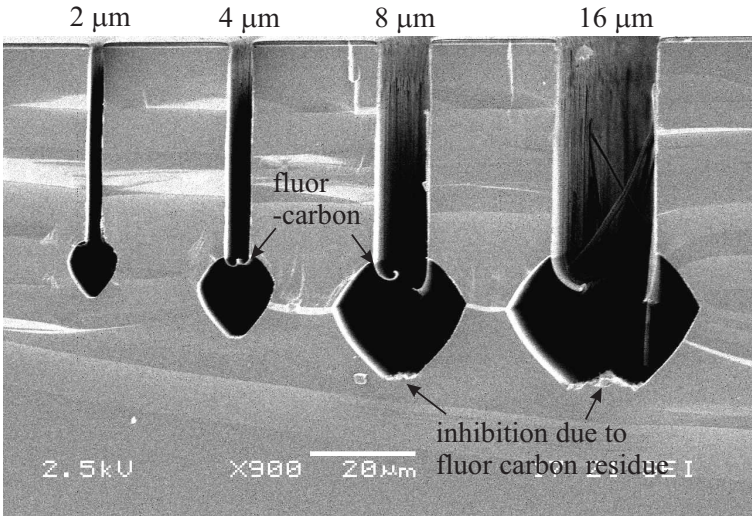

Figure 5.12: SEM picture of a cross-section of four trenches with decreasing aspect-ratio and the resulting isotropic profile.

The consequences of the isotropic release etch for the desired geometry are shown in figure 5.13 and figure 5.16 on pages 119 and 120 respectively. Figure 5.13 shows a detail of the L-torsion beam. Three geometric issues related to the isotropic release can be identified. Firstly, the grooves in the horizontal part of the L-torsion beam. These grooves result by the isotropic etch because the deep oxidation did not take long enough to completely oxidize the oxidation-trench walls. Secondly, the end-face where the horizontal beam is connected to the electrical probe-pad. A frontal view of this end-face is given next to the main picture. This damage is related to the mask design and will be explained later. The third issue is situated at the bottom of the fixation of the horizontal beam to the probe-pad and is indicated with the label "weakening". This issue is caused by loading.

The weakening is explained by figure 5.14 showing a schematic top-view and cross-section (A-A) of the attachment of the L-torsion beam. The cross-section makes clear that, a reduced depth of the etch-hole compared to the depth of the clearance around the torsion beam is the cause for erosion of the beam-attachment during isotropic etching. The thickness of the attachment is much reduced.

The side face damage is explained by figure 5.15 (left) showing a top-view of the mask-stack that defines the oxidation trenches for the torsion beam. The overlap (o_m) between mask 2 and mask 3 is required to safely align mask 2 to mask 3. As a consequence of the overlap the two small shaded squares (part of mask 2) will eventually be exposed to the directional Bosch etch and the isotropic release. To prevent this from happening, the shaded areas should be removed from mask 2 as shown in figure 5.15 (right).

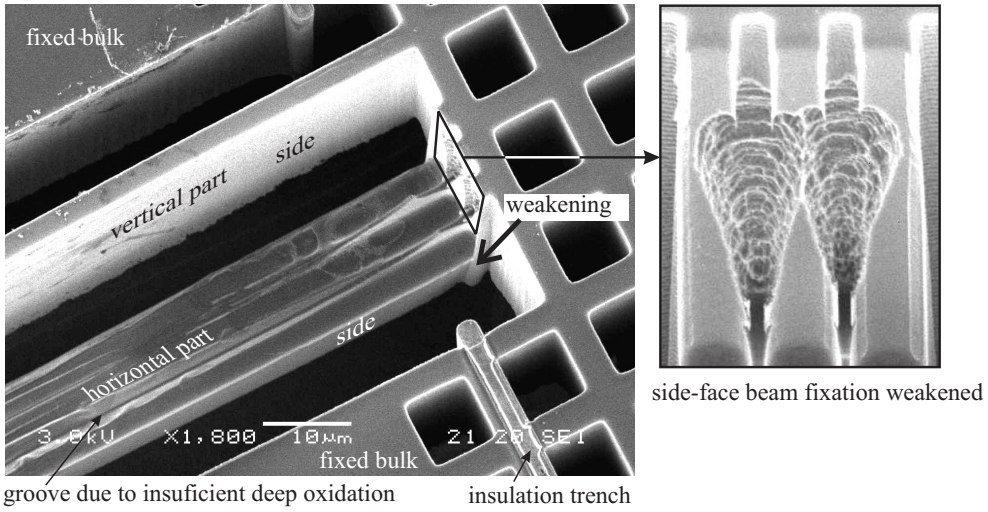

Figure 5.13: SEM picture showing a tilted view of a detail of the L-torsion beam and its fixation to an electrical probe-pad.

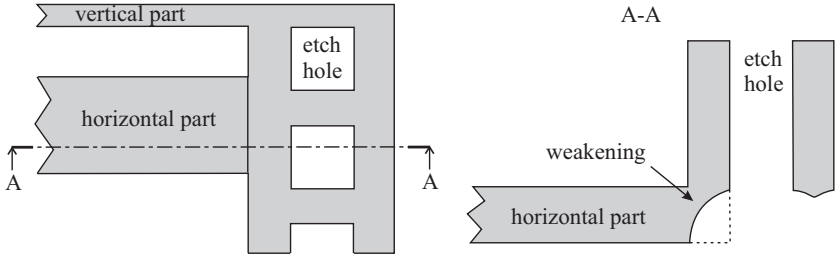

Figure 5.14: Schematic top-view showing the attachment of the L-torsion beam indicating cross-section A-A (left). Cross-section A-A showing the weakening in the attachment of the horizontal part (right).

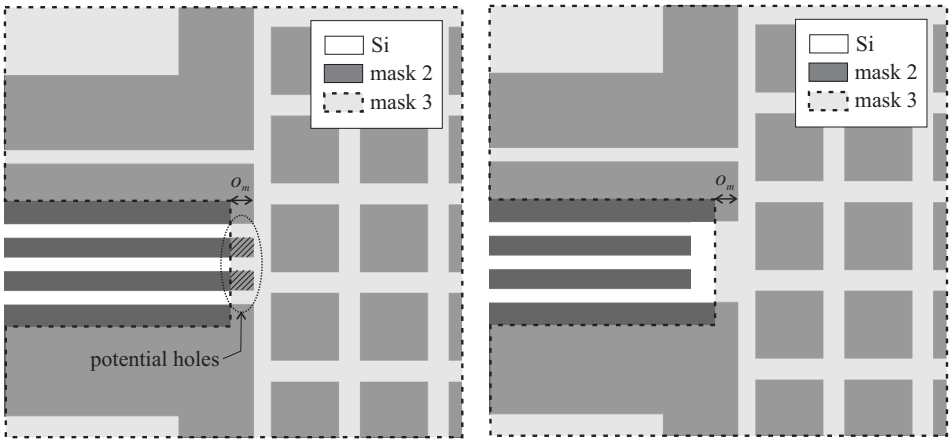

Figure 5.15: Top-view of the mask-stack defining the oxidation trenches for the L-torsion beam. The overlap between mask 2 and mask 3 (transparent) is marked as o_m (left). Correction applied to mask 2 (right).

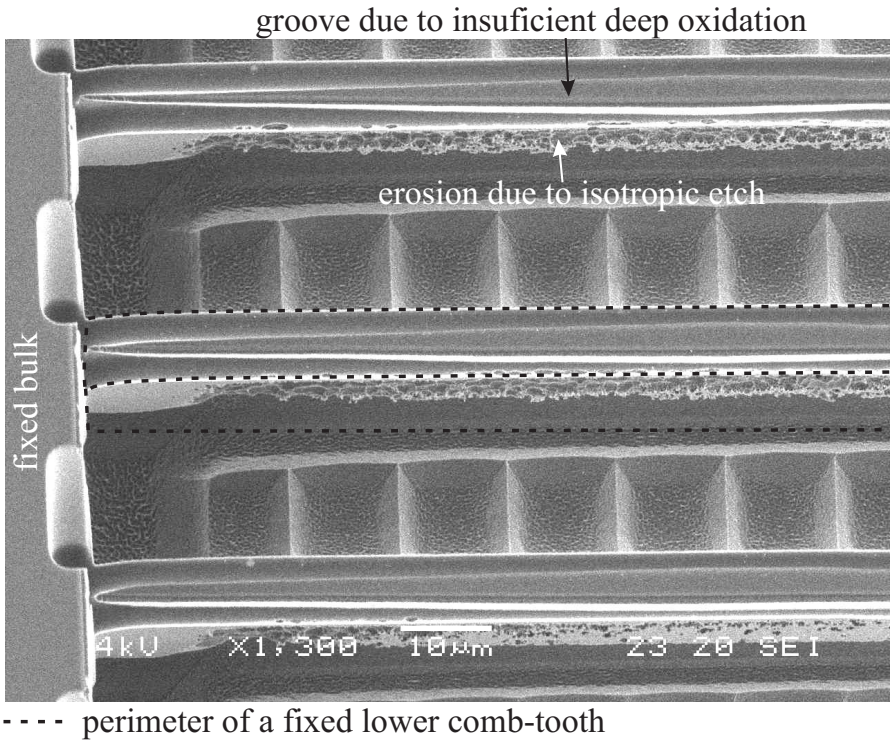

Figure 5.16: SEM picture showing a tilted view of three fixed lower comb-teeth of a device where the movable shuttle is removed.

Another two effects of the isotropic etch is shown in figure 5.16. The tilted view of the fixed lower comb-teeth (shuttle is removed) shows two effects of the isotropic etch. The first effect is again the groove in the top-side of the tooth caused by insufficient oxidation time. The second effect is erosion of the side-walls of the fixed comb-teeth. This is partly caused by deficiency in the fluor-carbon thickness and partly because the side walls are not protected as was previously discussed in section 5.3.3 on page 108. However, the effect is larger than expected.

Electrical insulation Most out-of-plane devices suffer from short-circuits (See figure 5.17). Since the electrical isolation trenches and the silicon mechanical structure are defined separately in two masks, an alignment tolerance t_m has to be taken into account. The drawing in figure 5.18 (left) shows a top-view of a probe-pad. The SiRN filled insulation trenches extent beyond the silicon structure. Although the tolerance is respected here, a short-circuit can still occur. The cause for this is shown in figure 5.18 (right). Both the cross-section of the silicon end-face and the longitudinal cross-section of the insulation trench can show a taper, taper 1 and taper 2 respectively. In the case shown here both tapers amplify the possibility of a short-circuit, as shown in figure 5.17 for a poor alignment between the insulation trench and the device edge.

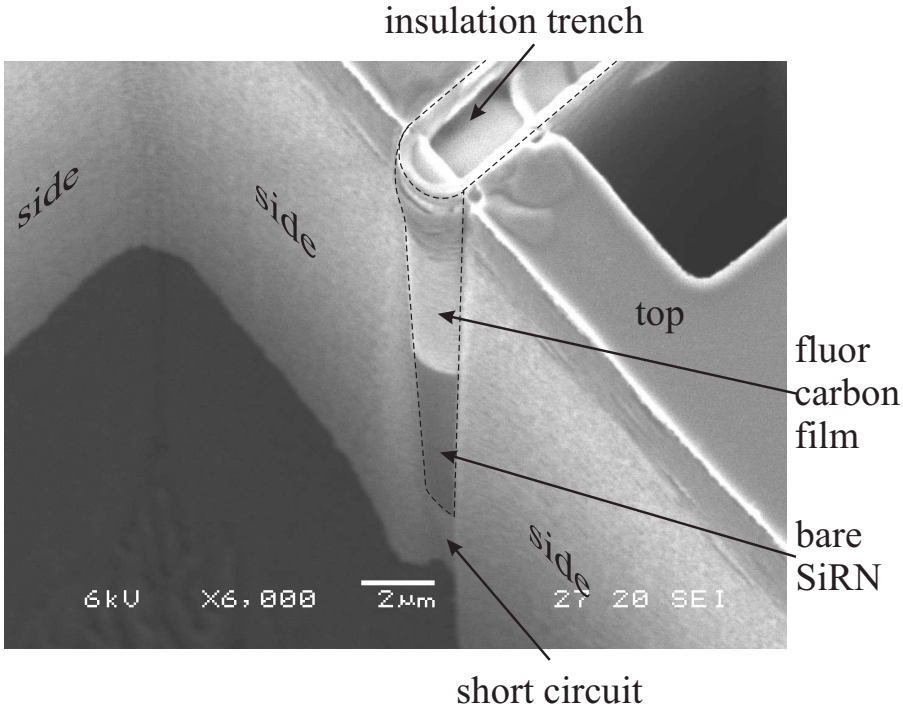

Figure 5.17: SEM picture showing a tilted view of an insulation trench in the Si structure, where a short-circuit occurs.

Since the etching process for the insulation trench is usually optimized for the profile of its transversal cross-section, optimizing the process for its longitudinal cross-section is not an option. Moreover, the chance both optima are in the same processing limits is very small. For this reason it is better to increase the tolerance of the mask. In stead of using 3 μm a tolerance of 6 μm improves the robustness of the mask.

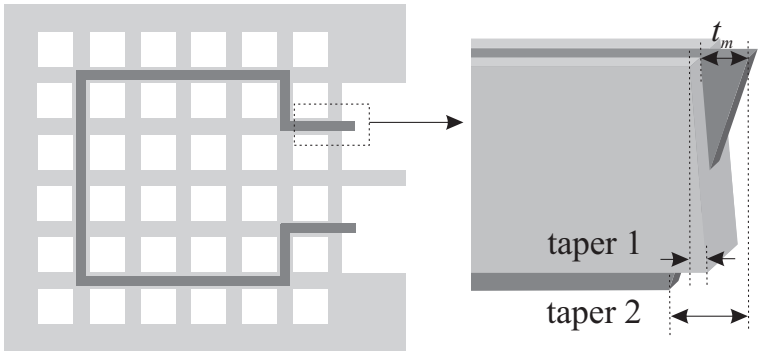

Figure 5.18: Example of an electrical insulated region, a probe-pad (left). 3D drawing showing a detail of the probe-pad (right). The effects of tapering of the insulation trench and of the silicon structure for the functionality of the insulation is indicated.

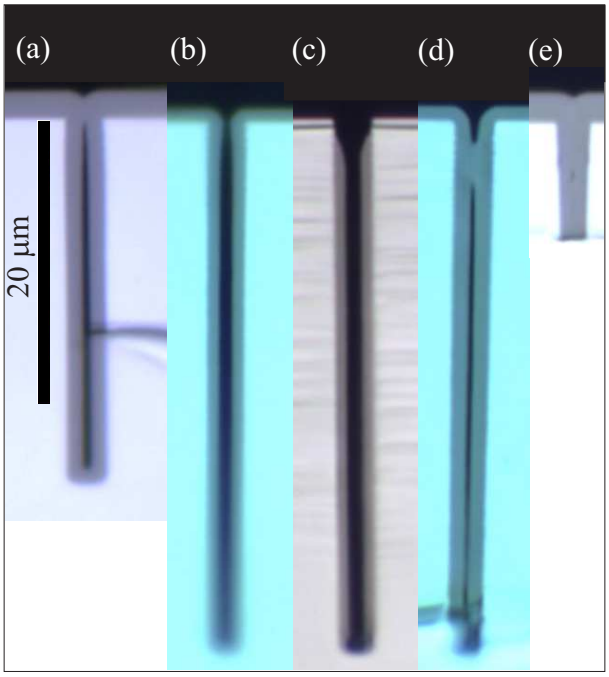

Figure 5.19: Microscope images showing cross-sections of filled trenches with voids. Void after trench filling with LPCVD SiRN (a), partially filled trench (b), SiRN removed from top-side and top-part of trench (c), and trench closed over a larger length after second fill (d). A void free filled shallow trench etched with a special Bosch process is shown in (e).

Voids After refilling of the electrical insulation trenches with LPCVD SiRN, voids where found as shown in the cross-section in figure 5.19 (a). Once the SiRN is removed from the topside, the risk exists the trench is opened at the topside, not offering robust mechanical fixation. To prevent this, trenches are filled in two stages. First the trench is partly filled as shown in figure 5.19 (b). Subsequently, the SiRN is etch by RIE etching from the top-side, which also removes the SiRN in the top-part of the trench as shown in figure 5.19 (c). Finally, the trench is filled a second time with LPCVD SiRN closing the top-part over a larger length as shown in figure 5.19 (d). In case the closure is long enough, etching of the SiRN on the topside will not result in opening the trench.

In [17] the relations between the trench profile and void-free filling are studied. For successful filling with LPCVD SiRN the trenches require a positive profile. Various Bosch etch recipes have been tried to obtain the required positive taper. Although not reported, one recipe was found capable of producing a positive profile that was completely filled with SiRN as shown in figure 5.19 (e). However, additional study is required to make this recipe suitable for higher aspect-ratios.

Improvements In the overview of the various fabrication aspects, some improvements have already been mentioned. Here a summary follows:

- ◇ Since the electrical insulation trenches cause problems during the LOCOS oxidation, the order in the fabrication process can be changed. In that case the LOCOS mask inversion and the deep oxidation should precede the etching and filling of the electrical insulation trenches. This requires an extra deposition of a layer of SiRN followed by a layer of TEOS (protection) in the beginning of the process to form the negative mask for the LOCOS oxidation. The insulation trenches have to be etched in the LOCOS formed oxide mask and continued into the Si. Subsequently the trenches are filled with SiRN and at the top- and bottom-side the SiRN is stripped. Especially, if the trench insulation requires multiple filling runs, the removal of the SiRN might cause considerable erosion to the LOCOS formed oxide mask. Because of that, this alternative route requires test runs.

- ◇ The mask tolerance and overlap of the third mask exposing the deep-oxidation structures for the lower comb-teeth and the suspension needs improvement to prevent misalignment resulting in damage to the comb-teeth and weakening of the suspension attachment.

- ◇ The mask tolerance for the alignment of the electrical insulation trenches to the edge of the mechanical Si structure should be doubled.

- ◇ To protect the sidewalls of the fixed lower comb-teeth, the process needs to be altered such that the isotropic dry release step does not damage the sidewalls. A possible solution for this is proposed in a process sequence in figure 5.20 on page 124. A fourth resist mask is applied to cover the openings for the comb-teeth gaps (figure 5.20 a)). Afterwards the process continues as before by Bosch etching of the devices structures and the dry isotropic release (figure 5.20 b)). The resist is removed in an oxygen plasma. The wafer returns to the Bosch etch reactor and the contours of the sofar etched structures are protected by a layer of fluor-carbon (figure 5.20 c)). An etch step follows to remove the fluor-carbon from the topside, uncovering the openings for the teeth gaps[1]. The gaps are etched into the Si by Bosch etching until the fluor-carbon layer is reached (figure 5.20 d)). Afterwards the process continues as before with removal of the fluor-carbon in an oxygen plasma, etching of the oxide in HF and finally freeze-drying (figure 5.20 e)). Some of these process steps are critical, especially since

[1]This might also remove the protecting fluor-carbon from the bottom, but additional etching into the bottom does not matter.

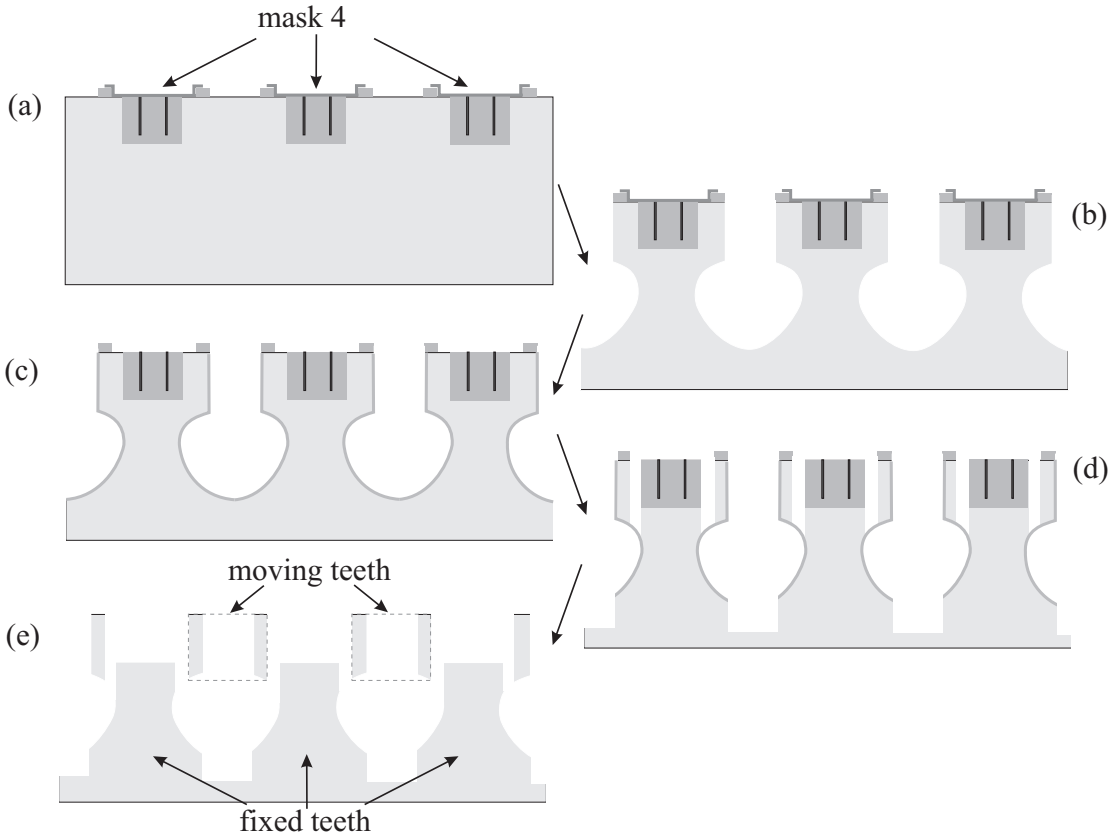

Figure 5.20: Sidewall protection for the comb-teeth by applying a fourth mask and etching the gaps between the teeth after the device dry release etch step.

after the first Bosch etch step, the structures are quite fragile. For this reason the proposed adaptation of the process requires testing.

- ◇ XeF_2 based etching used for the isotropic under-etch shows a true isotropic profile and is an interesting alternative for the isotropic release [18].

Apart from improvements to the process and design, there are some fabrication steps that require more understanding:

- ◇ The formation of the LOCOS mask and the erosion of the bird's beak. Once the influence of the processing parameters on the size of the mask openings are known, the design of the mask can be adapted to compensate for the erosion of the LOCOS mask

- ◇ The mechanism behind the dry isotropic release requires studying to inquire which process parameters determine the shape resulting from the etch step. Furthermore, the relations between the design and the distance over which the

structures can be undercut, without damaging the sidewalls of the structure, have to be determined. Figure 5.12 shows various trench-widths with the resulting isotropic profile. This gives an indication of the available undercut. Nonetheless, to be able to design for this it is required to know the how long the fluor carbon protecting the side-walls holds and how this is improved, the relation between trench width and profile of the isotropic etch and how this is influenced by the process conditions and the relation between depth of the trench has to the side-wall protection, the undercut and the isotropic etch profile.

◇ The amount of fluor-carbon deposition, serving for protection of the sidewalls during the isotropic release, should be tuned for the case of an oxide mask in stead of a photo-resist mask. This means tests should be performed with an oxide mask and preferably the LOCOS formed oxide mask. However, that is very laborious compared to just applying a resit mask.

◇ For the deep oxidation, the amount of under-etch during the Bosch etching of the oxidation-trenches has to be determined anew to apply the correct size of compensation in the mask design. This should be done in a test run with the exact same situation in terms of mask material, exposed silicon and etch-depth.

◇ The Bosch etch process and the mask-design should be tuned such that ARDE and loading have less influence on the overall depth of the etched structures. An attempt has been made to find the correct mask dimensions. A mask is made with various etch-hole sizes next to various trench widths. This mask is used to find the best etch-hole size combined with the 2 μm trench width between the comb-teeth (see figure 5.11 on page 117). However, a more general large scale investigation is required.

The points above show that, although testing some process steps along the way is possible, for proper guidelines to the process and mask design, thorough process development is required. Doing this on the side of making a device delivers results that are too fragmented and tent to get badly documented, because the focus is on making the device. As a consequence the fabrication issues discussed in this section do give a direction for a redesign and process development, but for an adequate set of design rules a lot more experimentation is required. Systematically developing the process parameters and design-rules should be regarded as a substantial, if not a single research goal.

5.4.2 Characterization

Due to the short-circuits, many devices for out-of-plane actuation did not work. Apparently, the trench insulation situated at sites of the torsion beams was not sufficient, since no problems with short-circuits were found for the in-plane 3 DOF manipulators (presented in chapter 3) residing on the same wafer[2]. Since the etched trenches bordering the torsion beams are wider than most other structures, the trenches are deeper. At least this increases the effect of the tapering in the isolation trenches and the chances of a short-circuit, discussed at page 120. Furthermore, the etching can be too deep, extending beyond the SiRN filled insulation trenches and allowing for a silicon bridge to form electrically shorting the Si structures at both sides of the insulation trench.

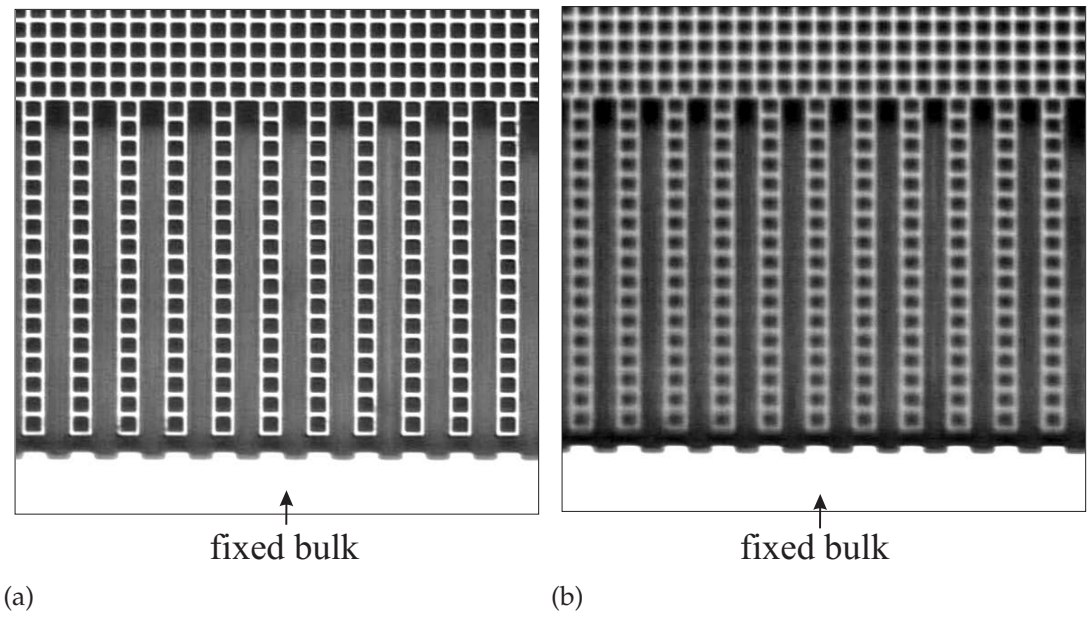

Figure 5.21: Micrographs showing top-views of the comb-teeth of a vertical comb-drive; no displacement at zero voltage (a) and about 10 µm displacement at 12 V (b).

Despite the large number of devices suffering from a short circuit, a rude characterization was performed on a working device. The micrographs in figure 5.21 show top-views of the comb-teeth in the situation without displacement and with a displacement of about 10 μm. The displacement was determined by focussing the microscope on the tips of the comb-teeth for both the non-displaced and displaced case and reading the scale on the focus-knop. For this displacement the comb-teeth touch

[2]These 3 DOF manipulators are successfully fabricated in the "3D process" as well.

the bottom of the structure, thus the maximum stroke is 10 μm. The displacement is achieved at a driving voltage of about 12 V.

Although this characterization does not give very detailed information, two aspects of the design can be verified. First of all the geometrically available stroke. This is limited by the profile under the moving teeth resulting from the isotropic release (visible in figure 5.16 on page 120). Second, the displacement is larger than expected at the given driving voltage. Although figure 4.11 on page 96 in chapter 4 shows a displacement of 10 μm at about 13 V, this plot is made for a comb-teeth gap of 2 μm. The gap in reality is 2.8 μm. Recalculation of the required driving voltage results in about 15 V for the L-torsion suspension and 11.5 V for the rectangular torsion beam. In other words the measured comb-drive behaves most according to the model for a rectangular suspension. This might reflect the weakening of the L-torsion beam attachment observed in figure 5.13 on page 119. However, with the comb-drive teeth approaching the grounded substrate, pull-in can be a reason for the lower voltage as well. A contribution due to pull-in can be calculated, although to verify if pull-in explains the lower voltage entirely, more accurate measurements are required. It is not expected that the process variation in the height of the horizontal beam part of the L-torsion beam causes a lower torsion stiffness. For instance with help of figure 5.13 but also with help of other SEM pictures made to characterize the device, the height of the horizontal beam part has been calculated knowing the tilt angle and using the scale-bar. This always resulted in a thickness of about 10 μm. This would mean a considerable larger torsion stiffness.

To obtain more information about the torsion suspension stiffness, vibrometric measurements have been performed. Because of the short circuits in the devices, the comb-drives could not be driven actively. Therefor the device wafer was put on a plate fixed to a piezo-shaker. Without giving a detailed description of the shaker-setup used, it is emphasized many aspects of the setup can be improved, e.g. the fixation of the device, and the type of piezo element. The measurement results did not provide a clear and reproducible insight in the dynamic behavior of devices with various suspensions. The setup for this "passive" actuation requires a more serious design and characterization of its own dynamics before this method offers trustworthy results. Investment of time and effort in the development of measurement setups and procedures should not be underestimated. However, before anything can be measured, a device should be fabricated, which in this case required most if not all available time and effort.

5.5 Conclusion and discussion

Despite the resolvable imperfections in the fabrication results, the 3D structuring with help of deep oxidized structures and the combination with the LOCOS mask to achieve the smallest possible comb-teeth gap[3], have proven the desired geometry is feasible. Especially, the proposed process has proven its compatibility with the basic process applied for the planar 3 DOF manipulator and enables successful fabrication of planar manipulators as well as out-of-plane manipulators.

Due to the short circuits and the weakening of the torsion beam attachments, a verification of the theory presented for the torsion suspension was not achieved. However, in case the desired geometry is successfully fabricated it is expected the improvement in stiffness by applying the L-torsion beam will not show a large difference in behavior compared to the predicted behavior from the model. Simply from geometrical perspective, the improvement in the kinematic constraint of the shuttle, resulting from the L-shaped cross-section is evident. Nevertheless, verification of the increase of torsion stiffness is desirable. First, of all since the improved suspension should not result in a large increase of torsion stiffness compared to the suspension with a rectangular torsion beam. Secondly, the equations used to find the torsion stiffness for the $\perp$- and L-shaped torsion beams are not very exact.

During the analysis, the compliance introduced by the square etch-holes, in both shuttle and probe-pads, has not been taken into account. In fact the attachments of the torsion beams to the shuttle and probe-pads were considered fully rigid. The compliance of the grid of etch-holes will certainly have a diminishing effect on the suspension stiffness, on the stiffness of the moving teeth and on the stiffness of the shuttle itself. An important improvement is the replacement of the square etch-holes by triangular ones. However, the exact consequences of doing so for the isotropic release etch and the extent of ARDE and loading are not known. To enable more robustness by stiffer design, these consequences should certainly be studied.

A large drawback of the application of the dry isotropic release is the profile resulting at the bottom-side of the mechanical structures, like vertical and especially horizontal beams. The Multilevel Beam SOI process discussed on page 105 would offer a great improvement to the definition of the bottom-side of the beams and it will introduce more variation to the mechanical structures that are realizable (e.g. no gap between the torsion beam parts and a larger width c for the horizontal beam part). In order to apply this process, successful mask integration in a custom SOI wafer should be developed in our laboratory and a method is required to allow for a small gap between the comb-teeth in this process.

[3] Achievable with our standard of lithography

As was mentioned in the summery of fabrication improvements, the focus on the fabrication of a device and the challenges that have to be overcome while doing so, compromise a thorough development of processes, fabrication guidelines and design rules.

References

[1] J.-H. Lee, Y.-C. Ko, B.-S. Choi, K.-M. Kim, and D. Y. Jeon, "Bonding of silicon scanning mirror having vertical comb fingers," *J. Micromech. Microeng.*, vol. 12, pp. 644–649, 2002.

[2] W. Piyawattanametha, P. R. Patterson, H. Toshiyoshi, and M. C. Wu, "Surface- and Bulk- Micromachined Two-Dimensional Scanner Driven by Angular Vertical Comb Actuators," *J. MEMS.*, vol. 14, no. 6, pp. 1329–1338, 2005.

[3] K.-H. Jeong and P. L. Luke, "A novel Microfabrication of a self-alinged vertical comb drive on a single SOI wafer for optical MEMS applications," *J. Micromech. Microeng.*, vol. 15, pp. 277–281, 2005.

[4] K. Jongbaeg, D. Christensen, and L. Lin, "Monolithic 2-D Scanning Mirror Using Self-Aligned Angular Verical Comb Drives," *IEEE Photonics Technology Letters*, vol. 17, no. 11, pp. 2307–2309, 2005.

[5] C. G. Keller and R. T. Howe, "Hexsil tweezers for teleoperated micro-assembly," in *IEEE MEMS*, (Nagoya, Japan), pp. 72–77, 1997.

[6] F. Ayazi and K. Najafi, "High aspec-ratio combined poly and single-crystal silicon (HARPSS) MEMS Technology," *J. MEMS*, vol. 9, no. 3, pp. 288–294, 2000.

[7] M. Wu and W. Fang, "A Molded Surface-Micromachining and Bulk Etching Release (MOSBE) Fabrication Platform on (111) Si for MOEMS," *J. Micromech. Microeng.*, vol. 16, no. 2, pp. 260–265, 2006.

[8] J. Kim, "Sacrificial bulk Micromachining SBM $\langle 111 \rangle$," in *IEEE MEMS*, (Maastricht, The Netherlands), pp. 556–559, 2004.

[9] K. A. Shaw, Z. L. Zhang, and N. C. MacDonald, "SCREAM I: a single mask, single-crystal silicon, reactive ion etching process for microelectromechanical structurs," *Sensors and Actuators A*, vol. 40, pp. 63–70, 1994.

[10] Q. X. Zhang, A. Q. Liu, J. Li, and A. B. Yu, "Fabrication technique for microelectromechanical systems vertical comb-drive actuators on a monolithic silicon substrate," *J. Vac. Sci. Technol. B.*, vol. 23, no. 1, pp. 32–41, 2005.

[11] V. Milanović, "Multilevel Beam SOI-MEMS Fabrication and Applications," *J. MEMS*, vol. 13, no. 1, pp. 19–30, 2004.

[12] E. Sarajlić, M. J. De Boer, H. V. Jansen, N. Arnal, M. Puech, G. J. M. Krijnen, and M. C. Elwenspoek, "Advanced plasma processing combined with trench isolation technology for fabrication and fast prototyping of high aspect ratio MEMS in standard silicon wafers," *J. Micromech. Microeng.*, vol. 14, pp. S70–S75, 2004.

[13] H. Jiang, K. Yoo, J.-L. A. Yeh, Z. Li, and N. C. Tien, "Fabrication of thick silicon dioxide sacrificial and isolation blocks in a silicon substrate," *J. Micromech. Microeng.*, vol. 12, pp. 87–95, 2002.

[14] R. Legtenberg, *Electrostatic actuators fabricated by surface micromachining techniques*, ch. 2, pp. 43–46. University of Twente, The Netherlands, 1996.

[15] H. Umimoto and S. Odanaka, "Three-dimensional numerical simulation of local oxidation of silicon," *IEEE Trans. Electron Devices*, vol. 38, no. 3, pp. 505–511, 1991.

[16] J. Frühauf, E. Gärtner, and E. Jänsch, "Silicon as a plastic material," *J. Micromech. Microeng.*, vol. 9, no. 4, pp. 305–313, 1999.

[17] B. R. De Jong, H. V. Jansen, M. J. De Boer, and G. J. M. Krijnen, "Tailored etch-profiles of high aspect ratio trenches to prevent voids after refill with lpcvd sirn.," in *MME*, (Göteborg, Sweden), pp. 60–63, 2005.

[18] G. T. A. Kovacs, N. I. Maluf, and K. E. Peterson, "Bulk micromachining of silicon," *Proc. IEEE*, vol. 86, no. 8, pp. 1536–1551, 1998.

Chapter 6

Stable electrostatic transducers

Two alternative electrostatic actuators are proposed, which do not show side pull-in instability as is found in a conventional comb-drive. The theory behind the actuators is explained analytically and a FEM simulation is performed to analyze the influence of the fringed fields. Electrode configurations for the actuators are discussed and a fabrication process is proposed to evaluate the feasibility of fabrication of the alternative actuators in MEMS technology.

6.1 Introduction

Electrostatic comb-drive actuators are widely applied in MEMS. Where it concerns planar actuation, comb-drives are relatively easy to integrate and in its most simple form a comb-drive can be structured with just one lithography step. The performance of the comb-drive with respect to power-density is reasonable[1] and the available stroke is usually in accordance to the requirements, without the need for a transmission. However a comb-drive (driven in voltage control) suffers from an instability issue known as side pull-in. This originates in the capacitance approaching infinity, when an out-of-center offset results in the sides of the moving teeth closely approaching the sides of the fixed teeth. The resulting attracting force between the opposite tooth sides approaches infinity as well. The partial derivative of this force in the sideways direction acts as a negative stiffness increasing faster with decreasing distance than any (physical) suspension stiffness can balance. As a result even with-

[1] Considering static positioning.

out a lateral off-set, side pull-in occurs once the applied voltage exceeds the pull-in voltage. This voltage is defined as the voltage where the lateral suspension stiffness and the electrostatic stiffness cancel each other[2]. The pull-in voltage for zero lateral offset is given by:

$$u_{pi} = \sqrt{\frac{c_l\, g^3}{4\,\varepsilon\, h\, x}} \tag{6.1}$$

Where c_l [N/m] is the lateral stiffness of the suspension, g [m] is the gap between the teeth, ε [F/m] is the dielectric constant of the medium between the plates, h [m] is the height of the teeth, and x [m] is the displacement coordinate.

The occurrence of pull-in during normal operation can be prevented if the conditions for pull-in are taken into account in the design. However, these design-rules limit the design freedom, with respect to a preferred small gap and low stiffness in actuation direction. Another solution to avoid side pull-in is application of charge control. Pure charge control is challenging to achieve, but theoretically charge control allows stable operation for any sideways position [1, 2]. Nevertheless, a phenomenon of charge pull-in is also known [3]. This occurs in case the charge is not homogenously distributed (for instance when a comb-tooth is bent and charge accumulates at the tip). Furthermore, the force in actuation direction of a charge controlled comb-drive is largely non-linear with respect to the position. A feedback loop can be applied to adjust the driving voltage when a too large sideways motion is sensed [4]. This only prevents damage, but will not extend the use of the comb-drive beyond instability limits, unless the system is over damped or critically damped [5].

Another method to prevent side pull-in is to apply a principle of electrostatic transduction where the capacitance will not approach infinity when the sides of the teeth touch each other. Two options are available. In the first option use is made of the fact that a plate of insulating material with a dielectric constant larger than 1 will be pulled in between to parallel plate electrodes. The second option uses the same geometry, but here the dielectric plate is replaced by a floating conductor.

In section 6.2 an analytical model for both transducers will be presented and the force will be compared to that of a comb-drive. Since the analytical model assumes ideal infinite plate dimensions, it is compared to the results obtained from a finite element model (FEM) model. Section 6.4 deals with the design aspects and in section 6.5 possibilities are given to fabricate the desired geometry. The conclusions follows in section 6.6.

[2]Here only static side pull-in is considered

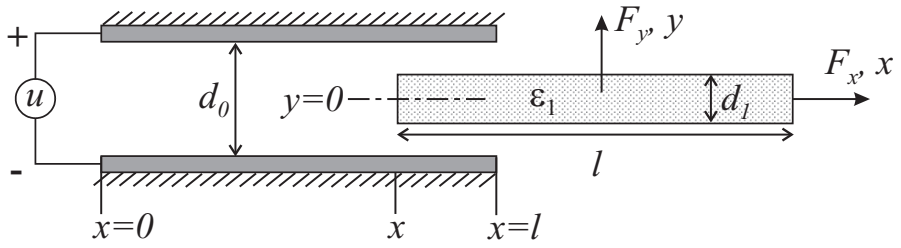

Figure 6.1: Schematic representation of a dielectric electrostatic transducer.

6.2 Theory

The analytical model for both the dielectric transducer and the floating plate transducer is given in sections 6.2.1 and 6.2.2 respectively. The FEM results are given in 6.2.4.

6.2.1 Dielectric electrostatic transducer

Figure 6.1 shows a schematic representation of the dielectric electrostatic transducer. Applying a voltage u over the two electrodes results in a force $-F_{x,d}$ [N] pulling the dielectric in between the plates. An expression for this force can be obtained by partial differentiation of a Legendre transform (E^*) of the energy with respect to x (See equation (6.2a)). Similarly an expression for the side pull-in force $F_{y,d}$ in the y direction can be found by partial differentiation with respect to y.

$$\begin{aligned}
\mathrm{d}E^*(x,y,u) &= \mathrm{d}E(x,y,u) - \mathrm{d}(u\,q) \\
\mathrm{d}E^*(x,y,u) &= F_x\,\mathrm{d}x + F_y\,\mathrm{d}y - q\mathrm{d}u \\
E^*(x,y,u) &= E_0 - \frac{C_t(x,y)\,u^2}{2} \\
F_x(x,y,u) &= \left[\frac{\partial E^*(x,y,u)}{\partial x}\right]_{y,u} \\
F_y(x,y,u) &= \left[\frac{\partial E^*(x,y,u)}{\partial y}\right]_{x,u}
\end{aligned} \tag{6.2a}$$

With help of the electrical replacement circuit in figure 6.2, the total capacitance is calculated. The resulting total capacitance C_t is given in equation (6.2b). C_0 is the capacitance without dielectric, which is connected in parallel to a series connection of $C_{\varepsilon 0}$ and $C_{\varepsilon 1}$. $C_{\varepsilon 0}$ resembles the capacitance over the combined air gaps above and below the dielectric and $C_{\varepsilon 1}$ resembles the capacitance over the dielectric. d_0 [m] is the distance between the electrode plates, d_1 [m] is the thickness of the dielectric, l [m] is its length, and w [m] is its width.

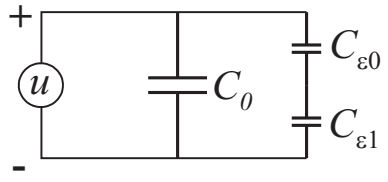

Figure 6.2: Electrical circuit used to calculate the total capacitance C_t.

$$
\begin{aligned}
C_t(x) &= C_0(x) + \frac{C_{\varepsilon 0}(x)\, C_{\varepsilon 1}(x)}{C_{\varepsilon 0}(x) + C_{\varepsilon 1}(x)} = \frac{\varepsilon_0\, w\, x}{d_0} + \frac{\varepsilon_1 \varepsilon_0\, w\, (l-x)}{\varepsilon_1\, d_0 + d_1(1-\varepsilon_1)} \\
C_0(x) &= \frac{\varepsilon_0\, w\, x}{d_0} \\
C_{\varepsilon 0}(x) &= \frac{\varepsilon_0\, w\, (l-x)}{d_0 - d_1} \quad C_{\varepsilon 1}(x) = \frac{\varepsilon_1\, \varepsilon_0\, w\, (l-x)}{d_1}
\end{aligned}
\tag{6.2b}
$$

Inserting the equation for $C_t(x)$ in equation (6.2a) results in the expression for $F_{x,d}$ given in equation (6.2c). In this model it is assumed the electric field lines cross rectilinearly from one electrode to the other, i.e. the infinite plate model for the capacitances is applied. As a result the position of the dielectric plate along the y axis does not change C_t and the force $F_{y,d}$ resulting from equation (6.2a) is zero.

$$
F_{x,d}(u) = \frac{\varepsilon_0\, w\, u^2}{2\, d_0} \left(\frac{d_1\, (\varepsilon_1 - 1)}{\varepsilon_1\, d_0 - d_1\, (\varepsilon_1 - 1)} \right) \tag{6.2c}
$$

Because the effects of fringed field lines at the boundaries of the capacitor plates are not taken into account in this model, it cannot be concluded there is no force $F_{y,d}$ at all. As part of the FEM simulations discussed later, it will turn out this force does exist.

6.2.2 Floating electrostatic transducer

The equation for the force $F_{x,f}$ is derived following a similar procedure as above. Figure figure 6.3 shows a schematic representation of the floating electrostatic transducer. The voltage u_2 on the floating plate will be determined by its position relative to the electrode plates, and the applied voltage u over the electrodes. The top-electrode and the bottom-electrode in combination with the floating plate can be modeled as a series capacitance of C_1 and C_2 as shown in figure figure 6.4. The voltage u_2 is calculated from the assumption that the charges on C_1 and C_2 are equal (as follows from the circuit in figure 6.4, while it is assumed no net charge resides on the floating plate). This procedure is shown in equation (6.3a).

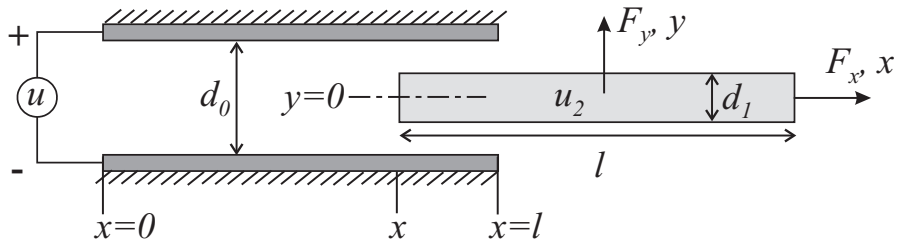

Figure 6.3: Schematic representation of a floating electrostatic transducer.

$$\begin{aligned} q_1 = q_2 \Rightarrow C_1\,(u - u_2) &= C_2\,u_2 \Rightarrow \\ u_2 = \frac{C_1}{C_1 + C_2}\,u &= \left(\frac{1}{2} + \frac{y}{d_0 - d_1}\right) u \end{aligned} \tag{6.3a}$$

The equation of the total capacitance is given in equation (6.3b). Although the capacitances C_1 and C_2 do depend on the y position of the floating plate, C_t does not. As a result also for this transducer the analytic model does not predict a side pull-in force $F_{y,f}$ in the y-direction.

$$\begin{aligned} C_t(x) &= C_0(x) + \frac{C_1(x,y)\,C_2(x,y)}{C_1(x,y) + C_2(x,y)} = \frac{\varepsilon_0\,w\,x}{d_0} + \frac{\varepsilon_0\,w\,(l-x)}{d_0 - d_1} \\ C_0(x) &= \frac{\varepsilon_0\,w\,x}{d_0} \\ C_1(x,y) &= \frac{2\,\varepsilon_0\,w\,(l-x)}{d_0 - d_1 - 2y} \quad C_2(x,y) = \frac{2\,\varepsilon_0\,w\,(l-x)}{d_0 - d_1 + 2y} \end{aligned} \tag{6.3b}$$

Partially deriving E^* with respect to x for constant y and u results in the force $F_{x,f}$ given in equation (6.3c). Like equation (6.2c), the terms are grouped such that the term $\dfrac{\varepsilon_0\,w\,u^2}{2\,d_0}$ is isolated. The remaining term can be seen as a *force-factor* to distinguish between the forces for the different transducers.

$$F_{x,f}(u) = \frac{\varepsilon_0\,w\,u^2}{2\,d_0}\left(\frac{d_1}{d_0 - d_1}\right) \tag{6.3c}$$

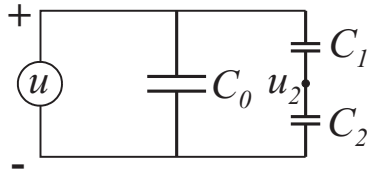

Figure 6.4: Electrical circuit used to calculate the total capacitance C_t.

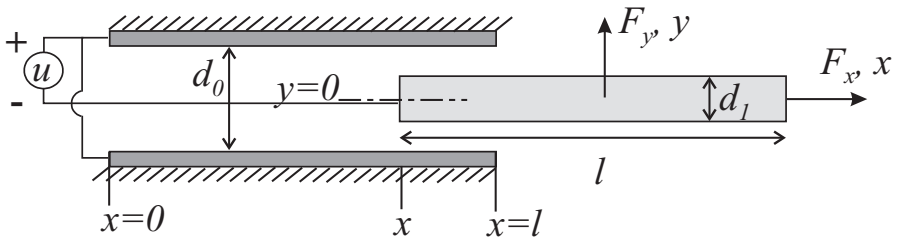

Figure 6.5: Schematic representation of a comb-drive.

6.2.3 Comb-drive forces

Using the *force-factor* mentioned above, a ratio is defined between the force of the alternative electrostatic transducers and the force that a normal comb-drive with equal dimensions delivers. The comb-drive forces in both the x- and the y-direction can be derived from energy analysis as well and it is shown, these are both unequal to zero in case $y \neq 0$ [3]. Figure 6.5 shows the schematic representation of a comb-drive, used to derive the forces $F_{x,cd}$ and $F_{y,cd}$ given in equation (6.4) (see equation (3.3) on page 53 in chapter3).

$$F_{x,cd}(x,u) = \frac{\varepsilon_0 w u^2}{2 d_0}\left[\frac{2 d_0}{d_0 - d_1 + 2y} + \frac{2 d_0}{d_0 - d_1 - 2y}\right] \tag{6.4a}$$

$$F_{y,cd}(x,y,u) = \frac{\varepsilon_0 w u^2}{2 d_0}\left[\frac{4 d_0 (l-x)}{(d_0 - d_1 + 2y)^2} - \frac{4 d_0 (l-x)}{(d_0 - d_1 - 2y)^2}\right] \tag{6.4b}$$

The forces in equation (6.4) are grouped in the same way as in equations (6.2c) and (6.3c). Considering the case where y is zero, the force ratios r_1 and r_2 for respectively the floating transducer and the dielectric transducer are written as shown in equation (6.5).

$$r_1 = \frac{F_{x,f}}{F_{x,cd}} = \frac{1}{4}\frac{d_1}{d_0} \tag{6.5a}$$

$$r_2 = \frac{F_{x,d}}{F_{x,cd}} = \frac{1}{4}\frac{d_1}{d_0}\left[\frac{(\varepsilon_1 - 1)\left(1 - \frac{d_1}{d_0}\right)}{(\varepsilon_1 - 1)\left(1 - \frac{d_1}{d_0}\right) + 1}\right] \tag{6.5b}$$

These ratios are plotted as a function of the ratio of the distance between the electrode plates and the thickness of the moving plate $\frac{d_1}{d_0}$. Figure 6.6 shows the plots where ε_1

[3] For $y = 0$, $F_{y,cd}$ is zero, however its partial derivative to y is not. The partial derivative is regarded as the electrostatic stiffness, which should be balanced by the stiffness of the suspension to for pull-in free operation.

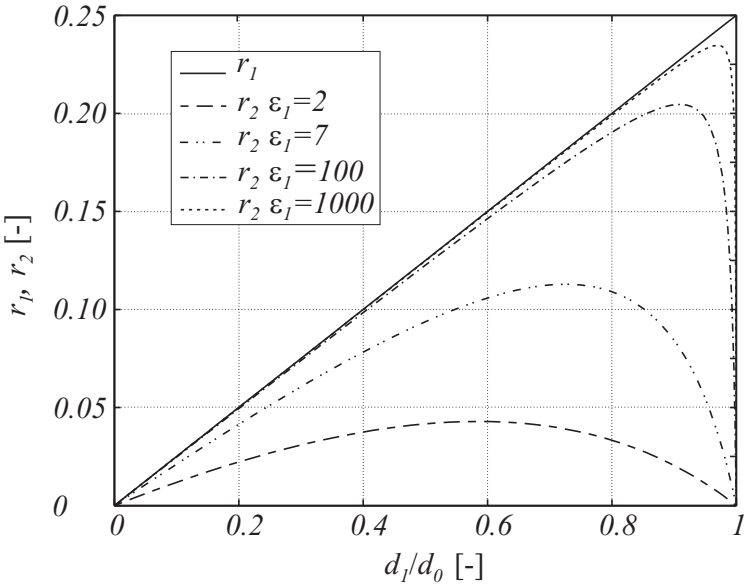

Figure 6.6: Ratios r_1 and r_2 plotted as a function of the relative dielectric or floating plate thickness.

is parameterized for r_2. Where $\varepsilon_1 = 7$ relates to Si_3N_4 [6] and $\varepsilon_1 = 1000$ relates to PZT [7]. Clearly, considering the delivered force, the alternative transducers are outperformed by the comb-drive. The maximum ratio that can be achieved according to the graph is 0.25. However, this is reached at a point near to or at $d_1 = d_0$ which in reality means a capacitance (and thus a force) approaching infinity for the comb-drive and the floating transducer. So for these two actuators this region is realistically not achievable, also because of effects like breakdown and electron-emission. r_2 for the dielectric transducer shows various maxima for the different values of ε_1. These maxima only tell that at the corresponding values for $\frac{d_1}{d_0}$ the force ratio with respect to an equally dimensioned comb-drive is most beneficial. The largest force that can be achieved with the dielectric transducer will be reached at $d_1 = d_0$. However, in practice there should be clearance for the dielectric to move without friction. Furthermore, in case the dielectric touches the electrodes charge can be injected in the material that influences the behavior of the transducer undesirably.

6.2.4 FEM modeling

The analytical model proposed in the previous section does not predict a side pull-in force for the dielectric and floating electrostatic transducer. Since the modeling assumes rectilinear electric field lines, fringing field lines at the boundaries of the plates and the geometrical field discontinuity over a dielectric boundary are not taken into account, i.e. the model is not complete. For this reason it is decided to model both

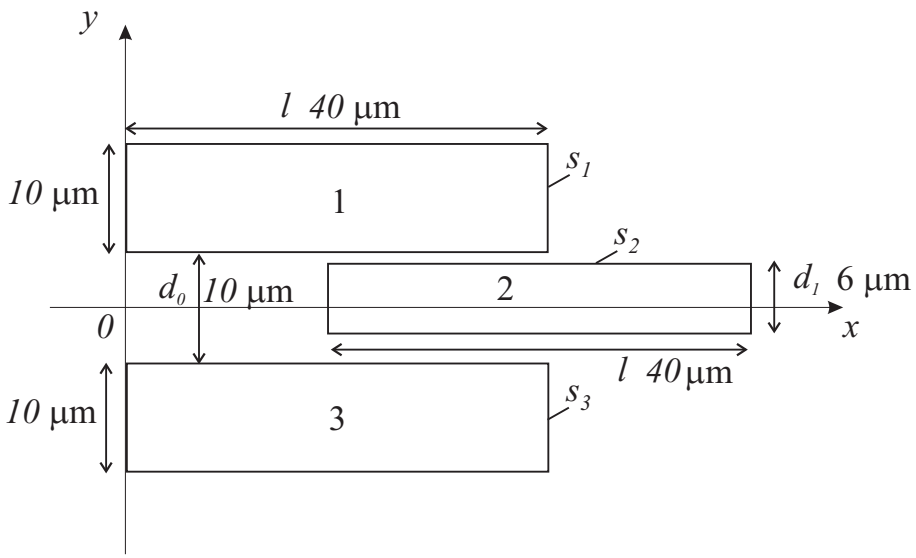

Figure 6.7: Configuration of the modeled 2D structure.

transducers with a two dimensional finite element model as well. The FEM modelling is performed in FlexPDE 4 [8].

Figure 6.7 shows the modeled structure. Box 1 and 3 represent the fixed electrode plates and box 2 is the movable plate, representing the dielectric plate or the floating conductor. At a reasonable large distance from the structure a domain boundary is defined such that its influence on the calculated potential distribution is minimal. At this boundary a *natural* boundary condition equal to zero is defined. The effect of this *general flux* boundary condition follows from the governing equation that is solved. Since the medium of the problem (excluding the conductors) is characterized by absence of free charges, Gauss's law in dielectric media is used as governing differential equation (see equation (6.6)). With the natural boundary condition the normal component of **D** is defined to be zero on the boundary. As a result the electric field lines near the simulation domain boundary are oriented tangentially to this boundary. As such, the boundary has a minimal contribution to the capacitance of the simulated structure.

$$\begin{aligned} &\nabla \cdot \mathbf{D} = \rho \quad \Leftrightarrow \quad \nabla \cdot \varepsilon_0 \varepsilon_1 \mathbf{E} = -\nabla \cdot (\varepsilon_0 \varepsilon_1 \nabla U) \\ &\text{with charge density } \rho = 0 \quad \Rightarrow \quad \nabla \cdot (\varepsilon_0 \varepsilon_1 \nabla U) = 0 \end{aligned} \tag{6.6}$$

Dielectric electrostatic transducer To solve the electric field in the system with the dielectric electrostatic transducer, voltages of $u_1 = 1$ V and $u_3 = -1$ V are defined respectively on the boundaries of box 1 and 3 . Box 2 is defined as a region with a relative dielectric constant (ε_1) of 7 (the assumed relative dielectric constant

of Si_3N_4 [6], while the surrounding region excluding the conductors has a relative dielectric constant of 1. The positions of the dielectric is varied along the x-axis from 0 to 44 μm and along the y-axis form 0 (centered between box 1 and 3) to 1.9 μm. Along the x-axis the step-size is 1 μm and the positions along the y-axis are $\{$ 0.0, 0.5, 1.0, 1.2, 1.4, 1.5, 1.7, 1.8, 1.9 $\}$ μm. At each x, y-position the energy E_w [J/m] per unit width of the system is calculated according to equation (6.7).

$$E_w(x_i, y_j) = \frac{\varepsilon_0}{2} \int_S \varepsilon_1 \, \mathbf{E}^2 \mathrm{d}s \tag{6.7}$$

Where **E** is the electric field, and the integral is numerically evaluated over the surface of the entire domain excluding the conductors (box 1 and 3).

With the energy per unit width known at all the positions of the dielectric, the force per unit width in x- and y-direction is calculated via discrete differentiation of E_w with respect to the steps in x- and y-direction.

$$F_{x,w}\left(\frac{x_{i+1} - x_i}{2}, y_j\right) = \frac{E_w(x_{i+1}, y_j) - E_w(x_i, y_j)}{x_{i+1} - x_i} \tag{6.8a}$$

$$F_{y,w}\left(x_i, \frac{y_{i+1} - y_i}{2}\right) = \frac{E_w(x_i, y_{j+1}) - E_w(x_i, y_j)}{y_{j+1} - y_j} \tag{6.8b}$$

Floating electrostatic transducer In the case of the floating electrostatic transducer the voltages on the boundaries of box 1 and 3 are again defined as $u_1 = 1$ V and $u_3 = -1$ V respectively. The voltage on the boundary of box 2 has to be defined such that no net charge resides on the boundary of the box, i.e. $q_2 = 0$. The capacitance network in figure 6.8 is used to calculate the voltage u_2. Equation (6.9a) op page 142 gives the charges on the capacitors in the network, depending on the voltages u_1, u_2 and u_3. These charges can be found with the FEM model by integration of the electric field over the boundaries of each box.

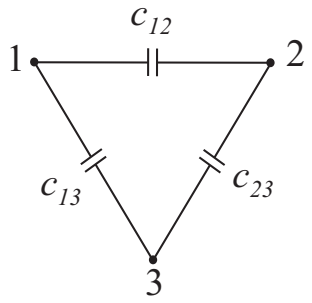

Figure 6.8: Capacitive network.

$$\begin{aligned} q_1 &= c_{12}(u_1 - u_2) + c_{13}(u_1 - u_3) = \int_S \mathbf{E}\,\mathrm{d}\mathbf{s}_1 \\ q_2 &= c_{12}(u_2 - u_1) + c_{23}(u_2 - u_3) = \int_S \mathbf{E}\,\mathrm{d}\mathbf{s}_2 \\ q_3 &= c_{23}(u_3 - u_2) + c_{13}(u_3 - u_1) = \int_S \mathbf{E}\,\mathrm{d}\mathbf{s}_3 \end{aligned} \tag{6.9a}$$

Equation (6.9b) shows once more how u_2 depends of the capacitance values c_{12} and c_{23} and the voltages u_1 and u_3. To solve the equation, the values for c_{12} and c_{23} are required. The capacitances depend of the position of the floating plate. Equation (6.9c) shows how the capacitance values can be deduced from the charges obtained with the FEM model. For $c_{12}(x_i, y_j)$ both u_2 and u_3 are 0 V while u_1 is 1 V. The value of q_2 depending on the position of box 2 is a direct measure for the capacitance $c_{12}(x_i, y_j)$. Similarly the position dependent value for $c_{23}(x_i, y_j)$ is found. The capacitance values are inserted in equation (6.9b) to obtain the position dependent voltage on the floating plate $u_2(x_i, y_j)$, given in figure 6.9. As expected, the voltage depends linearly on the y-position between the electrode plates ($x = 0$ to 40 μm). Beyond the plates the, the dependance of u_2 of both x and y is non-linear and thus governed by the fringing field.

$$\begin{aligned} &u_1 = 1\text{ V} \quad u_3 = -1\text{ V} \\ &q_2 = 0 \quad \Leftrightarrow \quad u_2 = \frac{c_{12}\,u_1 + c_{23}\,u_3}{c_{12} + c_{23}} \\ &\text{with } u_1 = 1\text{ V and } u_3 = 1\text{ V}, \quad u_2 = \frac{c_{12} - c_{23}}{c_{12} + c_{23}} \end{aligned} \tag{6.9b}$$

$$\begin{aligned} &u_1 = 1\text{ V} \quad u_2 = 0\text{ V} \quad u_3 = 0\text{ V} \\ &q_2 = -c_{12}(x_i, y_j)\,u_1 \quad \text{with } u_1 = 1\text{ V}, \quad q_2 = -c_{12}(x_i, y_j) \\ &u_1 = 0\text{ V} \quad u_2 = 0\text{ V} \quad u_3 = 1\text{ V} \\ &q_2 = -c_{23}(x_i, y_j)\,u_3 \quad \text{with } u_3 = 1\text{ V}, \quad q_2 = -c_{23}(x_i, y_j) \end{aligned} \tag{6.9c}$$

Using the derived position dependent voltage data u_2, the simulations are performed for the same position as for the dielectric transducer. The resulting values for the energy per unit width are used again to discretely derive the forces per unit width according to equation (6.8).

Forces in x- and y-direction compared to a comb-drive The forces in x- and y-direction obtained from the FEM models are compared to those delivered by a comb-drive. Hereto, FEM simulations have been performed on the comb-drive structure. In this case the voltages on box 1 and 3 are both 2 V and the voltage on box 2 is 0 V. The value of 2 is chosen since it is equal to the voltage difference over the electrodes of both alternative electrostatic transducers.

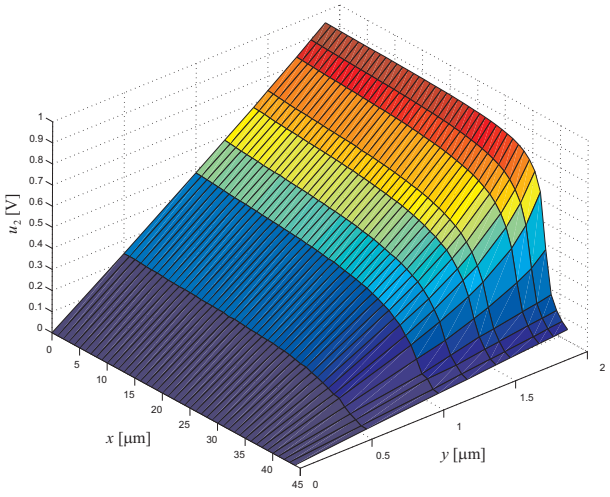

Figure 6.9: u_2 for each position of the floating plate.

In figure 6.10 on page 145 the values for $F_{x,w}$ and $F_{y,w}$ (normalized to w) are ploted above the x, y-plane for the dielectric transducer (6.10a and 6.10d), the floating transducer (6.10b and 6.10e) and the comb-drive respectively (6.10c and 6.10f). The plots of $F_{x,w}$ for both the dielectric and the floating transducers is nearly independent of the x, y-position once the moving plate is well between the electrode plates ($x = [5, 35]$ μm). This is expected, since the analytic model does not show any dependance of $F_{x,w}$ on the x, y-position. The "constant" force in x-direction normalized to w for the floating transducer found with the FEM model, is about 2 μN/m. With equation (6.2c) a value of 2.5 μN/m is found, meaning the analytical model is in fair agreement with the FEM model.

For the plate positions between $x = 9$ and $x = 0$ μm, the force gradually approaches zero. The analytical model does not predict this. Pushing the plate further into the electrodes (negative values for x) would result in a counter acting force just like a counter acting force occurs when the plate is pulled out of the electrodes (positive values for x). However, negative x-values are not considered in the analytical models given at the start of this chapter. Nevertheless, pulling the plate away from $x = 0$ or pushing it beyond $x = 0$ could in general be modelled analytically by an instant change in the direction of the force acting to restore the plates position to $x = 0$. Since the plates are not infinite, this transition is not instantly in the FEM model.

In the range, where x is between 44 and 39 μm, the moving plate goes from outside to in between the electrodes. For the lower values of y, $F_{x,w}$ gradually increases with increasing overlap until its constant force displacement relation as predicted by the simple analytical models discussed before. However, for the higher y values, the plot shows a peak. This peak has a maximum right were the corners of the fixed electrode

plate and the moving plate face each other. At this point the electric field strength is quite high, while it changes strongly for small changes in the position of the moving plate. This gives rise to the peak in the force. Presumably the field strength and thus the change in field strength will be smaller for realistic, less sharp shapes of the corners of the plates. For a realistic transducer, the situation were the moving plate is situated completely outside the electrodes, is not likely, since there usually is a minimal overlap between the moving plate and the electrodes. For those reasons these positions are not of too much concern for realistic devices.

$F_{x,w}$ for the comb-drive largely depends on the y-position as is expected from the analytical model. Once the moving plate approaches the fixed electrode, $F_{x,w}$ will increase beyond limits. The dependence of $F_{x,w}$ on the x-position is similar to that for the dielectric and the floating transducer. This dependence is also predicted by the analytical model.

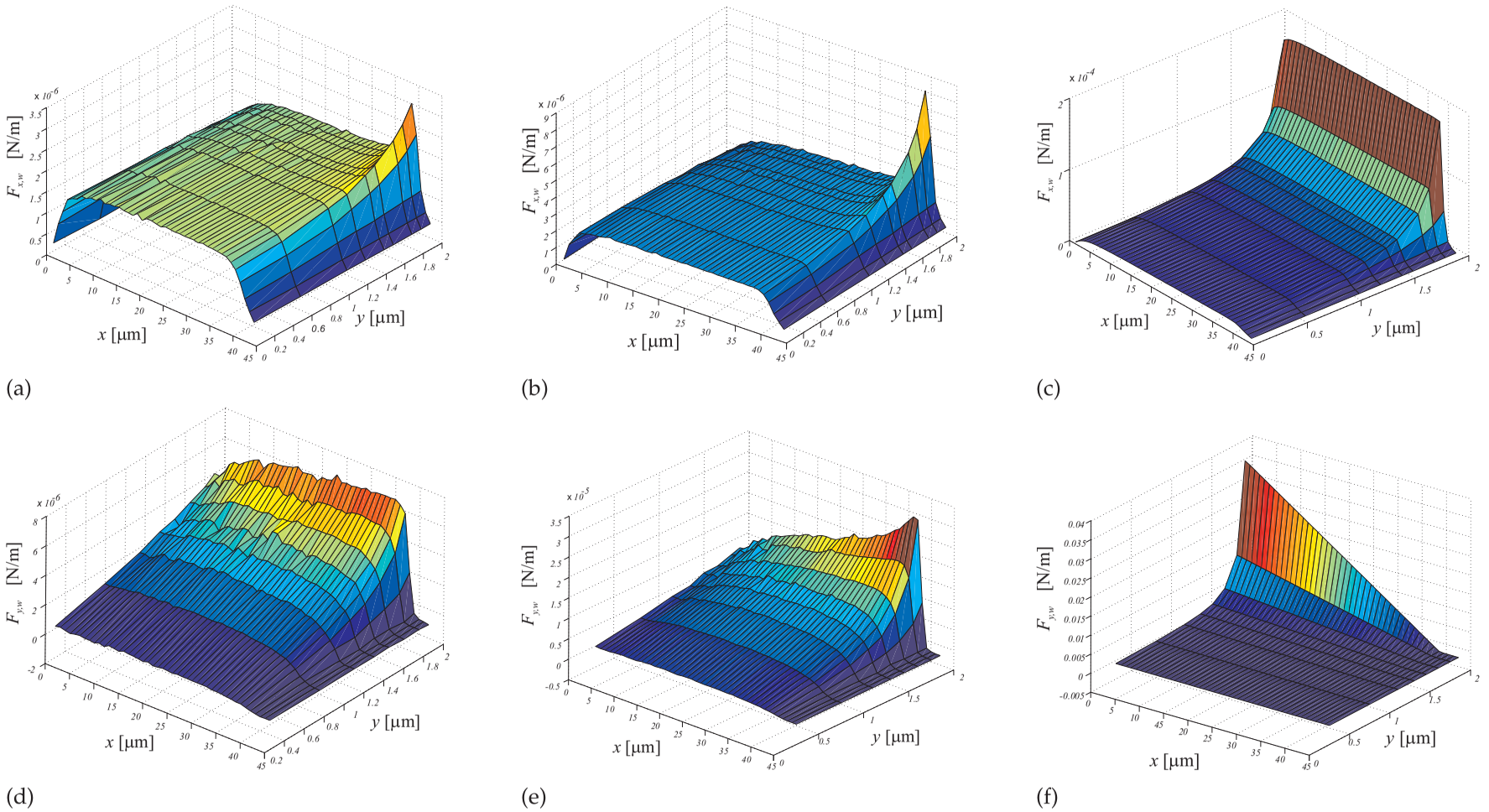

Figure 6.10: $F_{x,w}$ and $F_{y,w}$ for respectively the dielectric transducer (a and d), the floating transducer (b and e) and the comb-drive (c and f).

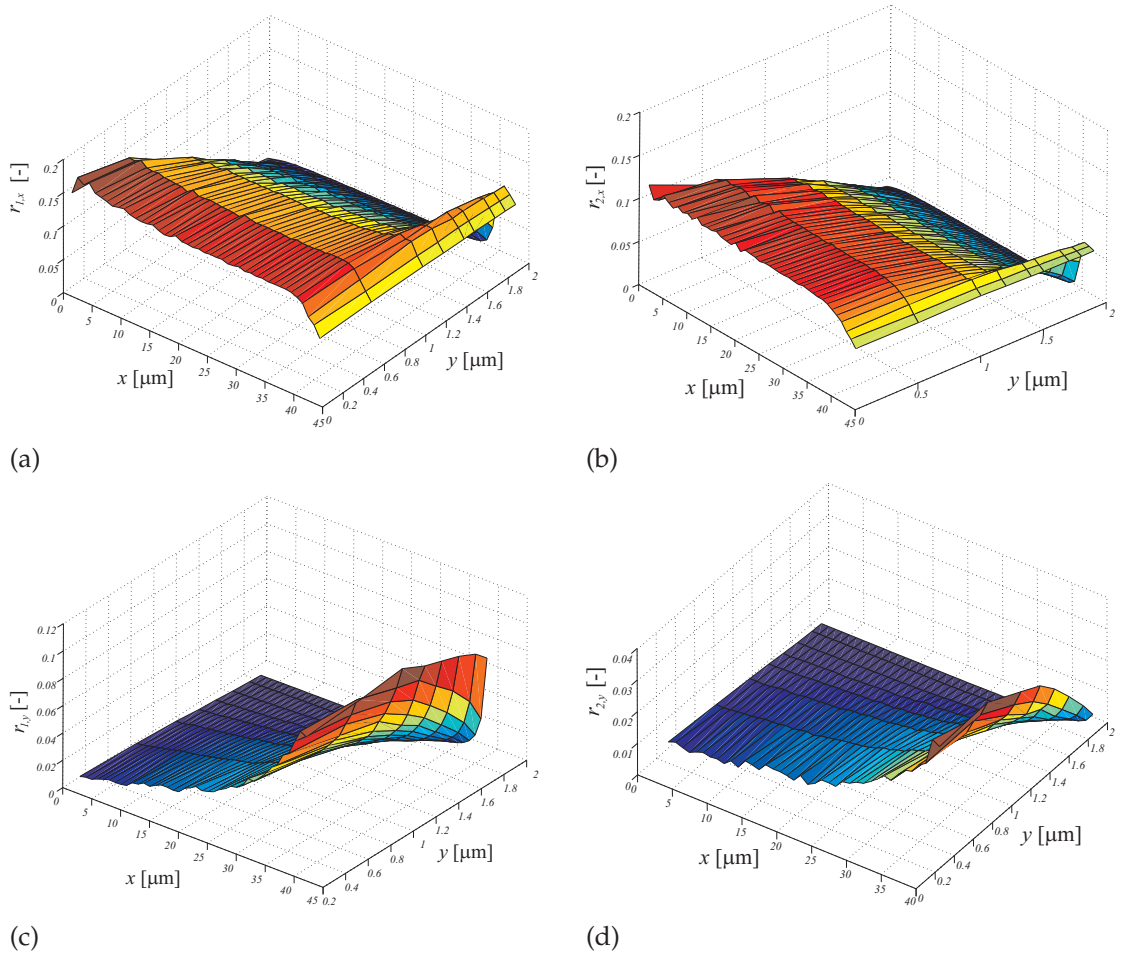

Figure 6.11: Force ratios for F_x and F_y for respectively the floating transducer (a and c) and the dielectric transducer (b and d)

$F_{y,w}$ for the dielectric transducer shows a non-linear dependence on the y-position. As the dielectric plate is inserted further between the electrodes, the force in the y-direction reduces. This can be attributed to the reduction in length of the part of the dielectric sticking out of the plates and being inside the fringe field. For the floating plate, the force shows a slightly different behavior. The dependance of the force on the x-position is much larger though. Here it can also be assumed the part of the plate under influence of the fringe field is responsible for the force in the y-direction.

The force $F_{y,w}$ for the comb-drive shows a very strong and non-linear dependence of the y-position. This is indeed predicted by the analytical model. The dependence of the force on the x-position is explained by the amount of insertion of the moving plate. The more the plate is inserted, the larger the overlap with the fixed electrodes, and thus the larger $F_{y,w}$. This is completely in agrement with the analytical model.

Figure 6.11 shows the ratios r_1 and r_2 of respectively the floating (figure 6.11a and

figure 6.11c) and the dielectric transducer (figure 6.11b and figure 6.11d) with respect to the comb-drive for both the forces in the x- and in the y-direction. The ratios for the force in the x-direction show a good agreement with figure 6.6 for $\frac{d_1}{d_0} = 0.6$, $\varepsilon_1 = 7$, and $y = 0$. The ratios for the force in the y-direction show that $F_{y,w}$ for the floating plate and the dielectric plate is hardly significant with respect to the side pull-in force of a comb-drive. Especially when a minimal overlap of 10 μm between the moving plate and the electrodes is assumed, which means x is limited to 30 μm.

From the FEM simulation results the following:

- ◇ The forces in x-direction obtained with the alternative transducers are indeed much smaller than the force in x-direction obtained with a conventional comb-drive having equal dimensions and for equal driving voltage.
- ◇ The forces in y-direction for the alternative transducers are not zero. However, they are far smaller than the force in y-direction for a conventional comb-drive. Because the forces are calculated by a discreet differentiation of the energy, the force at $y = 2$ μm, where the plates touch the electrodes is not calculated. However, the trend of $F_{y,w}$ for the alternative transducers does not indicate an infinite value for the force at $y = 2$ μm, while for the comb-drive it clearly does.
- ◇ Compared to an equally dimensioned comb-drive and for a given lateral suspension stiffness, the alternative transducers potentially operate at a larger driving voltage before pull-in occurs. This enables a larger stroke and/or force compared to the comb-drive.

The next section discusses the likelihood of side pull-in due to a net charge on the plates of the alternative transducers, since this is not addressed in the analytic and FEM model.

6.3 Influence of charge

The performance of dielectric and floating electrostatic transducers can be influenced by charging of the moving plate. Some mechanisms causing charging are: charge injection in a large field under direct mechanical contact with one of the driving electrodes or via a geometrical chain of capacitances connecting to the driving electrodes, and charge-injection as a result of electrical breakdown of the air-gap or the dielectric [9]. Furthermore, charging as a result of the fabrication processes (e.g. plasma etching) cannot be ruled out.

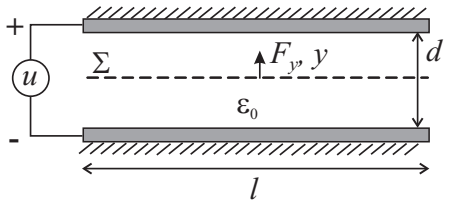

Figure 6.12: Schematic representations of a charge-sheet fully inserted between parallel electrodes.

In literature, models are found to describe the effects of charge in dielectric layers part of parallel-plate transducers [9, 10]. The geometry discussed there consists of a fixed conducting electrode plate covered by a dielectric layer, with a second moving conducting electrode plate suspended above and parallel to the first plate. These kind of structures are often used as variable capacitors or switches.

No examples of models have been found in literature, dealing with the geometry of two fixed parallel electrodes plates where a dielectric plate is inserted in between. For the alternative transducers proposed in this chapter, it is important to know if charging can be an extra cause of side pull-in. Hereto, the effect of a charge-sheet with a fixed charge distribution fully inserted between two electrodes will be considered.

Figure 6.12 shows schematic representations of a charge-sheet completely inserted between the electrodes. The parameters used in the scheme are explained in table 6.1. An energy analyzes is often applied to find expressions for the force a transducer can deliver. In case of a capacitor with plate dimensions l and w much larger than d, the electrostatic field is generally assumed to cross straight from on plate to the other, while there is no field outside the capacitor. Because of the charge-sheet, there is field presented outside the capacitor. For this reason an energy analysis would require to integrate the energy-density, due to the electrostatic field, over all space. This is not straightforward. One could reason, that to determine the forces on the charge-sheet by variations in the energy, all energy contributions that do not change with

Table 6.1: Explanation of the parameters

parameter	explanation	unit
l	plate length	[m]
w	plate width	[m]
d	distance between the plates	[m]
u	voltage over the electrodes	[V]
Σ	charge-density of charge-sheet	[C/m^2]
ε_0	electric permittivity	[F/m]

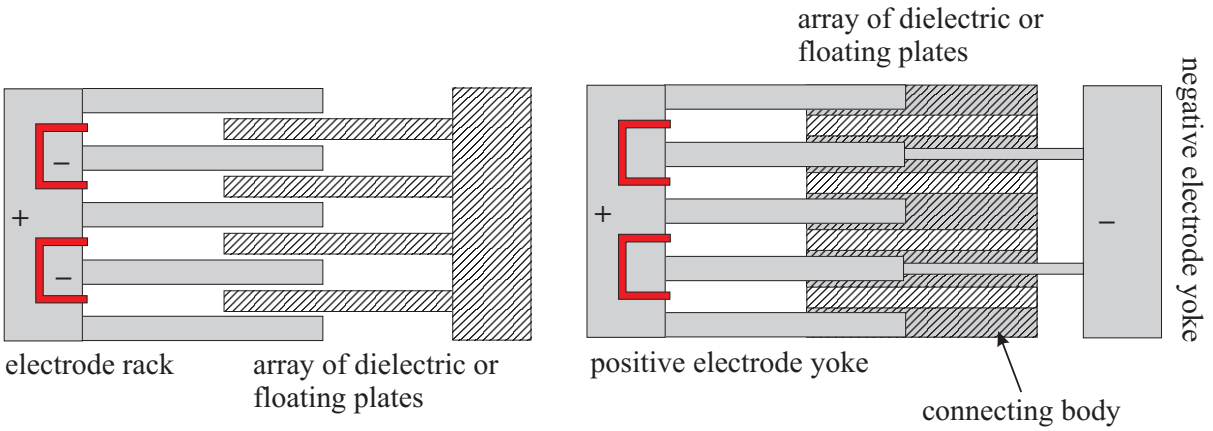

Figure 6.13: Electrode structures: Comb-drive layout (left) and alternative layout (right). The structures are meant to move in-plane in the longitudinal direction of the teeth. Here it is not yet decided which part will be fixed and which part will be moving.

the charge-sheet's position do not have to be taken into account. An energy analysis based on this assumption is presented in appendix C on page 181. The expression for the force in y-direction resulting from this analysis is finite and only depends on the y-direction in first order. As a consequence the electrostatic stiffness in the y-direction is constant, meaning no side pull-in instability will be expected. This means a charged dielectric will not lead to side pull-in. However, the model in its present form is not complete and its predictions are not fully understood yet.

Net charge on a floating conductor is not fixed, which means the results of the model for the charge-sheet cannot be used to model this situation. A suitable model for this situation was not formulated yet. The free charge on the floating plate should be considered an extra degree of freedom in the model. In light of the challenges met modelling a fixed charge, modelling a free charge is regarded a generalization for when the model for the fixed charge is completed and fully understood. For a solution on the device-level in the case of a net charge, the plate can be discharged periodically by connecting it to ground.

6.4 Geometry and design

Initially, the idea to fabricate a dielectric actuator was an early alternative for the vertical comb-drive. Unfortunately, the fabrication to enable the vertical motion met many problems. A new design and process is proposed meant for an in-plane actuator and the troublesome fabrication steps are not part of it anymore. However, due to the decision to give priority to the fabrication of the planar 3 DOF stage and the out-of-plane comb-drive, and due to the limited time available, a prove of principle for the

dielectric actuator has not been fabricated. In spite of that, this chapter is considered incomplete, without the reflections on the implementation of the dielectric actuator. In this section the required geometry is discussed, while in the next section the proposed fabrication process is explained.

The analysis in the previous sections shows the dielectric and floating plate transducers perform less well than a conventional comb-drive with respect to force density for equal driving voltages. For a relatively large force density the gap between the electrodes and the plates is best to be small. Preferably this gap should be below 2 μm, which is quite demanding for the fabrication. Furthermore, compared to a comb-drive, the alternative transducers need two electrode structures and an array of dielectric or floating plates. This means the routing of the electrode connections is more complicated. In a conventional comb-drive both comb-racks each have their particular voltage. For the alternative transducers there are two options for the electrode structures, shown in a top-view in figure 6.13. The first option shows an equivalent layout as the one used in a comb-drive, except that one rack shows alternating electrodes with a positive and negative voltage and the other is an array of dielectric or floating plates. To connect to the alternating electrodes a metal or doped poly-silicon layer insulated from the bulk is required. The second option uses two yokes, one with a positive and one with a negative voltage (voltages are arbitrarily defined on the yokes). Only the negative electrodes span between both yokes, while these are electrically insulated from the positive yoke. The distance of the negative electrodes to these plates is larger where they extent beyond the positive electrodes, to make sure the influence of the extended parts on the generated force is minimal. For the last option the electrical routing is less complex, but the plates need to be mechanically connected to each other via a body below or above the electrode structure.

Apart from the kind of electrode structure used, the a choice is made for either moving electrodes or moving dielectric/floating plates. It is not expected that one or the other option will make much of a difference for the dynamics of the system, since the moving masses in both situations do not need to be much different. Anyhow, for the ease of electrical interconnect it might be beneficial to decide for a fixed electrodes structure, since in that case the suspension is not subjected to demands with respect to electrical interconnect. On the other hand, if the second option for the electrode structure is chosen, it is technologically easier to have the dielectric/floating plates fixed to the bulk an the electrodes moving. Since in that case the required connecting body is formed by the substrate (see figure 6.13).

Because the fabrication process requires many more steps to interconnect the alternating electrodes of the first option, it is decided to proceed with the second option combined with moving electrodes. Figure 6.14 shows a detail of a 3D model of this

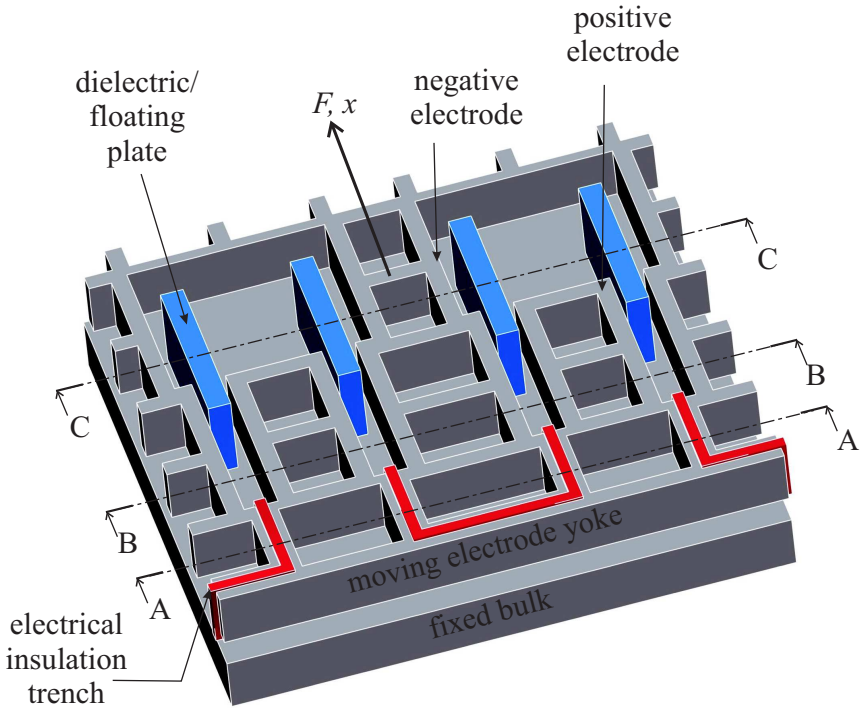

Figure 6.14: 3D design of the actuator applying moving electrodes of the second option.

concept. Mainly two parts can be distinguished; one moving part (the electrode yoke) and a fixed part (bulk) to which the dielectric or floating plates are fixed. The moving part might be suspended by folded flexures as done usually in a conventional comb-drive system. These flexures can be employed as electrical connections. Where the suspension connects to the bulk, electrical insulation trenches should be applied and the capacitance to the bulk is preferred to be as small as possible to ensure a small electrical coupling to the dielectric or floating plates. A small coupling reduces possible charging of the preferably neutral plates. Insulation trenches are also applied to electrically separate the negative from the positive electrodes. F and x respectively show the direction of the attracting force and the displacement. The rectangular holes in the electrode yoke serve as etch-holes used to release the yoke by means of isotropic dry etching.

Although the design shows a small gap between the electrodes and the plates, the electrode structure itself has relatively large dimensions. This still causes the force density to be below that of a conventional comb-drive. Nevertheless, a small gap is beneficial to reduce the voltage that is required for a certain delivered force.

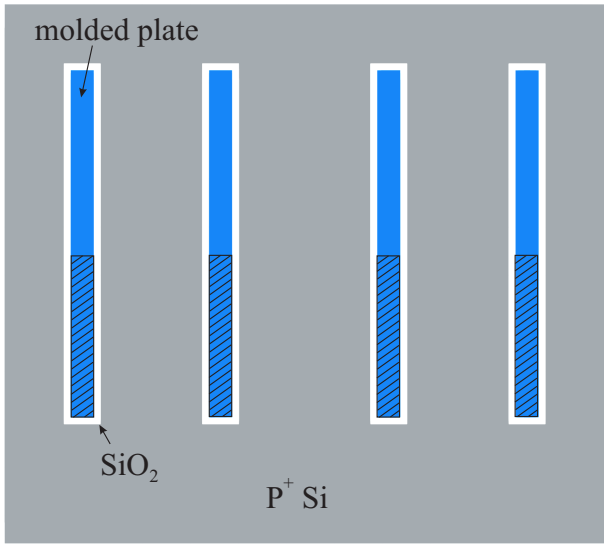

Figure 6.15: A schematic top-view showing the principle of molding the SiRN plates.

6.5 Proposed process

The requirements for the process are mostly concerned with the geometry, especially the small gap between the electrodes and the dielectric or floating plate. But also the structuring of the plate, and the required electrode structure pose challenges. An elegant method to fabricate features below the minimum feature size of the lithography (2 μm) employs a thin film as sacrificial spacer [11]. The dielectric or floating plates can be molded in a trench etched in highly doped Si. The walls and bottom of this trench are oxidized by thermal oxidation. This oxide is used as sacrificial spacer. The electrodes will automatically be formed by the Si at both sides of the molded plate. However, the molded plate should still be tailored in its longitudinal direction, since otherwise the plates have no clearance to move. In figure 6.15 a schematic top-view of four molded plates surrounded by a sacrificial oxide spacer is shown. The shaded part shows the length reduction of the plates required for movement of the electrode yoke.

In case of dielectric plates, the length of the plates can be reduced making use of a sacrificial filling with poly-silicon, which is removed by Bosch etching via a mask that only has openings over the non-shaded areas. The partially emptied trenches are subsequently filled with SiRN, forming the dielectric plates. SiRN is relatively resistant to the Bosch and isotropic release process, thus the structuring of the electrode yoke and its release will not harm the SiRN plates. Furthermore, during the etching, the remaining poly-silicon will be removed from the trenches, providing the required clearance to move.

In the proposed process, the etch selectivity of SiRN with respect to the etching of

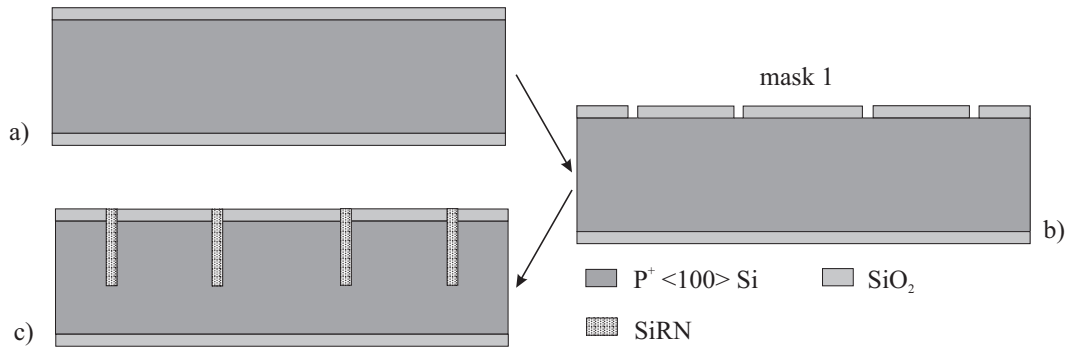

Figure 6.16: Process sequence for cross-section AA.

silicon is used to create dielectric plates. For conducting floating plates, doped poly-silicon could be used, however these will be etched during the etching of the bulk Si. Adapting the process for plates of doped poly-silicon will not be straightforward. Protecting the poly-silicon by oxidation will conflict with the oxide mask on the other structures. Presumably, the most feasible process to fabricate the transducer with conducting floating pates is a process used for normal comb-drives [12].

6.5.1 Process sequence

Figure 6.14 on page 151 indicates three cross-sections AA, BB, and CC. The process involves different structures for each of these cross-sections. Section AA goes through the electrical insulation trenches. Figure 6.16 shows this cross-section and the process-flow to obtain the insulation trenches. The process starts with a highly doped $\langle 100 \rangle$ Si wafer. By thermal oxidation a 3 μm thick layer of SiO_2 is grown, which is required mostly as a mask for other structures, figure 6.16a. The first mask is applied with openings for the insulation trenches, and the oxide is etched with DRIE etching, figure 6.16b. Subsequently the 2 μm wide trenches are etched in the Si by Bosch etching. These trenches are filled with LPCVD SiRN and the top- and bottom-side is stripped up to the oxide, either by RIE or by wet-etching in H_3PO_4, figure 6.16c.

From here on the process continues explaining the structuring of cross-section BB, shown in figure 6.17, that goes through the electrode yoke. After the insulation trenches are formed, a second mask is applied for the 4 μm wide slits in which the plates will be molded (figure 6.17d). The mask is transferred into the oxide by RIE (figure 6.17e) and before the slits are etched into the Si a third mask is applied to define the rest of the mechanical structure including the etch-holes for the release. This mask is etched into the oxide up to a depth of about 1 μm, and will be completed later in the process, figure 6.17f. Subsequently the slits are etched into the Si by Bosch etching. The walls are oxidized up to a thickness of 1 μm to form the sacrificial layer for the

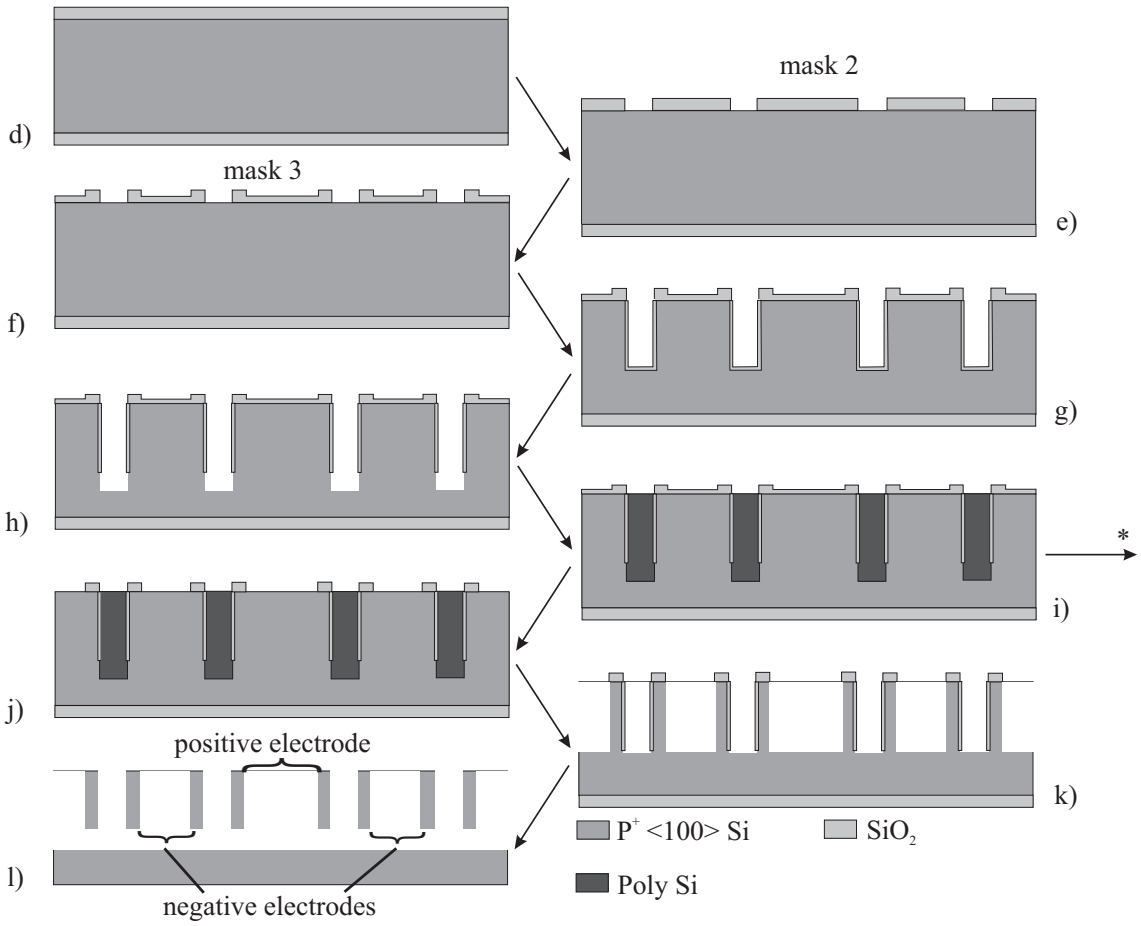

Figure 6.17: Process sequence for cross-section BB.

gap between the plates and the electrodes, figure 6.17g. The oxidation consumes Si and reduces the slit width to 3 μm.

Afterwards, the oxide on the bottom of the slitsis etched and the slits are extended further into the silicon to ensure a proper fixation of the plates, figure 6.17h. As a consequence of etching the oxide on the bottom, the oxide on the topside is also reduced in thickness. The slits are filled with LPCVD poly-silicon and the poly-silicon is removed from top- and bottom-side by RIE, figure 6.17i. This is the sacrificial filling. After this step the process overview shows a branch marked with *. Two extra steps involving the replacement of poly-silicon with SiRN to form the SiRN plates will follow, but these do not apply to cross-section BB. These steps are shown in figure 6.18 and will be discussed later. First, the remaining steps j) to l) in figure 6.17 are discussed. After the SiRN plates are formed, the oxide on the top-side is etched by RIE until the thin parts are removed, figure 6.17j. The thick oxide parts still form the mask for the mechanical structure. The etch-holes and mechanical structure are etched into the Si by Bosch etching up to a depth 3 μm less than the depth of the

insulation trenches, figure 6.17k. Also the poly-silicon is removed during this etching. Subsequently, the electrode yoke is released by dry isotropic etching [12] and all the oxide is etched in HF followed by freeze-drying, figure 6.17l.

Figure 6.18 shows cross-section CC. The steps j'), k') and l') involve the same processes as in steps j), k) and l) in figure 6.17, but than for cross-section CC. Steps i'_{I}) to i'_{III}) are an intermezzo in which the sacrificial poly-silicon in the molds is partly removed and replaced by SiRN. After the slits are filled with poly-silicon (figure 6.18i'_{I}), a fourth mask, with a rectangular opening exposing the slits over the length required for the SiRN plates, is applied (see figure 6.19 op page 156). The photo-resist together with the already present oxide-mask forms the combined mask to selectively remove the poly-silicon. This fourth mask does not need to be very precise. The poly-silicon is removed by Bosch etching (figure 6.18i'_{II}). Afterwards the photo-resist is removed and the opened slits are filled with LPCVD SiRN. The SiRN is subsequently removed from top- and bottom-side, either by RIE or by wet-etching in H_3PO_4 (figure 6.18i'_{III}). After this last step of the intermezzo, the process continues similar to the processing of cross-section BB, figure 6.18k' and l', with the exception that the SiRN is not etched during the Bosch etching and isotropic release.

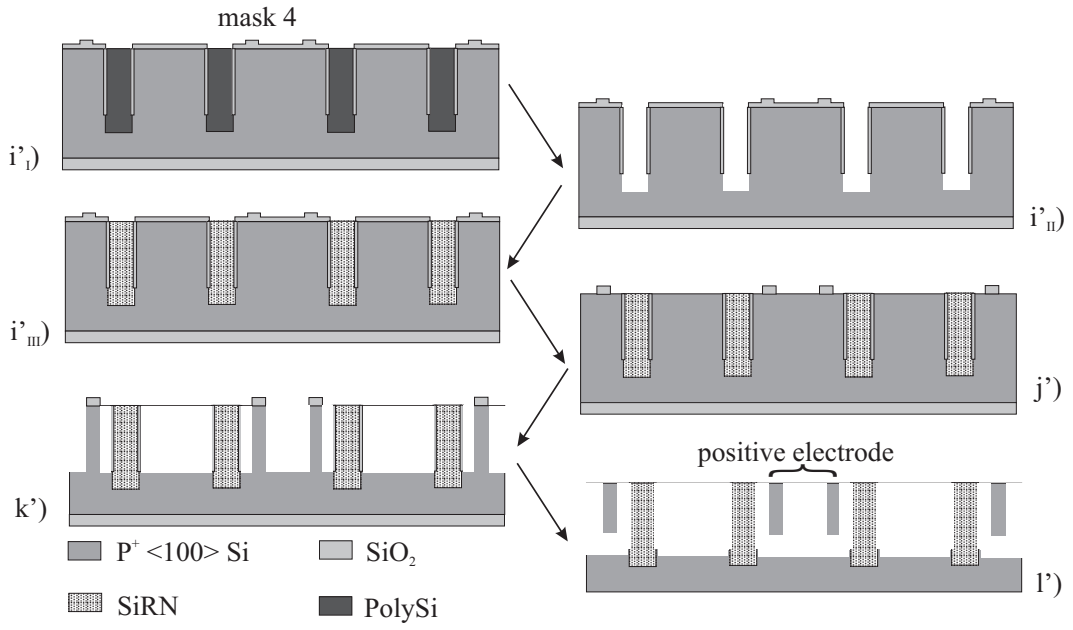

Figure 6.18: Process sequence for cross-section CC.

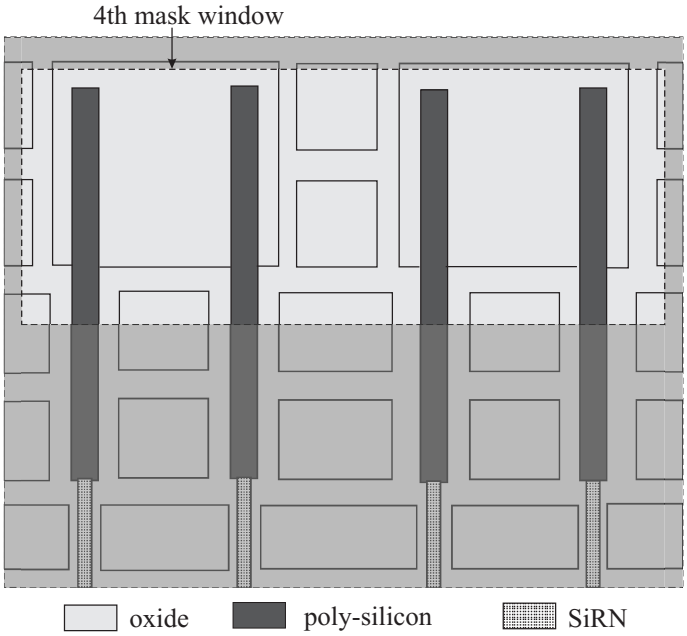

Figure 6.19: Fourth mask.

6.6 Conclusion and discussion

In this chapter two alternative electrostatic actuators are presented. One is based on the increase of the capacitance by inserting a dielectric plate between two fixed parallel-plate electrodes. The other is based on the increase of capacitance by geometrically decreasing the gap that the electric field bridges, by inserting a floating conductor between two fixed parallel-plate electrodes. In contrast to a conventional comb-drive, for side-ways displacement of the dielectric or floating plate, the capacitance does not approach infinity. For this reason, side pull-in is not expected for the alternative actuators. A first order analytic model for these actuators does not predict a force in side-ways direction. Since the analytic model does not take into account fringe fields, additional FEM modelling was performed. As a result, for both actuators, side-ways forces have been found. However, these forces are roughly three orders of magnitude smaller compared to the side pull-in force in a comb-drive. Furthermore, the trends of graphs of these forces do not show a tendency to approach infinity for the dielectric or floating plate touching one of the electrodes. Based on these results, side pull-in for the alternative actuators is not expected and the demands on the side-ways stiffness of the suspension are far less rigorous.

According to a model formulated to study the forces on a charge-sheet between parallel-plate electrodes (see appendix C), no side pull-in is expected for a dielectric charged with fixed charges. However, the validity of the model is not beyond dispute. The influence of charge on a floating plate cannot be studied with this model, because

the model assumes fixed charges. For this situation an the model should be extended with an extra degree of freedom for the charge distribution on the floating plate. However, first the model for a fixed charge-sheet should be fully understood.

The forces of the alternative actuators in actuation direction are relatively small compared to a comb-drive with similar dimensions. The pure theoretical upper limit is one-fourth of force a comb-drive can deliver. However, using a molding technique to fabricate the dielectric plates, a relatively small gap may be obtained between the plates and the electrodes. This process is based on the etch-selectivity of SiRN with respect to silicon. Since for the comb-drive and the floating transducer, both comb-racks are assumed to be made of silicon, the molding process cannot be applied directly to a comb-drive. This means, on basis of feasible geometry, the performance of the dielectric actuator increases compared to the comb-drive.

As was explained in section 6.4, the idea to apply an electrostatic actuator was originally meant as an alternative for out-of-plane actuation. Since the fabrication process to obtain the required geometry for vertical motion appeared to be too ambitious, this actuator has not been fabricated. Even though the process proposed for an in-plane moving alternative is less challenging, a proof of principle has not been fabricated. The reason for this is the decision of giving priority to fabrication of the 3 DOF planar stage and the vertical comb-drive. This decision is mainly driven by the larger flexibility the process for the vertical comb-drive offers.

References

[1] Y. Nemirovsky and O. Bochobza-Degani, "A methodology and model for the pull-in paramters of electrostatic actuators," *J. MEMS*, vol. 10, no. 4, pp. 601–615, 2001.

[2] R. Nadal-Guardia, Dehé, R. Aigner, and M. Castañer, "Current drive methods to extend the range of travel of electrostatic microactuators beyond the voltage pull-in point," *J. MEMS*, vol. 11, no. 3, pp. 255–263, 2002.

[3] O. Bochobza-Degani, D. Elata, and Y. Nemirovsky, "A general relation between the ranges of stability of eletrostatic actuators under charge or voltage control," *App. Phys. Lett.*, vol. 82, no. 2, pp. 302–304, 2003.

[4] B. Borovic, F. L. Lewis, A. Q. Liu, E. S. Kolesar, and D. Popa, "The lateral instability problem in electrostatic comb drive actuators: modeling and feedback control," *JMM*, vol. 16, pp. 1233–1241, 2006.

[5] L. A. Rocha, L. Mol, E. Cretu, and R. Wolffenbuttel, "Experimental verification of squeezed-film damping models for MEMS.," in *MME*, (Göteborg, Sweden), pp. 244–247, 2005.

[6] S. M. Sze, *Physics of Semiconductor Devices*. John Wiley and Sons Inc, New York, 1981.

[7] G. Zavala, J. H. Fendler, and S. Trolier-McKinstry, "Characterization of ferroelectric lead zirconate titanate films by scanning force microscopy," *J. Appl. Phys.*, vol. 81, no. 11, pp. 7480–7491, 1997.

[8] http://www.flexpde.com/.

[9] J. Wibbeler, G. Pfeifer, and M. Hietschold, "Parasitic charging of dielectric surfaces in capacitive microelectromechanical systems (MEMS).," *Sensors and Actuators A*, vol. 71, pp. 74–80, 1998.

[10] O. Bochobza-Degani, E. Socher, and Y. Nemirosky, "On the effect of residual charges on the pull-in parameters of electrostatic actuators.," *Sensors and Actuators A*, vol. 97-98, pp. 563–568, 2002.

[11] C. G. Keller and R. T. Howe, "Hexsil tweezers for teleoperated micro-assembly," in *IEEE MEMS*, (Nagoya, Japan), pp. 72–77, 1997.

[12] E. Sarajlić, M. J. De Boer, H. V. Jansen, N. Arnal, M. Puech, G. J. M. Krijnen, and M. C. Elwenspoek, "Advanced plasma processing combined with trench isolation technology for fabrication and fast prototyping of high aspect ratio MEMS in standard silicon wafers," *J. Micromech. Microeng.*, vol. 14, pp. S70–S75, 2004.

Chapter 7

Conclusions and outlook

7.1 Conclusions

As part of the Multi Axes Micro Stage project, the possibilities and requirements to design and fabricate a MEMS 6 DOF manipulation stage with nanometer resolution have been investigated. To enable precise, nanometer resolution manipulation, the application of design guidelines known from design theory for precision systems was considered the starting-point in the design phase. Design for macroscopic precision system differs from design for MEMS systems with respect to assembly, fabrication techniques and the feasibility of desired geometries. The insight this research has delivered will be summarized in this chapter with respect to design, modelling, fabrication and measurement results. Furthermore, the alternative electrostatic actuators are discussed. Finally, an outlook will be given, discussing the application of the results of this research and directions for further study.

7.1.1 Design

Exact kinematic constrained design The 2.5-dimensional nature of MEMS fabrication poses limitations to the realizable geometries. Especially structuring in the height direction complicates fabrication. Additionally, assembly in MEMS in most cases is no option, because it has limited accuracy, is time-consuming (and thus expensive) and the benefits of integration that characterize MEMS is lost. As a consequence the freedom to design kinematic constrained mechanisms is limited compared to design

for macroscopic systems. Flexible mechanisms in MEMS are dominated by a type of beam that is relatively long compared to its height and thickness. A real plate-spring with a sufficiently large height/thickness-ratio is often not achievable. For this reason the stiffness in height direction of the typical MEMS beam is situated somewhere between a real plate-spring and a slender beam with rectangular cross-section.

An important reason to apply exact kinematic constrained design is the fact that small mismatches in assembly are inevitable. This increases the chance of non-linear behavior in an over-determined mechanism. In MEMS most mechanisms do not require assembly because they are monolithic. Still stress accumulation due to an overconstrained design is possible in case of non-homogenous temperature increase within a device, or in case processing causes geometry variations in the mechanism elements (e.g. folded flexures in case of a comb-drive). As was shown in chapter 3, one cause of variation is caused by the orientation of the devices with respect to writing direction of the mask. Non-uniformity of the etching process is not expected to cause significant variations on the device level since the etch-process is usually uniform on the scale of the typical device dimensions.

The above only concerns the device itself. Important aspects which are not within the scope of this thesis are packaging and electrical interconnects[1]. Finding suitable solutions for the packaging and electrical interconnects will most certainly be far from trivial. Routing of the electrical interconnects within the device can be accomplished by extended use of electrical insulation trenches and serpentine like spring structures which are highly compliant. It should be taken into account that the solution for electrical routing potentially causes an overconstrained system. Additionally, packaging introduces deformations in the system. To prevent stress concentrations due to these deformations an exact kinematic constrained design is very important.

System concept The mechanism is based on flexures to avoid friction and play. It is chosen to fabricate the mechanism totally in single crystalline silicon because its mechanical properties of low hysteresis and creep are very suitable for precision systems.

A parallel kinematic mechanism is chosen because it is compact[2], allows easy electric interconnect and is potentially high frequent. For out-of-plane manipulation it was decided to use direct out-of-plane actuation in stead of a mechanism converting

[1]Most literature about MEMS devices in the experimental phase do not concern packaging and electrical interconnects. Since the design and fabrication of the bare device are often a large challenge, this is very understandable. However, by not taking into account packaging and electrical interconnect, important reliability issues are easily overlooked.

[2]In macroscopic systems compactness of parallel mechanisms is not evident. However in MEMS where the third dimension is often hard to employ for stacking, a parallel mechanism offers possibilities for a compact design.

in-plane to out-of-plane motion. As a consequence the choice was made to group the 3 in-plane DOFs in one parallel kinematic mechanism and the 3 out-of-plane DOFs in another parallel kinematic mechanism. The planar stage is embedded into the platform of the out-of-plane stage. Both stages consist of three actuators symmetrically placed around a platform, connected via a flexure mechanism. With actuators strokes of ± 10 μm the planar stage reaches a manipulation space of 20 by 20 μm for zero rotation, which decreases for increasing rotation. The out-of-plane stage is able to reach out-of-plane positions ranging from -10 to 10 μm for zero tilt rotations, which decreases for increased tilt rotations.

In the situation of the planar stage stacked on top of the out-of-plane stage, the R_x and R_y tilt angles are very limited, because the tilt stage needs to carry the planar stage and requires a certain size. Stacking the stages the other way around means a smaller R_z rotation with given actuator strokes. The stacking order means a trade off with respect to the obtainable rotations. By optimization of the required space a stage requires, an increase of the maximum rotations is possible. However, the bottleneck is the relatively small rotations obtainable with a flexure mechanism. In case the large tilt angles of $\pm 30^\circ$ and $\pm 70^\circ$ are desired, a hybrid solution is required, where a "conventional" precision machined tilt stage carries the MEMS-stage. Here the MEMS stage is used for fine manipulation.

Actuation Both for in-plane and out-of-plane actuation, comb-drives are used. Comb-drives are able to deliver the required force and stroke (although in many cases they require considerable space) and are most suited for integration in a system where one and the same process is used for the mechanism, the in-plane actuators and the out-of-plane actuators.

The planar comb-drives are suspended by folded flexures. The suspension has been analyzed with respect to side and rotational pull-in instability. For the given design dimensions and the required driving voltage, instability is not expected.

The vertical comb-drives are suspended by torsion beams. The comb-teeth are placed at a long arm from the torsion axis to amplify the moment required for torsion. Torsion over a long arm is also used to create the required vertical stroke. A combination of LOCOS and deep oxidation of silicon has been applied to successfully self align the mask defining the gap between the comb-teeth and the mask to reduce the height of the fixed comb-teeth. To increase the lateral stiffness of the suspension and prevent side pull-in, two types of torsion beams have been analyzed; one with a symmetric $\perp$-shaped cross-section and one with an asymmetric L-shaped cross-section. Both increase the lateral stiffness considerable compared to a torsion beam with rectangular cross-section. The $\perp$-shaped torsion beam delivers the largest

stiffness increase, however its torsion stiffness (which should not increase too much) is much more sensitive for process variation as the torsion stiffness of the L-shaped torsion beam.

7.1.2 Modelling

Analytical beam modelling To model the stiffness of the flexure beams in the various DOFs, exclusive use is made of analytical models. In most cases, first order expressions have been used. In case of the lateral stiffness of the planar comb-drive folded flexure suspensions, a non-linear model is applied for the stiffness decrease in length direction of a deflected beam. This is very important since a first order model would lead to a large over estimation of the pull-in voltage.

In the cases of the ⊥-shaped torsion beam and especially the L-shaped torsion beam, analytical modelling is limited. Analytical calculation of the torsion stiffness for an arbitrary shape of the beam's cross-section in many cases is not practical and warping of the beam is hard to model. Furthermore, once the cross-section is asymmetric, predicting the behavior of the beam for various loading conditions is only possible in a sensible way via FEM analysis.

Finally, the assumptions of rigid constraints for the beams are often not valid, because of the etch-holes required for the release of the movable and electrically insulated structures. The compliance contributions due to the etch-holes are hard to model analytically and the effect should be studied by FEM analysis.

System modelling The parallel kinematics for both parallel stages is modelled with inverse kinematic models. These are first order, purely geometric models. Measurements on the 3 DOF manipulator have shown that these simple models are quite suited for coarse positioning of the MEMS system.

For the 3 DOF manipulator a power-port based model has been implemented as well. In contrary to a purely geometric kinematic model, this model takes into account stiffness and geometrical imperfections. Non-linear stiffness equations are easily applicable, if necessary.

Electrostatic modelling For modelling of the electrostatic comb-drives and the alternative electrostatic actuators, analytical multi-port models are used, based on the exchange of energy between the electrical and mechanical ports. For comb-drives this type of relatively simple modelling, which does not take into account fringe fields between the conductors, has proved to provide the forces and electrostatic stiffness accurate enough for design purposes.

7.1.3 Fabrication

Both lithography and etching potentially cause relatively large deviations from the designed geometry. This should be taken into account when designing a MEMS system. The design should be robust for these variations[3] and in many cases tests should be performed to determine how the geometry is affected by the fabrication. Care should be taken not to lose oneself in optimization of the design prior to knowing what deviation from the designed geometry can be expected.

Realized degrees of freedom The fabrication process for the vertical comb-drive enables both the fabrication of the 3 DOF planar stage and the vertical comb-drive. Although the later requires an improved mask design and process tuning to improve the realization of the geometry and the electrical insulation. Considering the working devices, the following degrees of freedom are obtained: for in-plane manipulation a x, y-translation of 18 x 19 μm in combination with 0 $^\circ$ R_z-rotation, reaching to a maximum R_z-rotation of 4 $^\circ$ combined with zero x, y-translation; for out-of-plane translation a stroke of 10 μm is obtained. The strokes for planar manipulation can be increased since comb-drives with large strokes are feasible. For increased in-plane stroke, steppers might be used as well. The increase of the out-of-plane stroke is challenging and might require a technology not based on isotropic release/under-etching. However the displacement can be amplified with an arm. This option requires a trade-off between available stroke and force.

The mechanism for 3 DOF out-of-plane manipulation as proposed in chapter 2 was also part of the mask-design. Unfortunately, due to the low yield of the vertical comb-drives, no drivable stage was obtained. Apart from the malfunctioning of the vertical comb-drives, the stages were completely released and free to move. Furthermore, gently tapping on the vertical comb-drives (connected to the stage) with a probe needle roughly showed the expected response of the stage. For this reason it is expected, the proposed design for the 3 DOF out-of-plane mechanism is feasible, although actuation has not been achieved.

Lithography The lithography in our lab shows limitations with respect to the smallest feature-size of 2 μm and the variation in the smallest feature size up to 10 %. The smallest feature size limits the smallest thickness of beams and combined with the limited aspect-ratio of the etching process, the height/thickness-ratio of the beams is limited. This is the main reason why a (vertical) beam with real plate-spring geometry is not found in MEMS systems.

[3] For instance designs should cope with variations in geometry.

The variation on the beam thickness, potentially causes a large deviation from the designed value of the stiffness for bending in its thin direction. The transfer during etching of the variation in the feature-size over the complete height of the beam should still be determined.

Etching Various aspects of the applied etching methods influence the resulting geometry and pose limits to the design. The geometric definition of the vertical comb-drive is most influenced by these aspects, because of its three dimensional nature. Furthermore, successful functioning of the vertical comb-drive relies much more on an adequately defined geometry than the planar manipulator does.

Geometric definition by Bosch etching is dominated by tapering, loading and ARDE. Tapering has a large influence on the stiffness of vertical beams for bending in their thin direction. In combination with ARDE, tapering is crucial for the success of the electrical insulation with SiRN insulation trenches. ARDE and loading cause differences in etch-depth between trenches and etch-holes. In case this is not taken into account in the mask design the dry isotropic release can either be unsuccessful or cause damage to sidewalls of surrounding structures.

The dry isotropic release itself shows a profile and etch-speed depending on the aspect ratio of the trench or hole it starts from: The higher the aspect-ratio, the more the profile is stretched in vertical direction and the lower the etch-rate. The profile causes considerable roughness to the bottom-side of beams and in case of horizontal plate-springs, the bottom-side is far from flat.

7.1.4 Measurement results

Methodology A number of measurement methods have been applied; Laser doppler vibrometry, white light interferometry and video-based correlation techniques for in-plane measurements. For the first two methods the Polytec MSA-400 Micro System Analyzer was used exclusively. The last method was applied both with the MSA-400 Micro System Analyzer and with the National Instruments Vision Toolbox. The first two methods are based on interferometry and therefore offer measurement resolutions well below nanometer resolution. Pattern recognition potentially offers a resolution in the sub-nanometer range, however this depends much on the measured object. The grid structure of the devices posed limits to the resolution with which in-plane displacements could be measured, since it is a repeating pattern, complicating pattern recognition. In both cases the measurement error was in the order of 50 nm. As a consequence, in-plane characterization with respect to nanometer resolution positioning is beyond the scope of this thesis.

Nanometer resolution Although nanometer resolution positioning was not characterized, a flexure mechanism in SCS and the predictable response resulting form the position measurements of the 3 DOF manipulator, potentially enable nanometer resolution positioning. To confirm low hysteresis in SCS, a qualitative measurement was performed, not showing significant memory effects. This promotes the used of SCS for flexure based precision mechanisms. Furthermore, out-of-plane cross-talk due to imperfect beam geometries and orientations of the beams with respect to the crystal directions have been characterized. The results show, the out-of-plane position for pure planar manipulation is guaranteed well within a nanometer.

7.2 Alternative electrostatic actuators

Two alternative actuators which show very small (if any) sensitivity to side pull-in are investigated. In both cases a plate is inserted between two parallel electrode plates. This plate can either be a dielectric or a floating conductor. According to an analytic multi-port model not taking fringe fields into account, there is no force in lateral direction in these actuators. However, FEM simulations where fringe fields are taken into account, do show lateral forces. Compared to the comb-drive, the forces by far do not show an equally strong increase for the plate approaching one of the electrodes. To evaluate the influence of charge, an analytical model for a charge sheet between to electrodes has been derived. The validity of some of the assumptions this model is based on requires further study. As a result of this model, the lateral force acting on a charge-sheet is directly proportional to its lateral position. In other words, the resulting electro static stiffness will be constant.

All in all these actuators show to be far less sensitive to side pull-in than conventional comb-drives. Potentially larger driving voltages and strokes are allowed. The force obtained in driving direction is much smaller than that of a conventional comb-drive having equal dimensions. As shown in chapter 6 the dielectric actuator might be fabricated with a very small gap between the dielectric and the electrodes. This concept cannot directly be used for a comb-drive since the process is based on the selectivity of SiRN with respect to Si. The small gap allows a larger force for a given driving voltage. The process to enable the small gap is however relatively complicated. But also in general the fabrication process for the alternative actuators are shown to be more complex than for conventional comb-drive. A prove of principle is required to validate the benefits if these alternative actuators and decide if the improved stability weighs up against increased complexity of the fabrication process.

7.3 Outlook

A flexure mechanism for multi-DOF manipulation, fabricated in SCS, offers promising prospects for downscaling of high precision systems like manipulators. Miniaturization offers important benefits: High-frequent dynamics allowing predictable responses (no resonances induced by low frequent vibrations), small thermal drift due to rapid temperature stabilization, small form-factor for application in small volumes, complete, monolithic integration of all system parts, and potential cost-reduction at large numbers due to batch-fabrication.

Of these benefits, high-frequent dynamics, small thermal drift, and small form-factor give MEMS manipulators most potential compared to larger sized, conventional manipulators. The high frequent dynamics and small size allow for solutions where the manipulator is strongly coupled to a frame holding a measurement probe of some sort or a nano-machining tool. In this way there is no acceleration difference between the frame and the manipulator for low frequent vibrations in the frame. The small thermal drift can largely reduce the time required for sensitive equipment to stabilize. The work discussed in this thesis shows planar manipulation over tens of microns is possible. Out-of-plane manipulation is within reach. Applications demanding large rotation angles benefit more from precision machining solutions which are not based on flexible mechanism, but allow for rotation hinges with small play (by pre-tension) and very predictable friction[4].

Although cost reduction due to batch-fabrication is possible, the fabrication itself and especially the research and development of MEMS systems is very expensive. Commercial applications like printheads do show there is a market for MEMS in mass production. In case of the example of the digital mirror device used in beamers, one might wonder if the ten (or more) years of research and development pay off. Since MEMS-based precision systems currently require specialized and unique processes, potential applications should either be highly specialized or suitable for mass-production. An example of a specialized application is a manipulator, outperforming conventional manipulation techniques, for often expensive equipment used for e.g. nanometer characterization or nano-technology. While high density, shock-proof, fast accessible data storage is an example of a mass-production application. For intermediate numbers of devices, it is not beneficial to develop a unique process. These applications require standardization to enable manufacturing in a foundry process, where many sorts of devices of various costumers on a wafer are all fabricated with the same process.

[4]In these aspects, precision machined mechanisms allow more design freedom, but to meet the required demands, a highly specialized design is needed nevertheless.

Because the fabrication of MEMS often does not allow mechanical elements with a clear difference between rigid and compliant directions (like real plate-springs and fully rigid bodies) simulation tools capable of (non-linear) modelling of complex systems should be given increased attention over analytic modelling. Resulting from the numerical, non-linear simulations, analytical rules of thump can be derived to design system parts for well defined situations.

Defining geometry with MEMS technology is shown to be challenging. More knowledge on the influence of etch process-variables on the geometry definition is required. Using this knowledge the process can be tuned to obtain the desired geometry and design-rules can be derived for improved mask design. One should think of the influence of the process conditions with respect to tapering, the influence of loading, the amount of ARDE, the coverage and resistance of the protective fluor-carbon layers, the profile of the Bosch and dry isotropic etching and the selectivity of dry isotropic etching with respect to the fluor carbon protected sidewalls. Mask design rules and criteria are required defining the maximum spread in etch-hole sizes, the use of etch-holes combined with trenches, the shapes allowed for etch-holes and the required mask tolerances e.g. to ensure successful electrical insulation. Chapter 5 discusses many aspects that influence the geometry during fabrication. Some guidelines are given to improve the geometry, but it is also recognized that thorough process development and definition of design-rules is hard to combine with the desire to obtain a device in the available time.

For increased flexibility in mechanism design, process innovation needs to continue. Processes are looked for, enabling machining of the silicon wafer with high resolution from both top and bottom side like the Multilevel Beam SOI-MEMS process discussed on page 105. Additionally, application of mask-writing and alignment equipment capable of higher resolution and accuracy could mean a large improvement in cases of definition of micron-sized features on the masks and tolerances of mask alignment and wafer bonding.

In this research no attention is payed to packaging and electric interconnect. The probe-pads consisting of a mesh with etch-holes as obtained with the fabrications processes used in this work pose challenges for electric interconnect. Flip-chip techniques in combination with indium-solder might offer possibilities to mount a device on a printed circuit board. In cases were the electric field of the comb-drives causes interference e.g. with an electron-beam, the devices can be shielded by a highly doped silicon wafer bonded on top of the device wafer.

appendix A

Stiffness matrix reinforced plate-spring

The stiffness matrix for the reinforced plate-spring as given in figure A.1 is derived with help of the standard equation for the deflection (f) and the angle (ϕ) at the end of a beam as a function of the applied force (F) and moment(M) at the end of a beam [1]:

$$f(M,F) = \frac{ML^2}{2E_Y I} + \frac{FL^3}{3E_Y I} \tag{A.1a}$$

$$\phi(M,F) = \frac{ML}{E_Y I} + \frac{FL^2}{2E_Y I} \tag{A.1b}$$

The standard relations are based on the assumption that Hooke's law is valid, so deflections and angles are small relative to the thicknesses of the beams. Additionally this assumption allows the use of superposition. Accordingly, the total deflection (f_t) and angle (ϕ_t) at the end of the reinforced plate-spring is obtained by:

$$f_t(M,F) = f_3(M,0) + f_3(0,F) \tag{A.2a}$$

$$\phi_t(M,F) = \phi_3(M,0) + \phi_3(0,F) \tag{A.2b}$$

First, $f_3(M,0)$ and $\phi_3(M,0)$ are calculated for the case of $F = 0$:

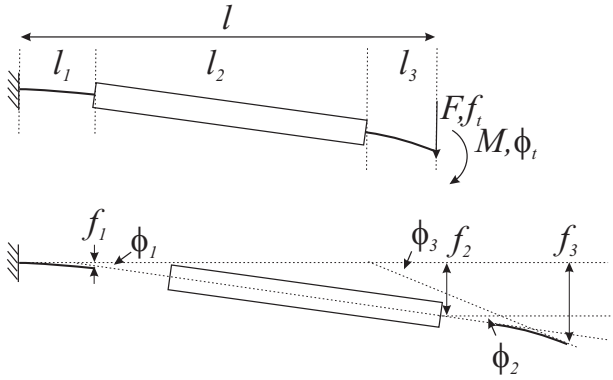

Figure A.1: Schematic of the reinforced flexure and the definition of the partial deflections and partial angles.

$$\begin{aligned} f_3(M,0) &= f_2 + \phi_2\, l_3 + \frac{M\, {l_3}^2}{2\, E_Y I} & \phi_3(M,0) &= \phi_2 + \frac{M\, l_3}{E_Y I} \\ f_2(M,0) &= f_1 + \phi_1\, l_2 & \phi_2(M,0) &= \phi_1 \\ f_1(M,0) &= \frac{M\, {l_1}^2}{2\, E_Y I} & \phi_1(M,0) &= \frac{M\, l_1}{E_Y I} \end{aligned} \tag{A.3}$$

Where E_Y is the Young's modulus and I the moment of inertia, both equal for part 1 and 3. The reinforcement, part 2 is assumed to be fully rigid.

Second, $f_3(0,F)$ and $\phi_3(0,F)$ are calculated for the case of $M = 0$:

$$\begin{aligned} f_3(0,F) &= f_2 + \phi_2\, l_3 + \frac{F\, {l_3}^3}{3\, E_Y I} & \phi_3(0,F) &= \phi_2 + \frac{F\, {l_3}^2}{2\, E_Y I} \\ f_2(0,F) &= f_1 + \phi_1\, l_2 & \phi_2(0,F) &= \phi_1 \\ f_1(0,F) &= \frac{F\, {l_1}^3}{3\, E_Y I} + \frac{M_F\, {l_1}^2}{2\, E_Y I} & \phi_1(0,F) &= \frac{F\, {l_1}^2}{2\, E_Y I} + \frac{M_F\, l_1}{E_Y I} \end{aligned} \tag{A.4}$$

Where M_F is the moment at the end of beam part 1 as a result of the force F multiplied by the arm $l_2 + l_3$. In other words, $M_F = F(l_2 + l_3)$.

Finally, by combining the partial results into (A.2), the following inverse stiffness matrix is found (where l is the total length of the reinforced plate-spring):

$$\begin{bmatrix} \phi \\ f \end{bmatrix} = -a \begin{bmatrix} \dfrac{l}{E_Y I} & \dfrac{b\, l^2}{2\, c\, E_Y I} \\ \dfrac{b\, l^2}{2\, c\, E_Y I} & \dfrac{d\, l^3}{3\, c^2\, E_Y I} \end{bmatrix} \begin{bmatrix} M \\ F \end{bmatrix} \tag{A.5a}$$

The coefficients a, b, c and d are given by:

$$
\begin{aligned}
a &= p - 1 && \text{with } p = \frac{l_2}{l} \\
b &= (p+1)(q-1) + 2 && \text{with } q = \frac{l_1}{l_3} \\
c &= q + 1 \\
d &= a^2 + c^2 + p\,(p+1)\,q\,(q-1) + 3p\,q - 1
\end{aligned}
\tag{A.5b}
$$

Inverting equation (A.5a) results in the stiffness matrix relating moment and force to deflection and angle:

$$
\begin{bmatrix} M \\ F \end{bmatrix} = -\frac{1}{a\,(4d - 3b^2)} \begin{bmatrix} \dfrac{4\,E_Y I\,d}{l} & \dfrac{-6\,E_Y I\,b\,c}{l^2} \\ \dfrac{-6\,E_Y I\,b\,c}{l^2} & \dfrac{12\,E_Y I\,c^2}{l^3} \end{bmatrix} \begin{bmatrix} \phi \\ f \end{bmatrix} \tag{A.5c}
$$

References

[1] J. M. Gere, *Mechanics of Materials*. Thomson Brooks/Cole, 6^{th} ed., 2004.

appendix B

L-torsion beam: Method 2

As discussed in chapter 4, the height d of the horizontal parts of the $\perp$-shaped torsion beam is of large influence for the torsion stiffness. Technologically, dimension d is hardest to control. An increase of the torsion stiffness results in an increase of the required driving voltage. The influence of d on the overall torsion stiffness can be reduced much by adding just one horizontal part to the vertical part. This results in a torsion beam with an L-shaped cross-section.

Since the cross-section of an L-torsion beam is not symmetric, the principle axes of rigidity are not parallel to the symmetry axis of the individual beam-parts [1]. To find the values for c_x, c_z k_x and k_z, first the orientation of the principle axes of rigidity is required. The shape factor for torsion can be found similar as described in section 4.3.1 on page 88.

Principle axes of rigidity For beam cross-sections with three or more axes of symmetry, each axis through the symmetry center is a principle axis and the moment of inertia about this axis is independent of the orientation-angle. For a cross-section with at least one axis of symmetry, one of the principle axis coincides with the axis of symmetry and the other is perpendicular to that axis (this case applies to the $\perp$-torsion beam). The axes cross each other in the *centroid*, which is located on the symmetry axis. The centroid is the point where an arbitrary couple of different neutral planes intersect with each other *and* the plane of the cross-section. The centroid can also be regarded as the "center of mass" of the cross-section [1].

For non-symmetric cross-sections, the principle axes of rigidity have to be found

by equating the product of inertia to zero. The resulting angle provides the orientation of the axis with respect to the cross-section. The principle axes are a couple of axes perpendicular to each other, where one is directed in the stiffest bending direction and the other in the most compliant bending direction.

The product of inertia for a certain set of orthogonal axes x_p and z_p is given by [1]:

$$\begin{aligned} I_{xpzp} &= \int_A x_p z_p \,\mathrm{d}A = \int_A (x\cos\theta + z\sin\theta)(z\cos\theta - y\sin\theta)\mathrm{d}A \\ &= \sin\theta\cos\theta \int_A (z^2 - x^2)\mathrm{d}A + (\cos^2\theta - \sin^2\theta)\int_A xz\,\mathrm{d}A \end{aligned} \tag{B.1a}$$

Where x and z form a coexisting set of orthogonal axes sharing the same centroid as x_p and z_p, and θ is the angle over which x turns counterclockwise to coincide with x_p (see figure B.1). In equation (B.1a) the integrals can be recognized for the moments of inertia I_x and I_z and the product of inertia I_{xz}. After some reordering of terms the expression reduces to equation (B.1b) [1].

$$I_{xpzp} = \frac{(I_x - I_z)}{2}\sin 2\theta + I_{xz}\cos 2\theta \tag{B.1b}$$

If x_p and z_p were to be the set of principle axes, I_{xpzp} would be zero. This results in the following expression for angle θ_p between set x, z and the set of principle axes x_p, z_p [1]:

$$\tan 2\theta_p = -\frac{2\,I_{xz}}{I_x - I_z} \tag{B.1c}$$

This equation yields two values for θ_p; one for the most stiff axis and one for the most compliant axis.

The moments of inertia and the product of inertia for an arbitrary set of axis x, z are required to find θ_p. Both for calculation of I_{xz} and of I_x and I_z it is easiest to have x parallel to the horizontal part of the L-torsion beam and z parallel to the vertical part, exactly as defined for the moments of inertia for the $\perp$-torsion beam on page 90.

Moments of inertia The moments of inertia are found similarly as discussed in section 4.3.1 on page 88. First the neutral-planes have to be determined. The neutral-plane distances Nx_L and Nz_L as defined in figure B.1 right are given by [1]:

$$Nx_L = \frac{a^2\,b + c^2\,d + 2\,c\,d\;(a+g)}{2\,(a\,b + c\,d)} \tag{B.2a}$$

$$Nz_L = \frac{a\,b^2 + c\,d^2}{2\,(a\,b + c\,d)} \tag{B.2b}$$

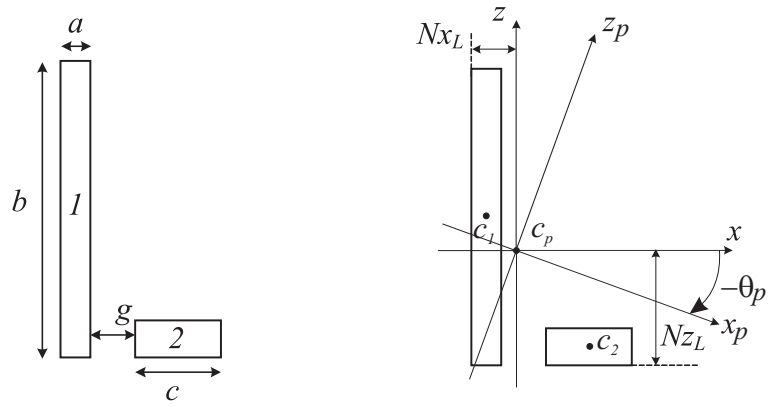

Figure B.1: Cross-sections of rectangular torsion beam (left), and L-shaped torsion beam (right), used to find the neutral-planes

With the neutral-planes known, the moments of inertia can be calculated [1]:

$$I_{xL} = \frac{a^2 b^4 + c^2 d^4 + 4\,a\,b\,c\,d\,\left(b^2 + d^2 - \frac{3}{2}\,b\,d\right)}{12\,\left(a\,b + c\,d\right)} \tag{B.3a}$$

$$I_{zL} = \frac{a^4 b^2 + c^4 d^2 + 4\,a\,b\,c\,d\,\left(a^2 + c^2 + 3\,g\,(a + c + g) + \frac{3}{2}\,a\,c\right)}{12\,(a\,b + c\,d)} \tag{B.3b}$$

Product of inertia The product of inertia $I_{xz_i}^{c_p}$ of each beam-part with respect to the centroid c_p for the complete cross-section is found by applying the *parallel-axis theorem for products of inertia* [1].

$$I_{xz_i}^{c_p} = I_{xz_i}^{c_i} + A_i\,d_{x_i}\,d_{z_i} \tag{B.4}$$

Where i is either 1 or 2, $I_{xz_i}^{c_i}$ is the product of inertia of part i with respect to its own centroid, A_i is the area of cross-section part i, while d_{x_i} and d_{z_i} are the x- and z-distances respectively between the centroids c_i and c_p for part i.

The total product of inertia I_{xzL} is found by superposition of $I_{xz_1}^{c_p}$ and $I_{xz_2}^{c_p}$ [1]. Since both beam-parts both have two symmetry axes, while x and z are oriented parallel to these axes, the products of inertia $I_{xz_1}^{c_1}$ and $I_{xz_2}^{c_2}$ are evaluated along the principle axes for each separate beam-part. This implies $I_{xz_1}^{c_1}$ and $I_{xz_2}^{c_2}$ are both zero, which reduces the calculation of I_{xzL} to multiplying of the distances d_{x_i}, d_{z_i} and area A_i followed by summation of over i.

The following values are inserted into equation (B.4) and the products of inertia with respect to c_p for both beam-parts are added:

$$\begin{aligned} A_1 &= a\,b & A_2 &= c\,d \\ d_{x_1} &= Nx_L - \frac{a}{2} & d_{x_2} &= a + g + \frac{c}{2} - Nx_L \\ d_{z_1} &= \frac{b}{2} - Nz_L & d_{z_2} &= Nz_L - \frac{d}{2} \end{aligned} \tag{B.5}$$

$$\begin{aligned} I_{xzL} &= I_{xz_1}^{c_p} + I_{xz_2}^{c_p} \\ &= \frac{a\,b\,c\,d(a^3\,b + c\,d^3 + 4\,a\,b\,g(a + c + g) + b\,c(2\,a^2 - 2\,d^2 + a\,c + b\,d)}{4\,(a\,b + c\,d)^2} \end{aligned} \tag{B.6}$$

With the expressions for I_{xL}, I_{zL} and I_{xzL} derived, the angle θ_p can be calculated. Using the values listed in table 4.2 on page 92 the two angles of -21° and 69° are found, respectively for the maximum and the minimum value for I_{xL} (and vise versa for I_{zL}).

Effects on stiffness values Since the forces and moments working on the suspension in the model shown in figure 4.4 on page 86 are not loading the L-torsion beam parallel to its principle axes of rigidity, the resulting displacements and rotation-angles of the beam-end will not be directed in the same direction as the applied loads.

In figure B.2 an example is given. In this example, the applied forces are assumed to load the beam in its *shear-center*. A force applied in this point does not result in any additional twisting of the beam [1]. For beam cross-sections with a double symmetric cross-section, the shear-center coincides with the centroid. In that case forces loading the beam at the centroid will never result in twisting of the beam. In the case of the L-torsion beam, there is no symmetry at all, hence the shear-center and centroid do not coincide. To avoid the need to take twisting into account in the analysis, the forces are assumed to affect the beam in its shear-center. Defining the position of the sheer-center and analysis of the influence in case forces do not affect the beam in its shear-center are not regarded part of the scope of this appendix. As a result, the analysis will give only an approximation of the stiffness values to expect. For calculation of more precise values, it is mores sensible to use finite element simulation.

In case a force F_x is loading the beam as shown in figure B.2 left, the resulting displacement f_{xr} (figure B.2 right) is found by decomposition of the F_x along the principle axes x_p and z_p. The two force components F_{x1} and F_{x2} together with the beam stiffness values in the x_p- and z_p-direction are used to find the displacement components f_{x1} and f_{x2}. Adding the displacement components yields f_{xr}. However this displacement is not directed in the same direction as F_x. The absolute difference between the angle ϕ (between f_{x1} and f_{x2}) and θ is used to calculate the displacement

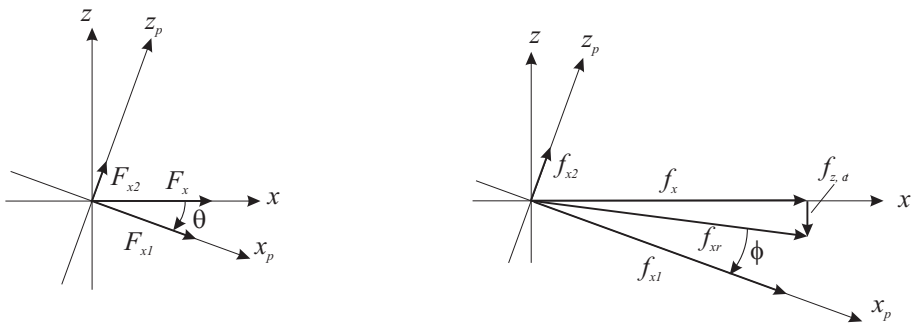

Figure B.2: Force decomposition along the principle axes (left), resulting displacements and cross-talk (right).

component f_x, directed along F_x, and the cross-talk component $f_{z,ct}$, directed along the z-axis. Following the same procedure the results of a force F_z and of moments M_x and M_z is obtained.

By the ratio of F_x and f_x a "pseudo-stiffness" is defined. For an estimation of the stiffness increase using the L-torsion beam, the pseudo-stiffness can be compared with the stiffness in the same direction of a beam with rectangular cross-section. The following equations are used to obtain the pseudo-stiffness. First the forces and the resulting displacements related to F_x are given. Here, I_{xp} and I_{zp} are the principle moments of inertia.

$$\begin{aligned} F_{x1} &= F_x \cos\theta \qquad F_{x2} = F_x \sin\theta \\ f_{x1} &= \frac{F_{x1}\, L^3}{3\, E_y\, I_{zp}} \qquad f_{x2} = \frac{F_{x2}\, L^3}{3\, E_y\, I_{xp}} \end{aligned} \tag{B.7a}$$

The resultant displacement f_{xr} and the angle ϕ between f_{x1} and f_{x2} are calculated:

$$\begin{aligned} f_{xr} &= \sqrt{{f_{x1}}^2 + {f_{x2}}^2} \\ \phi &= \tan\left(\frac{f_{x2}}{f_{x1}}\right) \end{aligned} \tag{B.7b}$$

With help of f_{xr} and the angle ϕ, the displacement in x-direction and the cross-talk displacement are found:

$$\begin{aligned} f_x &= f_{xr} \cos|\theta - \phi| \\ f_{z,ct} &= f_{xr} \sin|\theta - \phi| \end{aligned} \tag{B.7c}$$

The definition of the pseudo-stiffness for a force in x-direction:

$${c_{Fx}}' = \frac{F_x}{f_x} \tag{B.7d}$$

Note that this stiffness is only defined for the beam and not for the complete suspension. To find an estimation of the effect of the L-shape on the stiffness equations (4.12a) and (4.12b) found for the suspension on page 88, the effect on the standard relations for small deformations can be investigated. Since the stiffness equations for the suspension are linear combinations of these standard relations, the effects for the suspension are equal. The standard relations, all applying to the end of the beam, are given below.

$$f(M,F) = \frac{ML^2}{2E_Y I} + \frac{FL^3}{3E_Y I} \tag{B.8a}$$

$$\psi(M,F) = \frac{ML}{E_Y I} + \frac{FL^2}{2E_Y I} \tag{B.8b}$$

Comparing the stiffness following from the first relation, calculated for a force acting on the end of a beam with rectangular cross-section, to the pseudo-stiffness ${c_{Fx}}'$ results in a stiffness increase of 35 times. The values listed in table 4.2 on page 92 are used for this calculation. The same increase is found for the quotients of F_x and ψ_z, M_z and ψ_z, and for M_z and f_x (these quotients could be called the pseudo-stiffness values ${k_{Fx}}'$, ${k_{Mz}}'$ and ${c_{Mz}}'$). Similar comparisons are made for the quotients of F_z and f_z, F_z and ψ_x, M_x and ψ_x, and for M_x and f_z (pseudo-stiffness values ${c_{Fz}}'$, ${k_{Fz}}'$, ${k_{Mx}}'$ and ${c_{Mx}}'$). That comparison results in a stiffness increase of 1.1.

As discussed above, because the suspension stiffness equations are linear combinations of the standard relations, the stiffness increase factors apply directly to the suspension stiffness. All the stiffness ratios of the suspension for an L-torsion beam with respect to a rectangular torsion beam are given in table 4.3 on page 94.

Shape-factor The shape-factor for the torsion stiffness is estimated via the same procedure as described in section 4.3.1 on page 91. In this case there is just one horizontal beam-part as shown in figure B.3.
With help of figure B.3 the following equation is derived:

$$\begin{aligned} k_L &\approx 2\,(k_1 + k_2 + k_{c_{p1}} + k_{c-p2}) \\ k_L &\approx 2\,(k_1 + k_2 + {r_1}^2\, c_{p1} + {r_2}^2\, c_{p2}) \end{aligned} \tag{B.9}$$

Inserting the radii, shape-factors and stiffness constants for the beam-parts yields the following equation for k_L:

$$k_L \approx 2\left(k_1 + k_2 + \left(\frac{b}{2} - \frac{d}{2}\right)^2 c_1 + \left(g + \frac{c}{2} + \frac{a}{2}\right)^2 c_2\right) \tag{B.10a}$$

$$k_L \approx \frac{24\,E_Y}{L^3}\left(I_1\left(\frac{b}{2} - \frac{d}{2}\right)^2 + I_2\left(g + \frac{c}{2} + \frac{a}{2}\right)^2\right) + \frac{2\,G}{L}(\kappa_1 + \kappa_2) \tag{B.10b}$$

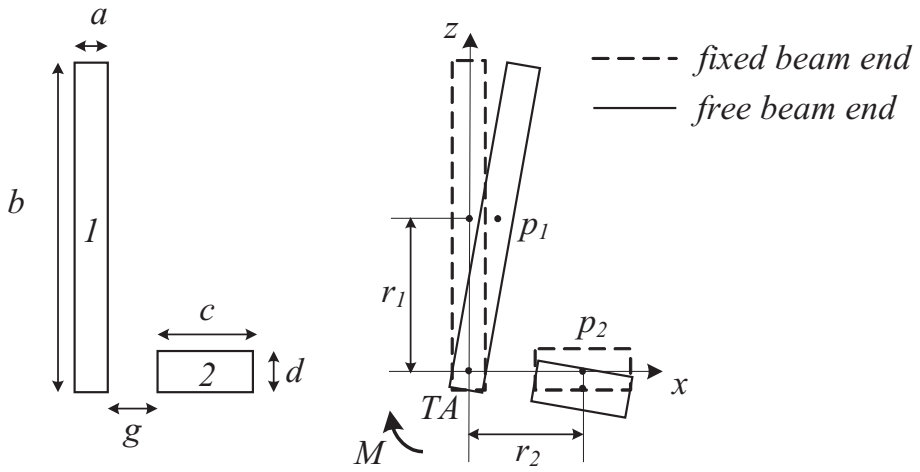

Figure B.3: L-torsion beam cross-section used to determine the location of the torsion axis TA.

$$\text{with} \quad \kappa_1 \approx \frac{a^3 b}{3} \quad \kappa_2 \approx \frac{c d^3}{3} \quad I_1 = \frac{a^3 b}{12} \quad I_2 = \frac{c d^3}{12} \tag{B.10c}$$

For the dimensions given in table 4.2 on page 92 the ratio of $\frac{k_L}{k}$ amounts to 1.71 (see table 4.3 on page 94 as well).

References

[1] J. M. Gere, *Mechanics of Materials*. Thomson Brooks/Cole, 6^{th} ed., 2004.

appendix C

A model for a charge-sheet between parallel electrode plates

In this appendix an energy analysis is presented for a charge-sheet inserted between two parallel electrode plates. The energy model is based on some assumptions of which the validity is not fully verified yet. Provided the assumptions on the energy are valid, energy minimization is a powerful method to analyze a multi-domain system. It often results in a relatively accurate prediction of system responses, like forces, without the requirement to specifically identify the various causes of the responces upfront. It is sufficient to identify the domain specific quantities and relate them to each other in (phenomenological) energy expressions.

The correct energy expression is crucial to obtain correct results from the model. For the model described here, the expressions found for the forces as a result of the energy analysis are not fully understood yet. This together with the incomplete verification of the assumptions makes the outcome of this analysis disputable. Nevertheless, it is decided to describe this model in the appendix since it addresses an interesting problem for which no adequate description has been found in literature. This is best regarded as a first step towards a complete model leading to comprehensible results. By not presenting this model, although incomplete, it most probably will be lost, which is a waste of opportunity and effort.

In the next section a simple version of the model is presented resulting in an equation for the force in lateral direction for the case of a completely inserted charge-sheet. Subsequently the model is extended to take into account partial insertion of the

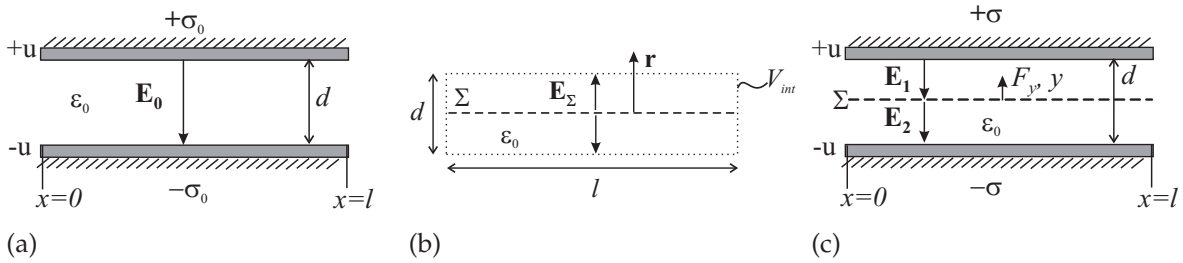

Figure C.1: Schematic representations of a charge-sheet fully inserted between parallel electrodes; empty parallel-plate capacitor a), charge-sheet with near field volume b), and the combination of both c).

charge-sheet as well.

C.1 Side-ways force on a charge-sheet

Figure C.1 shows schematic representations of the electrode combination and the charge-sheet separately (figure C.1a and figure C.1b) and of the charge-sheet completely inserted between the electrodes (figure C.1c). The parameters are explained in table C.1. For each of the three schemes an energy expression can be found. The energy in the parallel-plate capacitor is given by:

Table C.1: Explanation of the parameters

parameter	explanation	unit
l	plate length	[m]
w	plate width	[m]
d	distance between the plates	[m]
V_{int}	internal integration volume	[m^3]
u	voltage on plates	[V]
σ_0	charge-density on the plate; no charge-sheet	[C/m^2]
σ	charge-density on the plate; charge-sheet inserted	[C/m^2]
Σ	charge-density of charge-sheet	[C/m^2]
$\mathbf{E}_0$	electric field; no charge-sheet	[C/m^2]
$\mathbf{E}_\Sigma$	electric field of the charge-sheet	[C/m^2]
$\mathbf{E}_1$	electric field upper part; charge-sheet inserted	[C/m^2]
$\mathbf{E}_2$	electric field lower part; charge-sheet inserted	[C/m^2]
$\mathbf{r}$	distance vector	[m]
ε_0	dielectric permittivity	[F/m]

$$U_0 = \frac{\varepsilon_0}{2} \int_{V_{int}} {E_0}^2 \, \mathrm{d}V = \frac{l\, d\, w}{2\, \varepsilon_0}\, \sigma^2 \tag{C.1}$$

Here it is assumed the plates have a length and width much larger than the gap between the plates. In that situation all the energy can be assumed within the volume between the plates.

The energy because of the charge-sheet consists of a part near the plate, inside the volume V_{int}, and a part far from the plate, outside volume V_{int} (see equation (C.2)). The electric flux density inside the volume V_{int} is considered constant with the distance $\mathbf{r}$, since $|\mathbf{r}| \ll l, w$.

$$\begin{aligned} U_\Sigma &= \frac{\varepsilon_0}{2} \int_V (\mathbf{E}_\Sigma(\mathbf{r}))^2 \, \mathrm{d}V = \frac{\varepsilon_0}{2} \int_{V_{ext}} (\mathbf{E}_\Sigma(\mathbf{r}))^2 \, \mathrm{d}V + \frac{\varepsilon_0}{2} \int_{V_{int}} \left(\frac{\Sigma}{2\, \varepsilon_0} \right)^2 \mathrm{d}V \\ &= \frac{\varepsilon_0}{2} \int_{V_{ext}} (\mathbf{E}_\Sigma(\mathbf{r}))^2 \, \mathrm{d}V + \frac{l\, d\, w}{2\, \varepsilon_0} \left(\frac{\Sigma}{2} \right)^2 \end{aligned} \tag{C.2}$$

The energy of the complete system of electrode plates and inserted charge-sheet is given in equation (C.3). Again there is a part of the energy due to the charge-sheet outside the volume V_{int}. It is assumed the energy outside V_{int} will not change with a change in the charge-sheet position (x,y), since the variation of the opposite charges induced on the electrodes by the charge-sheet are not distinguishable at a large distance from the electrodes (i.e. the field outside the V_{int} seems constant at large distance). This is however an assumption that still requires verification! The other part of the energy is related to the electric fields $\mathbf{E}_1$ and $\mathbf{E}_2$. The volumes above and below the charge-sheet are considered depending on the y-position of the charge-sheet.

$$\begin{aligned} U_{tot} &= \frac{\varepsilon_0}{2} \int_{V_{ext}} (\mathbf{E}_\Sigma(\mathbf{r}))^2 \, \mathrm{d}V + \frac{\varepsilon_0}{2} \int_{V_{int}} E^2 \, \mathrm{d}V \\ &= \frac{\varepsilon_0}{2} \int_{V_{ext}} (\mathbf{E}_\Sigma(\mathbf{r}))^2 \, \mathrm{d}V + \frac{l\, w}{2\, \varepsilon_0} \left[\left(\frac{d}{2} - y \right) \left(\sigma - \frac{\Sigma}{2} \right)^2 + \left(\frac{d}{2} + y \right) \left(\sigma + \frac{\Sigma}{2} \right)^2 \right] \\ &= U_{ext} + \frac{l\, w}{2\, \varepsilon_0} \left[\left(\sigma^2 + \frac{\Sigma^2}{4} \right) d + 2\, y\, \sigma \Sigma \right] \end{aligned} \tag{C.3}$$

With help of U_{tot}, the force required to keep the charge-sheet at a given y-position can be found for charge control (with charge $q = l\, w\, \sigma$):

$$F_{y,q} = \left[\frac{\partial\, U_{tot}}{\partial\, y} \right]_\sigma = \frac{l\, w}{\varepsilon_0}\, \sigma \Sigma = \frac{1}{\varepsilon_0}\, q\, \Sigma \tag{C.4}$$

This means a positive charge-sheet is pulled towards the lower plate with a constant force. This is exactly what one would expect, since the charge sheet is repelled by the

charge on the top-plate and attracted by the charge on the bottom-plate. Since, the transducers will be used in voltage control an expression for q depending on u has to be found. Hereto, U_{tot} is partially differentiated with respect to q for constant y.

$$u = \left[\frac{\partial U_{tot}}{\partial q}\right]_y = \frac{d\,q}{l\,w\,\varepsilon_0} + \frac{y\,\Sigma}{\varepsilon_0} \quad \Rightarrow \quad q = \frac{l\,w\,\varepsilon_0\,u}{d} - \frac{y\,l\,w\,\Sigma}{d} \tag{C.5}$$

Inserting this expression for q into equation (C.4) leads to the following expression for the force to keep the charge-sheet at a given position under voltage control:

$$F_{y,u} = \frac{l\,w\,\Sigma\,u}{d} - \frac{y\,l\,w\,\Sigma^2}{\varepsilon_0\,d} \tag{C.6}$$

The force shows two parts, where the first part is related to the field because of the applied voltage u, working on the charge in the charge-sheet. The second part is not fully understood. Equation (C.5), predicts a charge q on the plates, even when $u = 0$. For electrodes to become charged in that situation, they should both be connected to ground, i.e. there a charge-source is required. The charging seems to occur due to image charges induced in the electrodes by the charge-sheet. However, the charge-sheet and its image would attract each other with a constant force (the field is constant in y-direction) meaning no net force results. Equation (C.6) predicts a force proportional to y. According to (C.5), side-ways displacement of the charge-sheet does increase the absolute charge in the capacitor formed by the electrodes. This is often explained as a minimization of the overall energy of the system including the voltage-source, since charge flows from the voltage-source to the capacitor. A similar situation occurs for a voltage controlled comb-drive, where the charge on the teeth of both comb-racks increases as the overlap of the teeth increases.

Clearly, the force in y-direction does not show run-away behavior when the charge-sheet approaches one of the electrodes (the *extra* charge on the electrodes will not be larger than $0.5\,w\,l\,\Sigma$). Furthermore, partially differentiating the force with respect to y (for constant u) results in a constant negative electrostatic stiffness, which is easily balanced by a suspension with properly chosen stiffness.

Returning to the energy expressions derived in equations (C.1) and (C.2), a difference in energy for the separate systems (of parallel electrodes and charge-sheet) and the combined system of the charge-sheet fully inserted between the electrodes can be found:

$$\Delta U = U_{tot} - U_0 - U_\Sigma = \frac{l\,w}{\varepsilon_0}\,y\,\sigma\,\Sigma \tag{C.7}$$

This difference means that inserting the charge sheet between the electrodes, i.e. moving the sheet in x-direction (see figure C.1), causes a change in the energy, leading to a force in the x-direction. Based on energy minimization, in case of charge control

and for a positive charge-sheet and positive y-position, ΔU is positive, meaning the energy increases and the sheet is pushed out from between the plates. For a negative y-position, the energy decreases, thus the sheet is pulled between the plates. In the next section an attempt is made to find an expression for the force depending on the x-position of the charge-sheet.

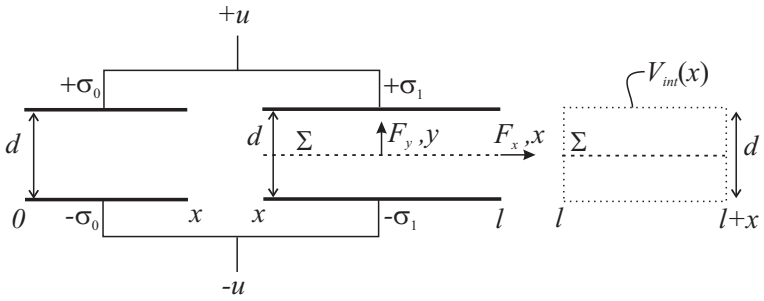

Figure C.2: Model used to describe the case where the charge-sheet is partially inserted between the electrodes.

C.2 Extension with force in the longitudinal direction

To model the situation where the charge-sheet is only partially inserted between the electrodes, the system is split up in three parts as shown in figure C.2. From left to right, the first part is the part without a charge-sheet between the electrodes, stretching from 0 to x; in the second part, stretching from x to l, the charge-sheet is inserted; the third part consist of the charge-sheet outside the electrodes, stretching from l to $x + l$. The first and second part both have the same voltage difference, but their charge-densities may be different, while the overall charge is considered constant (charge controlled system).

The model only regards fields in the y-direction, meaning fringe fields are not taken into account. Comparable to the situation often applied to model a comb-drive, the energy contribution due to the fringe fields is assumed not to vary with position of the charge-sheet, meaning fringe fields would not lead to forces. The validity of this assumption however still needs verification! Furthermore, this assumption implies the distance between the electrodes is very small compared to the length of the electrode parts. This means, for the model to give the most trustworthy result, x should neither be close to 0, nor should x be close to l.

$$U_{tot} = U_{ext} + \frac{x\,d\,w}{2\,\varepsilon_0}\,{\sigma_0}^2 + \frac{(l-x)\,w}{2\,\varepsilon_0}\left[\left({\sigma_1}^2 + \frac{\Sigma^2}{4}\right)\,d + 2\,y\,\sigma_1\Sigma\right] + \frac{x\,d\,w}{8\,\varepsilon_0}\,\Sigma^2 \qquad \text{(C.8)}$$

Equation (C.8) gives the energy equation for the proposed model. It consists of four parts (from left to right); the first part is the energy of the charge-sheet outside the volume between the electrodes and the volume in the direct surrounding of the charge-sheet (again assuming not to change with the position of the charge-sheet); the second part is the energy in the capacitor formed by the electrodes without charge-sheet; the third part is the energy for the part where the charge-sheet is inserted; the fourth part gives the energy in the direct surrounding of the part of the charge-sheet out-side the plates.

The charge densities σ_0 and σ_1 residing on the plates of part 1 and part 2 respectively, relate to the initial charge-density σ as follows:

$$\begin{aligned} \sigma_0 &= \sigma + \delta_0 \\ \sigma_1 &= \sigma + \delta_1 \end{aligned} \tag{C.9a}$$

Where δ_0 and δ_1 represent the separation in charge density due to the inserted charge-sheet. This means the charge-density is considered varying in the x-position on the electrodes, which is modelled with a zeroth order model. This is certainly a crude representation of what would happen in reality, where a gradual change in charge density is expected. Allowing a variation of the charge-density over the electrodes, enables an energy variation even in a case where the overall charge on the plates is zero. A similar situation of a varying charge-density is also considered in [1]. The assumption of a discontinues transition in the charge density might cause additional energy minimization to be overlooked.

Taking into account the variation in charge-density should not result in a variation of the overall charge q, the following relation is found between δ_0 and δ_1:

$$\Delta q = 0 \quad \Rightarrow \quad (l - x)\, w\, (\sigma_1 - \sigma) + x\, w\, (\sigma_0 - \sigma) = 0 \tag{C.9b}$$

$$\delta_1 = -\delta_0 \left(\frac{x}{l - x} \right) \tag{C.9c}$$

To find an expression for δ_1, it is considered, the value of δ_1 is such that the energy U_{tot} is minimized. The expressions for σ_0 and σ_1 are inserted into the energy equation (C.8) and the minimum for δ_1 is determined setting $\dfrac{\partial U_{tot}}{\partial \delta_1}$ to zero and checking if $\dfrac{\partial^2 U_{tot}}{\partial {\delta_1}^2} > 0$ holds for the value found for δ_1. This procedure results in the following expressions for δ_0 and δ_1:

$$\begin{aligned} \delta_0 &= \left(\frac{l - x}{l} \right) \frac{y}{d}\, \Sigma \\ \delta_1 &= -\frac{x}{l}\, \frac{y}{d}\, \Sigma \end{aligned} \tag{C.9d}$$

The voltages of the first part (u_0) and the second part (u_1) in figure figure C.2 require to be equal. This condition is successfully checked for the values found for δ_0 and δ_1.

$$\begin{aligned} u_0 &= \frac{\sigma_0}{\varepsilon_0} d = (\sigma + \delta_0)\frac{d}{\varepsilon_0} = \frac{d}{\varepsilon_0}\left(\sigma + \left(\frac{l-x}{l}\right)\frac{y}{d}\Sigma\right) \\ u_1 &= \frac{1}{\epsilon_0}\left(\sigma_1 - \frac{\Sigma}{2}\right)\left(\frac{d}{2} - y\right) + \frac{1}{\epsilon_0}\left(\sigma_1 + \frac{\Sigma}{2}\right)\left(\frac{d}{2} + y\right) = \\ & \frac{d}{\varepsilon_0}\sigma_1 + \frac{y}{\varepsilon_0}\Sigma = \frac{d}{\varepsilon_0}\left(\sigma + \left(\frac{l-x}{l}\right)\frac{y}{d}\Sigma\right) = u_0 \end{aligned} \tag{C.10}$$

The values found for σ_0 and σ_1 are inserted into equation (C.8), making U_{tot} only dependent on the variables x, y, and σ (Σ is considered a parameter):

$$\begin{aligned} U_{tot} = U_{ext} + \frac{(l-x)\,w}{2\,\varepsilon_0}\Bigg[\left(\left(\sigma - \frac{x\,y}{l\,d}\Sigma\right)^2 + \frac{\Sigma^2}{4}\right) d + 2\,y\,\left(\sigma - \frac{x\,y}{l\,d}\Sigma\right)\Sigma\Bigg] \\ + \frac{x\,d\,w}{2\,\varepsilon_0}\left(\sigma + \left(\frac{l-x}{l}\right)\frac{y}{d}\Sigma\right) + \frac{x\,d\,w}{8\,\varepsilon_0}\Sigma^2 \end{aligned} \tag{C.11}$$

For the situations of the charge-sheet completely outside the electrodes ($x = l$) and the situation where the charge-sheet is completely inserted ($x = 0$), the energy difference $\Delta U = U_{tot}(x = 0) - U_{tot}(x = l)$ can be calculated, which will lead to the same results as in equation (C.7).

By partial differentiation of U_{tot} with respect to x and y (under the condition that the remaining variables are constant), the forces $F_{x,q}$ and $F_{y,q}$ for charge control are found:

$$F_{x,q}(x, y, \sigma) = \left[\frac{\partial U_{tot}}{\partial x}\right]_{y,\sigma} = -\frac{w\,y\,\Sigma}{\varepsilon_0}\left(\sigma + \frac{y\,(l - 2\,x)\,\Sigma}{2\,d\,l}\right) \tag{C.12a}$$

$$F_{y,q}(x, y, \sigma) = \left[\frac{\partial U_{tot}}{\partial y}\right]_{x,\sigma} = (l - x)\,w\,\Sigma\left(\frac{\sigma}{\varepsilon_0} - \frac{x\,y}{l\,d}\Sigma\right) \tag{C.12b}$$

These are the forces required to keep the charge-sheet at its x, y-position. In case the charge-sheet is exactly between the electrodes ($y = 0$), there is no force in the x-direction. This is probably caused by the fact that the geometrical relation between q and u is not affected if the charge-sheet is inserted at $y = 0$ (see equation (C.13a)). Furthermore, one might reason a charge-sheet is not affected by an electric field perpendicular to the sheet. However, for $y \neq 0$ the field is still perpendicular, while there is a force $F_{x,q}$ unequal to zero. This seemingly contradiction needs further attention!

Considering the special case of zero overall charge on the electrodes ($\sigma = 0$), the force in x-direction is zero for $y = 0$, while for $y \neq 0$ the force is positive up to $x = 0.5\,l$ and negative for $x = 0.5\,l$ to l. Furthermore, the force is proportional to

y^2. A positive force means the sheet is pulled in between the electrodes unless it is held at its position. This means up to $x = 0.5\,l$, the sheet is pulled in between the electrodes, while beyond $x = 0.5\,l$ it is pushed outward. With help of equation (C.9a), it can be shown that for $x = 0.5\,l$ the charge separation along x on the electrodes is at maximum (largest difference between the first and the second part in figure C.2). In the general case of $\sigma \neq 0$, the transition point where $F_{x,q}$ changes sign depends on y and σ, however it still coincides with the largest charge separation. Apparently, to minimize the energy, the system first pursuits to compensate the charge on the sheet, but beyond a certain x-position of the sheet, further charge separation leads to an energy increase. It is nut fully understood why the the energy would minimize in the is way.

$F_{y,q}$ shows dependence on x as well. Apart from the component already found in equation (C.4) (which is now increasing with increasing overlap of the sheet and the electrodes) an additional component is present, which gives rise to a force in y-direction even in case $\sigma = 0$. For $\sigma = 0$ the dependence of this force on x causes it to be at maximum for $x = 0.5\,l$. This is again linked to the maximum charge separation. Furthermore, this force component is directed in opposite direction to y, meaning the plate will be pulled in the direction of the closest electrode ($F_{y,q}$ is the force required to keep the sheet at its position). The reason for this behavior is also not fully understood.

To find the forces in x- and y-direction for voltage control, an equation for q depending on the applied voltage u is derived. To this extent, U_{tot} is partially differentiated with respect to q (after replacing σ by $\frac{q}{w\,l}$), under the condition of constant values for x and y. This result in an expression for u, from which the equation for q is derived.

$$u(x,y,q) = \left[\frac{\partial U_{tot}}{\partial q}\right]_{x,y} = \frac{q\,d}{w\,l\,\varepsilon_0} + \left(\frac{l-x}{l}\right)\frac{\Sigma\,y}{\varepsilon_0} \tag{C.13a}$$

$$q(x,y,u) = \frac{w\,l\,\varepsilon_0\,u}{d} - \frac{w\,(l-x)\,y\,\Sigma}{d} \tag{C.13b}$$

Equation (C.13b) is inserted into equations (C.12a) and (C.12b) to obtain the forces $F_{x,u}$ and $F_{y,u}$ for voltage control.

$$F_{x,u}(y,u) = \frac{y\,w\,\Sigma}{d}\left(\frac{y\,\Sigma}{2\,\varepsilon_0} - u\right) \tag{C.14a}$$

$$F_{y,u}(x,y,u) = \frac{(l-x)\,w\,\Sigma}{d}\left(u - \frac{y\,\Sigma}{\varepsilon_0}\right) \tag{C.14b}$$

$F_{x,u}$ is independent of x, but there is a dependence of y and again the force is zero for $y = 0$. Once again this is difficult to interpret, since the explanation that the sheet

moves perpendicular to the electric field does not explain why there is a force if $y \neq 0$. The forces in both x- and y-direction show dependance of y even when $u = 0$. Similar to the explanation proposed for equation (C.6), the charge on the plates increases if the sheet comes closer to one of both electrodes. This can again be compared to a comb-drive, where the charge on the teeth increases for increasing overlap of the teeth.

Differentiating $F_{y,u}$ partially with respect to y for constant x, results in the electrostatic stiffness, which is constant with y (as was found earlier in section C.1) and is linearly depending on x, i.e. $c_{el,y}$ increases for increasing overlap of electrodes and charge-sheet. Since $c_{el,y}$ does not show dependence on y, the electrostatic stiffness is balanceable with a well dimensioned suspension.

$$c_{el,y}(x) = -\frac{(l-x)\, w\, \Sigma^2}{\varepsilon_0\, d} \tag{C.14c}$$

References

[1] X. Rottenberg, B. Nauwelaers, W. De Raedt, and H. A. C. Tilmans, "Distributed dielectric charging and its impact on RF MEMS devices.," in *34th European Microwave Conference*, (London, United Kingdom), pp. 77–80, 2004.

Summary

This thesis reports about a six degrees of freedom (DOF) precision manipulator in MEMS, concerning concept generation for the manipulator followed by design and fabrication (of parts) of the proposed manipulation concept in MEMS. Researching the abilities of 6 DOF precision manipulation in MEMS is part of the Multi Axes Micro Stage (MAMS) project in which the disciplines of precision engineering, control engineering and micro mechanical engineering are represented.

Micro Electro Mechanical Systems, or MEMS technology is generally based on lithographic, deposition and etching techniques also applied in the integrated circuits (IC) industry. The basis for these microsystems is a thin polished substrate usually consisting of very pure single crystal silicon, called a wafer. Roughly, since the 1980's a lot of mechanical devices on the micrometer scale have been developed in MEMS technology. Some strikingly resemble machines that are very common in the large world, consisting of down-scaled gears, ratchets, racks, pinions, sliders and hinge mechanisms. Others are based on flexure mechanisms resembling large scale systems used for precision position adjusting and manipulation. There are also large differences between MEMS systems and macroscopic mechatronical systems. Where actuation in macroscopic systems is dominated by electromagnetic transduction, the preferred principle of actuation in MEMS systems is far less pronounced. Efficient electromagnetic transducers are difficult to realize in MEMS while actuators based on electrostatic attraction are more simple to fabricate and generally show better performance. On the micrometer scale, large electrical fields can be obtained at relatively low voltages and the breakdown fields scales favorable due to Paschen's law. Other actuation principles often encountered in MEMS are electrothermal and piezo-electric actuation.

Another aspect in which MEMS differ from macroscopic systems is the fabrication method, characterized by a "2.5 dimensional" design freedom. This largely complicates the design of 3 dimensional geometries, especially regarding structuring of devices in the direction normal to the wafer-plane. This is one of the main reasons, the design of a 6 degrees of freedom stage for precision manipulation is a large challenge.

However, the potential improvements obtained by downscaling a manipulation system encourage to research the feasibility of a 6 DOF precision MEMS manipulator. A miniaturized precision system does not only benefit because of reduction in size, but thermal drift is substantially reduced as well and the primary resonance frequency increases considerably. To put the development of a 6 DOF precision MEMS stage in a practical perspective, specifications are defined for a sample manipulator in a transmission electron microscope (TEM), capable of imaging resolutions in the Å-range. This application requires a highly stable system capable of strokes of ± 10 μm and nanometer resolution positioning.

In this thesis a concept for 6 DOF manipulation is presented, based on stacking of two 3 DOF parallel kinematic manipulators. One is used for the three planar DOFs and stacked on top of the other, manipulating the three out-of-plane DOFs. The design of the flexure based mechanisms is largely based on exact kinematic constraining of the DOFs. Limitations to fabrication of the desired mechanism rising form MEMS technology are identified and solutions are proposed. The planar 3 DOF manipulator actuated by electrostatic comb-drives is successfully fabricated in bulk SCS. Characterization shows largely linear mechanical behavior on the sub-micron scale.

For actuation of the out-of-plane stage, a vertical comb-drive suspended by torsion beams is designed. To increase stability with respect to electrostatic side pull-in, the torsion beam consists of vertical and horizontal parts. A process is developed to enable fabrication of the required geometry for the torsion beams and the vertical comb-drive teeth in SCS. This process is compatible with the fabrication of the planar 3 DOF stage. Fabrication of the special 3 dimensional geometry still requires improvement and many out-of-plane devices show short circuits. However, out-of-plane actuation with a stroke of 10 μm has been observed.

Increased stability with respect to side pull-in might also be obtained by a different kind of electrostatic transduction. In this case a dielectric plate or a floating conduction plate is partially inserted between to parallel electrodes. A voltage over the electrodes will result in a force pulling the plate inwards. In a first order approximation no forces in lateral (pull-in) direction are found. Finite element simulations (FEM) reveal forces in lateral direction do occur, however these are much smaller compared to the case of a comb-drive. Additionally, in case of charging, the lateral forces on a charge sheet between two parallel electrodes are modelled. The dependance of the lateral force on the lateral position of the charge sheet is found not to be highly non-linear like in the case of a comb-drive. This encourages the expectation that the alternative electrostatic actuators are far less sensitive to side pull-in than comb-drives. However, a proof of principle has not yet been realized.

Samenvatting

In dit proefschrift is een precisie manipulator met zes vrijheidsgraden in MEMS beschreven met betrekking tot de totstandkoming van he manipulator concept, gevolgd door het ontwerp en de fabricage van (delen van) het voorgestelde manipulatieconcept in MEMS. Onderzoek naar de mogelijkheden van precisie manipulatie in zes vrijheidsgraden in MEMS maakt onderdeel uit van het Multi Axes Micro Stage (MAMS) project, waarin de disciplines precision engineering, regeltechniek en micro mechanical engineering vertegenwoordigd zijn.

Micro Electro Mechanical Systems of MEMS technologie is over het algemeen gebaseerd op lithografische, depositie en ets technieken bekend van de integrated circuits (IC) industrie. De basis voor deze microsystemen is een dun, gepolijst substraat wat doorgaans bestaat uit zeer zuiver één-kristal silicium. Dit substraat wordt ook wel wafer genoemd. Grofweg sinds the tachtiger jaren van de vorige eeuw zijn er vele mechanische apparaatjes met afmetingen op de micrometer schaal ontwikkeld in MEMS technologie. Sommige vertonen opvallend veel overeenkomsten met machines die men normaal in de grote wereld aantreft. Zij bestaan uit miniaturen van tandwielen, palraderen, tandheugels, geleiders en scharnieren. Andere zijn gebaseerd op flexibele mechanismen overeenkomstig met grote apparaten die worden toegepast voor precisie positie instelling en manipulatie. Er zijn echter ook grote verschillen tussen MEMS systemen en macroscopische mechatronische systemen. Wordt actuatie in macroscopische systemen gedomineerd door elektromagnetische transducenten, in MEMS systemen is er niet zo'n duidelijke voorkeur. Efficiënte elektromagnetische transducenten zijn erg moeilijk te maken in MEMS technologie, terwijl actuatoren die gebaseerd zijn op elektrostatische transductie veel simpeler gefabriceerd kunnen worden en over het algemeen beter presteren. Op microschaal kunnen grote elektrische velden opgewekt worden bij relatief lage voltages en de doorslag veldsterkte schaalt gunstig vanwege Paschen's wet. Andere actuatie principes die veel voorkomen in MEMS zijn (elektro-)thermische en piëzo-elektrische actuatie.

Een andere aspect waarin MEMS verschillen van macroscopische systemen is de fabricage methode, die gekenschetst wordt door "2.5 dimensionale" ontwerpvrijheid.

Hierdoor wordt het ontwerpen van 3 dimensionale geometrieën enorm bemoeilijkt, in het bijzonder voor vormgeving van structuren in de richting loodrecht op het wafer-oppervlak. Dit is een van de hoofdredenen waarom het ontwerpen van een precisie manipulator met zes vrijheidsgraden een enorme uitdaging vormt. Desalniettemin, sporen de mogelijke verbeteringen door miniaturisering van een manipulatie systeem aan om de haalbaarheid van een zes vrijheidsgraden MEMS manipulator te onderzoeken. Een miniatuur precisie systeem profiteert niet enkel van de afgenomen afmetingen, maar ook van een substantile afnamen in de thermische drift en van een behoorlijke toename in de laagst eigenfrequentie. Om de ontwikkeling van een zes vrijheidsgraden precisie manipulator in MEMS in een praktisch perspectief te plaatsen, zijn specificaties gedefinieerd aan de hand van sample manipulatie in een transmissie elektronen microscoop (TEM). Met de TEM is het mogelijk beelden te verkrijgen met resoluties op Å-niveau. Deze toepassing vraagt om een hoogst stabiel systeem met nanometer resolutie positionering over slagen van ± 10 μm.

In dit proefschrift wordt een concept voorgesteld voor manipulatie in zes vrijheidsgraden, gebaseerd op stapeling van twee parallelle manipulatoren ieder voor drie vrijheidsgraden. The ene wordt gebruikt voor de drie vrijheidsgraden in het vlak en wordt gestapeld op de andere, die in de vrijheidsgraden uit het vlak manipuleert. Het ontwerp van de flexibele mechanismen is gebaseerd op statisch bepaald construeren. Beperkingen in de fabricage van het gewenste mechanisme zijn beschreven en oplossingen zijn voorgesteld. De manipulator voor drie vrijheidsgraden in het vlak wordt aangestuurd door elektrostatische comb-drives en is met succes gefabriceerd in één-kristal silicium. Uit karakterisatie komt een hoofdzakelijk lineair gedrag op micrometer schaal naar voren.

Voor aandrijving van de uit het vlak manipulator zijn vertical comb-drives met een torsie ophanging ontworpen. Om de stabiliteit met betrekking tot zijwaartse pull-in te vergroten bestaan de torsie balkjes uit verticale en horizontale delen. Er is een proces ontwikkeld om de vereiste geometrie voor de torsie balkjes en de verticale comb-drive tanden in één-kristal silicium te fabriceren. Het proces maakt ook de fabricage van de in het vlak manipulator mogelijk. Fabricage van de drie dimensionale structuren vereist nog verbetering en veel van de uit het vlak systemen hebben last van kortsluiting. Ondanks dat, is een uit het vlak actuatie met een 10 μm slag waargenomen.

Vergroting van de stabiliteit met betrekking tot zijwaartse pull-in zou ook verkregen kunnen worden door middel van een ander type elektrostatische transducent. In dat geval wordt een dielectrische plaat of een zwevende geleider gedeeltelijk tussen twee parallelle elektrode platen geschoven. Als er een voltage over de elektrodes wordt aangebracht wordt een kracht opgewekt die de plaat verder naar binnen trekt. Volgens eerste orde benaderingen is er geen kracht in laterale (pull-in) richting. Finite

element simulation (FEM) laat wel krachten in laterale richting zien, maar deze zijn veel kleiner in vergelijking met de comb-drive. Voor het geval van oplading van de plaat is er een model opgesteld voor een geladen film tussen de elektrodes. De manier waarop de kracht op de geladen film in laterale richting afhangt van de positie is niet sterk alineair zoals bij de combdrive. Dit versterkt de verwachting dat deze alternatieve elektrostatische actuatoren veel minder gevoelig zijn voor zijwaartse pull-in dan comb-drives. Een demonstratie hiervan heeft echter nog niet plaatsgevonden.

Dankwoord

Aan alle goede dingen komt helaas een eind, zo ook aan het promoveren bij de MicMec. Velen hebben er toe bijgedragen dat ik dit werk als erg plezierig heb ervaren, hetzij door ondersteuning, hetzij met puur vermaak. Ik zou graag beginnen mijn promotoren Miko en Herman te bedanken. Miko, ik heb veel van je colleges genoten. Ik verdiep me graag in de natuurkunde, maar vindt daar helaas lang niet genoeg tijd voor. Jouw boeiende lezingen hebben gelukkig toch een belangrijke bijdrage geleverd aan mijn begrip van dit vakgebied. Herman, dank je wel voor alle keren dat je de tijd vond om mij bij te spijkeren in de werktuigbouwkunde. Ik heb er veel van geleerd. Het is erg waardevol gebleken om in het multidisciplinaire MEMS-vak, en in het MAMS project in het bijzonder, een eenduidige koers te kunnen varen zonder veelvuldige overwegingen of de gekozen aanpak werktuigbouwkundig gezien geoorloofd is.

Vervolgens wou ik mijn directe begeleider en assistent promotor, Gijs, bedanken voor zijn inzet en begeleiding gedurende de afgelopen vier jaar. We hebben veel nuttige en leerzame gediscussies gevoerd over de aanpak van de zeer diverse aspecten van dit project. Daarbij werd mijn overtuigingskracht menig maal getest, want je laat je zeker niet zomaar iets wijs maken. Je hebt steeds tijd gehad als ik bij je aan de deur kwam en je hebt mijn publicaties en proefschrift met veel aandacht en zorgvuldigheid gelezen en becommentarieerd. Dat heeft in belangrijke mate bijgedrage aan de kwaliteit van dit proefschrift. Je hebt altijd achter mij gestaan en als het minder ging mij toch weer gemotiveerd en gestimuleerd. Dank je wel!

Dan ben ik aangekomen bij mijn directe collega en kamergenoot, Dannis. Zonder onze samenwerking en praktisch niet te stoppen grappenmakerijen was het project niet half zo leuk geweest. Je hebt me veel bijgebracht over construeren en mij doen inzien dat, hoewel werktuigbouwkunde aanvankelijk best makkelijk lijkt, het toch bijzonder ingewikkeld is. De in MEMS zo geliefde analytische aanpak van de vele mechanische proplemen bleek al snel te verzanden in oeverloos gereken zonder het bedoelde inzicht op te leveren. Voor inzicht blijken de werktuigbouwkundige zo hun eigen, beproefde methodes te hebben. Jouw van nature sterk ontwikkelde relati-

veringsvermogen heeft mij doen inzien niet alles even zwaar te laten wegen. Verder heb je ook mij aan de mountainbike gekregen en daar heb ik niet de minste spijt van. Het is een erg leuke sport in ik hoop in de toekomst nog eens wat rondjes met je te biken. Succes met de laatste loodjes!

De overige leden van het MAMS-team wou ik ook graag bedanken voor hun bijdrage aan een plezierige samenwerking en aan de nuttige en leerzame MAMS-dagen. Stefano en Johannes bedankt voor jullie inzet. I would like to thank Wei as well for is cooperation in this project. I wish you lots of success, now that the last period of the project also dawns for you.

Dit project was nergens geweest zonder de adviezen en technologische ondersteuning van Meint, Henri en Erwin. Voor het oplossen van de complexe fabricage problemen in dit project hebben jullie alles uit de kast gehaald. De uitstekende technologische ervaring en innovatie bij de MicMec is onmisbaar voor het succes van het onderzoek en dient gekoesterd te worden. Ook Rik verdient hier een vermelding. Dank je wel voor de fabricage run die je voor mij hebt gedaan toen ik inmiddels mijn handen vol had aan het schrijven van dit proefschrift.

Pino, hartelijk dank voor je hulp bij al mijn wilde meetplannen. Jij, en in het bijzonder je lunch-opmerkingen, dragen voor een belangrijk deel bij aan goede MicMec-sfeer. Je enorme aandeel in allerlei MicMec activiteiten dient hier ook niet vergeten te worden. Zelfs bij *mijn* promotie bleef jou een optreden als paranimf niet bespaard, ook hiervoor dank.

Het onderzoek in dit project heeft ook zeer gebaad bij de inzet van Tijs en Johan, die binnen dit project respectievelijk hun afstudeeropdracht en eigen onderzoeksopdracht met succes hebben vervuld. Dank jullie wel.

De cleanroom kan gezien worden als een erg belangrijke en vaak ook onvoorspelbare factor in het slagen van het onderzoek. Ik wou daarom het cleanroom personeel van harte bedanken voor hun inzet de faciliteiten draaiende te houden; Bert, Dominique, Eddy, Gerard, Gerrit, Hans, Huib, Ite-Jan, Marion, Peter, Rene, Samantha.

Dan zijn er nog een heel aantal collega's bij de MicMec, oud en nieuw, die allen bijdragen aan de goede sfeer en het succes van deze groep; Arjan, Berker, Deladi, Dennis, Dick, Doekle, Duy, Edin, Edwin, Florian, Han, Hanh, Henk van W., Henk W, Hien, Imran, Ingrid, Jeroen, John, Joost, Judith, Kees, Laura, Luis, Marcel, Marcus, Martijn, Mink, Nataliya, Niels, Philip, Regina, Remco, Roald, Sandeep, Saravanan, Satya, Siebe, Srinivas, Stefan, Theo V., Theo L., Toon, Vitaly, Willem, Yiping. Dank jullie wel voor een fijne tijd.

Tenslotte, maar zeker niet op de laatste plaats wil ik mij richten tot mijn ouders, familie en vriendin. Papa en mama, door jullie toedoen heeft het mij aan niets ontbroken om dit alles te bereiken. Bedankt voor jullie onuitputtelijke steun (en geduld) bij

alles wat ik gedaan heb, ook als het nog zo ingewikkeld was. Ook dank aan mijn lieve zus, Rachel, die wat ik heb gedaan erg knap vindt. Ik vind jouw kunde om het leven van verstandelijk gehandicapte mensen zoveel plezieriger te maken ook erg knap en zou dat zelf echt niet kunnen. Dan mijn opa, die mij als jongetje de opengewerkte vliegtuigen in de hangaars op Schiphol liet zien en zo mijn liefde voor de techniek aanwakkerde. Dank u wel!

Maryana, mijn lieve vriendinnetje, jij kwam van ver en hebt mijn leven verrijkt. De afgelopen twee en een half jaar heb je voor mij onvergetelijk gemaakt en ik weet zeker dat er nog heel veel van zulke jaren zullen volgen. Dank je wel voor je onvoorwaardelijke steun en begrip voor mijn toewijding aan het proefschrift. ¡Muchas gracias niña linda, te amo! Ook dank aan je ouders en familie die mij zo geweldig gastvrij ontvangen hebben tijdens mijn laatste vakantie voor het grote schrijfwerk. Die adempauze is geen overbodige luxe gebleken.

Boudewijn de Jong
Enschede, oktober 2006

Biografie

Boudewijn Ruben de Jong is geboren op 7 maart 1978 te Zaandam. Na het behalen van het vwo-diploma aan het Pascal College te Zaandam in 1996, is hij elektrotechniek gaan studeren aan de Universiteit Twente. Naast zijn studie is Boudewijn actief als lid van E.T.S.V. Scintilla's jaarboek commissie 1998 en bij de openlucht theater commissie voor het zomerseizoen van 1999.

Vooral aangetrokken door de natuurkundige kant van de studie en de tot de verbeelding sprekende micromechanica, gaat hij van augustus t/m december 2001 stage lopen bij Sercalo Ltd., via Samlab IMT onder leiding van Prof. Nico de Rooij in Neuchâtel, Zwitserland. Dit spin-off bedrijf geleidt door Cornel Marxer maakt optische componenten voor glasfiber communicatie netwerken, gebaseerd op MEMS technologie. Tijdens de stage is een computerprogramma geschreven voor automatische componentkarakterisatie en testrapportgeneratie in een database.

Weer terug in Nederland gaat Boudewijn beginnen aan een afstudeeropdracht bij de Transducer Science and Technology groep (TST) onder leiding van Miko Elwenspoek. Tijdens het afstuderen, begeleid door Remco Wiegerink, zijn teststructuren gemaakt voor een high-frequency power sensor in MEMS. In oktober 2002 studeert Boudewijn af en wordt elektrotechnisch ingenieur.

Opzoek naar een uitdaging in het MEMS onderzoek, begint Boudewijn in november 2002 aan zijn promotieonderzoek binnen het Multi Axes Micro Stage (MAMS) project, begeleid door Gijs Krijnen en wederom bij TST. Het werken aan een zes vrijheidsgraden precisie manipulator in MEMS boeit enorm en ook naast het werk is er volop tijd om promotie filmpjes te maken, te zeilen en te moutainbiken met collega's.